MODELING MICROSTRUCTURALLY SMALL CRACK GROWTH IN AL 7075-T6

A Thesis
Presented to
The Academic Faculty

by

Conor Daniel Hennessey

In Partial Fulfillment
of the Requirements for the Degree
Master of Science in the
School of Mechanical Engineering

Georgia Institute of Technology
August 2015

MODELING MICROSTRUCTURALLY SMALL CRACK GROWTH IN AL 7075-T6

Approved by:

Dr. David McDowell, Advisor
School of Mechanical Engineering
Georgia Institute of Technology

Dr. Richard Neu
School of Mechanical Engineering
Georgia Institute of Technology

Dr. Shuman Xia
School of Mechanical Engineering
Georgia Institute of Technology

Date Approved: 18 July, 2015

“The purpose of computing is insight, not numbers.”

-Richard Hamming

ACKNOWLEDGEMENTS

I would first like to thank my advisor, Dr. David McDowell, as his tremendous knowledge and insight were instrumental to the progression of this research. Additionally, I would like to thank the members of my thesis reading committee, Dr. Richard Neu and Dr. Shuman Xia.

I am particularly indebted to Dr. Gustavo Castelluccio, who developed a large portion of the computational framework upon which my research is based. I am also grateful for the weekly video conferences and innumerable emails that Dr. Castelluccio and I exchanged, as they were invaluable to my progress as a researcher.

I also want to express my gratitude to my fellow graduate students in the McDowell lab. The daily discussions, interchange of ideas, and even office pranks that I shared with them made the experience of graduate school that much more rewarding and enjoyable. I'd like to extend a special thanks to Matthew Priddy, whom I could always count on for advice, whether it was about the intricacies of crystal plasticity and UMATs, or just life in general.

Finally, I want to thank my family for their unwavering support and encouragement, not just during my time here at Georgia Tech, but always. I wouldn't be where I am today with their many years of love and guidance.

TABLE OF CONTENTS

LIST OF TABLES

Page

LIST OF FIGURES

Page

LIST OF ABBREVIATIONS AND SYMBOLS

AF	Armstrong and Frederick
EPFM	Elastic Plastic Fracture Mechanics
FCC	Face-Centered Cubic
FEM	Finite Element Method
FIP	Fatigue Indicator Parameter
FIP^{α}	Fatigue Indicator Parameter on slip system α
FIP_0	Fatigue Indicator Parameter prior to cracking grain
FS	Fatemi-Socie
HCF	High Cycle Fatigue
ISV	Internal State Variable
LCF	Low Cycle Fatigue
LEFM	Linear Elastic Fracture Mechanics
MSC	Microstructurally Small Crack
OW	Ohno and Wang
PSB	Persistent Slip Band
PSC	Physically Small Crack
UEXTERNALDB	User EXTERNAL DataBase subroutine
UMAT	User MATerial subroutine

b_i	Saturation level of i^{th} back stress term
σ	Cauchy stress tensor
ΔCTD	Cyclic crack tip displacement
ΔK	Range of stress intensity factor

ΔJ	Range of J-Integral
C_{ijkl}	4^{th} Order anisotropic elastic stiffness tensor
$\bar{C}_{ijkl}$	4^{th} Order anisotropic elastic stiffness tensor with damage
$\delta^{\alpha\beta}$	Kronecker delta
$\tilde{d}$	Scalar damage parameter
E^{ed}	Elastic-damaged Green strain tensor in intermediate configuration
F	Deformation gradient
F^{ed}	Elastic-Damaged deformation gradient
F^{p}	Plastic deformation gradient
$\dot{\gamma}^{\alpha}$	Shear strain rate of slip system α
g^{α}	Drag stress on slip system α
$\dot{g}^{\alpha}$	Rate of change of drag stress on slip system α
$h^{\alpha\beta}$	Plastic hardening modulus matrix
k	Fatemi-Socie constant
L	Velocity gradient in current configuration
L^{ed}	Elastic-damaged velocity gradient in current configuration
L^{p}	Plastic velocity gradient in current configuration
m^{α}	Slip plane normal of slip system α
m_0^{α}	Slip plane normal of slip system α in intermediate configuration
m_i	Exponent controlling the activation of the recall term in OW back stress hardening law
N_{total}	Total fatigue life
$N_{inc,part}$	Life to incubate crack at particle-matrix interface
N_{nuc}	Life to grow the crack through the nucleant grain

N_{MSC}	Microstructurally small crack life
N_{PSC}	Physically small crack life
N_{LC}	Long crack life
s^{α}	Slip direction vector of slip system α
s_0^{α}	Slip direction vector of slip system α in intermediate configuration
T	Second Piola-Kirchoff stress tensor in intermediate configuration
χ^{α}	Back stress on slip system α
$\dot{\chi}^{\alpha}$	Rate of change of back stress on slip system α

SUMMARY

The objective of this work is to model the nucleation and propagation behavior of microstructurally small fatigue cracks in Al 7075-T6. This regime of crack growth accounts for much of the scatter present in fatigue lives, and can consume up to 90% of the total fatigue life during high cycle fatigue loading. To accomplish this objective, this thesis extends the doctoral and post-doctoral research of Gustavo Castelluccio, who developed a framework to model microstructurally small fatigue cracks in nickel-based superalloy RR1000.

The major contributions of this work are twofold. First, the introduction of a crystal plasticity constitutive relation for Al 7075-T6, which correlates well to experimental stress-strain data over a large range of loading conditions, including loading with a mean stress or strain, and the incorporation of the fatigue algorithms of Castelluccio with this constitutive model. Second, the enhancement of the mesoscale fatigue modeling framework developed by Castelluccio to allow for Stage II growth along non-crystallographic planes of lowest life.

CHAPTER 1: INTRODUCTION

1.1: Introduction

Fatigue of metals is a problem that affects almost all sectors of industry, from energy to transportation, and failures to account for fatigue or incorrect estimations of service life have cost many lives. This is especially true in aerospace applications, where the consequences of a failure are particularly high and there is a strong motivation to reduce weight as much as possible. Aluminum alloys are widely used in the aerospace industry for their high specific strength, and thus large amounts of effort have been expended to characterize the performance of these alloys under cyclic loading.

Obtaining the fatigue properties of a material under a wide range of loading spectra and environments, such as a component might see over the course of its service life, has traditionally required exhaustive experiments to generate the constants used in empirically-based laws. Although these relations are adequate for the prediction of fatigue lives under some conditions, because of their empirical nature they offer little insight into the underlying physical phenomena that govern the fatigue behavior of a particular material. The accumulation of fatigue damage is a complex multi-scale process, with length domains ranging from atomistic to structural, and is driven by multiple mechanisms that may compete with or enhance one another, and may change over the life of a specimen. While some aspects of the process are well understood, such as the growth of long cracks, there are still a number of open questions.

One such open issue is modeling fatigue cracks with dimensions on the order of the microstructure, the propagation of which is dominated by influence of the local

heterogeneity of the microstructure. Even for materials that been in use for many years, this process is not fully understood. For example, Al 7075-T6, a high-strength, low density precipitation hardened alloy used extensively in aerospace applications, was introduced to market in 1943 [1] and many researchers are still actively working towards better understanding microstructurally small crack (MSC) growth in this alloy. The creation of a computational model based on the governing physics of MSC growth in Al 7075-T6 allows us to perform simulations evaluating the fatigue performance of the alloy under a large range of loading spectra much more rapidly than equivalent experiments could be performed. The insight gained from these simulations is twofold. First, we can gain insight into the microstructural parameters that control the fatigue life, and this knowledge can guide the modification of materials to enhance fatigue resistance. Second, comparison of the simulated results to experimental data gives us insight into the model itself, allowing us to assess if we are truly capturing the governing physics of the problem.

In order to successfully model the growth of these microstructurally small cracks (MSCs), two computational frameworks are necessary. First, the local behavior of the material must be captured, necessitating a constitutive relation with resolution on the scale of grain size. Second, a physically based model for the nucleation and growth of microstructurally small fatigue cracks is needed. The overall objective of this thesis is best summarized as the introduction these two computational frameworks, the constitutive model and fatigue model, specifically for aluminum alloy 7075-T6.

1.2: Scope of Thesis

This thesis is primarily an extension of the research performed by Castelluccio [2], who introduced a crystal plasticity based, mesoscale fatigue model for nickel-based

superalloy RR1000. The model employed by Castelluccio is mesoscale in two senses. First, each computational loading cycle typically corresponds to many hundreds or thousands of simulated loading cycles. Second, the model simulates cracks propagating in increments comprising many cycles on the order of grain size, reducing the number of computational cycles that must be applied.

The constitutive behavior of Al 7075-T6 differs substantially from that of RR1000, necessitating the use of a different constitutive model. Therefore, this work introduces a crystal plasticity constitutive model for aluminum alloy 7075-T6 based on the work of McGinty [3]. Additionally, the Al 7075-T6 constitutive model includes an Ohno-Wang type backstress evolution law adapted for crystal plasticity in order to better capture the material response under asymmetric cyclic loading. This is the first time such a back stress formulation has been employed in a crystal plasticity model, representing a key novel contribution of this work.

The two materials also exhibit somewhat different underlying fatigue processes. When cyclically loaded the Ni-based superalloy tends to deform heterogeneously, with slip localizing in persistent slip bands which largely control the nucleation and MSC propagation behavior of the alloy. In contrast, cyclic loading of Al 7075-T6 produces more homogeneous deformation. The nucleation behavior of Al 7075-T6 is dominated by the effect of cracked second-phases and cracks may propagate on multiple slip systems within a grain. Therefore, this research extends the fatigue model of Castelluccio in order to consider the driving force of cracks propagating on multiple slip systems, and to allow for propagation on non-crystallographic planes.

1.3: Thesis Outline

This thesis begins with a brief historical overview of the commonly employed fatigue life estimation methodologies, as well as some of the drawbacks to these traditional approaches. Critical plane and Fatigue Indicator Parameter (FIP) concepts are then introduced, along with a short review of recent advances in the field of computational fatigue modeling. The remainder of Chapter 2 covers the physical processes of fatigue, focusing on precipitation hardened aluminum alloys with specific attention given to Al 7075 in the peak aged condition.

The constitutive modeling of Al 7075-T6 is covered in Chapter 3, which begins with an introduction to the kinematics of crystal plasticity. Once these kinematics have been established, the three forms of constitutive laws used in this research are presented, and the motivation behind the introduction of each model form is discussed. Focus then shifts to the implementation of the kinematics and constitutive laws within ABAQUS [4], a popular commercial finite element analysis software. Finally, the cyclic stress-strain responses of the three model forms are compared under fully reversed loading and loading with an imposed mean stress/strain.

The mesoscale fatigue model is presented in Chapter 4. The conceptual and theoretical underpinnings of the fatigue model are presented first, including estimation of the driving force for MSC crack growth, the creation of digital microstructures, and the volume averaging scheme. After a brief review of the Stage I fatigue crack growth model developed by Castelluccio, a Stage II model is presented which incorporates the driving force on multiple slip systems and allows for crack growth across arbitrarily defined planes within the microstructure. The implementation of this fatigue model within the Abaqus environment is then discussed.

Chapter 5 focuses on the application of the mesoscale fatigue model to Al 7075-T6 and begins with the calibration of the model to experimental data. The chapter then examines impact that the specific forms of the constitutive models introduced in Chapter 3 have on the simulated FIP values and predicted fatigue lives. Next, results from simulations under uniaxial and shear loading applied at different amplitudes are presented and the agreement with experimental data and trends is examined. In addition, the impact of periodic overloads and combined uniaxial and shear loading are explored. The chapter closes with a discussion of the effects of mesh refinement and simulated microstructural volume.

Finally, the contributions of this thesis are summarized in Chapter 6, along with conclusions and directions for future research. An appendix is included that provides further information regarding the implementation of the fatigue algorithms and crystal plasticity model in the ABAQUS [4] environment.

CHAPTER 2: FATIGUE OVERVIEW

2.1: Introduction

Fatigue is the process of crack formation and growth when materials are subjected to cyclic loads. This process occurs at load amplitudes below the static strength of the material and can result in the component failure with catastrophic consequences, including significant losses of both human life and capital. To mitigate such fatigue failures, engineers must be able to reliably predict the fatigue life of components under service conditions. Great progress has been made in this regard in the past 40 years. An aspect of fatigue that is still being actively researched is the behavior of microstructurally small cracks (MSCs), which can diverge significantly from that of long cracks. The portion of life spent nucleating and growing a MSC over the first few grains/phases can consume over 90% of the total fatigue life under High Cycle Fatigue (HCF) conditions and is the primary source of the scatter in fatigue lives. Therefore, the development of robust fatigue design methodologies requires that the MSC regime of crack growth can be adequately modeled.

This chapter begins by discussing classical approaches to fatigue design and life prediction, as well as the limitations of these methodologies, in order to illustrate the motivation for the modeling preformed during the course of this thesis. Focus then shifts to the physical basis of the fatigue damage process in precipitation hardened aluminum alloys, particularly Al 7075-T6, which is the main focus of this work.

2.2: Fatigue Overview

The first widely adopted tool for predicting the fatigue lives of metals subjected to cyclic loading was the stress-life (S-N) approach, which is still commonly used today. Although pioneered by Wöhler (1860) it was Basquin in 1910 who related the applied stress range and fatigue life above the endurance limit through a power-law formulation

$$\frac{\Delta\sigma}{2} = \sigma_{\mathrm{f}}^{'}\left(2N_{\mathrm{f}}\right)^{b} \qquad (1)$$

where the constant $\sigma_{\mathrm{f}}^{'}$ is the fatigue strength coefficient and b is the fatigue strength exponent. This equation is typically referred to as either the Basquin Equation or the stress-life approach, and is valid in the high cycle fatigue (HCF) regime where the material deforms elastically on a macroscopic scale.

The second widely used approach to fatigue life estimation is the strain-life methodology. This approach is a combination of a modified form of the Basquin equation with a power law relation based on the separate work of both Coffin and Manson in 1954. The strain-life approach is expressed mathematically as

$$\frac{\Delta\varepsilon}{2} = \frac{\sigma_{\mathrm{f}}^{'}}{E}\left(2N_{\mathrm{f}}\right)^{b} + \varepsilon_{\mathrm{f}}^{'}\left(2N_{\mathrm{f}}\right)^{c} \qquad (2)$$

where the constants $\varepsilon_{\mathrm{f}}^{'}$ and c are referred to as the fatigue ductility coefficient and the fatigue ductility exponent, respectively, and are used to fit the model to experimental data. The first term on the right hand side of Eqn. 2 captures the effect of the elastic component of strain and the second term the influence of the plastic component of the total strain. This particular approach is well suited for analyzing Low Cycle Fatigue (LCF) loading where significant levels of macroscopic plastic strain occur during cycling.

The development of linear elastic fracture mechanics in the 1900's by researchers such as Inglis (1913), Griffith (1921), and Irwin (1957) laid the foundation for the introduction of fatigue laws based on the driving force at the crack tip. In 1961 Paris et al. [5] published a paper relating the driving force at the crack tip (quantified using the change in stress intensity factor, ΔK, over the loading cycle) to the increment in crack growth per cycle. This relation is known as the Paris law and is typically given in the form

$$\frac{da}{dN} = C\left(\Delta K\right)^m \qquad (3)$$

where C and m are constants used to fit the equation to experimental crack growth data. Various modifications to the Paris law have been proposed in order to capture effects such as the influence of R-ratio or periodic overloads on the rate of crack propagation. When the relation between da/dN and ΔK is plotted schematically as in Figure 1, there are three distinct regimes of crack growth. In Regime A the diving force (ΔK) is near or below the threshold level (ΔK_{th}) for long crack growth. This can occur either because the crack is long and the far-field stresses in the body are low, or the crack is very short, typically less than a mm long. Regime B is referred to as the Paris Regime, and the relationship given by Eqn. 3 is valid. In Regime C the crack driving force (ΔK) approaches the level of the materials fracture toughness of the material (K_{IC}) and the crack propagates rapidly until failure.

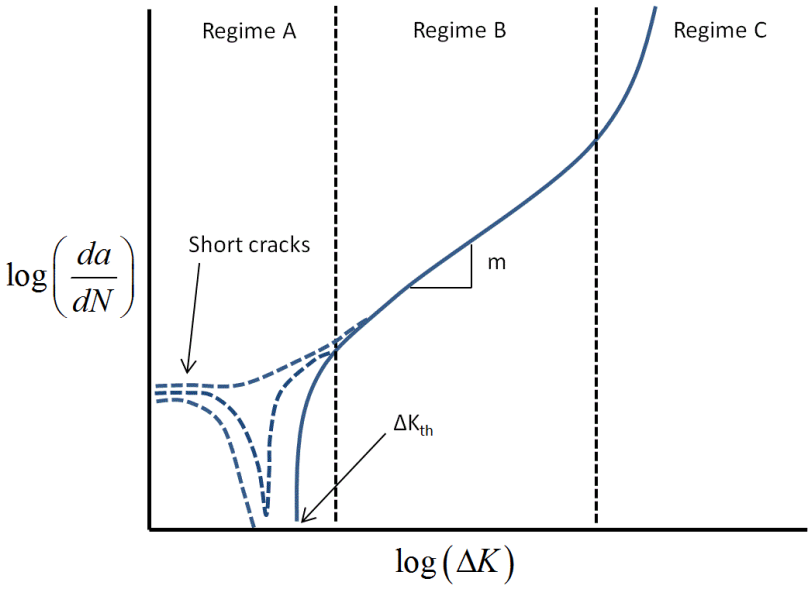

Figure 1. Three regimes of crack growth and small crack effects. Adapted from [6].

While the Paris law can adequately model the growth of long cracks (typically on the order of millimeters), small cracks can grow orders of magnitude faster than long cracks for the same level of nominal driving force. This is shown in Regime A of Figure 1 where short cracks (dashed blue lines) propagate below the long crack threshold. Failure to account for this phenomenon could result in non-conservative fatigue life and have potentially disastrous consequences. The inability of the Paris law to adequately characterize the behavior of small cracks is due to the violation of the LEFM assumptions underlying the calculation of ΔK. At very small crack lengths the material can no longer be considered homogeneous and the local microstructure has a strong influence on the stress state at the crack tip. A crack is classified as a microstructurally small crack (MSC) when all dimensions are on the scale of the characteristic microstructural length, such as the grain size. For a microstructurally short crack, however, the crack size in the direction of propagation is on the order of the characteristic microstructural dimension, but the

other dimensions such as crack periphery may be large. The difference between a microstructurally short crack and a microstructurally small crack is illustrated schematically in Figure 2.

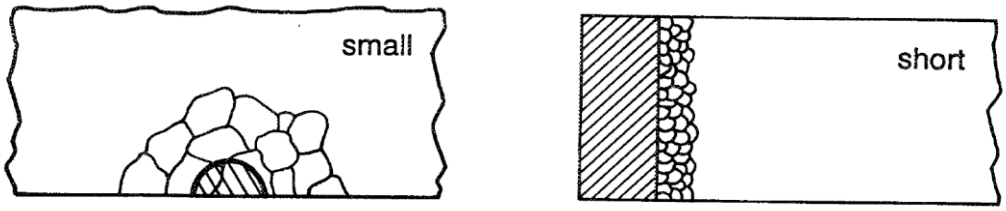

Figure 2. Diagram illustrating the difference between short and small cracks [7].

Microstructurally small crack growth begins following nucleation, and as the crack grows through the MSC regime, it may retard or arrest as the crack front encounters microstructural barriers, which in Al 7075-T6 are primarily grain boundaries. The influence of the microstructure diminishes as the crack propagates and the crack front samples an increasing number of grains, until the crack has grown long enough that the cyclic plastic zone can be considered to be a homogeneous material and the crack growth rate is largely independent of microstructure. At this point the crack may still be small compared to the dimensions of the specimen or part geometry, and are thus classified as Physically Small Cracks (PSCs). Although there is not a sharp transition from MSC growth to PSC growth, many researchers consider a crack depth of 3-10 grains to be sufficient [8].

Of the three fatigue analysis methodologies discussed, the stress-life and strain-life approaches are both total-life approaches to a given, pre-defined crack size or definition of failure (e.g., specimen separated into two pieces), combining the multi-stage process of crack nucleation and growth into a single life value. This can obscure the

underlying physical phenomena that govern the nucleation and various stages of growth of a crack, which may change depending on a large number of factors such as the length, loading type, or environment. Additionally, all approaches discussed thus far are essentially macroscopic or at best mesoscopic (over many grains), empirical relations that fail to capture the influence of the microstructure on the driving force of small cracks with size on the order of individual grains or phases. Consequently, these laws provide little insight into the fatigue damage process and no guidance for the predictive design of materials and microstructures with enhanced fatigue resistance.

2.3: Critical Plane Approaches and FIPs

A large number of enhanced stress, strain, and energy based models have been introduced to address the shortcomings associated with the basic stress- and strain-life approaches [9] and to address multiaxial fatigue loading. With regard to multiaxial loading, the most notable and arguably successful of these models are based on the concept of a critical plane. Brown and Miller [10] argued that the because fatigue damage is driven by cyclic slip, which is in turn reflected by shear strain, it is the plane of maximum shear strain range that best captures the crack driving force and and likely crack orientation for transgranular fatigue crack formation and growth. Additionally, they included the effect of tensile strain on the plane of maximum shear to account for enhancement of dislocation mobility and the decohesion process at the crack tip. This relation (slightly modified from the original form) is given by

$$\Delta\gamma_{\max} + S\Delta\varepsilon_n = f(N_{\mathrm{i}}) \qquad (4)$$

where $\Delta\gamma_{\max}$ is the maximum shear strain range, $\Delta\varepsilon_n$ is the strain normal to the plane of maximum shear strain range, S is a parameter that controls the influence of the tensile strain term, and $f(N_i)$ is a constant for a given number of cycles to initiate a crack.

Fatemi and Socie [11] proposed a modification to the approach of Brown and Miller, replacing the term capturing the normal strain on the plane of maximum shear with the peak stress normal to the same plane. To retain the dimensionless nature of the Brown and Miller parameter, Fatemi and Socie normalized the stress on the plane of maximum shear by the material cyclic yield strength. The macro-scale form of the equation is commonly expressed as

$$\frac{\Delta\gamma_{\max}}{2}\left(1+k\frac{\sigma_n^{\max}}{\sigma_{ys}}\right)=f(N_i) \qquad (5)$$

where $\sigma_n^{\max}$ is the stress normal to the plane of maximal shear, σ_{ys} is the yield strength of the material, and k is a constant that controls the influence of the normal stress term. The physical basis for the enhancement effect of normal stress in the Fatemi-Socie parameter is that tensile stress act to separate the crack surfaces and thus reduce frictional forces along the length of the crack that dominantly propagates in shear. This leads to an increase of stress at the crack tip and increased rates of crack growth [9]. This effect is illustrated schematically in Figure 3, which compares two shear cracks: one loaded entirely in shear (left), and one with an additional tensile stress acting normal to the plane of the crack (right).

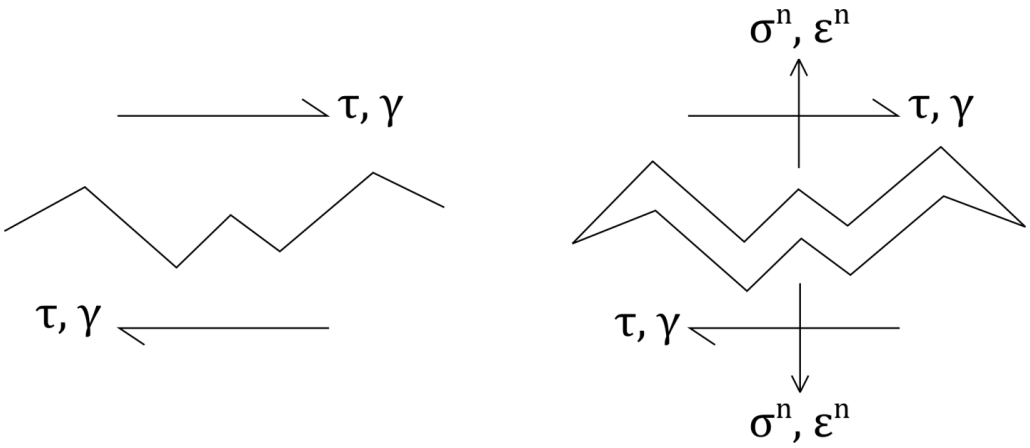

Figure 3. A diagram of the effect of normal stress on a crack propagating in shear. Adapted from [12].

Numerous researchers have demonstrated ability of the Fatemi-Socie critical plane approach to predict fatigue lives under multiaxial conditions for a range of materials. Notably, McDowell and Berard [13] demonstrated that for Stage I dominated growth the Fatemi-Socie parameter has an interpretation analogous to the ΔJ-integral of elastic-plastic fracture mechanics (EPFM), capturing the driving force for microcrack propagation. McDowell [14] further showed that the Fatemi-Socie parameter resulted in a parametric form across a range of strain states in multiaxial fatigue that reflected typical experimental findings.

While originally derived for macro-scale analysis, critical plane approaches have recently been adopted for use on a microstructural scale in the form of Fatigue Indicator Parameters (FIPs), reviewed in depth by McDowell and Dunne [15]. When the stress and strain fields within a grain are computed using crystal plasticity constitutive models, the planes of maximum plastic shear strain range tend to align with the crystallographic planes on which Stage I fatigue cracks form. Therefore, FIPs may be employed to capture the local driving force within a grain for the nucleation and growth of short

cracks. Good correlation has been shown by several researchers between local, microstructurally based FIPs and fatigue lives [2, 16, 17].

Recently, detailed modeling efforts have considered different aspects of fatigue crack formation specifically in Al 7075-T6. This body of work included:

I. Probabilistic simulation of constituent particle cracking in Al 7075-T651 [18].
II. Physically based modeling of microstructure-dependent slip localization and crack nucleation mechanisms in Al 7075-T651 [19].
III. Development of a semi-empirical model for nucleation [20].

This approach employed a crystal plasticity constitutive model [18] along with a model for predicting cracking of constitutive particles under an applied load. This model was coupled with a slip-based, non-local nucleation metric [19] and five separate nonlocal nucleation parameters (including a FS-based parameter) were investigated, and these were compared to experimental results [20]. Using EBSD data, the microstructure of experimental specimens was represented in a finite element model, and the nucleation driving forces calculated. In Figure 4, an example is presented of a finite element reconstruction of an actual microstructure and subsequent calculation of one metric that can be used for fatigue crack nucleation, namely the maximum accumulated slip on a slip system (referred to as metric D1 in [20]).

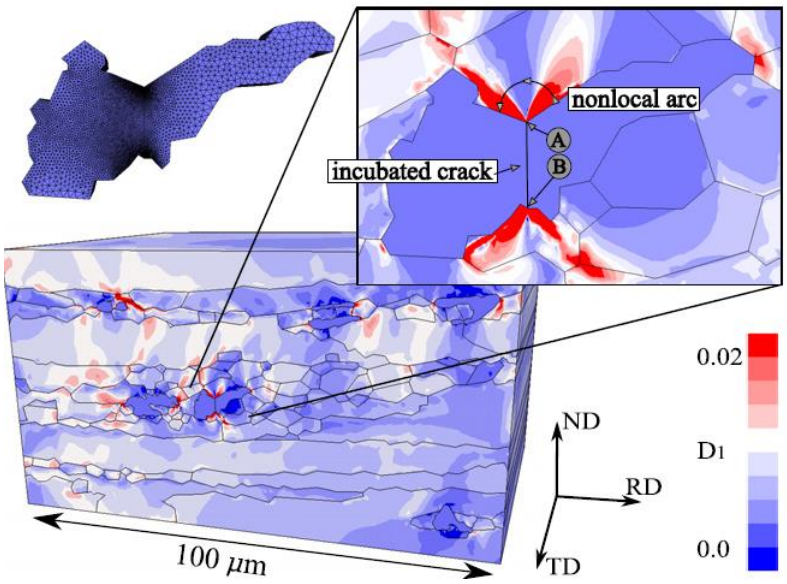

Figure 4. Finite element representation and analysis of an Al 7075-T6 microstructure [20].

The study concluded that the computed magnitude of slip localization and accumulation provided a valid metric for determining which incubated cracks would nucleate, and that the computed tangential stress in the matrix surrounding the incubated the crack could be used to predict the number of cycles until nucleation [20]. The direction of nucleation and propagation of the crack was also shown to be strongly correlated with the peak tangential stress. An example of the correlation is shown in Figure 5.

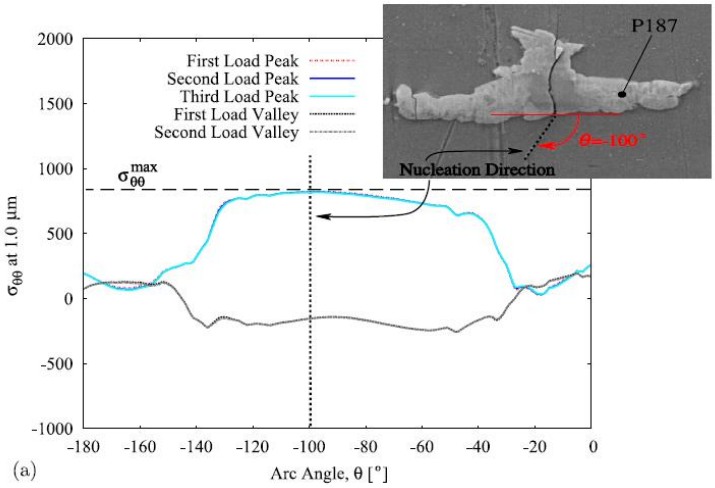

Figure 5. Simulated tangential Stress versus arc angle compared to observed fatigue crack nucleation orientation [20].

Execution of a model as detailed as the one developed by Hochhalter et al. and coupling it with crack extension through the microstructure to simulate both crack nucleation and MSC growth would be prohibitively computationally expensive. However, there are still a number of important results that can be incorporated into our nucleation and early growth models:

- Slip based metrics are valid for fatigue crack formation and early crack growth under these conditions.
- Normal stress strongly influences the direction of crack propagation, albeit in perhaps a more subtle way from a physical standpoint (slip irreversibility and local crack advance) than is reflected by typical normal stress parameters and formulations.

As noted by Castelluccio et al. [21], the work of Hochhalter et al. reinforces the importance of both selecting an appropriate FIP and an appropriate domain of FIP computation that captures the underlying physical processes, i.e. because fatigue damage occurs in a finite physical volume, calculating a FIP value at a single point may result in a poor characterization of nucleation and growth behavior.

Modeling of fatigue crack formation and MSC propagation in Al 7075-T6 was also performed by Xue et al in 2007 [22], and was based on an earlier companion study of micromechanics in 7075-T6 [23] and earlier modeling work in cast aluminum alloy A356-T6 [24]. Analysis of multiple finite element models of a fractured spherical inclusion embedded in an Al matrix was done to evaluate the effect of size of initiating particle on resulting plastic strain accumulation at the micronotch root formed by the fractured inclusion. A non-localized metric of the maximum plastic shear strain at the micronotch root was determined as a function of remote applied strain amplitude and was related to the incubation life through a modified Coffin-Manson law. A Fatemi-Socie model for nucleation life was also proposed, but not discussed in detail. The study also modeled crack growth in the MSC and PSC regime. Growth rate of the crack was related to the range of the crack tip displacement via the relation

$$\left.\frac{da}{dN}\right|_{\text{MSC/PSC}} = \phi\left(\Delta CTD - \Delta CTD_{th}\right) \qquad (6)$$

where ϕ is a material constant that accounts for crack tip irreversibility, and ΔCTD_{th} is the threshold crack tip displacement. The cyclic crack tip displacement range (ΔCTD) provides common ground for growth laws for all stages of fatigue beyond nucleation, and is often used as a driving force to model the growth of short cracks. Xue and coworkers found a good correlation between experimental data and the model for the 7075-T651 alloy, for both high cycle and low cycle fatigue.

Johnson and coworkers [25] used a three dimensional crystal plasticity model to investigate the effect of grain orientation on the driving force of microstructurally small cracks in 7075-T651. The variability of the modeling results was compared to small crack

data obtained by Lankford et al. [26], and was found to be of the same order of magnitude. Johnson et al. [25] concluded that the scatter in small fatigue crack growth was due in large part to crystallographic orientation effects. The results also showed that orientations with multiple slip systems at the crack tip exhibited faster growth rates and a larger ΔCTOD. Burns and coworkers [27] performed further analysis of the work performed by Johnson et al. to attempt to quantify the contribution of crystallographic orientation in their own data. It was hypothesized that if the mean peak equivalent plastic strain ($\varepsilon_{p\text{-}max}$) was proportional to da/dN, then the +/- 80% variation in $\varepsilon_{p\text{-}max}$ in the simulations of five different crystallographic orientations done by Johnson et al. could explain +/- 80% of the variability found in the experimental results obtained by Burns and coworkers. This is a significant proportion of the total variability the experimental results (+/- 130%). The remaining difference in the variability between the FEA model and the experimental data was attributed to the effects of roughness induced closure, crack deflection and interaction with grain boundaries.

2.4: Physical Basis of Fatigue in Al 7075-T6

Al 7075 is a wrought Aluminum alloy based on the quaternary Al-Zn-Mg-Cu system. The nominal composition of Al 7075-T6 is given in Table 1.

Table 1. Nominal composition of Al 7075-T6 [1]. Elements are listed by wt. %.

Zn	Mg	Cu	Fe	Si	Cr	Ti
5.1-6.1	2.1-2.9	1.2-2.0	0.5	0.4	0.18-0.28	0.2

The alloy is precipitation hardened, with most applications typically using a peak aged (-T6) or overaged (-T7) temper. In precipitation hardened Al alloys secondary phases are

typically categorized as precipitates, dispersoids, or constituents [28]. Typical sizes of these particles and examples in Al-7075 are listed in Table 2.

Table 2. Secondary Phases in Al 7075

Type	Size	Examples
Constituent	1-50 μm	Al_7Cu_2Fe, Mg_2Si
Dispersoid	20-500 nm	$CrMg_2Al_{12}$
Precipitates	1-10 nm	GP Zones, η and η'

Strengthening precipitates harden the alloy by impeding the migration of dislocations and largely control the slip behavior of the alloy. The general trend is that increasing precipitate size and spacing (longer aging treatments) results in increasingly wavy slip and less coarse spacing of slip bands [29]. Differences in precipitate size and spacing due to aging treatments are visible in Figure 6 which compares a peak aged 7075-T6 alloy to an overaged 7075-T73 alloy.

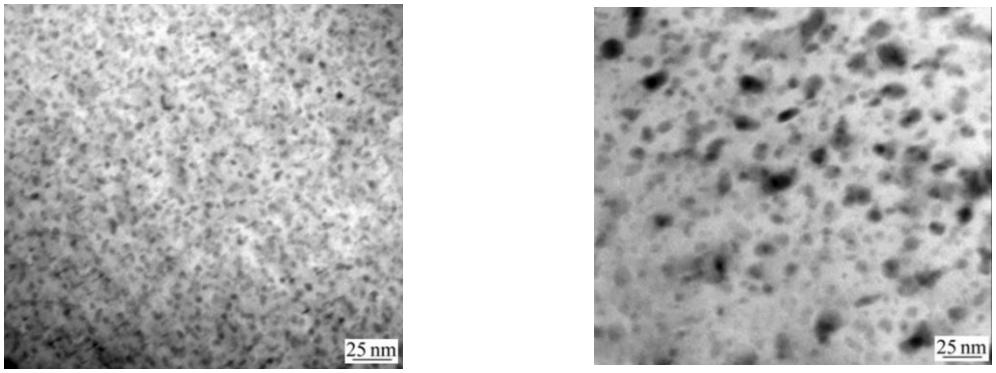

Figure 6. A comparison of TEM bright field micrographs of a grain interior of an Al 7075 alloy with T6 (left) and T73 (right) heat treatments [30].

LaFarie-Frenot and Gasc [31] conducted fatigue testing of several different heat treatments of 7075 under vacuum and identified the effect of precipitates on slip character. They found that precipitates in the underaged (UA) heat treatments consist of small Guinier Preston (GP) zones that are coherent with the matrix, and are easily sheared by moving dislocations. The presence of sheared GP zones results in mechanically reversible migration of dislocations, leading to planar slip and crystallographic fatigue facets. Crack propagation in this heat treatment was characterized by low growth rates due to the relatively higher degree of reversibility of planar slip compared to wavy slip. In general, the role of extrinsic plasticity- and roughness-induced closure is less prominent for microstructurally small cracks; accordingly, intrinsic effects such as degree of slip planarity play a more important role [32].

In the peak-aged condition the material contains the highest volume fraction of closely-spaced η and η' ($MgZn_2$) precipitates, resulting in maximum strength. These precipitates are larger than the GP zones of the under-aged alloy, but are still amenable to shearing by dislocations. At low cyclic stress levels, only one slip system may be active, leading to a failure mode similar to the UA alloy; at higher stresses, multiple slip systems are activated, resulting in more homogeneous deformation, similar to the overaged (OA) condition and a flat crack path. This transition was found to correspond to a cyclic plastic zone size of 80 μm (compared to a grain size of 150 μm).

In the OA alloy, particles are large and partially-incoherent with the Al matrix. They are not as easily shearable, so dislocations tend to loop (Orowan mechanism) or cross-slip

around these particles, creating a diffuse and wavy slip character. The higher irreversibility of this slip mode results in increased fatigue crack propagation rates.

For 7000 series Al alloys, Lin and Starke [33] demonstrated the effect of Cu content on slip behavior; lower Cu-content Al-Zn-Mg-Cu alloys had a greater quantity of shearable precipitates, which led to strain localization and coarse planar slip. Increases of Cu content (up to 2.1%) were associated with increasingly diffuse slip and wavy slip-bands, since strengthening precipitates are looped rather than sheared. Images comparing coarse planar slip to more diffuse slip are shown in Figure 7.

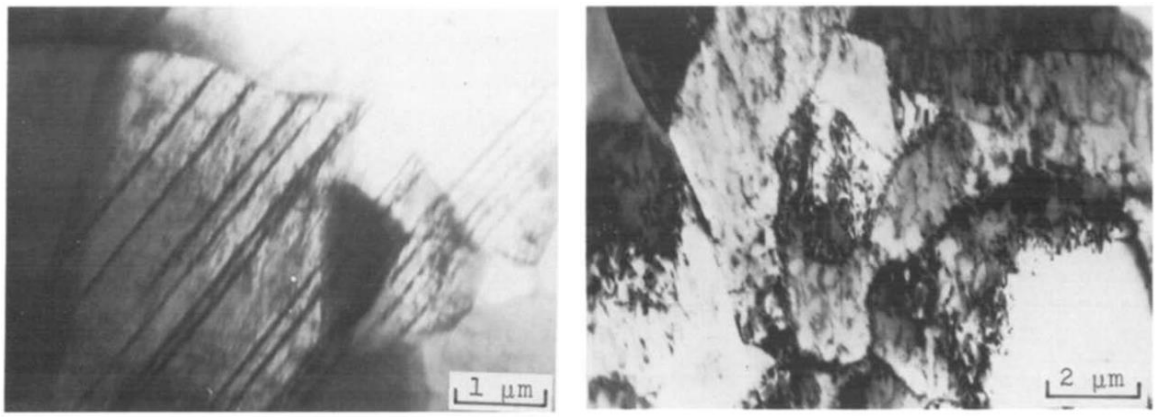

Figure 7. Planar slip in a an Al-Zn-Mg-1%Cu alloy (left) compared to more homogeneous deformation in an Al-Zn-Mg-2.1%Cu alloy (right). Photographs from [33].

These changes in slip behavior observed by Lin and Starke had a direct effect on crack growth rates and propagation direction. Decreasing copper content resulted in decreasing crack growth rates, and was associated with zigzag crack growth and crack branching through slip plane decohesion. Higher Cu-content resulted in non-crystallographic crack growth and a straight crack path running perpendicular to the loading axis, typical of Stage-II growth.

Dispersoids are larger than precipitates and are formed in Al 7075 through solid state precipitation of chromium and serve to retard grain growth and prevent recrystallization during processing. The $Al_{12}Mg_2Cr$ dispersoid particles formed in Al 7075 are incoherent with the matrix and do not have a substantial effect on strength. Some researchers have documented influence of dispersoid particles on fatigue behavior is at high ΔK values that approach the critical fracture toughness (K_{IC}) [34].

Constituent particles (or secondary intermetallics) are the largest second-phase in the matrix and play an important role in the nucleation of fatigue cracks. Damage to these brittle particles can also contribute to the Bauschinger effect during reversed loading [35]. Typical constituent particles present in 7075-T6 include $MgZn_2$, $Mg_3Zn_3Al_2$, Al_7Cr, Mg_2Si and Al_7Cu_2Fe [36].

2.4.1: Fatigue Crack Nucleation

In precipitation hardened Aluminum alloys, fatigue crack formation is dominated by existing defects within the material. For material exposed to corrosive atmospheres the initiating feature is typically a pit formed by corrosion. For normal ambient environments cracks typically form at fractured or debonded constituent particles, sometimes referred to as inclusion particles. These particles typically have a size of approximately 5 to 50 μm, an elongated aspect ratio along the rolling direction, and sometimes the cluster in small groups that are more detrimental to life. This has been documented by many different researchers for many different precipitation Al alloy systems and heat treatments including 7075-T6 [23, 27, 36-42], 2024-T3 [43-48] and 2024-T4 [49].

To facilitate discussion and analysis of crack formation of this particular alloy system, the total fatigue life (N_{total}) can be decomposed according to an hierarchical approach [24], i.e.,

$$N_{total} = N_{part,inc} + N_{nuc} + N_{MSC} + N_{PSC} + N_{LC} \quad (7)$$

The incubation life ($N_{part,inc}$) is the number of cycles required to form a crack within or at the interface of a constituent particle/inclusion at the sub-grain scale, which may occur during the first few loading cycles depending on stress/strain amplitude. The nucleation life (N_{nuc}) is the number of cycles between the occurrence of a crack emerging from a constituent particle (cracked or debonded) and propagation of this crack into the surrounding matrix to a prescribed extent, typically on the order of the size of the nucleant grain or phase. In this work, the first two terms comprise the process of fatigue crack "formation", whereas the remaining terms characterize fatigue crack growth. The relative contributions of the MSC, PSC and LC fatigue crack growth regimes are discussed in greater detail later in this chapter.

Early work on 2024-T3 by Grosskreutz and Shaw [50] found that fatigue cracks formed in the vicinity of large inclusion clusters containing iron and silicon. Bowles and Schijve [48] obtained results in good agreement with Grosskreutz and Shaw, and also noted that particles at which fatigue cracks formed were typically 1 μm to 10 μm in size. For 2024-T4, Kung and Fine [49] found that cracks initiated from either S-phase (Al_2CuMg) or β-phase (Al_7Cu_2Fe) particles, typically larger than 6 μm.

Laz and Hillberry [47] performed statistical analysis of constituent particles in fatigued samples of 2024-T3. Inclusions that formed cracks were found to be in the tail end of the constituent particle distribution, as illustrated in Figure 8.

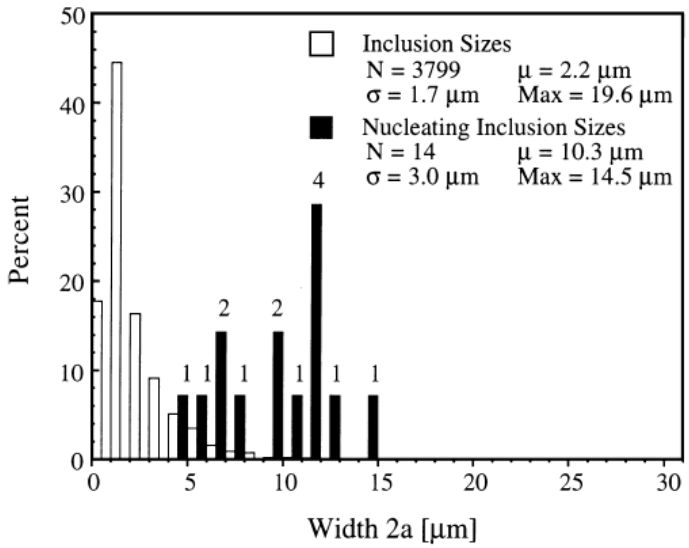

Figure 8. Size of particles/inclusions at which cracks formed compared to the overall particle distribution [47].

In addition, Laz and Hillberry measured the composition of the crack formation sites using EDS. The majority of particles that nucleated fatigue cracks contained iron, manganese, copper and Al. Iron containing particles were likely Al_7Cu_2Fe, consistent with the results obtained by Kung and Fine.

Recent work by Mayer et al. [43] investigated the fatigue behavior of 2024-T351 in the high cycle fatigue (HCF) and very high cycle fatigue (VHCF) regime. In samples that survived stressing for up to 10^{10} cycles, fatigue cracks were observed to form at constituent particles or clusters of particles situated at or close to the surface. Mayer and coworkers suggest that these initiating particles are either Al_7Cu_2Fe or Al_7Cu_2Mn.

In pristine samples of 7075-T6 fatigued at room temperature and in ambient air, cracks formed almost exclusively at fractured iron-bearing constituent particles, commonly reported to be Al_7Cu_2Fe, sometimes referred to as the β-phase [38, 40]. The size of these particles varies from study to study, but most researchers report a typical

diameter of 4-50 μm [36, 39]. Xue et al. [23] reported that iron-bearing constituent particles 4-8 μm x 8-12 μm in size served as the sites of fatigue crack nucleation in 50.8 mm thick 7075-T651 plate.

Li et al. [40] investigated the effect of temperature on crack formation and early growth in 7075-T6 under LCF conditions. At temperatures below 120^{o}C, cracks formed at constituent particles with little or no evidence of localized plastic deformation adjacent to the particles in the form of slip bands or slip lines. At high temperatures (260 ^{o}C), competition between formation within persistent slip bands and formation via grain boundary cracking was observed.

Payne and coworkers [38] made direct observations of notched fatigue specimens of 7075-T651 under LCF testing and found that cracking (rather than debonding) of iron-bearing constitutive particles was the only cause of fatigue crack formation. It was also found that Mg_2Si particles did not contribute to fatigue crack formation. This was attributed to the difference in elastic moduli between the particles and the matrix; iron-bearing particles (Al_7Cu_2Fe) are stiffer than the aluminum matrix with an elastic modulus of approximately 135 GPa, while Mg_2Si particles are more compliant with a modulus of approximately 50 GPa, thus creating less of a stress concentration effect [51]. The sequence of crack formation from a typical constituent particle is shown in Figure 9.

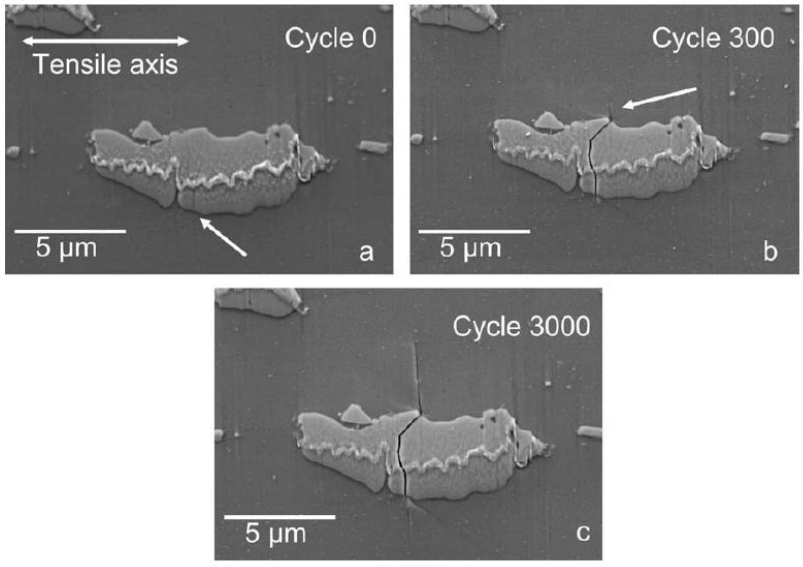

Figure 9. (a) and (b) Crack incubation and (c) nucleation via growth into the matrix [38].

Payne et al. [38] recorded information on the number of particles that had reached each stage of growth with progression of fatigue cycling, with results shown in Figure 10. Several trends are immediately clear from examination of Figure 10. First, incubation of the crack occurs within the first cycle for the majority of particles that fail; approximately 2/3 of particles that form cracks are fractured prior to fatigue cycling, presumably in the processing stages. Second, nucleation of the crack via extension into the matrix trails incubation by a significant number of cycles, and growth lags yet further behind nucleation. The definitions of incubation and nucleation employed by Payne et al. differ from those presented in Eqn. 7. Payne el al. consider the incubation process to consist of cracking the constituent particle, and define nucleation as the first appearance of a crack at the particle/matrix interface. Together, these two events comprise the incubation life ($N_{part,inc}$) term in Eqn. 7. Furthermore, Payne et al. do not differentiate crack growth

within the nucleant grain (N_{nuc}) and MSC propagation within adjacent grains, labeling both as growth in Figure 10.

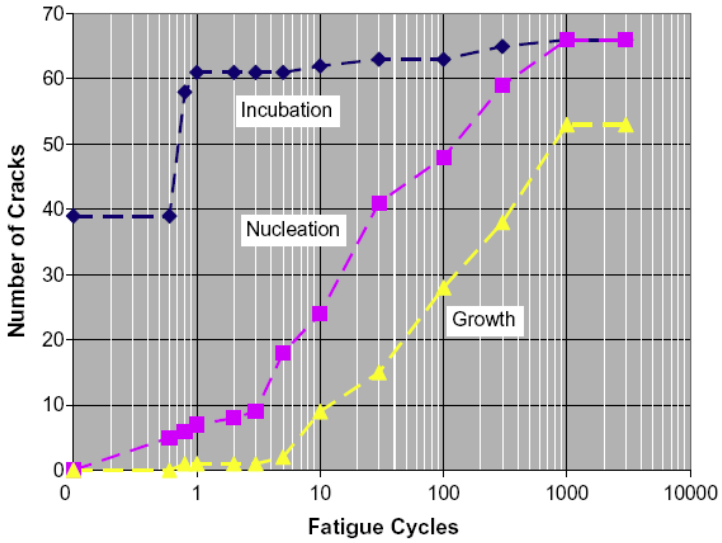

Figure 10. Hard particles in the incubation, nucleation or growth phase vs. cycle [38].

Similar results were obtained by Weiland et al [39], who analyzed constituent particles in 76.2 mm thick 7075-T651 plate subjected to LCF loading. It was found that particle debonding occurred but did not contribute to the formation of cracks within the Al matrix, which were instead only associated with cracked particles. Only a small portion of cracked particles nucleated cracks that grew into the matrix, attributed to the availability of active slip systems in the matrix next to the particle.

2.4.2: Fatigue Crack Propagation

The application of ΔK-based growth laws to the MSC growth regime violates several of the assumptions required for valid LEFM analysis, including a region of K-dominance, self-similitude, local mode mixity at the crack tip, and material homogeneity [8, 52]. However, this approach was widely used in early studies of MSC crack growth and much of the data for Al 7075-T6 collected from 1975 to the early 1990's are usually

presented in the form of da/dN vs ΔK [26, 41, 42, 53-58]. These type of data provide evidence for general growth rate trends and the effects of loading ratio, environment, etc. on growth rates, but is not as useful for calibration of mesoscale fatigue crack growth models in the MSC regime because crack length must be backed out of the ΔK values. This is often difficult as some sources do not publish exactly how ΔK was calculated, or if it is applicable to a given length of crack considered.

Lankford [41] observed the formation and propagation of small surface cracks in Al 7075-T6 specimens and was one of the first to quantify the growth rates of small cracks for this alloy. Figure 11 shows the results obtained by Lankford compared to long crack propagation data, and illustrates the "anomalous" behavior of small cracks. Lankford noted that the cracks formed at fractured intermetallic inclusions and had a half-penny geometry oriented normal to the loading direction.

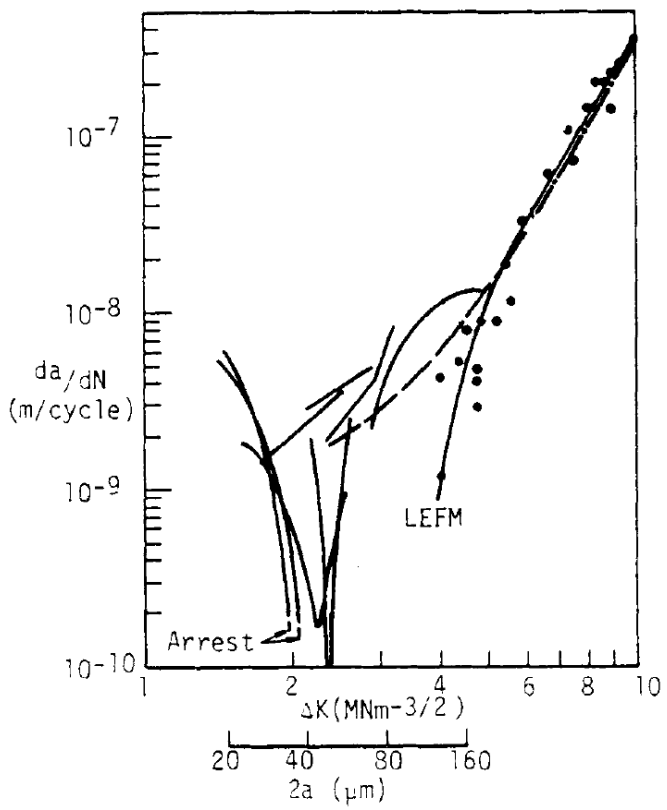

Figure 11. MSC versus long crack (LEFM) fatigue crack growth data for 7075-T6 [41].

Lankford observed that very short cracks exhibited a high initial growth rate that decelerated as the half crack length approached a dimension approximately equal to the grain size in the propagation direction, typically between 30 μm to 40 μm for the samples tested. At this length, the growth of some cracks was arrested, while others began to grow an accelerated rate, up to two orders of magnitude faster than growth rates of long cracks subjected to the same nominal ΔK.

Akiniwa et al. [59] found that the crack growth rate for small surface cracks in 2024-T3 was highly variable and had a large dependence on microstructure. Figure 5 shows a sketch of a small surface crack above a plot of crack propagation rate. The crack was observed to arrest at the first few grain boundaries it encountered. These results

clearly depict the “anomalous” small crack effect [8] in Aluminum alloys for relatively low amplitude fatigue and crack lengths on the order of the grain size.

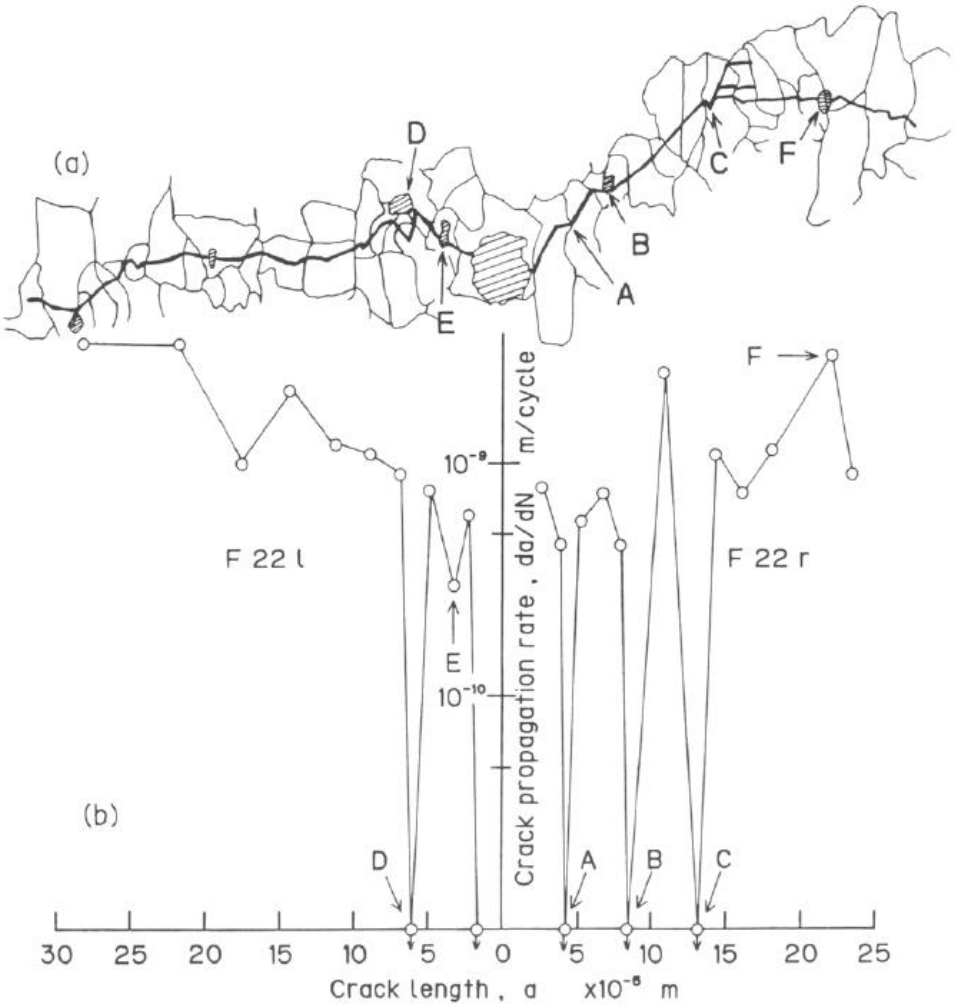

Figure 12. (a) Propagation path of a small surface crack, and (b) plot of corresponding crack growth rate [59].

Akiniwa et al. also plotted the small crack growth rate against the cyclic stress intensity factor, ΔK. Figure 13 shows the maximum bound, mean, and minimum bound growth rates for crack growth in the low ΔK regime. Also included is the growth rate for a single crack, which exhibits behavior similar to the cracks observed by Lankford in 7075-T6. The high initial growth rate quickly decelerated as the crack approached the

first grain boundary. Here the crack can either arrest or continue growing through the boundary. If the crack penetrated the first grain boundary, it continued to grow at a rate that is decreasingly influenced by microstructure and grain boundary effects, until the growth rate merged with long crack data.

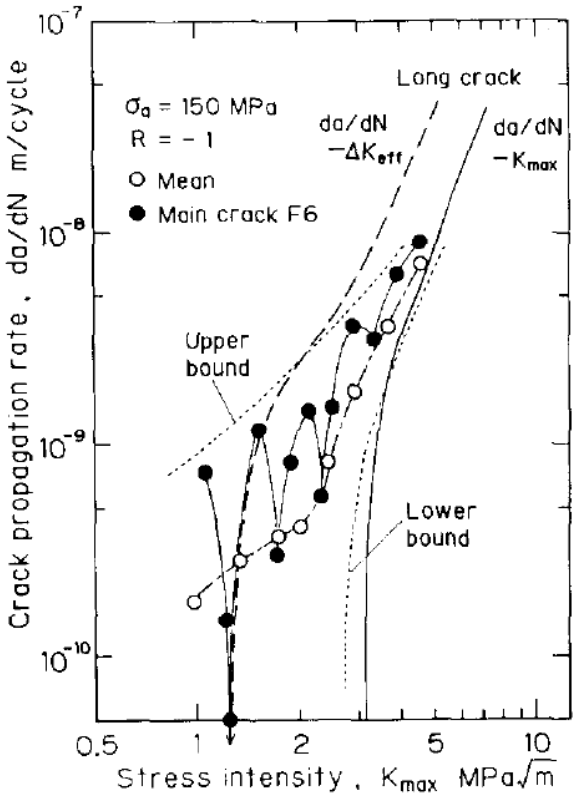

Figure 13. Short crack growth in 2024-T3 [59].

The results obtained by Lankford [41, 60] and Akiniwa et al. [59]are representative of the large body of small crack growth data available for Al alloys 2024 and 7075. Research findings generally agree that the crack growth rate in the small crack region is usually considerably higher than expected from extrapolation of long crack data, even for ΔK values below the crack arrest threshold (ΔK_{th}). The large variability of crack growth rates for the same nominal ΔK value is a result of microstructural influence on the local crack

driving force. To accurately predict MSC crack growth rates, a local rather than a far field driving force (e.g., ΔK) must be used.

The need for a local measurement of driving force was further reinforced by the work of Chan et al. [61], who calculated ΔJ-integral contours around the tip of a small half-penny surface crack (36 μm) in an overaged 7075 alloy based on stereoimaging measurements of crack-tip displacement fields. They found that for small cracks the ΔJ-integral was path dependent, decreasing in magnitude with increasing distance from the crack tip. Additionally, the local ΔJ-integrals were substantially larger in magnitude than the nominal far-field values. This means that the ΔJ-integral cannot be employed to characterize the growth of microstructurally small cracks. Chan et al. suggest that a more fundamental parameter describing crack tip fields would be based on the ΔCTD and thus offer better correlation with crack growth data.

Early data for crack growth rates were typically obtained using only surface measurements, but more recent work has measured crack growth rates in three dimensions using load histories that are programmed to produce marker bands on the crack surface, allowing crack growth rates to be determined along the entire crack front [27, 62]. Burns et al. [27] used marker-band growth rate measurement in pre-corroded and two-holed specimens to determine crack contours and crack growth rates in Al 7075-T651 along multiple radial directions as shown in Figure 14(a); their results show the high degree of variability present in early crack growth. Growth rate from a controlled corrosion pit for one specimen is shown in Figure 14(b). Each line represents growth rate along a vector drawn from the center of the corrosion pit outwards in the direction of crack propagation.

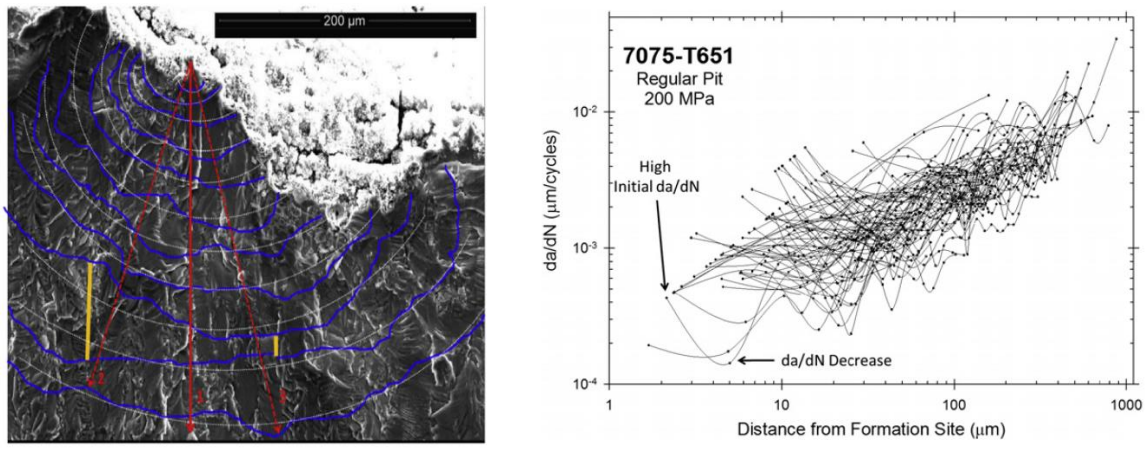

Figure 14. Crack growth from a controlled pit specimen [27]. (left) Crack contours and arrows indicating radial directions along which crack growth rates were measured. (right) Crack growth rates for multiple radial directions.

The variability of the growth rate in Figure 14 is approximately an order of magnitude, but decreases as the crack grows and the influence of the microstructure is reduced. Less variability in the growth rates of two-holed samples was observed, with a maximum da/dN variation of +/-130% occurring between 7 µm and 10 µm from the microstructure nucleant feature. The crack shown in Figure 14 is propagating in the T-S plane of the microstructure, which had a grain size between 50-74 µm in the transverse dimension, and 8-19 µm in the short direction. At the largest contour shown in Figure 14 left, the crack had grown to an approximate size of 200 µm.

Burns and coworkers also compared the results of their marker-band growth rate analysis to earlier results obtained through surface measurements of cracks with the notable result that unlike studies done using surface measurements, no crack arrest at grain boundaries was ever observed on the interior crack front. They suggest that studies

done using only surface measurements of crack growth fail to capture the actual growth rate over a significant portion of the crack front in the sample interior.

2.4.3: Stages of Crack Growth

Currently there is a lack of consensus within the literature on whether nucleation and early crack growth in Al 7075-T6 alloys is a Stage-I or Stage-II process, and the issue is further clouded by the large number of factors that can influence crack propagation behavior in this alloy, such as applied load amplitude [31], stress ratio [56, 58], and environment [63, 64].

The terminology differentiating the Stages of fatigue crack growth was introduced by Forsyth [65] in 1963 based on his work in aluminum alloys. A Stage I crack grows primarily by single shear, propagating in the direction of the primary slip system, while Stage II crack growth duplex or multi-slip process with cracks typically propagating normal to the tensile loading axis. This is illustrated in Figure 15.

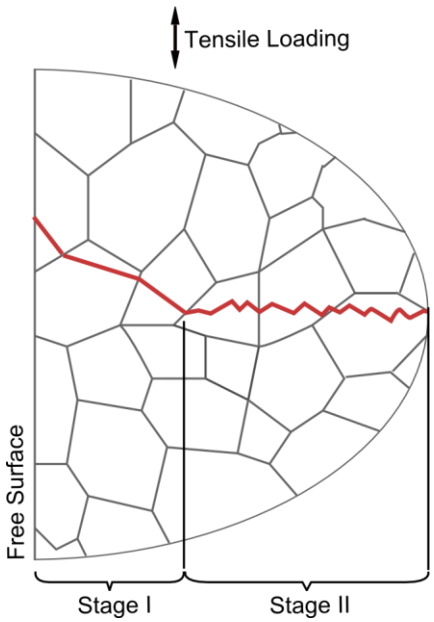

Figure 15. Schematic of the Stages of fatigue crack growth according to Forsyth [65].

In practice, the assessment of Stage I to II for growth for small cracks can be difficult to determine, given the three-dimensional nature of the crack surface and the transitional period between the regimes of growth that occur as the primary slip system hardens and the stresses at the crack tip activate conjugate slip. Additionally, there is always the question of the scale of observations. For example, a crack may propagate normal the tensile loading axis in a macroscopic sense, but locally grow along crystallographic planes in a shear-dominated fashion. Conversely, a crack may appear to grow on a plane of maximum shear at the mesoscale, but may locally grow at the tip in an alternating non-crystallographic sense via mixed conjugate slip system growth.

Several researchers have introduced extensions to the traditional dual-Stage growth model. Li [66] framed the crack growth process in terms of the crack tip displacement vector ($\overline{\Delta \mathrm{CTD}}$), defined as

$$\overline{\Delta \mathrm{CTD}} = \overline{\Delta \mathrm{CTSD}} + \overline{\Delta \mathrm{CTOD}} \qquad (8)$$

where $\overline{\Delta \mathrm{CTSD}}$ and $\overline{\Delta \mathrm{CTOD}}$ are vectors quantifying the crack tip opening and crack tip sliding displacements, respectively. Li classified Stage I growth as a pure shear crack propagating along a slip plane. Additionally, Li proposed the term ‘extended Stage I growth’ when a short secondary slip band is activated at the crack tip, which commonly occurs in single crystals and large grain polycrystalline materials. During Stage II growth (assuming that at the crack tip there exists a conjugate pair of slip systems with nearly equal Schmid factor) the crack propagates alternatively among slip bands on the conjugate slip systems in nearly equal increments. Figure 16 is a schematic representation of the types of crack growth and the resultant $\overline{\Delta \mathrm{CTD}}$ at the crack tip. In the Figure slip bands are shown by dashed lines.

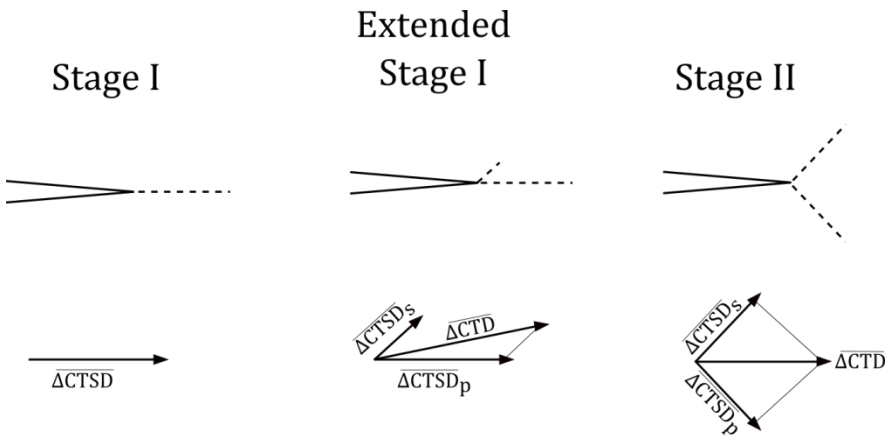

Figure 16. Illustration of the slip band profiles of the primary and secondary slip system, and resultant vector displacements at a crystallographic crack tip. Adapted from [66].

Note that in Figure 16 the crack tip displacements along slip bands are sliding displacements and that in absence of any opening displacements, the $\overline{\Delta CTD}$ is a sum of only the $\overline{\Delta CTSD}$ vectors on the primary and secondary slip system. This is a consequence of the assumption that for a crystallographic crack tip all displacements occur by shearing along slip planes, even for a Stage II crack. When the calculated $\overline{\Delta CTD}$ at the crack tip for extended Stage-I cracks was compared to the growth rates of such cracks in aluminum bicrystals, good agreement was obtained. Li's description of Stage II growth is somewhat similar to the coarse slip model of fatigue proposed by Neumann [67, 68], who observed the process in copper single crystals.

Petit and Kosche [57] conducted experiments on single and polycrystalline Al-Zn-Mg alloys under vacuum to identify the "intrinsic" Stages of crack growth that occur in the absence of environmental effects. They defined a period of "Stage I like" propagation where macroscopically the crack grows on a plane of maximum tensile stress, but within a grain propagates along crystallographic planes. They noted that this regime of growth was marked by a significant degree of crack branching and deviation at grain boundaries

and was slower than either of the Stage I or Stage II intrinsic regimes of growth. Petit and Kosche found that intrinsic Stage I propagation occurs at a higher rate that Stage II growth under vacuum, and that large and incoherent precipitates as well as the presence of grain boundaries promoted Stage II growth. Additionally, they observed evidence of Stage I crystallographic crack growth within the nucleant grain of the Al 7075-T6 alloy when tested in vacuum.

Experimental research conducted by Agnew and co-workers [36, 69, 70] suggests that within the LCF regime, nucleation and early growth is essentially a Stage-II event. This assumption is reflected by the modeling work conducted by Hochhalter [71], who argued that within the nucleant grain, cracks tended to propagate on planes of maximum normal stress. Other research [23, 38, 39, 56, 72] suggests that nucleation and early growth occurs on crystallographic planes of maximum shear (Stage-I response), even within the LCF regime.

In a study of legacy and modern Al-Zn-Mg-Cu alloys, Gupta and Agnew [36] measured the crystallography of fatigue crack surfaces near initiating particles using SEM-based stereology and EBSD. The tests were conducted under LCF conditions with a stress ratio of 0.5, loaded at a frequency of 5 Hz in warm-humid air and 10 Hz in cold-dry N_2 environments. Analysis of the fatigue crack surface in close proximity to the nucleant particle (1 to 50 μm) produced no evidence of extended {111} slip plane cracking commonly observed in pure face centered cubic metals with moderate to low stacking fault energy. In fact, no facets were found to have a crystallographic orientation within 15^o of the {111} planes in either environment. This occurred for fatigue tests of both 7075-T651 and 7050-T7451.

Weiland et al. [39] used focused ion beam (FIB) milling and orientation imaging microscopy (OIM) to evaluate the three dimensional shape and crystallography of an individual crack growing from an initiating particle in 7075-T651 under low cycle fatigue conditions conducted at R=0. They found that nucleation and subsequent growth into the Al matrix for the surface portion of the crack was aligned with an available slip plane. However, after approximately 5μm of growth within the nucleant grain, the crack appears to change direction sharply and begin propagating perpendicular to the loading axis.

Tokaji and Ogawa [56] investigated the effect of stress ratio on nucleation and MSC growth in 7075-T6. They observed that for tests conducted at R = -1 and R = -2, cracks nucleated and grew within the first grains in Stage-I, and that the lower the cyclic load level, the farther the crack propagated in Stage-I before transitioning to Stage-II growth. For fatigue tests conducted at R = 0, cracks nucleated from inclusions, and exhibited only Stage-II growth.

Misak et al. [73] conducted fatigue tests on pre-cracked, cruciform specimens of Al 7075-T6 to assess the effect of biaxiality on fatigue crack propagation. They found that higher ratios of biaxiality promoted higher growth rates than the equivalent uniaxial loading, and had lower crack growth thresholds (ΔK_{th}). In addition, the surfaces of cracks from the uniaxially loaded specimens were typically smooth, while the surfaces of cracks under higher biaxiality ratios were rougher. This was attributed to the biaxial loading conditions promoting wavy slip, in contrast to the more planar slip in the uniaxially loaded specimen.

2.4.4: Environmental Effects

It is well established that the presence of humidity in ambient air has a detrimental effect on fatigue properties. In aluminum alloys, this effect is attributed to the production of hydrogen by the interaction of water vapor with freshly exposed surfaces at the crack tip [63, 74, 75]. The mechanism of hydrogen-enhanced crack propagation in Al alloys is not fully understood, but it is attributed to:

1) Hydrogen-enhanced localized plasticity (HELP) – where the presence of solute hydrogen in aluminum matrix near crack tip enhances dislocation emission. Sun et al. [76] performed molecular dynamics studies of the interaction of Hydrogen atoms with crack tips in aluminum and found that the presence of adsorbed could both enhance or suppress dislocation emission.
2) Hydrogen-enhanced decohesion (HEDE) – where small amounts of hydrogen on the crack front can reduce cohesive strength, leading to brittle cleavage. Underaged, planar-slip 7075 alloys have been found to be more susceptible to hydrogen embrittlement than peak or overaged alloys of the same temper [63].

It is likely that HELP and HEDE mechanisms operate in some combination, with transport of hydrogen by dislocations serving to bridge them. The formation of oxides on crack surfaces can also effect crack growth. Vasudevan and Suresh [74] showed that the effect of oxide-induced crack closure in 2024-T3 and 7075-T6 alloys is not significant, unlike overaged alloys of the similar composition. In the overaged alloys oxide layer thicknesses on the order of the near-threshold CTOD were observed to form, leading to crack arrest.

2.4.5: Effects of Overloads and Underloads

Numerous researchers have explored the impacts of overloads and underloads on the long crack growth behavior of aluminum alloys [62, 77-79]. However, the impact of overloads during MSC propagation is not well-studied for this alloy, and there is no research exploring the phenomenon in Al 7075-T6 of which this author is aware. However, Suresh [80] has suggested that in addition to the commonly listed mechanisms for growth retardation following overload (such as crack tip blunting, compressive residual stresses, crack closure in the wake of the crack, etc.), the effective stress intensity range at the crack tip can be reduced to such an extent that locally growth becomes Stage I, i.e. the crack grows along a single crystallographic slip system in shear despite nominally tensile loading conditions.

2.5: Summary

This Chapter has presented a brief historical overview of the methods used to predict fatigue phenomenon, as well as the physical basis of fatigue crack nucleation and growth in precipitation hardened aluminum alloys, with a focus on Al 7075-T6 which is the material modeled in this Thesis. The propagation of microstructurally small cracks is a complex phenomenon influenced by numerous factors, and traditionally employed fatigue design methodologies are often inadequate for the characterization of the behavior of small cracks. The difficultly of modeling the behavior of microstructurally small cracks is the motivation for this thesis, which seeks to do so by employing a FIP-based, mesoscale modeling approach introduced in Chapter 4.

CHAPTER 3: CONSTITUTIVE MODELING OF AL 7075-T6

3.1: Introduction

To accurately predict the fatigue behavior of a material it is first necessary to accurately model the response of the material to applied cyclic loads with a constitutive model. This constitutive model serves as the basis from which the stress and strain quantities used in any fatigue analysis are derived. Modeling microstructurally small crack growth requires a constitutive model that can resolve the stress-strain response within individual grains to capture the local driving forces on the crack. This is achieved through the use of a finite element based crystal plasticity model (CPFEM) calibrated to cyclic loading data for Al 7075-T6. This chapter will begin with a brief introduction to the mathematics underlying crystal plasticity constitutive models, and will then present three different crystal plasticity constitutive models for Al 7075-T6. The chapter will conclude with a discussion of the models and key differences between them, as well as the implications that these models have on modeling microstructurally small crack growth.

3.2: Kinematics of Crystal Plasticity

The mathematical underpinnings of crystal plasticity models have been presented in great rigor and detail in numerous sources, but for the sake of completeness this document will present an overview of the basic physical and mathematic principles. Note that the fatigue algorithms (introduced in Chapter 4) allow for the possibility of introducing damage to an element through the isotropic degradation of the elastic stiffness tensor. Thus, in introducing the kinematics of crystal plasticity, all elastic terms

are replaced by their elastic-damaged equivalents, i.e., F^e becomes F^{ed} following the introduction of damage.

Assuming a continuous distribution of dislocations, the local deformation in the neighborhood of an infinitesimal point can be represented by the deformation gradient F,

$$\dot{F}^p = \left(\sum_{\alpha=1}^{N_\alpha} \dot{\gamma}^\alpha s_0^\alpha \otimes m_0^\alpha \right) \cdot F^p \qquad (9)$$

where x is the position vector of the particle in the reference configuration and X is the position vector of the same particle in the deformed configuration. Following the methodology of Bilby et al. [81] for deformed crystals and Lee for macroscale plasticity [82] the deformation is decomposed into elastic-damaged (F^{ed}), and plastic (F^p) components according to

$$L_0^p = \dot{F}^p \cdot \left(F^p \right)^{-1} \qquad (10)$$

with F^{ed} representing the elastic deformation gradient, which includes damage, and F^p representing the plastic component of the deformation gradient. This decomposition is shown schematically Figure 17.

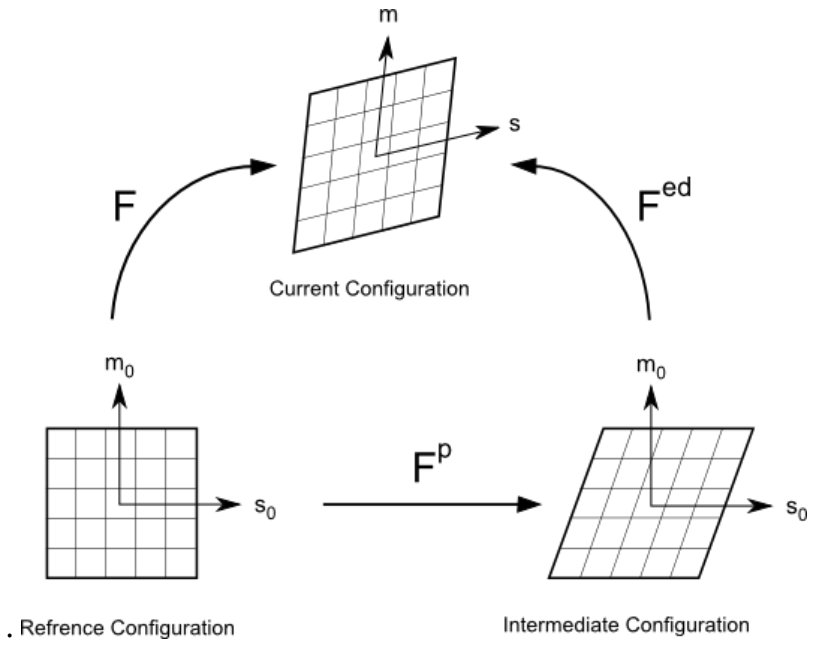

Figure 17. . Schematic showing the multiplicative decomposition of the deformation gradient. Adapted from [83].

In Figure 17, s_0 is the slip direction vector in the reference configuration, and m_0 is the slip plane normal, also in the reference configuration. Note that the slip direction and normal vectors are unchanged by the plastic deformation gradient during the transformation from the reference to intermediate configuration because it is assumed that the lattice itself is undisturbed by the dislocation motion that occurs during plastic straining, and that any deformation of the crystal lattice is elastic in nature.

Following the arguments presented by Asaro [83], the material time derivative of the plastic deformation gradient is related to current plastic deformation gradient by the relation

$$\dot{F}^p = \left(\sum_{\alpha=1}^{N_\alpha} \dot{\gamma}^\alpha s_0^\alpha \otimes m_0^\alpha \right) \cdot F^p \qquad (11)$$

where $\dot{\gamma}^{\alpha}$ is the shearing rate on slip system α, s_0^{α} is the slip direction vector in the intermediate configuration, and m_0^{α} is the slip plane normal vector also in the intermediate configuration. The plastic velocity gradient in the intermediate configuration may then be obtained by the following expression,

$$L_0^p = \dot{F}^p \cdot \left(F^p\right)^{-1} \tag{12}$$

which simplifies to

$$L_0^p = \sum_{\alpha=1}^{N_\alpha} \dot{\gamma}^{\alpha} s_0^{\alpha} \otimes m_0^{\alpha} \ . \tag{13}$$

The plastic velocity gradient in the current configuration is related to the plastic velocity gradient of the intermediate configuration through

$$L^p = F^{ed} \cdot L_0^p \cdot \left(F^{ed}\right)^{-1} \tag{14}$$

and the elastic velocity gradient is given by

$$L^{ed} = \dot{F}^{ed} \cdot \left(F^{ed}\right)^{-1}. \tag{15}$$

Summing the elastic damaged and plastic velocity gradients yields the total velocity gradient in the intermediate configuration, i.e.,

$$L = L^{ed} + L^p = \dot{F} \cdot \left(F\right)^{-1}. \tag{16}$$

The 2nd Piola-Kirchhoff stress, T, is then obtained by multiplying the elastic damaged Green strain tensor, E^{ed}, with elastic stiffness tensor, i.e.,

$$T = \bar{C} : \mathrm{E}^{ed} \tag{17}$$

where the elastic damaged Green strain tensor is defined by

$$E^{ed} = \frac{1}{2}\left[(\mathrm{F}^{ed})^T \cdot \mathrm{F}^{ed} - I \right]. \tag{18}$$

The Cauchy stress (σ) is then related to the 2nd Piola-Kirchhoff stress tensor through

$$\sigma = \frac{1}{\det(\mathrm{F}^{ed})} \mathrm{F}^{ed} \cdot T \cdot (\mathrm{F}^{ed})^{T} \qquad (19)$$

The resolved shear stress on slip system α is then obtained by

$$\tau^{\alpha} = \sigma : \left(s_0^{\alpha} \otimes m_0^{\alpha} \right). \qquad (20)$$

With these kinematics in place, the next step is to introduce material-specific constitutive laws that relate the shearing rate on slip system α to the resolved shear stress on that slip system, τ^{α}, through the flow rule, as well as slip system hardening laws.

3.3: Al 7075-T6 Crystal Plasticity Constitutive Models

During the research conducted for the completion of this thesis, three different crystal plasticity models for Al 7075-T6 were considered. The crystal plasticity modeling framework of McGinty [3], applied originally to Oxygen Free High Conductivity (OFHC) Cu, serves as the basis for the constitutive model implementation. The flow rule is defined as

$$\dot{\gamma}^{(\alpha)} = \dot{\gamma}_0 \left| \frac{\tau^{(\alpha)} - \chi^{(\alpha)}}{g^{(\alpha)}} \right|^{m} sgn(\tau^{(\alpha)} - \chi^{(\alpha)}), \qquad (21)$$

where $\dot{\gamma}^{(\alpha)}$ is the shearing rate for slip system α, $\dot{\gamma}_0^{(\alpha)}$ is the reference shearing rate, and τ^{α} , χ^{α} and g^{α} are the corresponding slip system shear stress, back stress and drag stress, respectively. Here m is the strain rate sensitivity exponent.

The three models used in this research differ primarily in the forms of the hardening laws that govern the evolution of the back stress and the drag stress on each slip system. These laws have the general form

$$\dot{g}^{\alpha} = \hat{g}(\dot{\gamma}^{\beta}, \mathrm{g}^{\alpha}) \text{ and } \dot{\chi}^{\alpha} = \hat{\chi}(\dot{\gamma}^{\alpha}, \chi^{\alpha}). \quad (22)$$

In Eqn. 22 the rate of evolution of the drag stress, representing isotropic hardening, is a function of the shearing rate on all slip systems as well as the current value of the drag stress. However, the kinematic hardening response, captured by the evolution of the back stress, is only a function of the shearing rate on the current slip system as well as the current value of the back stress.

3.3.1: Model Forms

For the sake of brevity each of the three models is referred to by the designation used during development and calibration: models G31, OW44 and OW57. The first model form employed for fatigue simulations in Al 7075-T6 was model G31. In this model the back stress is governed by an Armstrong-Frederick [84] type non-linear relation and evolves according to

$$\dot{\chi}^{(\alpha)} = h\dot{\gamma}^{(\alpha)} - r\chi^{(\alpha)} |\dot{\gamma}^{(\alpha)}| \quad (23)$$

where h and r are constants that capture the hardening and recovery of the back stress. With the AF form of the back stress hardening law, the saturation value of the back stress, b, is given by the ratio

$$b = \frac{h}{r}. \quad (24)$$

The G31 model assumes that the drag stress on each slip system, g^{α}, is a constant throughout the simulation, i.e., no isotropic hardening.

Model OW44 was introduced in order to address some of the shortcomings of the Armstrong-Frederick back stress formulation when loaded cyclically with an imposed mean strain. The OW44 model incorporates a two-term, Ohno-Wang [85] (OW) type

equation for the back stress, adapted from a polycrystal macroscopic model proposed by McDowell [86]. The rate of change of this from of the back stress is given by

$$\dot{g}^{(\alpha)} = H_{dir} \sum_{\beta=1}^{N_{sys}} h^{\alpha\beta} \left| \dot{\gamma}^{(\beta)} \right| - H_{dyn} g^{(\alpha)} \sum_{\beta=1}^{N_{sys}} \left| \dot{\gamma}^{(\beta)} \right| \qquad (25)$$

where $h^{\alpha\beta}$ is the latent hardening matrix, controlling the relative contributions of self and latent hardening of the slip systems. In the OW57 model the latent hardening matrix is defined as a function of the latent hardening ratio

$$h^{\alpha\beta} = q + (1 - \mathrm{q})\delta^{\alpha\beta} \qquad (26)$$

where $\delta^{\alpha\beta}$ is the Kronecker delta. For FCC materials typical values given for the latent hardening ratio are between 1 and 1.4 [87]. Work by Yan et al. [88] on cyclically loaded pure aluminum single crystals suggests a latent hardening ratio between 0.9 and 1.1, with only a slight variance occurring during cycling. A value of 1.1 was selected for latent hardening ratio in the OW57 constitutive model.

3.3.2: Implementation in Abaqus

The crystal plasticity constitutive models are implemented in an Abaqus 6.9.1 [4] User MATerial (UMAT) subroutine. The UMAT subroutine allows the user to define a material constitutive model not included in the standard Abaqus models and the ability to interface with other user subroutines. The UMAT is called for every material calculation point of all elements for a given increment. The primary inputs into the UMAT from Abaqus are the deformation gradients at the beginning and end of the increment, F_t and $F_{t+\Delta t}$, respectively. The UMAT calculates the Cauchy stress tensor, σ , and the material Jacobian matrix, $J = \frac{\partial \Delta\sigma}{\partial \Delta\varepsilon}$ and then updates the internal state variables associated with

the solution before returning to Abaqus. This functionality of the UMAT in relation to Abaqus and solving the actual finite element equation is summarized in Figure 18.

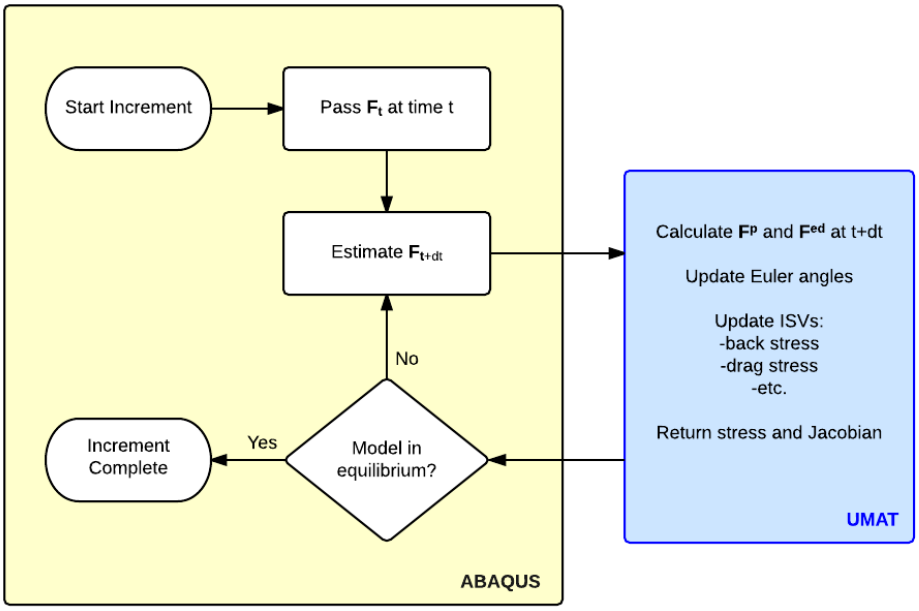

Figure 18. Diagram showing the basic interaction between Abaqus and the UMAT. Adapted from [3].

The implementation of the crystal plasticity constitutive model within the UMAT closely follows the general methodology employed by McGinty [3], employing a Newton-Raphson implicit integration scheme coupled with a line search algorithm to improve convergence. A detailed flowchart of the UMAT is shown in Figure 19.

In Abaqus Implicit, the simulation is divided into monotonic changes in the applied boundary conditions. These are the loading steps and for the fatigue simulations are performed under strain control. Each loading step is further divided into loading increments by Abaqus. At this point, Abaqus calls the UMAT subroutine for each material integration point within the mesh. The UMAT then begins the process of sub-incrementation where the increment passed in by Abaqus is divided into a number of

smaller increments. During the first attempt to solve the constitutive equations, the increment and sub-increment are the same size. If the Newton-Raphson and line search loop are unable to converge to a solution, the increment is divided into twice as many sub-increments and the Newton-Raphson/line search algorithm begins again. This process continues until the solution converges or the number of sub-increments grows too large. In the case of non-convergence within the maximum number of sub-increments, the UMAT requests that Abaqus restart the current increment with half of the original time. If the solution has converged within the UMAT, the internal state variables (ISVs) associated with the solution are updated, and the Cauchy stress and Jacobian are returned to Abaqus.

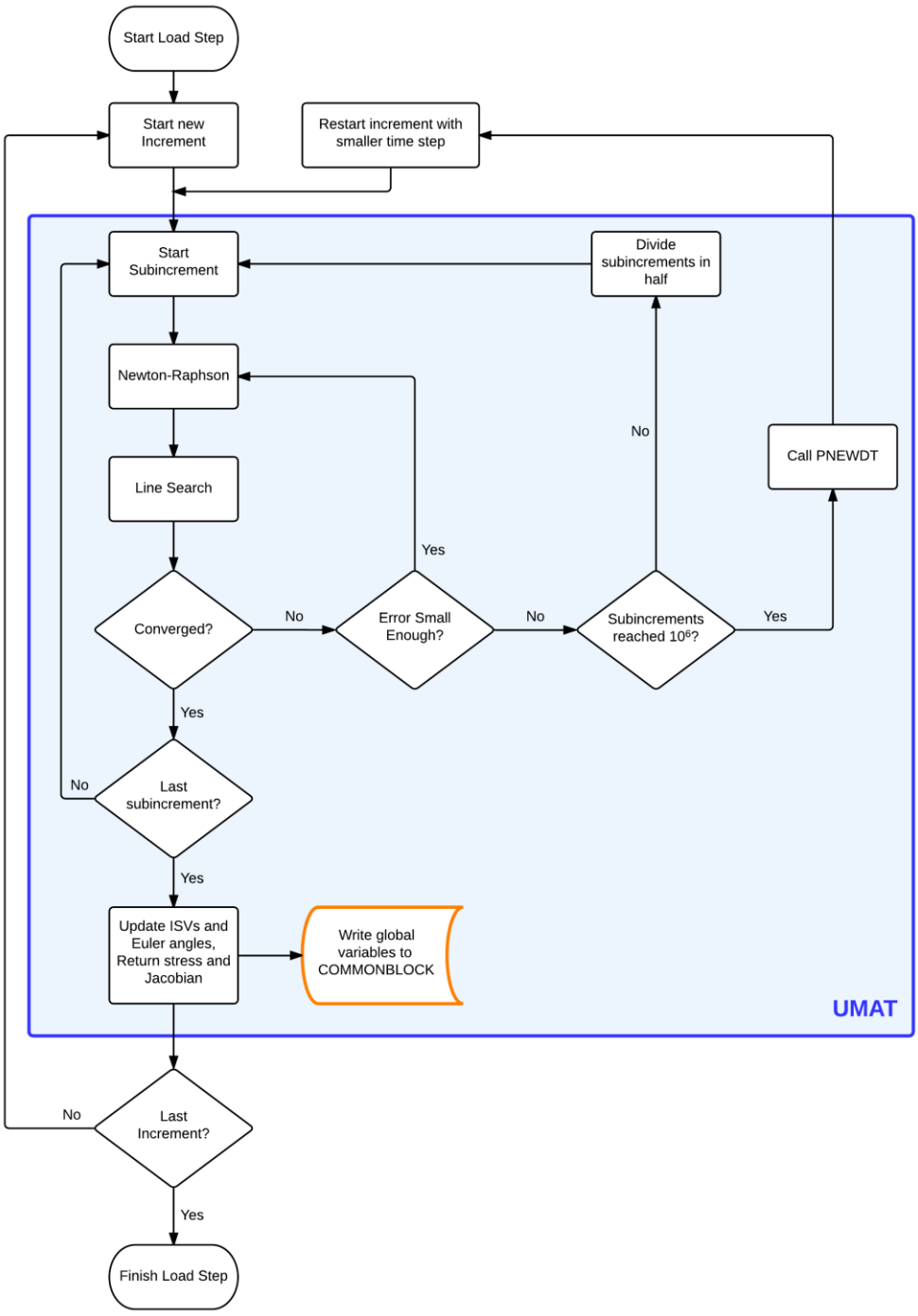

Figure 19. Flowchart summarizing the steps executed by the Abaqus UMAT subroutine during a loading step. Adapted from [3].

Additionally, the UMAT writes the variables and arrays needed by the fatigue algorithms to the COMMONBLOCK, a feature of Fortran 95 that allows data to be shared between

separate Fortran programs, in this case the UMAT and the UEXTERNALDB subroutines. The COMMONBLOCK allocates a region of computer memory for storage of variables and arrays that is accessible by all programs that share the same COMMONBLOCK declaration. Note that COMMONBLOCK variables are persistent over the execution of the simulation, meaning that they remain unchanged from step to step and increment to increment unless explicitly modified. After these arrays are written, the UMAT exits and Abaqus then checks the global equations for convergence. If convergence is not obtained, the last increment is restarted with a smaller time step. It is important to note that the UMAT does not know if the converged solution it obtains for each material integration point will produce a converged solution for the global FE equations that Abaqus attempts to solve, and writes data to the COMMONBLOCK during each call. This can cause issues if the data is read by the other programs with the shared COMMONBLOCK before global convergence is obtained. Once the global FE equations have converged, Abaqus begins the next increment of the step. This process continues until all loading steps are completed.

3.4: Model Calibration

To accurately model the fatigue behavior under the loading conditions of interest the material constitutive model must be able to correctly predict the stress-strain response under that loading. To do so requires that the model be calibrated to data that matches the loading conditions of interest. For the mesoscale fatigue model, the stabilized material response to cyclic loading is the main interest, therefore the model is calibrated using primarily the cyclically stable stress-strain hysteresis loops.

Under monotonic loading Al 7075-T6 exhibits a low degree of work hardening, typical of high stacking fault energy materials. When loaded cyclically the material displays slight cyclic hardening behavior that stabilizes after approximately 10 to 100 cycles, depending on strain amplitude [89]. Both of these behaviors are illustrated in Figure 20, which was adapted from experimental work conducted by Colin [90].

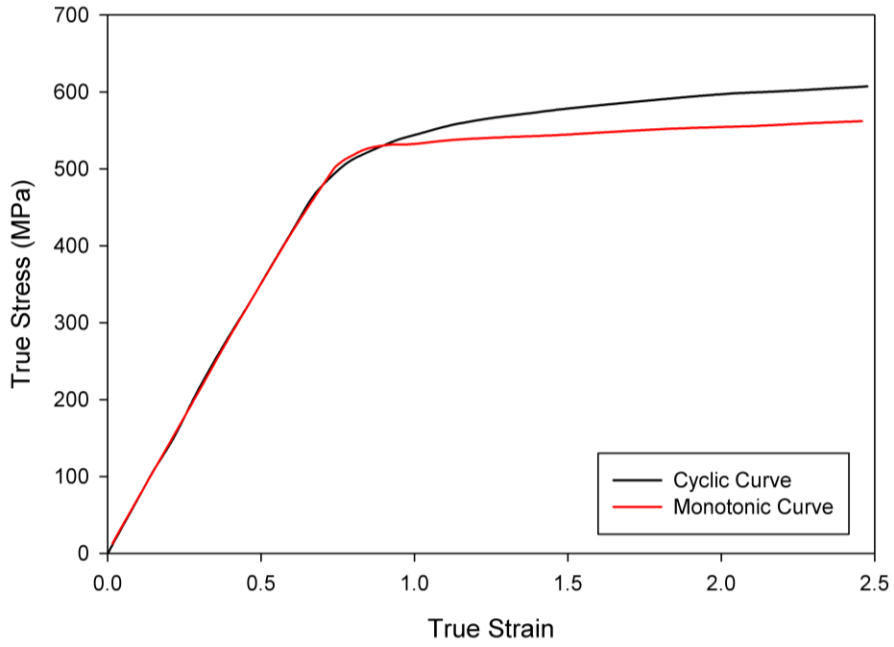

Figure 20. Comparison of monotonic and cyclic stress/strain curves for Al 7075-T6. Adapted from [90].

Several of the parameters within the flow rule are either known material properties or scaling parameters, and these parameters were held constant for all models and were not used to fit the material response. First among these parameters are the elastic constants that comprise the anisotropic stiffness tensor, C_{ijkl}. The values of these consents were chosen to match those used in the Al 7075-T6 modeling work of Bozek et al. [18] and provided good agreement with experimental results within the elastic regime. For all

models, $\dot{\gamma}_0$ is taken to be 0.001. The values of the elastic constants and $\dot{\gamma}_0$ used in this work are summarized in Table 3 .

Table 3. Common parameters between models G31, OW44 and OW57

C_{11}	C_{12}	C_{44}	$\dot{\gamma}_o$
107.3 GPa	60.9 GPa	28.3 GPa	0.001 s^{-1}

The strain sensitivity exponent of the flow rule, m , was taken to be 150 for model G31 and 75 for models OW44 and OW57. The lower value of m was employed in models OW44 and OW57 in order to increase the speed of convergence. In comparison, Bozek et al. [18] used a strain sensitivity exponent of 200. When loaded quasi-statically in the strain ranges of interest for fatigue simulations, varying the value of m between 75 to 200 had only a negligible effect on the constitutive response, justifying employing a reduced value to obtain increased convergence speeds.

The initial fitting of all models was conducted using fully reversed cyclic stable stress-strain data obtained by Arcari [91] at strain amplitudes of 1% and 1.8%. Comparisons between the experimental data of Arcari and each of the three models are shown Figure 21. The simulations performed to generate the results in Figure 21 were conducted on a single microstructural instantiation with approximately 700 randomly oriented, equiaxed grains with a 14 μm mean grain diameter. The mesh has cubic geometry with 100 μm side lengths and 5 μm elements (for a total of 8000 elements) and was subjected to uniaxial, quasi-static, strain-controlled cyclic loading with 3D periodic boundary conditions. A more in-depth discussion of the meshes employed and the process of generating these meshes is presented in Chapter 4.

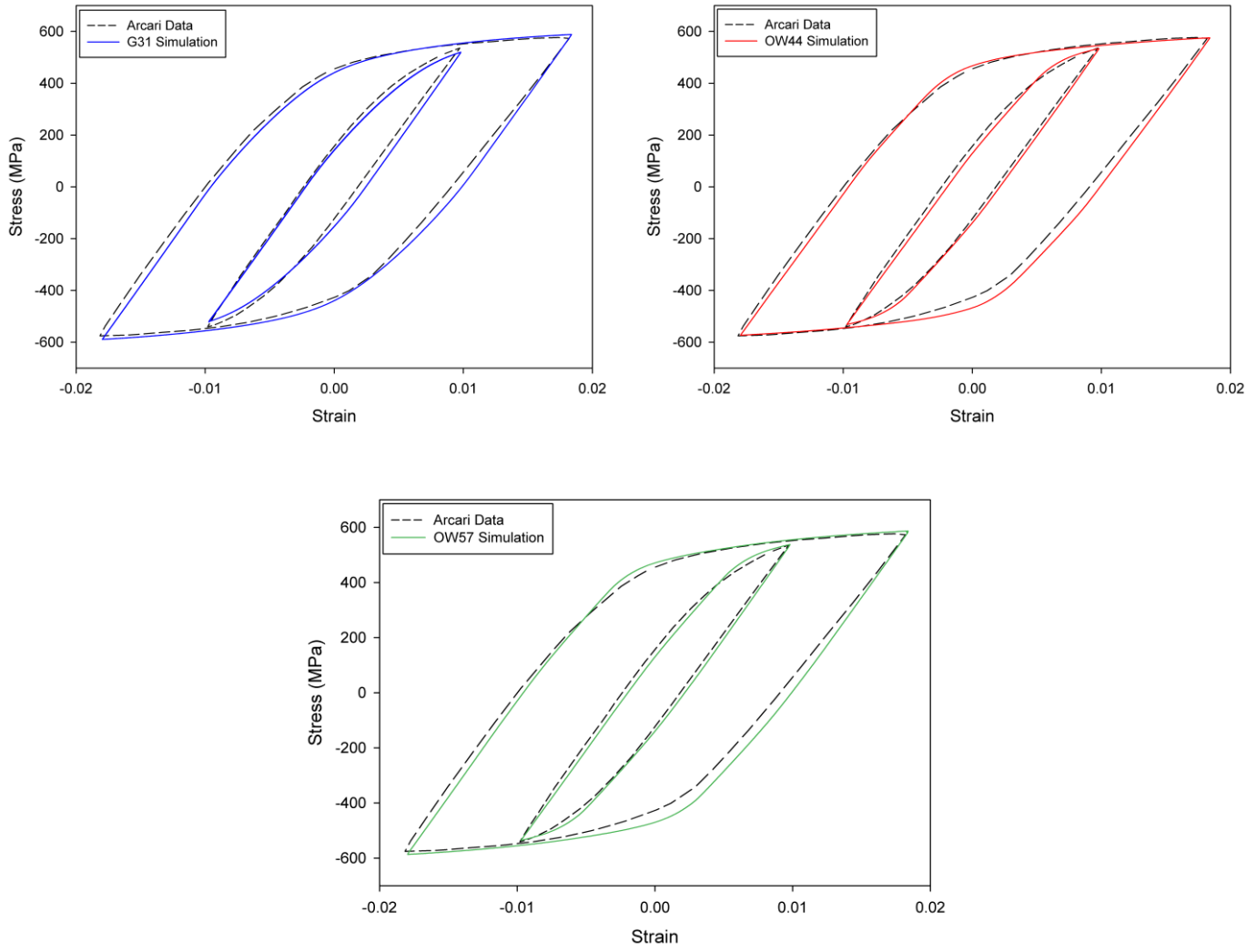

Figure 21. Upper Left: best fit to experimental data using model G31. Upper Right: current best fit to experimental data using model OW44. Lower Center: Fit using model OW57. Plots are of saturated response after 12 cycles.

As seen in the Figure, all three models do an adequate job matching the shape of the experimental hysteresis loops, however model G31 slightly underpredicts the peak stress at the 1.0% strain amplitude and slightly over-predicts peak stress at the 1.8% strain amplitude. This is because fitting the back stress evolution constants of the G31 model is essentially a compromise between matching experimental data at various strain amplitudes; one set of values for h and r can provide an excellent fit at a given strain

amplitude, but will provide erroneous results at a different applied strain amplitude. With the introduction of a multi-term equation, the total evolution of the back stress can be partitioned into short range components (quickly evolving terms that control the response at small cyclic strains) and long range components (slowly evolving terms that control the response at large cyclic strains). This allows the model response to be calibrated over the entire range of strains for which data is available. Additionally, the fitting procedure is made less difficult by the near linearity of the individual back stress components for the models with the Ohno-Wang type hardening law. The model parameters for models G31, OW44 and OW57 used to generate the plots in Figure 21 are listed in Table 4.

Table 4. Summary of the constitutive model constants for Al 7075-T6.

Model	m	G_0 **(MPa)**	H_{dir} **(MPa)**	H_{dyn}	q	h_1 ***(MPa)***	r_1	h_2 ***(MPa)***	r_2	m_i
G31	150	130	-	-	-	7.56×10^4	720	-	-	-
OW44	75	35	-	-	-	2×10^6	2×10^4	1.35×10^5	1421	200
OW57	75	30	1×10^6	1×10^4	1.1	5×10^5	1.43×10^4	1.35×10^5	1421	200

The ability of the OW44 model to match experimentally observed results over a larger range of strains is illustrated in Figure 22. To generate the Figure, experimental data obtained by Renard et al. [92] are plotted along with data generated by model G31, OW44 and OW57 under fully reversed uniaxial loading with applied strain amplitude varying from 0.2% to 2%.

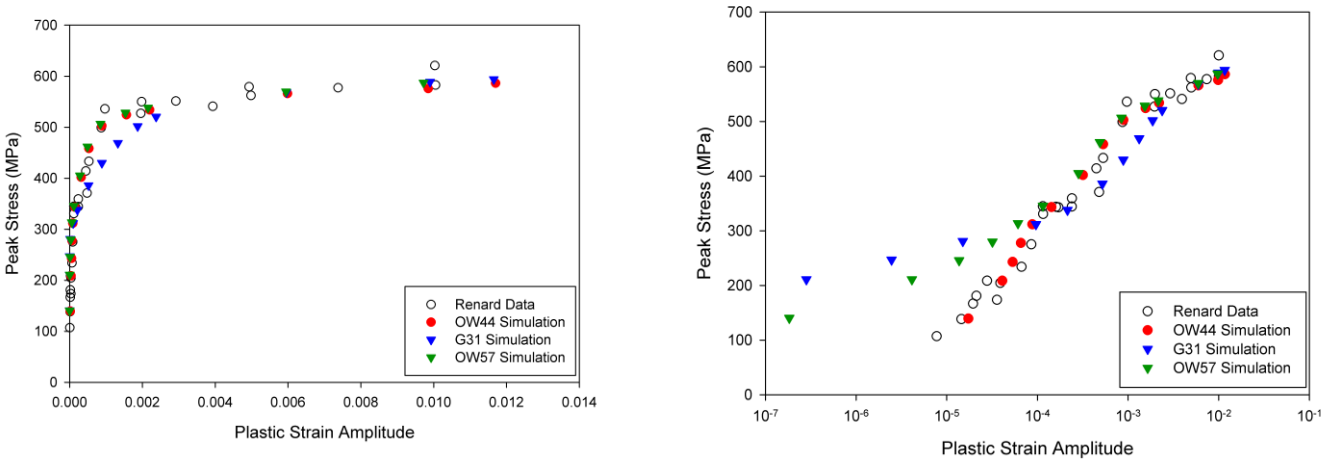

Figure 22. Peak stress vs. plastic strain amplitude data [92] compared to results of simulations. Left: Data presented on linear plot. Right: Same data presented on semi-log plot.

The semi-log plot on the right side of Figure 22 shows the close agreement between the plastic strains predicted by OW44 and the experimental data over the entire range of peak stresses considered. For the G31 model, the simulated plastic strain amplitude and the experimental results diverge significantly around a peak stress value of 280 MPa (corresponding to an applied strain amplitude of 0.4%). The OW44 model is able to capture plastic strain amplitude at and below applied strain amplitudes of 0.4% through the use of a much lower value of drag stress (35 MPa compared to 130 MPa in the G31 model) coupled with a very rapidly evolving first back stress term. Under a peak stress of 300 MPa, the results from the OW57 model lie in-between those of models OW44 and G31. However, the predicted plastic strain amplitudes in this regime are still up to orders of magnitude lower than the experimental data of Renard et al. This suggests that the saturation value of drag stress employed in the calibration of the OW57 model of 100 MPa is too high, and that future calibrations should employ a lower value.

The importance of Figure 22 is to illustrate that matching the macroscopic stress-strain response (see Figure 21), while necessary for calibrating a constitutive model, does not ensure that the model will accurately predict plastic strains at lower applied cyclic stress amplitudes. Therefore, it is critical that the constitutive model be calibrated to experimental stress-strain data within the range of stress amplitudes of interest.

3.5: Model Response to Asymmetric Cyclic Loading

While the agreement between the constitutive models and experimental results are adequate under fully reversed loading, the models must also be able to capture the material response when cyclically loaded in the presence of a mean stress or strain. Early results obtained using the G31 model with the AF hardening law for back stress accurately predicted the macroscopic material response under fully reversed conditions, but predicted large ratcheting strains when cyclically loaded with an imposed mean stress/strain. Ratcheting is the accumulation of a directional plastic strain under cyclic loading, shown schematically in Figure 23 for one complete loading cycle.

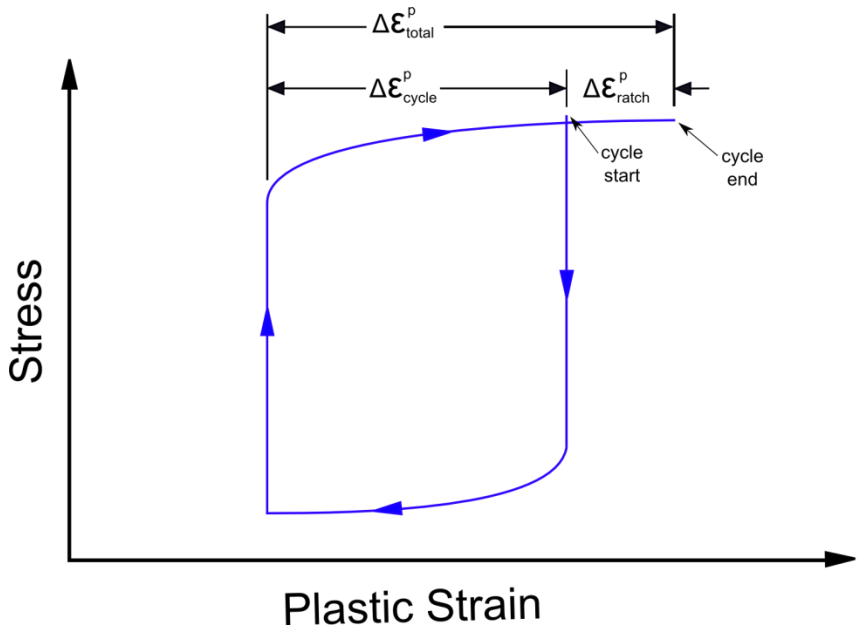

Figure 23. Schematic of a single loading cycle with a mean stress showing ratcheting behavior.

In Figure 23, the total strain range is the difference between the maximum and minimum plastic strain over the complete cycle. The ratcheting strain is defined as the difference in plastic strain at the end and beginning of the loading cycle. The cyclic plastic strain range is then obtained by subtracting the ratcheting strain from the total plastic strain range over the cycle.

The response of the G31 model when cyclically loaded with an imposed mean stress/strain is shown in Figure 24. This simulation was performed under uniaxial, strain-controlled loading with an applied strain amplitude of 0.4% and an imposed mean strain of 1.4%. The simulation was conducted for a total of 100 computational cycles. The strain ratio was R_ε =0.556 , and produces an initial equivalent stress ratio, R^*_σ , of approximately 0. As cycling progresses, the equivalent stress ratio is reduced through the effect of mean stress relaxation. The plot on the left of Figure 24 presents stress vs. total

strain, and the rectangle indicates the area of focus for the plot on the right, which presents stress vs. plastic strain.

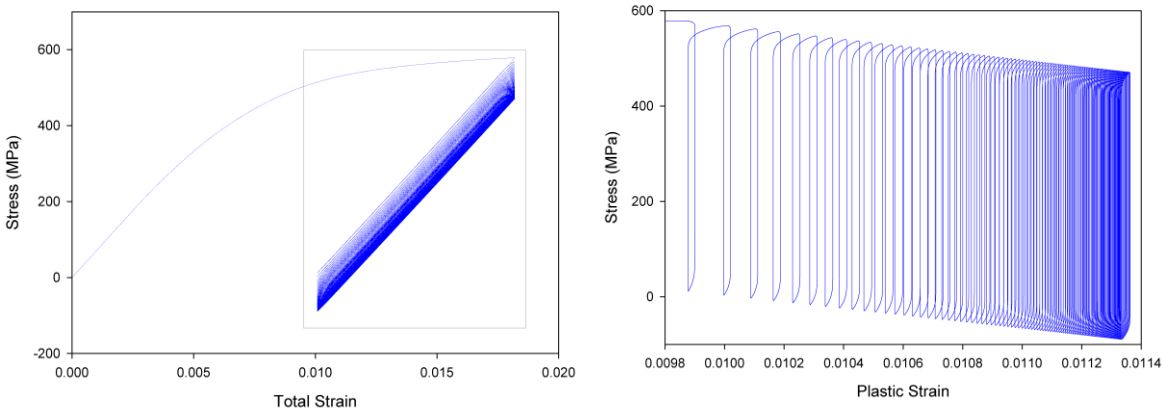

Figure 24. Cyclic stress-total strain (left) and cyclic stress-plastic strain curve (right) for 100 computational cycles at $\varepsilon_a = 0.4\%$, $R_\varepsilon = 0.556$ using the G31 model.

In Figure 24 both mean stress relaxation and ratcheting behavior are observed, and there is a large transient in the predicted response, with the magnitude of ratcheting strain decreasing as the simulation progresses.

Survey of the available literature for Al 7075-T6 suggests that ratcheting is not a commonly encountered phenomenon in room temperature fatigue of this alloy. There is a good consensus among sources considered that in ambient, room temperature environments, nucleation and early growth behavior is transgranular in character [23, 33, 38-41, 54, 60]. However, at higher temperatures (180 ºC - 270 ºC), ease of plastic deformation is increased and research has shown that cracking along grain boundaries becomes an increasingly important mechanism for crack formation and growth [40]. The pronounced absence of observed grain boundary cracking at room temperature suggests that ratcheting does not play a large role in fatigue damage of 7075-T6, and supports the case that the significant ratcheting behavior predicted by the constitutive model is an

artifact of the model form. The over prediction of cyclic strain accumulation by the AF rule under asymmetric loading has been widely noted in the literature of J_2 plasticity [85, 86, 93-96], so it is not surprising that the same issue persists when the model is adapted for use in crystal plasticity.

To correct the deficiencies of the G31 model, additional forms of the back stress evolution equation were investigated. These model forms included multi-term Armstrong-Frederick and Ohno-Wang formulations. The most satisfactory results were obtained using a multi-term Ohno-Wang back stress evolution equation, and was introduced as model OW44. During the initial fitting process for this model, a 4-term form was used, but 2-terms were found to be sufficient to capture experimentally observed trends.

To illustrate the evolution of the back stress with the G31 model form and fitting constants, Figure 25 presents the calculated value of back stress on a single slip system using prescribed values for $\dot{\gamma}^{(\alpha)}$ and time increment. The back stress evolution in Figure 25 is governed by the Armstrong-Frederick hardening law, given in Eqn. 22.

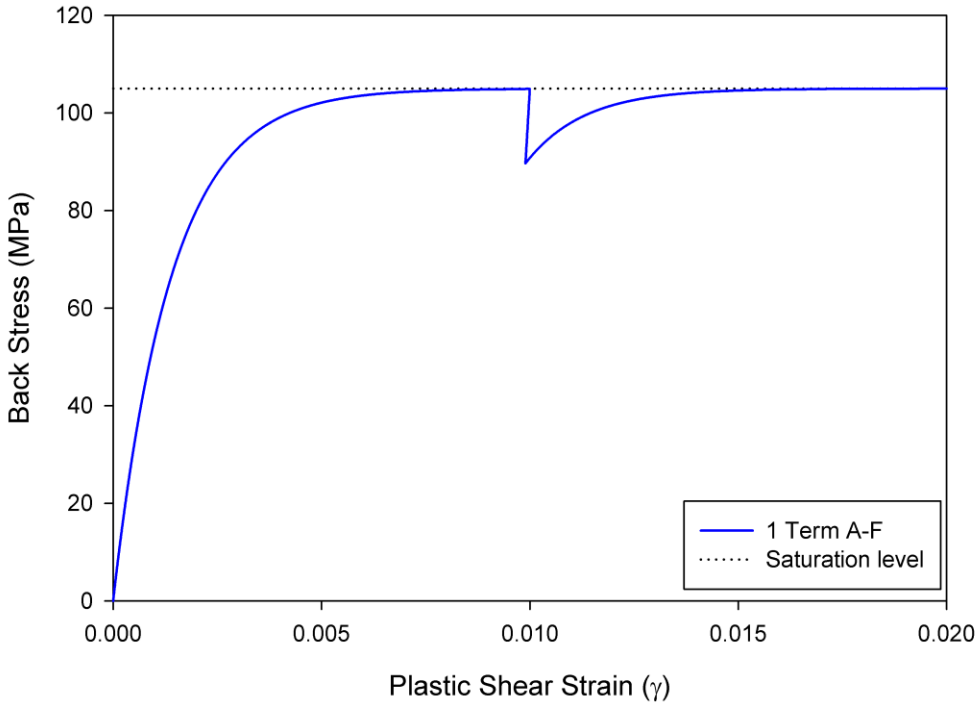

Figure 25. Evolution of the single term A-F back stress model.

The loading shown in Figure 25 consists of 3 steps: an initial positive loading to a plastic shear strain of 0.01, a short reversal in the loading direction to a plastic shear strain of 0.0099, and finally re-loading in the original direction to a final plastic shear strain of 0.02. Although the values of $\dot{\gamma}^{(\alpha)}$ and time increment used to generate this plot are taken to be constants over each loading step, the Figure serves as a useful aid in the discussion of the general features of AF hardening laws and for comparison with OW hardening laws.

During the first loading step we can see that rate at which the back stress evolves decreases as it approaches the saturation level, b. The relative rate at which the back stress approaches the saturation level is related to the magnitude of the difference between h and r; the larger the difference, the faster the back stress approaches

saturation. The non-linearity is introduced by the second term in Eqn. 23, the dynamic recovery term. When the loading is reversed (seen in Figure 25 as the sharp decrease in the back stress level) the back stress level decreases at a high rate because the first term of Eqn. 23 (now negative due to the negative $\dot{\gamma}^{(\alpha)}$) is increased in magnitude by the subtraction of a positive dynamic recovery term. When the loading is again reversed and proceeds in the original direction, the back stress evolves at a much slower rate than during the previous reverse loading step. It is this difference between the rate of back stress evolution in forward and reverse loading directions (when the back stress remains near saturation levels during the full cycle) that produces the ratcheting effect observed in the simulations. In Figure 25 the difference in plastic strain between the reverse loading step and the return to saturation is analogous to ratcheting; if the amount of plastic strain required to return to saturation levels is reduced, ratcheting is similarly reduced.

A 4-term Ohno-Wang back stress model was fit to match the response of the AF model in Figure 25 during the initial loading to a plastic shear strain of 0.01. Note that the 4-term OW back stress evolution is governed by Eqn. 25, with the exception that the summation is conducted with *i* from 1 to 4. The single term AF and 4-term OW models are compared in Figure 26, using the same imposed values for $\dot{\gamma}^{(\alpha)}$ and time increment as in Figure 25. The overall response of the 4-term OW model is shown as a solid red line, while the contributions of each of the 4 terms are shown by dashed red lines.

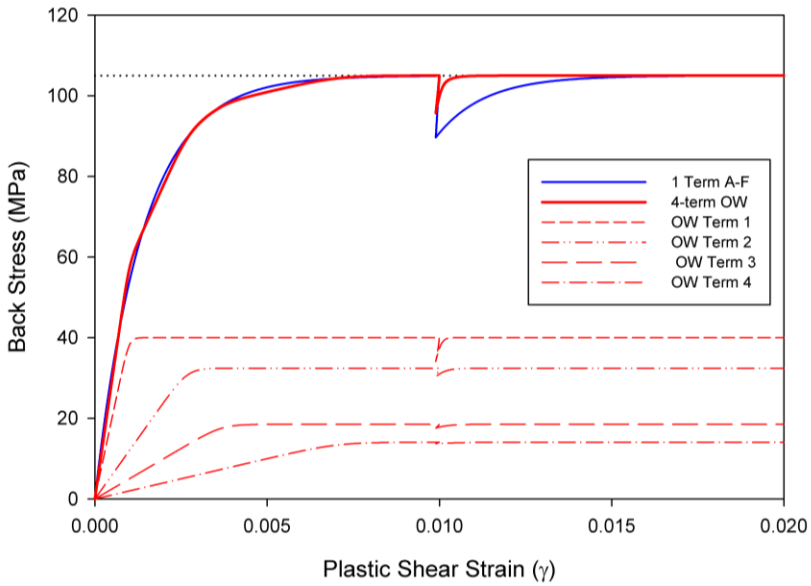

Figure 26. Evolution of the 4-term Ohno-Wang back stress model compared to single term model.

To generate Figure 26, the value m_i was taken to be 12 for all terms in the OW hardening law. The OW model form provides a large improvement in the predicted response to load reversal while closely matching the stress-strain response during the initial loading. Increasing the value of m_i further decreases the amount of plastic strain required to return to saturation levels following a load reversal, but at the cost of decreasing the smoothness of the initial loading response. This is shown in Figure 27.

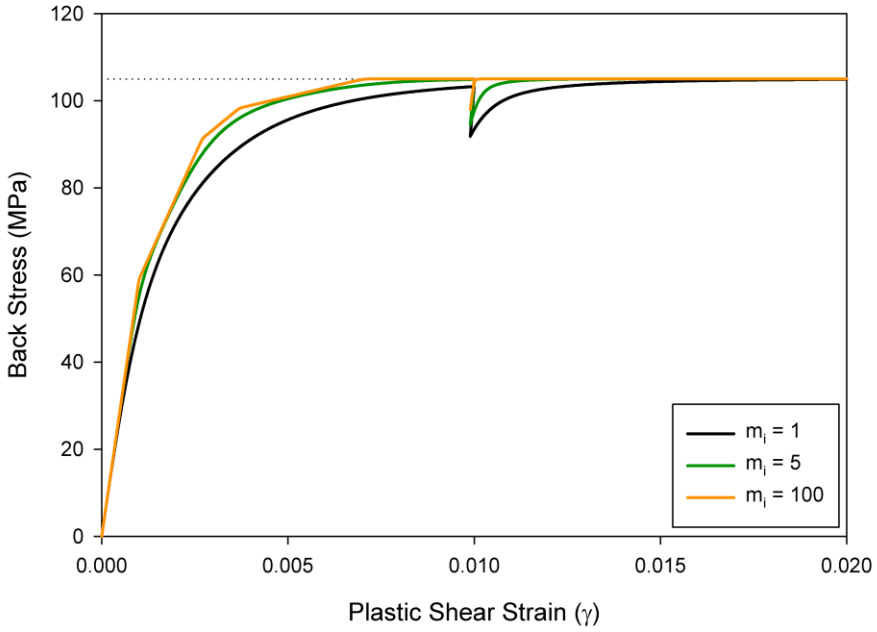

Figure 27. A comparison of back stress evolution for varying values of m_i in the Ohno-Wang model.

Figure 27 illustrates that as the values of m_i is increased, the back stress evolution approaches a piecewise-linear form and the plastic strain required to return to saturation following load reversal is decreased.

No experimental data in the form of complete hysteresis loops like those used to fit the fully-reversed cyclic response were found during a survey of the literature on Al 7075-T6. Therefore, experimental mean stress relaxation data obtained by Arcari et al. [97] was used to assess the accuracy of the predicted cyclic response in the presence of a mean stress or mean strain, and to fit the value of m_i used in the models with OW back stress evolution.

To choose a value of m_i for the OW backstress evolution equation, simulations were conducted with varying m_i values under fully reversed loading and loading with an

imposed mean strain. Although it is possible to have two separate values for m_i, each controlling the activation of a different recall term, the simulations focused on finding a single constant value for both terms. Despite having only one value, we will continue to refer to the exponent as m_i to differentiate it from the strain rate sensitivity exponent. The value of m_i has only a small effect on fully reversed simulations, shown in Figure 28, which plots the stress vs. plastic strain at over 5 cycles at an applied strain amplitude of 0.8%.

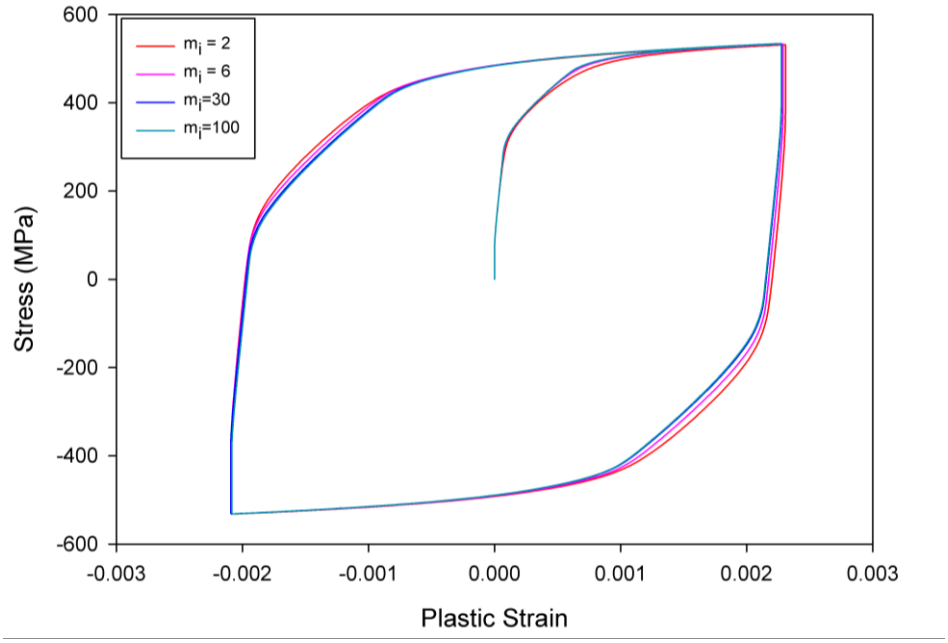

Figure 28. Comparison of response obtained by varying values of m_i in the OW44 model. Loading is fully reversed with ε_a=0.8%.

While some variation in the hysteresis loops is visible in Figure 28 for differing values of m_i, simulations using values larger than 30 produce nearly indistinguishable results.

The value of m_i has a larger effect on the stress-strain response under asymmetrical loading. A series of simulations with values of m_i ranging between 10 and

400 were conducted in order to select a value that best fit experimental observations. These simulations considered uniaxial cyclic loading and were conducted at an imposed strain amplitude of 0.4%, with a mean strain (ε_{mean}) of = 1.4% (R_ε = 0.556), for a total of 100 computational cycles. The simulations were compared to a baseline simulation using calibration G31 with the same mesh and loading conditions. To compare the overall response predicted by the new OW44 model and that of the G31 model, Figure 29 presents the stress vs. plastic strain over the entire 100 computational cycles.

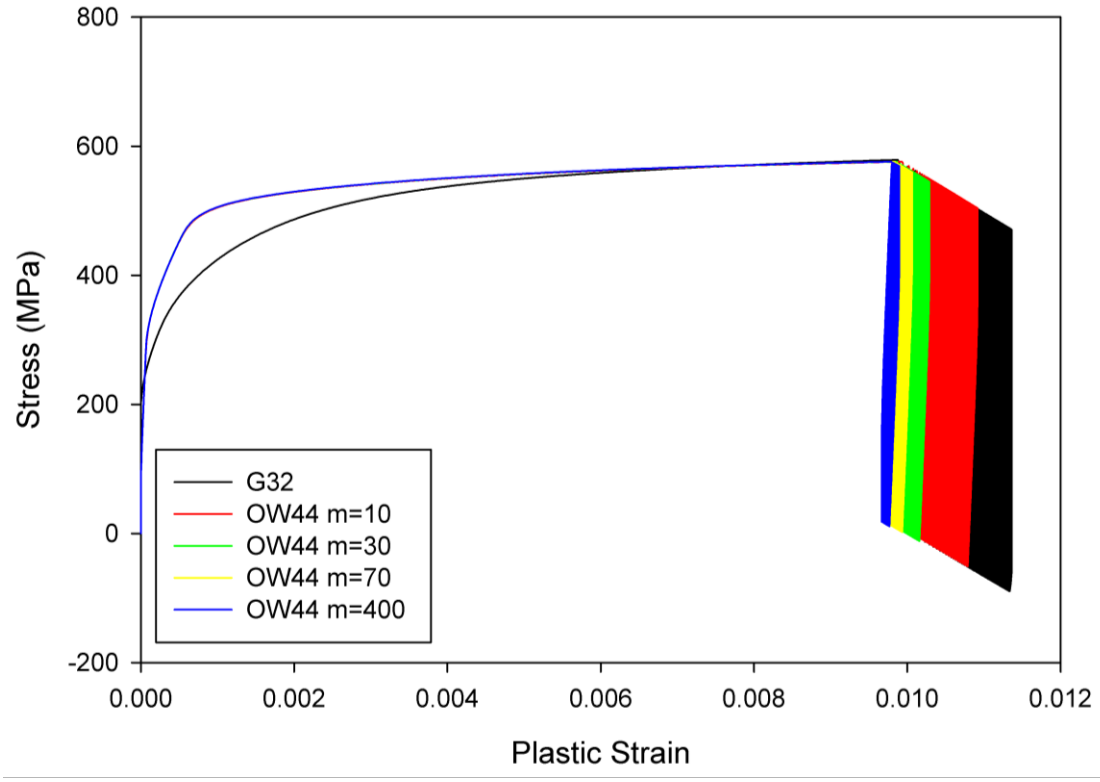

Figure 29. Cyclic Stress-Plastic Strain Curve comparison between two models over 100 computational cycles at ε_a = 0.4%, ε_{mean} = 1.4%, and R_ε = 0.556 loading.

The general trend observed in Figure 29 is that the OW44 model predicts a reduced amount of ratcheting and mean stress relaxation compared to the G31 model, with higher values of m_i reducing the degree of ratcheting and mean stress relaxation. Also visible is

the difference in the responses between the models during the initial load up before cycling is applied. However, as discussed previously different values of m_i (at least above some threshold) do not have a large effect in this region of monotonic loading, and the results for values of m_i ranging from 10 to 400 are indistinguishable during the initial loading.

Figure 30 is a semi-log plot of the ratcheting strain per cycle vs. the computational cycle number for model G31 and model OW44 with varying values of m_i. This Figure illustrates the trend of decreasing ratcheting strain with increasing m_i very clearly, as well as the large reduction in ratcheting when compared to model G31.

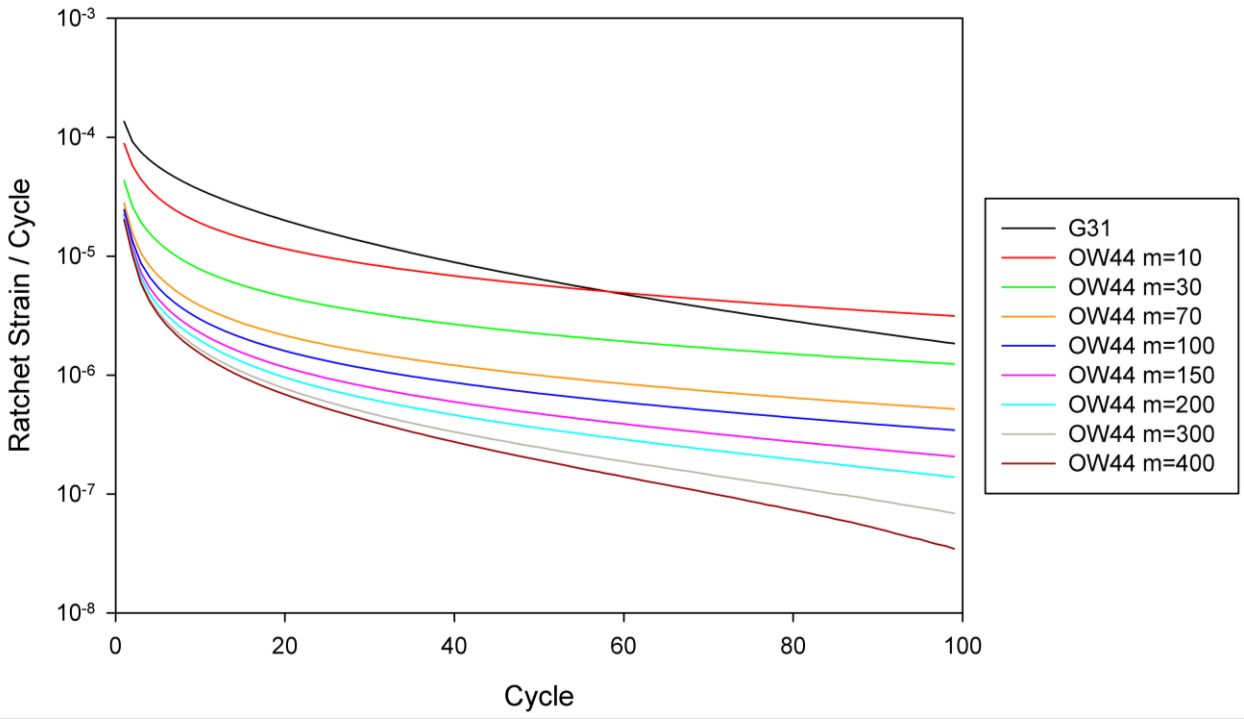

Figure 30. Ratcheting strain per cycle over 100 computational cycles at ε_a = 0.4%, ε_{mean} = 1.4%, and R_ε = 0.556 loading.

Another interesting feature in Figure 30 is the crossover in predicted ratcheting strain by model G31 and OW44 with m_i=10 around cycle 60. This indicates the tendency of the OW44 model to approach a saturated value in fewer cycles than the G31 model.

In absence of available data regarding ratcheting strain in Al 7075-T6 at strain amplitudes around 0.4% and at room temperature, mean stress relaxation data can serve to validate the computational results and determine which value of m_i should be used. Figure 31 plots mean stress relaxation data for Al 7075-T6 [97] against simulated results using the two models. Both models predict an initial mean stress about 6 MPa higher (approximately 2% higher) than the results reported by Arcari et al. [97], but predict differing amounts of mean stress relaxation.

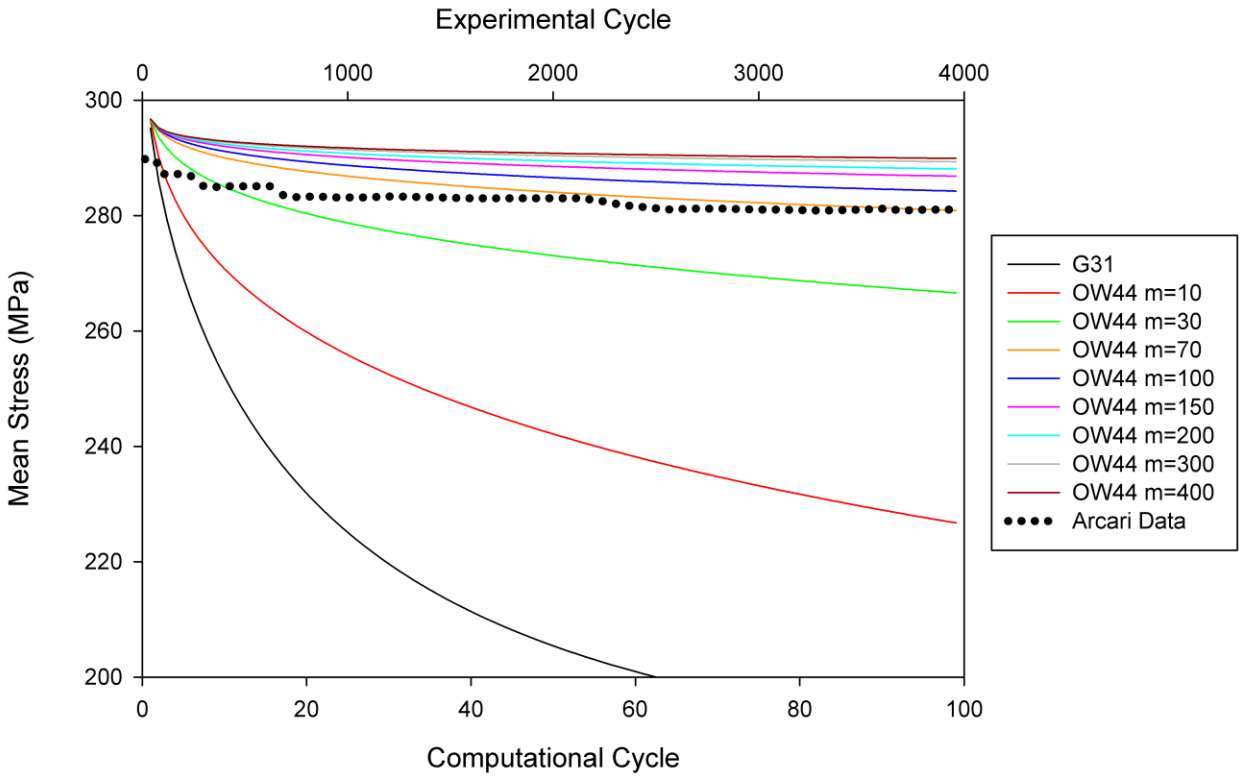

Figure 31. Mean stress relaxation over 100 computational cycles at ε_a = 0.4%, ε_{mean} = 1.4%, and R_ε = 0.556 loading.

Clearly visible in Figure 31 is that increasing values of m_i result in reduced degrees of mean stress relaxation, but have little effect on the initial mean stress during the first cycle. The G31 model over predicts the degree of mean stress relaxation by almost 100 MPa. At the end of the 100 computational cycles the OW44 model with m_i = 70 matches the experimental results obtained by Arcari et al., however it predicts a slightly larger amount of total mean stress relaxation. A comparison of the total mean stress relaxation over 100 cycles predicted by the OW44 model with different m_i values is shown in Figure 32. The horizontal dashed line indicates the value of the experimental mean stress relaxation from the beginning of cycling until half of the fatigue life of the specimen [97]. An inverse 3rd order polynomial was fit to the simulated results and plotted in the Figure.

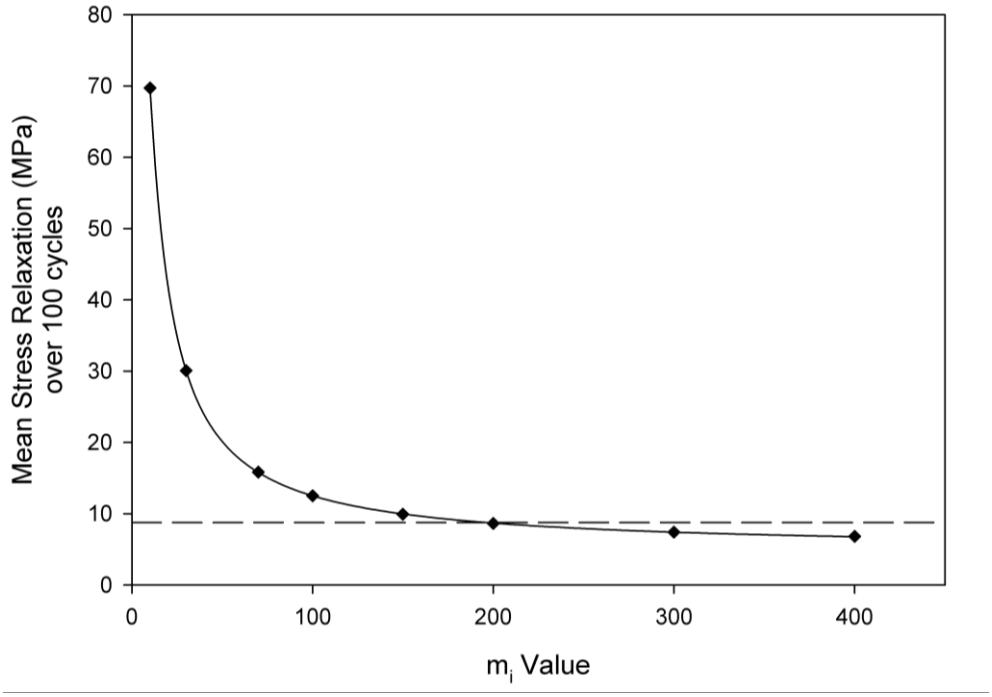

Figure 32. Simulated mean stress relaxation over 100 cycles using the OW44 model with varying values of m_i. Uniaxial loading with ε_a = 0.4%, ε_{mean} = 1.4%, and R_ε = 0.556.

Under these particular loading conditions, an m_i value of 200 provides the best agreement with the experimental total mean stress relaxation obtained by Arcari et al. However, the key point from Figure 32 is that values of m_i ranging from 100 to 400 all provide a predicted total mean stress relaxation that are of the same order of magnitude as the experimental data. To more clearly illustrate this we can compare the difference between the simulated mean stress relaxation and experimental mean stress relaxation to the magnitude of the mean stress at the half-life of the specimen. This provides a sense of the absolute error in the simulated mean stress induced by using differing values of m_i and can be represented by

$$\text{Absolute error} = \left(\frac{\left| \Delta\sigma_{mean}^{sim} - \Delta\sigma_{mean}^{\exp} \right|}{\sigma_{mean}^{\exp}} \right) \times 100 . \qquad (27)$$

The absolute error in simulated mean stress compared to the experimental value is plotted in Figure 33 for simulations conducted using model OW44 with different values of m_i.

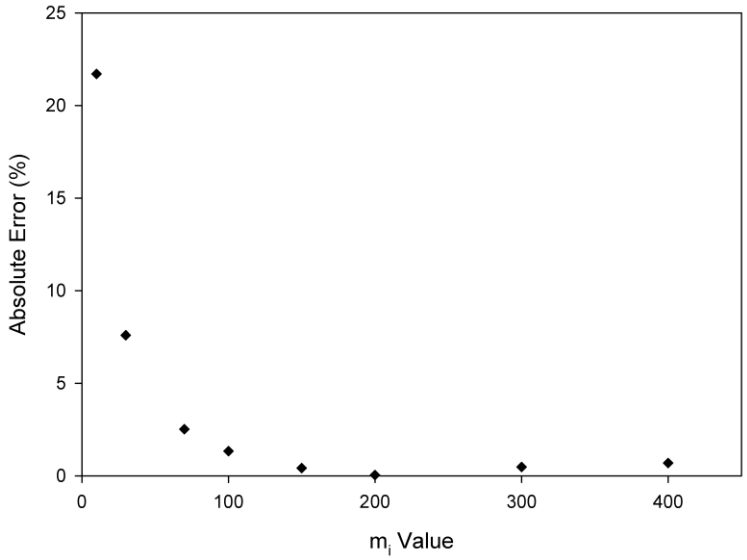

Figure 33. Absolute error in simulated mean stress response for varying values of m_i subjected to uniaxial loading with ε_a = 0.4%, ε_{mean} = 1.4%, and R_ε = 0.556.

As in Figure 32, it is evident in Figure 33 that for this particular loading, an m_i value of 200 provides the best agreement with experimental results. Figure 33 also shows that for m_i values from 100 to 400, the absolute error in predicted mean stress is 1% or less.

The simulated cyclic plastic strain range for both models over 100 computational cycles is plotted in Figure 34. The cyclic plastic strain range predicted by the OW44 model under fully reversed, uniaxial loading with an applied strain amplitude of 0.4% is represented by the red horizontal dashed line, while the cyclic plastic strain range predicted by the G31 model is indicated by the black dashed line. Figure 18 captures the large difference in predicted cyclic strain between the two models (shown previously in Figure 22), with the OW44 model predicting approximately 4 to 5 times as much plastic strain under both fully reversed loading and loading with a mean strain.

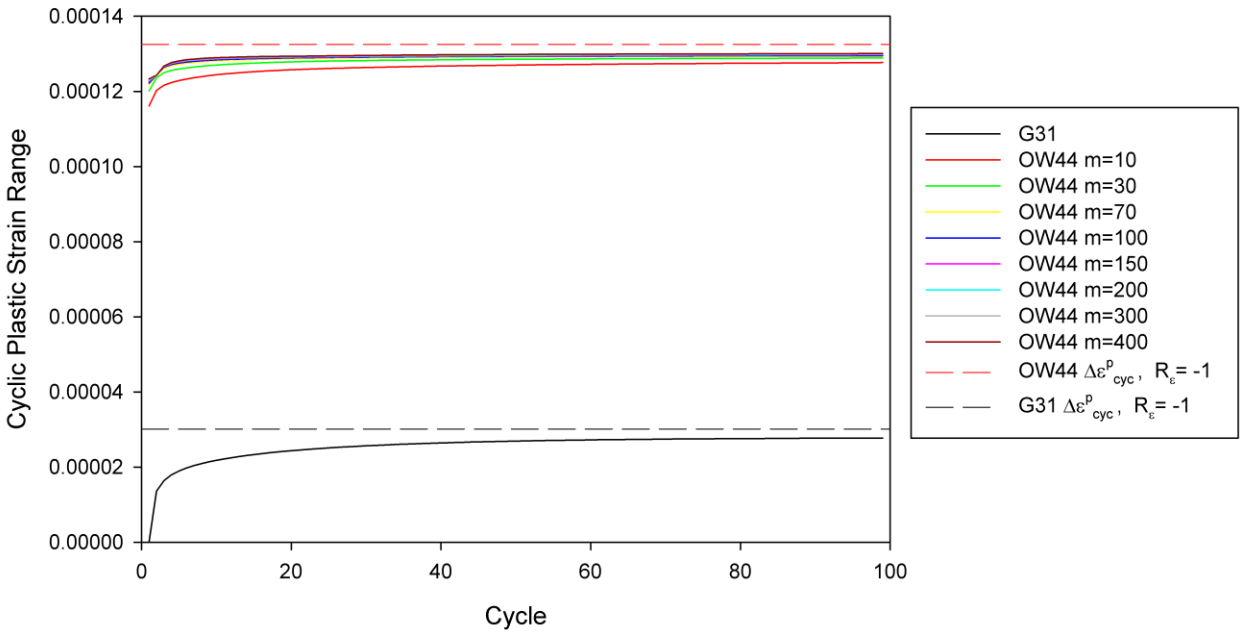

Figure 34. Cyclic plastic strain range over 100 cycles at ε_a = 0.4%, ε_{mean} = 1.4%, and R_ε = 0.556 loading.

Figure 34 also shows that both models predict smaller plastic strains when loaded with a mean strain than when loaded under fully reversed conditions for the same applied strain amplitude. Plotting the cyclic plastic strain range during the mean strain simulations as a fraction of the cyclic plastic strain under fully reversed loading results in the plot is shown in Figure 35. The Figure illustrates that model G31 predicts a much smaller cyclic plastic strain range when loaded with a mean strain than the OW44 model regardless of the value of m_i chosen. For the OW44 model with values of m_i over 30, the cyclic plastic strain range reaches 95% of its value under R_ε = -1 loading by the 5th computational cycle and saturates to 97% of the value by the 100th cycle. In comparison, the G31 model takes over 50 computational cycles to reach a cyclic plastic strain range that is 90% of its value under R_ε = -1 loading and approaches 93% percent of the value by the 100th cycle. Also shown in Figure 35 are dashed vertical lines corresponding to the 2nd, 4th and 6th complete computational cycles. During early fatigue simulations, the nucleation life of the nucleant grain and the 2nd and 3rd grain to crack were evaluated at these cycle counts under similar loading conditions. On the 2nd, 4th and 6th cycles the G31 model predicts 45%, 60% and 66% of the fully reversed cyclic plastic range, respectively. This resulted in longer fatigue lives when cycling was conducted under conditions that introduce a mean stress, opposite of experimental observations. For simulations conducted with the G31 model, the fraction of the fully reversed cyclic plastic strain range continues changing rapidly until around the 60th complete cycle (121 loading steps).

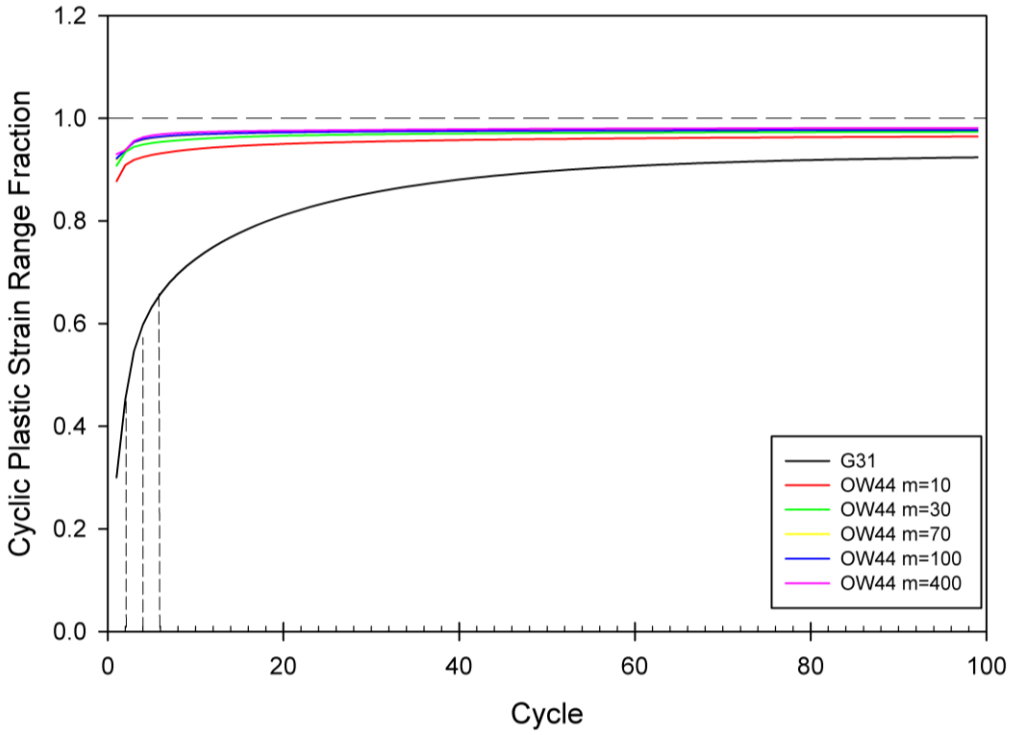

Figure 35. Cyclic plastic strain range over 100 cycles at ε_a = 0.4% and R_ε = 0.556 as a fraction of cyclic plastic strain range at ε_a = 0.4% and R_ε = -1 using the same model and mesh instantiation.

The initially rapid changes and large number of cycles to approach a saturated response are undesirable in a mesoscale model because it would require the simulations to be run using a much larger number of computational steps before an accurate prediction could be made. The OW44 model approaches a saturated level of cyclic plastic strain much more rapidly than the G31 model, which is another advantage to using this model form.

One complication introduced by the Ohno-Wang formulation is that the derivative of the back stress with respect to $\dot{\gamma}^{(\alpha)}$ changes rapidly whenever any of the back stress terms approaches saturation, especially if the value of m_i is high, O(10^2). This can introduce some numerical instabilities in the solution which prevent convergence, requiring additional sub-incrementation in order to find a solution. This can lead to longer

simulation times when compared to simulations conducted with the G31 model and its AF based back stress evolution. The computational times and wall times required to perform the simulations with varied values of m_i for 100 cycles are presented in Table 5. Also included in the table are CPU times for each simulation normalized to the baseline G31 simulation.

Table 5. Computational Speed of Models and Calibrations

	Model								
	G31	**OW44**	**OW44**	**OW44**	**OW44**	**OW44**	**OW44**	**OW44**	**OW44**
	N/A	m=10	m=30	m=70	m=100	m=150	m=200	m=300	m=400
CPU Time (hrs)	451	495	442	451	508	523	538	570	565
Normalized CPU Time	1	1.10	0.98	1.00	1.13	1.16	1.19	1.26	1.25
Wall Time (hrs)	73	78	71	73	83	85	86	90	89

There is some variability in the relation of m_i to the CPU time required to complete the simulation, but the overall trend is a slight increase in CPU time with increasing values of m_i. Over the course of a typical fatigue simulation this results in an increase in wall time of less than 5 hours. Considering the large improvements using the OW44 model this is a very acceptable increase over the G31 model.

3.5.1: Performance at Different Applied Strains

Additional simulations were conducted to evaluate the performance of the OW44 model over a range of applied cyclic strain amplitudes and mean strains. All of these simulations were conducted with uniaxial loading conditions and for 100 computational cycles. The applied strains during these simulations were selected to match those of Arcari et al. [97] and are summarized in Table 6. Note that the results presented thus far

for mean stress relaxation simulations using model OW44 have been loaded to correspond to Test 9 in the Table.

Table 6. Test details for mean stress relaxation experiments conducted by Arcari et al. [97].

	Arcari 7076-T6 Test Number				
	4	**5**	**6**	**7**	**9**
Cyclic Strain amplitude (%)	0.72	0.675	0.63	0.5	0.4
Mean Strain (%)	1.08	1.125	1.17	1.3	1.4
Maximum Strain (%)	1.8	1.8	1.8	1.8	1.8
Minimum Strain (%)	0.36	0.45	0.54	0.8	1
Strain Ratio	0.2	0.25	0.3	0.444	0.556

The simulations were conducted using the same mesh and a single value of m_i. The results from these simulations are compared to data from Arcari et al. [97] in Figure 36 and Figure 37. In both Figures, the simulation data is presented by solid lines, and the experimental data by dashed lines.

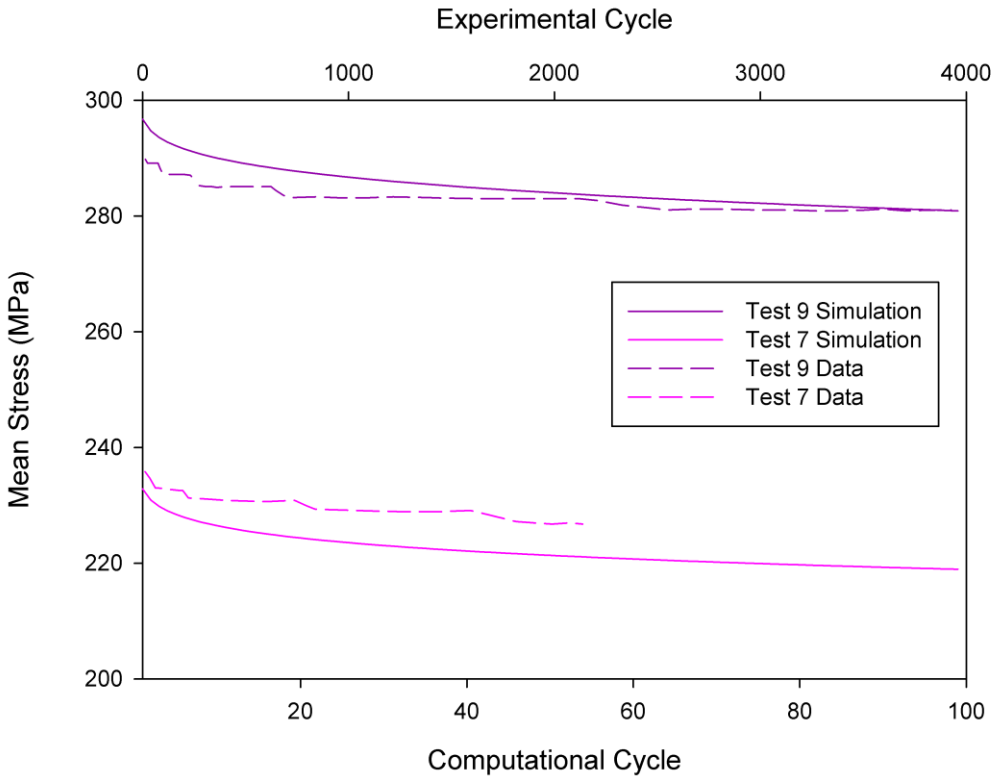

Figure 36. Comparison of simulations using model OW44 with m_i=70 to experimental data of Arcari et al. [98] for loading conditions 7 and 9.

The simulations shown Figure 36 correspond to Tests 7 and 9 in Table 6, with applied strain amplitudes of 0.5% and 0.4%, respectively. In this regime, the agreement between the experimental results of Arcari et al. and the simulations is adequate, with absolute errors of less than 10 MPa. As the applied strain amplitude increases in Tests 4, 5, and 6 (corresponding to applied strains of 0.72%, 0.675% and 0.63%) the response of the model becomes increasingly poor with absolute errors in excess of 50 MPa.

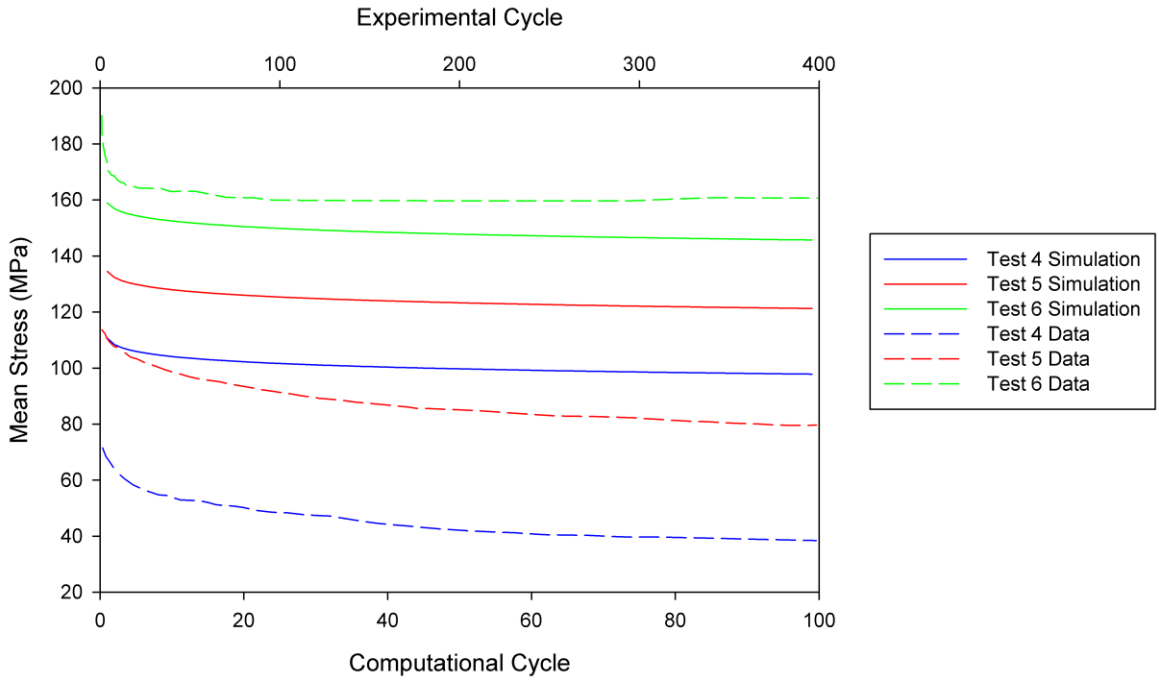

Figure 37. Comparison of simulations using model OW44 with m_i=70 to experimental data of Arcari et al. [98] for loading conditions 4, 5, and 6.

The error in the mean stress response between the experimental results and the simulations can be broken into two components, error in the initial mean stress during the first cycle, and error in the magnitude and rate of relaxation during subsequent cycling. These errors are summarized in Table 7 for each loading condition as a percent of the experimental values.

Table 7. Table comparing the error between simulations using model OW44 with m_i=70 to experimental data of Arcari et al [98].

	Test Number				
	4	**5**	**6**	**7**	**9**
Error in initial mean stress	55%	18%	-7%	-1%	2%
Error in mean stress relaxation	-53%	-26%	2%	2%	3%

Additional calibration of the constitutive model would be needed in order to match the results of Arcari et al. [97] over the entire range of applied strains. This would require data in the form of complete stress/plastic strain hysteresis loops for the simulations conducted, which are not typically published.

The magnitude of mean stress relaxation over 100 computational cycles shows very little variation between the simulations conducted with model OW44, despite significant differences in applied strain amplitude. Simulated mean stress relaxation over 100 cycles is plotted against the applied strain amplitude in Figure 38.

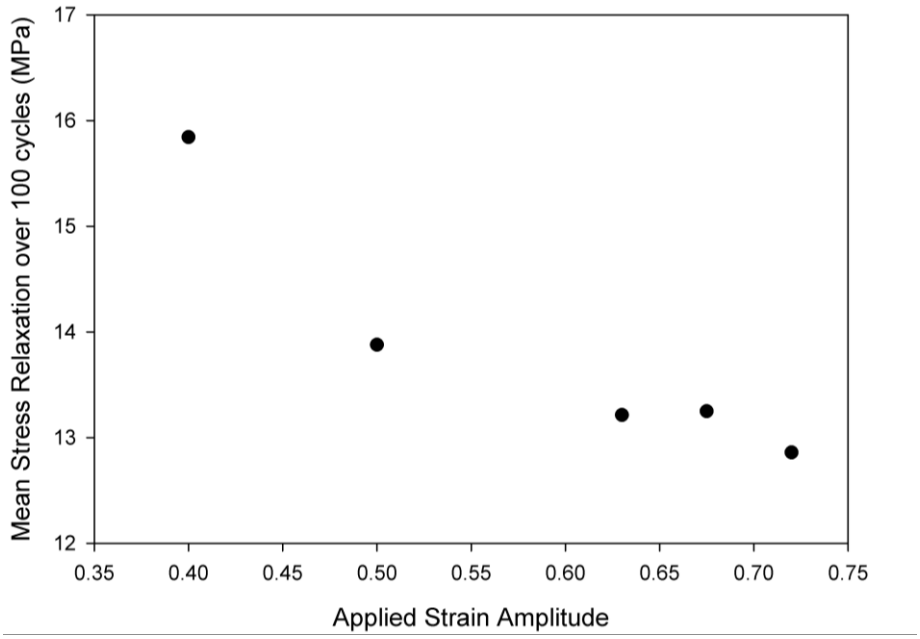

Figure 38. Simulated mean stress relaxation over 100 computational cycles using the OW44 model with $m_i = 70$.

The difference between the largest and smallest predicted mean stress relaxation is less than 3 MPa, and the trend is that increasing applied strain amplitude results in decreasing amounts of mean stress relaxation, opposite of what is typically observed experimentally. This suggests that to capture the magnitude of the mean stress relaxation effect over a

range of loading conditions, m_i should be formulated as a function of the applied strain or the cyclic plastic strain. However, in absence of the data needed to obtain better agreement between the experimental and simulated initial mean stress values, such a formulation will not be pursued.

3.5.2: Performance of the OW57 Model

During the calibration process of model OW44 it was noted that the low valued, constant drag stress (35 MPa) resulted in slip activity among almost all slip systems during cyclic loading. The activation of all slip systems during loading is possibly unrealistic, and therefore an evolving drag stress was introduced to model OW44 in order to reduce the degree of slip system activation. This new model is referred to as OW57. During calibration, a saturation value of 100 MPa was selected for the drag stress, with an initial value of 30 MPa. This section will compare the performance of the OW44 and OW57 models when cyclically loaded with an imposed mean strain.

The cyclic plastic strain responses of the two models when loaded with an applied strain amplitude of 0.4% and a mean strain of 1.4% (corresponding to loading 9 in Table 6) for a total of 100 computational cycles are compared in Figure 39. The plot on the left side of the Figure compares the absolute value of cyclic plastic strain range during cycling to the stabilized cyclic plastic strain range obtained using the same model cycled under fully reversed loading conditions at the same amplitude. The plot on the right of the Figure compares the cyclic plastic strain ranges of the two models both normalized to their cyclic plastic strain range responses under fully reversed loading (referred to here as the cyclic plastic strain range fraction).

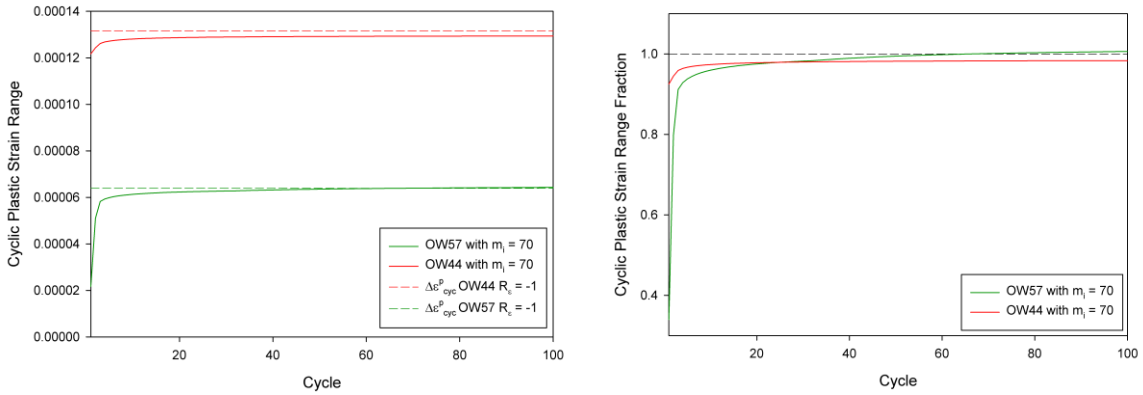

Figure 39. Comparison of the cyclic plastic strain range over 100 cycles for models OW44 and OW57 with $m_i = 70$. Applied loading conducted at $\varepsilon_a = 0.4\%$, $\varepsilon_{mean} = 1.4\%$, and $R_\varepsilon = 0.556$.

Both plots of Figure 39 illustrate that the OW57 model has a more pronounced transient in the cyclic plastic strain range response than the OW44 model. During the first 5 cycles, the cyclic plastic strain range of the OW57 model increases from approximately 34% of its saturated value to 94% of the same value. In comparison, the OW44 model increases from 93% to 96% of its saturated cyclic plastic strain range under fully reversed loading during the first 5 cycles. Additionally, the cyclic plastic strain range fraction of the OW57 model continues to increase during cycling, reaching a value of 1 by loading cycle 67. In the mesoscale approach to fatigue life modeling employed by this thesis, simulations are typically conducted for 40 computational cycles or less and the evaluation of nucleation life is delayed until a near stable cyclic response is obtained, largely avoiding any inaccuracies that would be introduced by the large transients in cyclic plastic strain range. The left hand plot of Figure 39 shows that for both fully reversed cyclic loading and cyclic loading with a mean strain the OW57 model predicts a smaller plastic strain range than the OW44 model. At an applied strain of 0.4%, the OW57 model predicts less than

50% of the plastic strain range of the OW44 model, consistent with the results shown in Figure 22.

A comparison of the ratcheting strain per cycle obtained with the two models is presented in Figure 40. The magnitudes of the ratcheting strains over 100 cycles are shown in the left side of the Figure, while the ratcheting strain of the OW57 model as a percent of the OW44 model is shown on the right. The overall responses of the two models are very similar, but again the OW57 model exhibits a larger transient in response over the first 5 cycles.

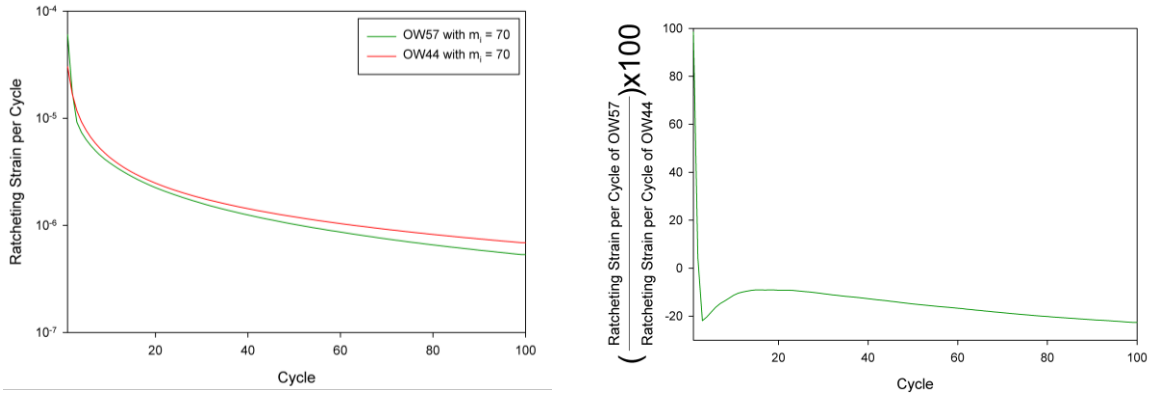

Figure 40. Comparison of the ratcheting strain per cycle for 100 cycles using models OW44 and OW57 with m_i = 70. Applied loading conducted at ε_a = 0.4%, ε_{mean} = 1.4%, and R_ε = 0.556.

During the 1st cycle, the OW57 model predicts a ratcheting strain almost double that of the OW44 model. Then by the 3rd computational cycle, the OW57 model predicts smaller ratcheting strains than the OW44 model, which continues until the end of the simulation.

The mean stress responses for each of the five loading conditions listed in Table 6 are plotted in Figure 41 for models OW44 and OW57, both with an m_i value of 70. In the Figure dashes lines correspond to results from model OW57 and solid lines to the

results from OW44. Simulations with the same applied loading are plotted in the same color.

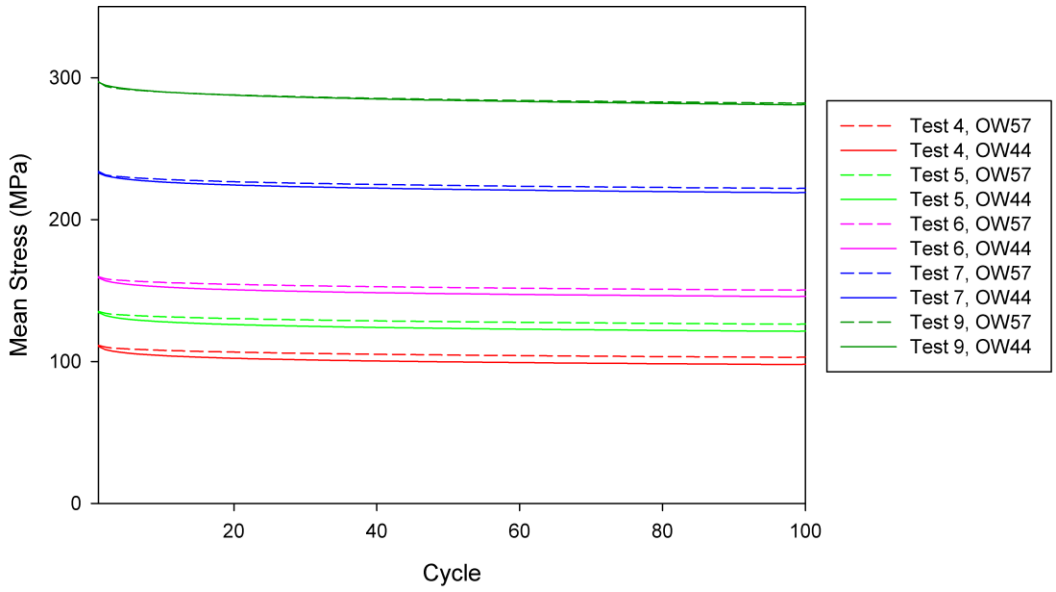

Figure 41. A comparison of the mean stress relaxation between models OW44 and OW57 over 100 computational cycles at 5 different applied strain amplitudes, with $m_i = 70$.

The OW57 model predicts less mean stress relaxation over 100 cycles than the OW44 model for all five loading conditions; although maximum the difference between the two models for any loading and cycle is less than 5 MPa. The magnitude of the mean stress relaxation predicted by the OW57 model increases with decreasing applied strain amplitude, consistent with the trend observed for the OW44 model.

Overall, the addition of an evolving drag stress in the OW57 model has little effect on the ratcheting and mean stress relaxation response of the model compared to model OW44, which uses a constant valued drag stress. The OW57 model does introduce a steeper transient response during the first few loading cycles, but as long the evaluation of fatigue parameters is delayed until after the response stabilizes the impact of this is

negligible. The most critical differences between models OW44 and OW57 are the cyclic plastic strain ranges. For example, at a strain amplitude of 0.4% (typical strain amplitude of interest for the fatigue simulations conducted in this thesis), model OW44 predicts more than twice the cyclic plastic strain range of model OW57 under both uniaxial loading conditions and when loaded with a mean strain. The OW44 model is in good agreement with the data of Renard et al. [92] in this regime, so the difference between the models represents a significant under-prediction of cyclic plastic strain range by model OW57. The impact of the differences in cyclic plastic strain range on predicted fatigue lives are examined in Chapter 4.

3.5.3: Influence of Integration Increment Size on Ratcheting

The magnitude of the ratcheting effect predicted by the simulations can depend not only on the material model form and calibration, but on the size of the increments used during the loading step. When conducting a FE simulation with Abaqus it is possible to limit the maximum increment size, preventing the automatic increment size control procedures from attempting increments larger than a certain value. If the maximum increment size provides stable convergence over the entirety of a step, then this value essentially prescribes the increment size Abaqus will use to complete this step. In other words, by varying the allowable maximum increment size the actual increment size can be kept nearly constant over the step, provided good convergence is obtained.

Simulations were conducted using the OW44 model with a value of m_i=200 for a total of 5 complete computational cycles with varying values of maximum increment size to quantify this effect of increment size on ratcheting. For all simulations the loading was uniaxial with a strain amplitude of 0.33% and a strain ratio R_ε = 0.5. The step size was

30 s ($\dot{\varepsilon} = 1.1\times10^{-4}\ s^{-1}$) and all maximum increment sizes had good convergence over the cyclic loading steps, requiring no sub-incrimination by Abaqus. All simulations produced nearly the same values of cyclic plastic strain range, seen in Figure 42.

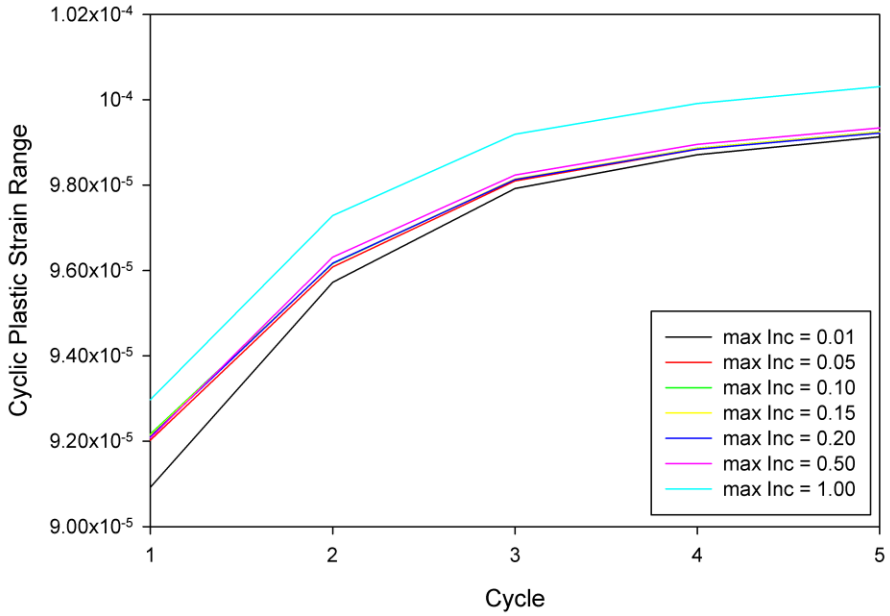

Figure 42. Cyclic plastic strain range over 5 computational cycles for varying values of maximum increment size. Loading is uniaxial with ε_a = 0.33%, and R_ε = 0.5.

The larger maximum increment sizes produced larger cyclic plastic strain ranges for a given cycle, but overall the difference is negligible considering that by cycle 5 the largest increment size of 1.00 s results in a cyclic plastic strain approximately 1% larger than obtained using a maximum increment size of 0.01 s. Similarly, the mean stress relaxation behavior appears to be nearly independent of the maximum increment size, varying less than a tenth of a percent between simulations. The ratcheting strain, however, exhibited non-negligible dependence on the maximum increment size. This is illustrated in Figure 43, a plot of the ratcheting strain per cycle normalized by the cyclic plastic strain per cycle.

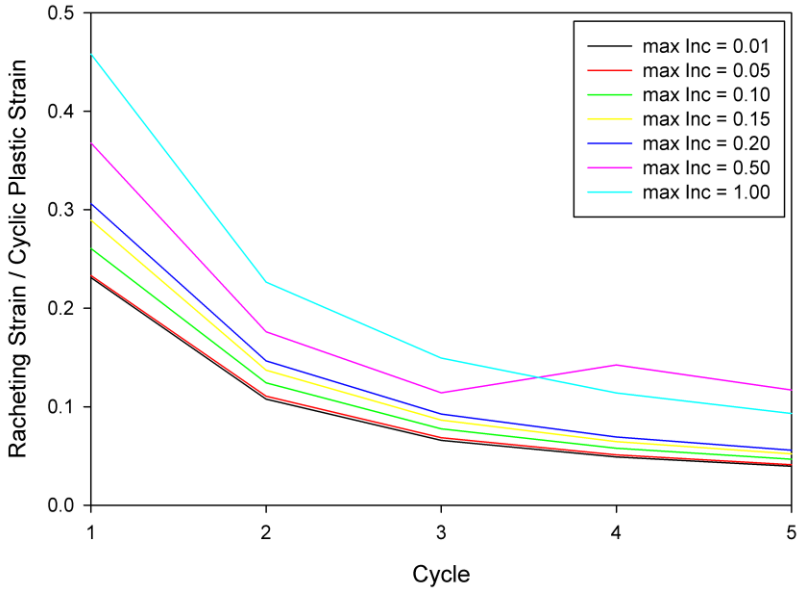

Figure 43. Ratcheting strain as a fraction of cyclic plastic strain range over 5 computational cycles for varying values of maximum increment size. Loading is uniaxial with ε_a = 0.33%, and R_ε = 0.5.

The general trend observed in the Figure is that decreasing increment sizes result in decreased ratcheting strain per cycle, although results using a maximum increment size of 0.50 s are anomalous over the 4th and 5th cycle. On the 5th cycle of these simulations, the ratcheting strain with the maximum increment size of 0.50 s was almost three times larger than the ratcheting strain when the maximum increment size was 0.05 s. The difference decreases substantially when the maximum increment size is below 0.2 s, but the ratcheting strain of the 0.2 s maximum increment size is still approximately 40% larger than the ratcheting strain of the 0.01 maximum increment size case. These simulations were conducted using a material model and calibration that produces a small degree of ratcheting in comparison to the G31 model (see Figure 30), but the dependence of ratcheting strain on increment size is similar between the two models. This can lead to drastic overpredictions of the ratcheting strain when the already large ratcheting strain

predicted by the AF back stress is coupled with inappropriate control of the maximum increment size.

The value of the maximum increment size also has a strong effect on the time it takes to complete a simulation. The wall times and CPU times required to complete the simulations done to evaluate the effects of maximum increment size are listed in Table 8, along with the wall times and CPU times normalized to the respective values of the 0.05 maximum increment size simulation which required the lowest CPU time to complete out of all the simulations conducted. All simulations were conducted with the same strain rate, $\dot{\varepsilon} = 1.1 \times 10^{-4}\ \mathrm{s}^{-1}$.

Table 8. Effect of maximum increment size on the execution speed of simulations.

Max Inc Size (s)	Strain per Inc	CPU Time (h)	Wall Time (h)	Normalized CPU Time	Normalized Wall Time
0.01	1.1E-6	307.6	44.3	3.24	3.4
0.05	5.5E-6	95.1	12.9	1.00	1.0
0.1	1.1E-5	95.3	12.6	1.00	1.0
0.15	1.7E-5	95.9	12.4	1.01	1.0
0.2	2.2E-5	108.9	14.0	1.15	1.1
0.5	5.5E-5	208.3	35.5	2.19	2.8
1	1.1E-4	DNF	DNF	DNF	DNF

There is only a negligible difference between the CPU and wall times of the simulations conducted with maximum increment sizes between 0.05 and 0.15 s. In these simulations, almost no sub-incrimination by Abaqus was required in order to obtain a converged solution. At a maximum increment size of 0.01 s, no sub-incrimination by Abaqus was required, but the large number of increments required to complete a step results in the

implicit solver not being fully utilized and therefore increases the simulation time. At the larger maximum increment sizes of 0.2, 0.5, and 1.0 s, sub-incrimination was required frequently during the first loading step (the initial pre-strain before cycling, which larger in magnitude than the cyclic strain range). This wastes significant computational resources as the UMAT attempts to converge (and does so successfully for many elements) before requesting that Abaqus reduce the increment size further. This caused the simulation conducted with the maximum increment size of 1.0 s to fail to complete the 1st loading step (the initial pre-strain) over the entire 48 hour wall time, as indicated by the DNF entries in Table 8. The simulation was repeated with an initial maximum increment size of 0.05 s for the first step and a maximum increment size of 1.0 s for steps 2-11 (corresponding to cycles 1-5) in order to generate the data in Figure 42 and Figure 43. The total wall time for this simulation with mixed maximum increment sizes was approximately 9.5 hours, suggesting that the maximum larger increment size allows for better utilization of the implicit solver during cycling.

To aid in the explanation of why the increment size has such a strong impact on the predicted ratcheting strain, the stress vs. plastic strain data for the 1st complete loading cycle of the simulations conducted using a maximum increment sizes of 1.00 s and 0.01 s are plotted in Figure 44 and Figure 45. In both Figures, diamond markers indicate the output at the end of an increment. The two steps comprising the loading cycle were completed in a total of 105 increments when the maximum increment size was limited to 1.00 s, and a total of 6,022 increments when the maximum increment size was 0.01 s.

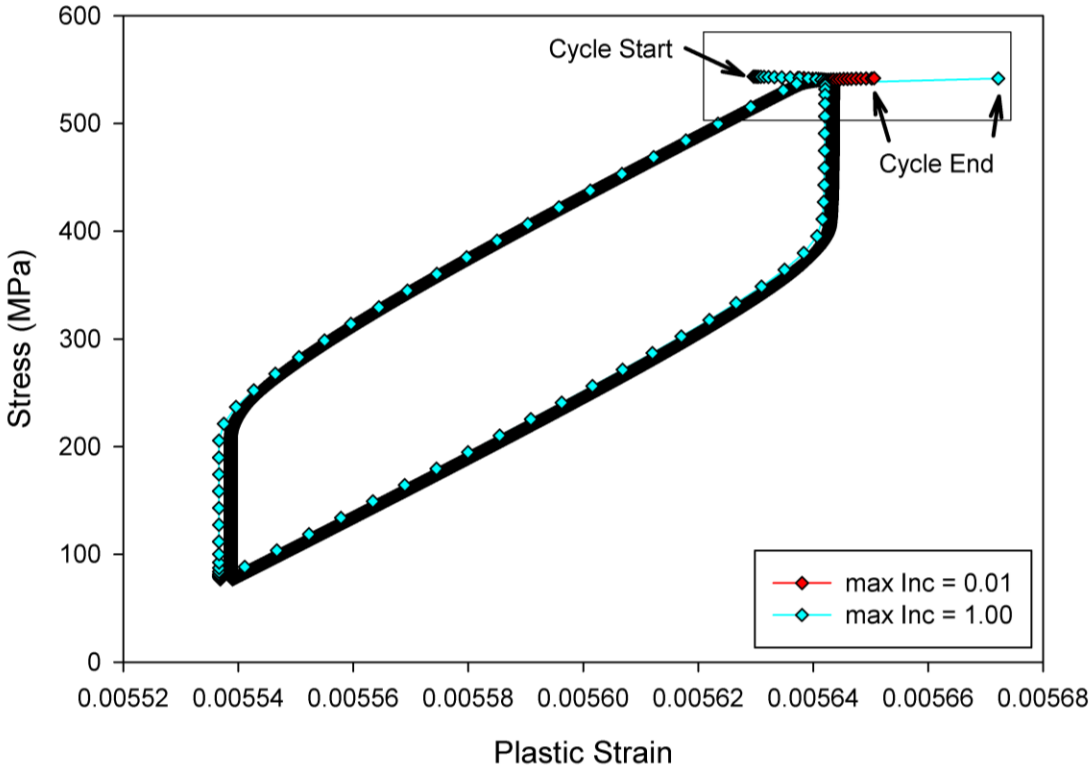

Figure 44. Comparison of the hysteresis loops of the first complete loading cycle for the simulations conducted with max increment sizes of 0.01 and 1.00 s. Results from the 0.01 maximum increment simulation are shifted right by a plastic strain of 4.8×10^{-6} such that both cycles begin at the same plastic strain. Loading is uniaxial with $\varepsilon_a = 0.33\%$, and $R_\varepsilon = 0.5$.

It is clear in Figure 44 that both simulations produce similar cyclic plastic strain ranges; however, there is significant divergence in predicted plastic strain at the end of the cycle despite both cycles beginning at the same value of plastic strain. Additionally, the magnitude of this difference is significant in comparison to the cyclic plastic strain range of the cycle. Figure 45 presents a magnified view of the stresses and plastic strains at the beginning and end of each of the two cycles, with the area of focus indicated by the rectangle in Figure 44.

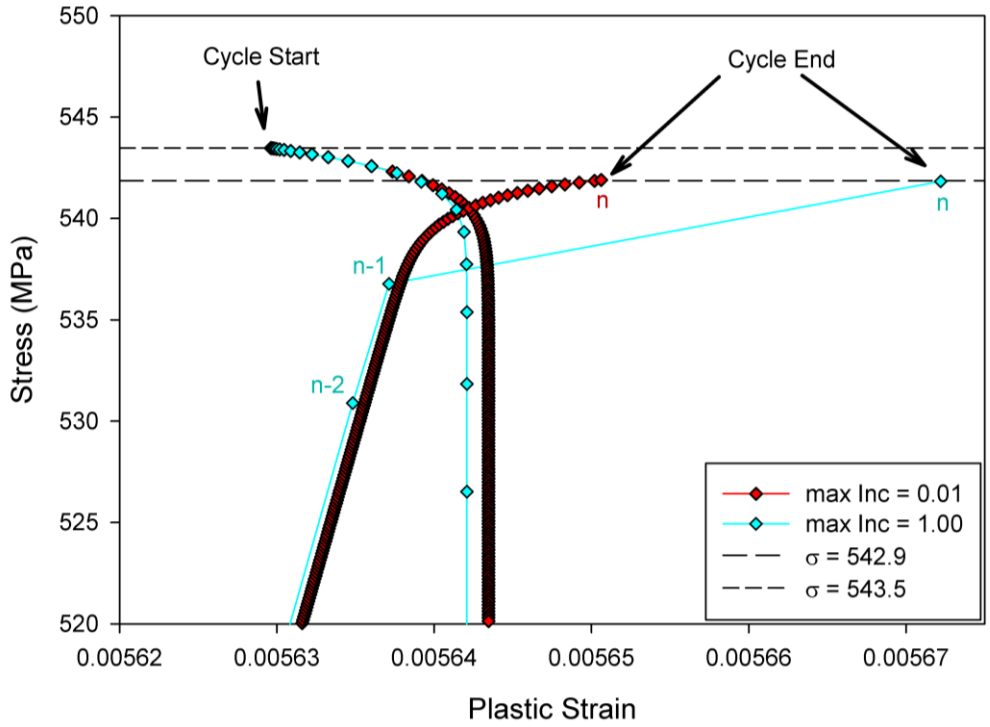

Figure 45. Magnified comparison of the hysteresis loops of the first complete loading cycle for the simulations conducted with max increment sizes of 0.01 and 1.00 s. Results from the 0.01 maximum increment simulation are shifted right by a plastic strain of 4.8×10^{-6} such that both cycles begin at the same plastic strain. The last 3 increments are labeled for the maximum increment size of 1 s case, and the last increment is labeled for the maximum increment size of 0.01 s case. Loading is uniaxial with $\varepsilon_a = 0.33\%$, and $R_\varepsilon = 0.5$.

When starting a new step, Abaqus begins with a prescribed increment size and then increases the size of the increments if convergence is obtained without the need for sub-incrementation. This leads to the overlap of the increment markers for the two simulations at the beginning of the cycle in Figure 45. After approximately the first 15 increments the plastic strains begin two diverge between the two simulations, however, it is not until the last increment of the simulation plotted in cyan (maximum increment size of 1.00 s) that the magnitude of the difference is significant. Note that the last increments of both simulations converge to the same stress at the end of the cycle, despite large differences in the maximum increment size.

This is a result of how the UMAT determines the plastic strain: Abaqus passes in the deformation gradient at the beginning ($\mathbf{F}_t$) and end of the increment ($\mathbf{F}_{t+\Delta t}$) to the UMAT, which must then calculate a kinematically admissible plastic deformation gradient for the increment based on the individual contributions of each slip system shearing rate. The plastic strain over the increment is then obtained by multiplying the converged plastic shearing rate on each slip system by the time step of the increment. This results in an estimate of plastic strain that is a constant over the increment. If the size of the increment is fairly large (1 s in the example shown in Figure 45) and converged plastic shearing rates are very different from the end of one increment to the next, a large error in the estimated plastic strain may be introduced. The stress and plastic strain data plotted in Figure 45 are volume averaged macroscopic quantities, but the principal behind the increment size induced ratcheting effect is the same. For these macro-scale stresses and plastic strains we can define a plastic tangent stiffness as

$$\frac{\partial \varepsilon^p}{\partial \sigma}. \tag{28}$$

For the increment of both simulations considered in Figure 45 (labeled with a color-coded “n”) the plastic tangent stiffnesses are roughly the same. When the maximum increment size is limited to 0.01 s, the second and third to last increments (n-1 and n-2, respectively) have tangent stiffnesses very similar to the tangent stiffness of the final increment. However, when the maximum increment size is increased two orders of magnitude, the plastic tangent stiffnesses at increments n and n-1 differ substantially, resulting in a poor approximation of plastic strain.

In simulations where the ratcheting strains are of interest (such as during fretting fatigue analysis) care must be taken to ensure that the ratcheting strains converge with

decreasing increment size, and that the increment size is limited where the plastic tangent stiffness changes rapidly. One possible solution to this problem is to limit the maximum increment size over the entire step, which was the methodology employed in the simulations investigating the ratcheting effect. However, this can limit the effectiveness of the implicit solver. A more efficient solution would be to require sub-incrementation in the case that some averaged measure of the plastic shearing rates diverges significantly from the same measure taken at the end of the previous increment.

3.6: Conclusions

This chapter introduced three crystal plasticity constitutive models for Al 7075-T6, all based on a common flow rule but differing in the forms of the hardening equations and model calibration. The performance of the models was compared when subjected to both symmetric and asymmetric cycling loading across multiple applied strain ranges.

It was shown that although each of the models was calibrated to the same fully reversed, macro-scale cyclic stress-strain data, there are large differences in the responses of the models at small applied strain amplitudes and when loaded cyclically with a mean strain. The model with an Armstrong-Frederick back stress evolution equation exhibited significant ratcheting strains that were determined to be an artifact of the model form, and were corrected through the implementation of a multi-term Ohno-Wang type hardening law. To summarize, the advantages of moving to a two-term Ohno-Wang type formulation of the back stress evolution equation from a single term Armstrong-Frederick model are:

- Enhanced ability to capture the magnitude of the plastic strain over a larger range of applied strains.
- Increased ease of fitting due to nearly linear, independent terms.
- Ability to match experimental mean stress relaxation data under asymmetric loading through selection of m_i, which has only a minor effect on the shape of the fully reversed hysteresis loops.
- Loading with an imposed mean strain results in only a slight reduction in cyclic plastic strain amplitude when compared to fully reversed loading conducted with the same applied strain amplitude.
- Model approaches a near saturated value of cyclic plastic strain rapidly when loaded with an imposed mean strain.

An evolving drag stress was added to the improved model, and while this addition had little effect on the ratcheting and mean stress relaxation response of the model, it reduced the magnitude of the cyclic plastic strain significantly under applied strain amplitudes of 0.4% or less. A comparison of the fatigue lives obtained with each of the three models is presented in Chapter 5, but most of the results in that Chapter are obtained using model OW44, as it was best able to match cyclic plastic strain data over the entire range of applied strains investigated.

Additionally, the effect increment size on predicted ratcheting strain per cycle was investigated. Changing the increment size between simulations resulted in less than a 1% change in the cyclic plastic strain range from the largest to smallest increment size used, but produced variation in the ratcheting strain per cycle of almost three times the value obtained using the smallest increment size. This is a significant change, and caution is

advised regarding incrementation control if the magnitudes of the ratcheting strains are of interest. To summarize, the numerical convergence of an increment does not insure similar convergence of the ratcheting strains. The fatigue modeling in this work was conducted with the maximum increment size limited to 0.05 s in order to ensure convergence of the ratcheting strains.

CHAPTER 4: MESOSCALE FATIGUE MODEL

4.1: Introduction

This Chapter presents the mesoscale fatigue model including the algorithms for both Stage I and Stage II crack growth. The chapter begins with discussion of concepts central to fatigue algorithms and simulations, including the crystallographic FIPs, mesh generation and element band averaging scheme, and the incorporation of damage. The Stage I fatigue algorithm of Castelluccio is then introduced, along with the modifications necessary to model a Stage II crack propagating on multiple slip systems. The implementation of the Stage II model in the ABAQUS [4] environment is then discussed.

4.1.1: Fatigue Indicator Parameter

To quantify the local driving force within the microstructure, this work employs a crystallographic fatigue indicator parameter (FIP) based on the macroscopic quantity originally suggested by Fatemi and Socie [11]. During the simulations, the FIP is evaluated over every cycle for each of the slip systems within an element, i.e.,

$$\mathrm{FIP}^{\alpha} = \frac{\Delta\gamma_p^{\alpha}}{2}\left(1 + k\frac{\sigma_n^{\alpha}}{\sigma_y}\right). \qquad (29)$$

Here, $\Delta\gamma_p^{\alpha}$ is the cyclic plastic shear strain range on slip system α, σ_n^{α} is the stress normal to slip system α, and σ_y is the cyclic yield strength of the material. The value of k is typically taken to be between 0.5 and 1, and in this work a value of 0.5 is used due to an absence of sufficient data for correlation. The cyclic plastic shear strain range in Eqn.

29 corresponds to the reversed cyclic plastic strain range ($\Delta\gamma_p^\alpha\big|_{\text{cyc}}$) over the cycle, calculated according to

$$\begin{aligned}\Delta\gamma_p^\alpha\big|_{\text{ratch}} &= \Delta\gamma_p^\alpha\big|_{\text{end of cycle}} - \Delta\gamma_p^\alpha\big|_{\text{start of cycle}} \\ \Delta\gamma_p^\alpha &= \gamma_{\text{max,cycle}}^\alpha - \gamma_{\text{min,cycle}}^\alpha \\ \Delta\gamma_p^\alpha\big|_{\text{cyc}} &= \Delta\gamma_p^\alpha - \Delta\gamma_p^\alpha\big|_{\text{ratch}}\end{aligned} \qquad (30)$$

where $\Delta\gamma_p^\alpha\big|_{\text{ratch}}$ is the ratcheting shear strain accumulated during the cycle. McDowell [99] has argued that a parameter based on a measure of reversed cyclic plastic strain is most appropriate from modeling crack decohesion in slip bands, and that ratcheting strain based measures are better mechanistically suited for Zener-Stroh cracking. In absence of experimental observations of either ratcheting or crack formation due to dislocation pileups at grain boundaries in Al 7075-T6 fatigued in ambient environments (see discussions in Chapters 2 and 3), the ratcheting strains are subtracted from the cyclic plastic strain quantity employed in the FIP calculation.

4.1.2: FIP to ΔCTD Relation

The foundation for the meso-scale fatigue model is the relation between band averaged FIP values and the cyclic crack tip displacement, ΔCTD, for a microstructurally small crack. The cyclic crack tip displacement is defined as

$$\Delta\text{CTD} = \sqrt{\Delta\text{CTOD}^2 + \Delta\text{CTSD}^2} \qquad (31)$$

where ΔCTOD is the crack tip opening displacement and ΔCTSD is the crack tip sliding displacement. Following the work of Castelluccio [2], the band averaged FIP on a slip plane and the ΔCTD are related through a power law formulation

$$\Delta \mathrm{CTD} = A\left(\mathrm{FIP}^{\alpha}\right)^{b}. \qquad (32)$$

Here A and b are constants that can be found through simulations of explicitly modeled cracks or fit to experimental results. Castelluccio conducted simulations using two different material models and multiple crack geometries and levels of mesh refinement, loaded under uniaxial, shear, and mixed conditions, and found that for both Copper and Nickel-based superalloy RR1000 the $\Delta \mathrm{CTD}$ scales nearly linearly with FIP^{α}, with $b \sim 1$. This work assumes that the relation between $\Delta \mathrm{CTD}$ and FIP^{α} retains the same from when applied to Al 7075-T6. The calibration of the constant A is presented in Chapter 5.

4.2: Mesh Generation

The simulations presented in this research were conducted on microstructural instantiations created using a Mesh Generator program originally developed by Musinski [100] and further extended by Castelluccio [2] to generate the additional files utilized by the fatigue algorithms. The process of mesh creation begins with a voxellated mesh of reduced 8-node linear brick elements (C3D8R) created through the python-based ABAQUS Scripting Interface [4]. Elements of the mesh are then assigned to grains using a spherical packing algorithm, with the grain size distribution assumed to follow a lognormal distribution. The probability density function of the lognormal distribution is given by

$$f(\mathrm{x};\mu,\sigma) = \frac{1}{x\sigma\sqrt{2\pi}} \exp\left[\frac{-\left(\ln(x)-\mu\right)^{2}}{2\sigma^{2}}\right]. \qquad (33)$$

In absence of quantitative data on grain size distributions in Al 7075-T6, it is assumed $\mu = -0.1$ and $\sigma = 0.4$ following the approach employed by Castelluccio [2].

Once all elements have been assigned to a grain, crystallographic orientation of each grain is assigned randomly so that there is no initial texture. The Mesh Generator then writes the information regarding the mesh, crystallographic orientation of elements and loading conditions to the ABAQUS input file. An example of a cubic mesh geometry with voxellated grains is shown in Figure 46.

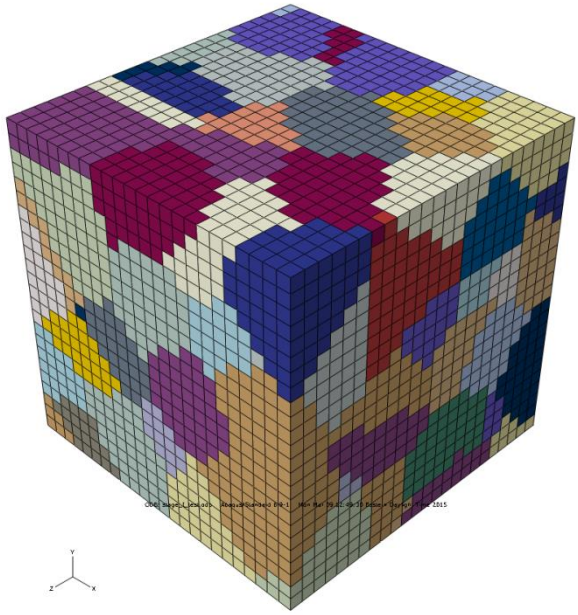

Figure 46. Example mesh of an instantiation with 14 μm mean grain diameter, 60 μm side length, and 2.5 μm element size. Different colors indicate distinct grains.

The Mesh Generator also performs the task of dividing each grain into bands of elements over which FIP values are averaged and cracks can propagate, described in greater detail in the next section. The current mesh generation and element banding algorithm allows the creation of meshes up to about 128,000 elements in approximately 2 hours; although such refinement is not needed for a mesoscale characterization of the fatigue evolution.

The limitations of the Mesh Generator necessitate making some simplifying assumptions regarding the microstructure morphology in the alloy. Processing of plate

and sheet aluminum products typically produces a flattened and elongated grain structure, often referred to as a pancake microstructure. Typical aspect ratios of grains can be up to 100:10:1, in the rolling direction (RD), transverse direction (TD), and short transverse or normal direction (ND), respectively. The rolling process can also introduce significant crystallographic texture [101].

The mesh generator cannot currently reproduce either the high aspect ratio grains or the rolling texture, and is limited to the creation of equiaxed, randomly oriented grains. In order to minimize any error introduced by the assumption of equiaxed grains, the average grain diameter in the model is chosen to be representative of the first grain diameter encountered in the direction of propagation during experiments. In applications and experiments, loading is typically applied in the RD, and crack growth occurs on a plane roughly normal to the loading axis. A schematic of a half-penny shaped surface crack shown in Figure 47 illustrates that the first grain boundary encountered by the crack front is likely to be in the normal direction, i.e., the shortest grain dimension in rolled aluminum products.

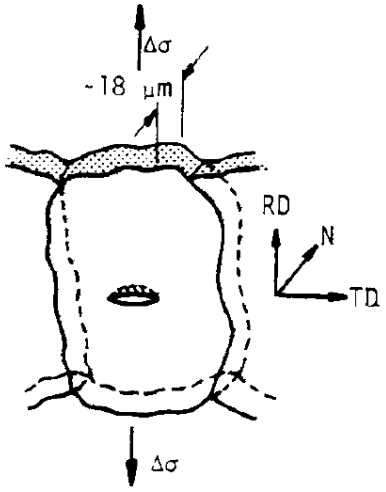

Figure 47. Schematic of a crack growing within the first grain for 7075-T6 [41].

In small crack growth experiments conducted by Lankford [41], cracks were observed to arrest or slow down as they approached a surface length ($2a$) of approximately 30-40 microns, which corresponds to a depth in the normal direction of 15-20 microns, very close to the average grain size in the normal direction of 18 um. This supports using the average grain size in the normal direction as the average equiaxed grain size in simulations.

Work is currently underway to augment the in-house mesh generator for fatigue simulations with DREAM.3D [102], a free, open source program that supports the generation of synthetic microstructures as well as reconstruction of actual microstructures from EBSD data. DREAM.3D can create microstructures with elongated grains, match experimentally observed distributions of crystallographic texture, and handle multi-phased materials. When integration of the DREAM.3D outputs with the current in-house mesh generator is complete, minor changes to the fatigue algorithms and material models will allow constituent particles in the aluminum matrix to be explicitly included in simulations. Additionally, the effects of grain aspect ratio and texture will also be able to be incorporated, and these initial simulations with equiaxed grains will serve as a useful comparison.

4.3: Element Averaging Bands

The fatigue algorithm uses FIP values averaged over bands parallel to the slip planes in a given grain in order to capture the driving force in the process zone of a Stage I crystallographic crack. For an FCC material there are four slip planes, thus each element within a grain is assigned to four different bands. The process of assigning elements to

bands is shown schematically for a 2D, voxellated grain in Figure 48. First, the centroid of the grain (shown in red on the left of the Figure) is determined. Next, sets of planes perpendicular to the slip plane normal direction are created, and they are spaced one band width apart. In cases of Stage I, shear-dominated MSC growth the band width corresponds physically to the shear bands that form under cyclic loading. For materials that do not exhibit coarse localization of slip in bands and instead exhibit more homogeneous deformation, the width of the bands has less of physical basis. Note that practically the minimum band width in the simulations is limited by the size of the elements: bands of less than one element width tend to be discontinuous and have elements that are not all connected.

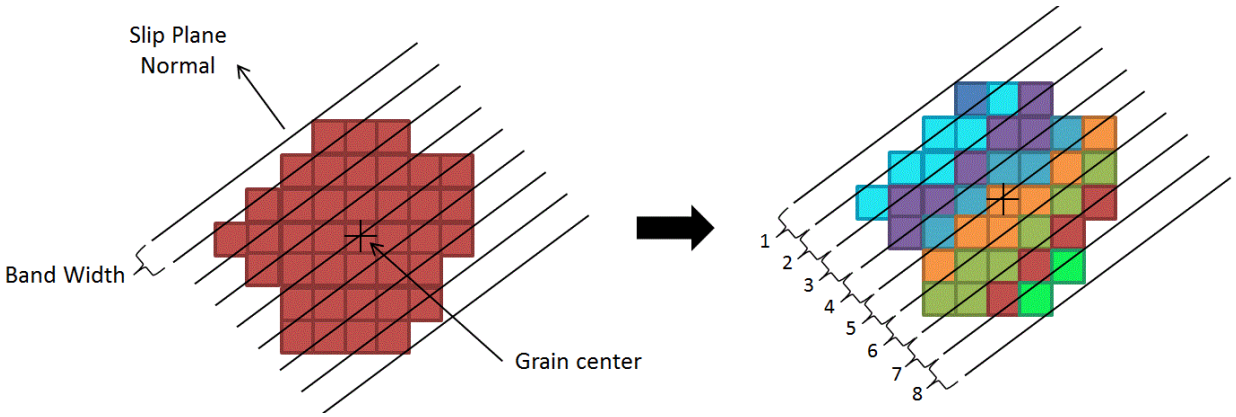

Figure 48. A schematic of the process of assigning elements to bands for one grain and slip plane.

Elements with centroids that lie in between two planes are assigned to the band formed by the plane, which are then numbered. In the example, shown in Figure 48, the grain is divided into 8 bands of elements parallel to the slip plane under consideration (each band is assigned a unique color for visualization in the Figure). The number assigned to a band during pre-processing of the mesh becomes its layer number. For example in Figure 48 layer five corresponds to the orange band of elements. Provided the orientation of the

grain is known (which it is in the simulations) it is possible to identify a unique crystallographic band within the mesh given its Grain number, layer number and plane number, abbreviated as GLP within the code.

The four sets of bands corresponding to the four slip planes of an FCC material for a selected grain within a voxellated mesh are shown in Figure 49. The voxellated mesh in the Figure contains 150 grains, and Grain #3 on the surface (light green) was selected for the example.

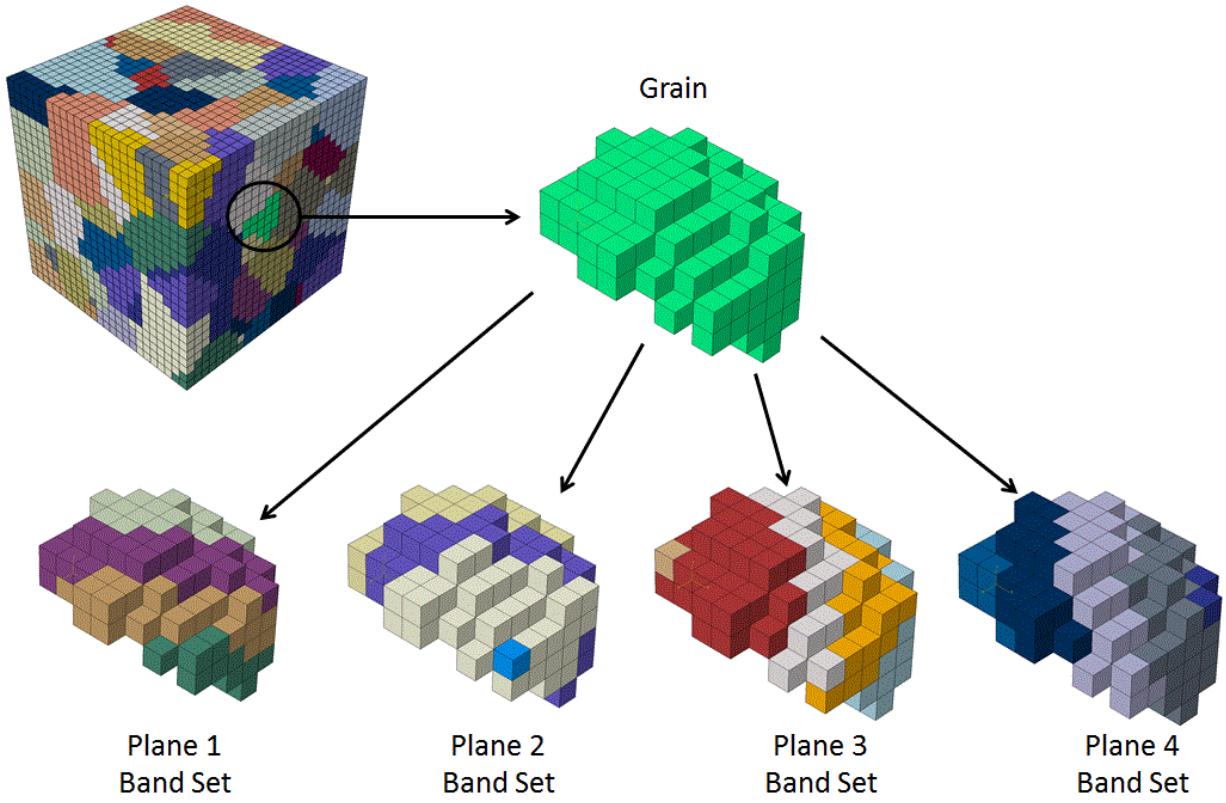

Figure 49. Four sets of bands for a selected grain within a voxellated mesh. Average grain size is 14 μm, mesh size is 2.5 μm, band width is 5.0 μm.

Each band of elements is assigned a unique color within the Figure. Grain #3 is comprised of 211 elements which are assigned to 20 overlapping sets of elements or bands.

As stated before, the purpose of the bands of elements is to capture the physical process zone of a propagating fatigue crack. When modeling the growth of a Stage I crack, the planar bands of elements correspond to persistent slip bands (PSBs), where slip becomes highly localized and the crack growth through shear decohesion. Therefore, in the Stage I growth focused implementation of Castelluccio, these element bands served as the volume averaging domain of the FIP, and the propagation path of the crack. Modeling a crack propagating in Stage II introduces additional complexity, as multiple slip systems are active and the path of crack growth is no longer planar and perpendicular to a single slip plane within a grain. Modifications to the Stage I crack growth implementation of Castelluccio were made to capture Stage II MSC growth, and are discussed in detail in the Stage II section. The band averaging scheme also helps to mitigate the effect of extreme FIP values at the crack tip and issues associated with mesh dependence [2].

4.4: Incorporation of Fatigue Damage

There are several methodologies employed in FEM based research in order to explicitly simulate a propagating crack, such as extended FEM (XFEM) or cohesive zone models. However, the code implementing of these approaches remain proprietary to ABAQUS, and they are thus not fully transparent to the user or easily controlled by user subroutines. Therefore, this work models the crack through the degradation of the elastic stiffness tensor of elements within the crack, when the plane of the crack is in tension.

This methodology is transparent to the controlling fatigue algorithms, and easily implemented in the user subroutines. Through this methodology it is possible for the effects of stress and strain redistribution due to the crack, as well as the effects of crack closure, to be accounted for in fatigue life calculations and updated as the crack propagates. For elements within the crack damage is applied according to

$$\bar{C}_{ijkl} = \left(1 - \tilde{d}\right) C_{ijkl} \qquad (34)$$

where $\tilde{d}$ is a scalar parameter representing the damage within an element, and varies between 0 when the crack plane is in compression and 0.99 when the crack plane is in tension, and C_{ijkl} is the anisotropic, 4th order elastic stiffness tensor. In order to prevent the degradation of the elastic stiffness tensor from introducing numerical instabilities, the damage is applied to the tensor isotopically and limited to a maximum value less than 1. The value of $\tilde{d}$ is also increased or decreased gradually over the duration of a loading step by the relation

$$\tilde{d}_{t+\Delta t} = \tilde{d}_t \pm v\left(\frac{\Delta t}{t_{step}}\right) \qquad (35)$$

where $\tilde{d}_{t+\Delta t}$ is the damage value for the current increment, $\tilde{d}_t$ is the damage value of the previous increment, Δt is the length of the current increment, t_{step} is the time to complete the step, and v is a constant that controls how quickly the damage is ramped over the step. Typically, a value of 5 is used for v, meaning that it takes slightly less than 1/5th of a step for the damage to vary from 0 to 0.99 or vice versa. The $\pm$ in Eq. 35 is controlled by the stress normal to the crack plane within the individual element; if the crack plane is in tension the damage is increased and if the crack plane is in compression the damage is

decreased. Additionally, when elements are damaged the UMAT will request that ABAQUS reduce the increment size (Δt) if it is larger than ($t_{step}/100$) to avoid increasing or decreasing the damage too rapidly.

4.5: Nucleation Life

Following the approach employed by Castelluccio [2], the number of cycles to nucleate a crack within a grain is modeled using a power-law relation based on a simplified dislocation model proposed by Tanaka and Mura [103] and extended by Chan [104] and Shenoy [16], i.e.,

$$\mathrm{N_{nuc}} = \frac{\alpha_g}{d_{gr}}\left(\mathrm{FIP}^{\alpha}\right)^{-2}. \qquad (36)$$

where d_{gr} is the size of the current grain plus a contribution of the neighboring grain that depends on the misorientation between the two grains. The number of cycles to nucleate a crack is correlated to experimental data by parameter α_g, which is a measure of mechanical irreversibility during the nucleation process. As discussed in Chapter 2, nucleation behavior in Al 7075-T6 is reported to be dominated by the effect of cracked iron-bearing constituent particles. The mesh generator and fatigue growth algorithms currently lack the capability to explicitly include a cracked particle within the simulation, so the simulations conducted in this thesis incorporate their effect implicitly through in the α_g constant in the equation for nucleation life, the which is estimated based on experimental data in Chapter 5.

In the MSC regime, crack growth rate is modeled according to

$$\left.\frac{da}{dN}\right|_{msc}^{\alpha} = \phi\left\langle \beta_i A(\mathrm{FIP}^{\alpha})^b - \Delta\mathrm{CTD}_{th}\right\rangle. \qquad (37)$$

Here, A and b are scaling constants relating FIP^{α} to the $\Delta\mathrm{CTD}$, and ϕ is the mechanical irreversibility at the crack tip. The $\Delta\mathrm{CTD}_{th}$ is the crack tip opening displacement threshold; it is assumed that no crack advance occurs when the $\Delta\mathrm{CTD}$ lower than this value. The constants A and $\Delta\mathrm{CTD}_{th}$ have associated units of length. The unitless parameter β accounts for grain size effects and the influence of neighboring grains and is given by

$$\beta_i = \frac{\mathrm{D}_{st} + \sum_i^n \omega^i \, \mathrm{D}_{nd}{}^i}{d_{gr}^{ref}} \qquad (38)$$

where D_{st} is the diameter of the current band being evaluated, d_{gr}^{ref} corresponds to the mean grain size of the material employed to calibrate the constitutive model. The term $\sum_i^n \omega^i \, \mathrm{D}_{nd}{}^i$ accounts for the influence of the neighboring grains with low misorientation. In that summation term, n is the number of neighboring bands, $\mathrm{D}_{nd}{}^i$ is the diameter of the i^{th} neighboring band, and ω is the disorientation factor, calculated according to

$$\omega = \left\langle 1 - \frac{\theta_{dis}}{20} \right\rangle . \qquad (39)$$

Here, θ_{dis} is the angle of disorientation (in degrees) between two adjacent bands. For bands that have no disorientation, ω is 1, and the full length of the band is added to the sum. The Macaulay brackets enforce that ω is zero if the misorientation angle is greater than 20 degrees, which is generally the taken to be the cutoff between low and high angle grain boundaries.

To carry out the analytical integration of the MSC growth rate over the length of the band, the variation in driving force must be known as a band is cracked. Castelluccio

[2] found that the evolution of FIP within a band as the band was cracked could be modeled by the relation

$$\mathrm{FIP}^{\alpha}\left(a_i\right) = \mathrm{FIP}_0^{\alpha}\left(1 - P_g a_i^{\,n}\right) \qquad \textbf{(40)}$$

where FIP_0^{α} is the initial band averaged FIP value on slip system α before damage is applied, a_i is the fraction of the band currently cracked (varying between 0 initially and 1 when the band is fully cracked) and n and P_g are constants with values of 2 and 0.5, respectively.

Once FIP^{α} as a function of a_i is known, analytically integrating the crack growth rate over the length of the band yields

$$N_i\big|_{msc}^{\alpha} = \int_0^1 \frac{da_i}{dN}\bigg|_{msc}^{\alpha} = \frac{1}{\sqrt{c_1 c_2}} \tanh^{-1}\left(\mathrm{D}_{st}\sqrt{\frac{c_1}{c_2}}\right) \qquad (41)$$

where c_1 and c_2 are constants defined according to

$$c_1 = \phi\left(\beta_i A(\mathrm{FIP}_0^{\alpha})^b - \Delta\mathrm{CTD}_{th}\right)$$
$$c_2 = \frac{\phi 2\beta_i A\left(\mathrm{FIP}_0^{\alpha}\right)^b}{\left(\mathrm{D}_{st} + \sum_i^n \omega^i \mathrm{D}_{nd}{}^i\right)^2} \qquad (42)$$

Due to the mesoscale nature of the model, grains are cracked sequentially during the progression of a simulation. Therefore, in order to account for the possibility of the crack growing simultaneously in multiple grains that are in contact with the crack, the $N_{history}$ term is introduced and subtracted from the calculated life of the band, i.e.,

$$N\big|_{msc}^{\alpha} = N_i\Big|_{msc}^{\alpha} - N_{history} \qquad (43)$$

The history term becomes active when evaluating the life of the second grain to crack and beyond, and is not active during the evaluation of the nucleation life and the life of the first grain to crack.

The functionality of the history counting term is best explained through an example. Consider the hypothetical voxellated microstructure shown in Figure 50 consisting of 6 uncracked grains numbered G1 through G6, and a crack in the plane of the paper. At the start of the simulation there are four grains in contact with the crack, G1, G2, G3 and G5. The life of all the bands in contact with the crack within these four grains is evaluated, and the crack extends into the grain containing the band of lowest life, which is G3 in this example.

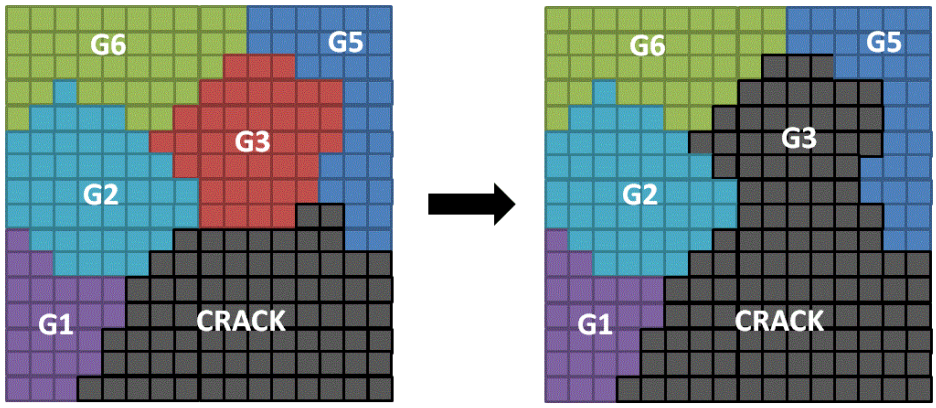

Figure 50. Hypothetical mesh for the example illustrating the function of the history counting algorithm and the propagation of the crack into Grain 3.

The algorithm then evaluates the fatigue lives of bands contacting the crack in grains G1, G2, G4, G5 and G6. The grains G1, G2, and G5 were in contact with the crack during the previous life evaluation, and have the life of the previous grain (G3 in the example) to crack, $N_{history}$, subtracted from the lives calculated according to Eqn. 43. It is important to

note that the simulations conducted for this thesis only consider the history of the previous band to crack, rather than a summation of the history values over the course of the simulation. This means that only the life of the previous grain to crack is subtracted from elements that have been in contact with the crack during previous fatigue life evaluations.

4.6: Stage II Fatigue Crack Growth Algorithm

The Stage II fatigue crack growth algorithm is an extension of the Stage I growth algorithms developed by Castelluccio [2] that considers the driving force across multiple averaging volumes and allows for crack propagation along planes of arbitrary orientation with minimum life. The main difference between the two algorithms is the separation of the crack propagation and FIP averaging volumes. The Stage I model employs the crystallographic bands of elements as both the volume over which the FIPs are averaged, and the potential propagation paths of the crack. While such a model is appropriate for materials that exhibit coarse slip band localization such as the Ni-based super alloy considered by Castelluccio, Al 7075-T6 deforms more homogeneously when cyclically loaded and the local crack front may meander among slip systems as it propagates within a grain.

Implementation of the Stage II code is similar to that of Castelluccio, relying on the ABAQUS UEXTERNALDB subroutine. However, in order to handle complications introduced by arbitrarily oriented element sets, the functionality of the UEXTERNALDB is extended through the use of a sub-program written in the Python programming language [105]. This subsection will focus on presenting both the mathematics and

physical justifications behind the Stage II code as well as the details of implementation in the UEXTERNALDB and Python sub-program.

4.6.1: Description of Stage II Model

The goal of the Stage II algorithm is to consider the driving force across multiple crystallographic planes and to determine the path of the propagating crack given the FIP values on the various planes. Additionally, due to the large computational cost of crystal plasticity constitutive models it is important that the model retain its meso-scale character, cracking multiple elements and entire grains at a time so that the simulations can be completed within a reasonable time frame. To achieve these goals the Stage II algorithm employs the concept of an intermediate plane representing the path of crack growth. The life of the plane is based on an intermediate plane FIP that has contributions from both the parent planes. Consider the diagram in Figure 51 showing a voxellated representation of a cracked grain adjacent to an uncracked grain. The cracked grain will be referred to as Grain 1 and represented by blue voxels, and the uncracked grain referred to as Grain 2 and represented by the grey voxels. The crack is represented by the black voxels.

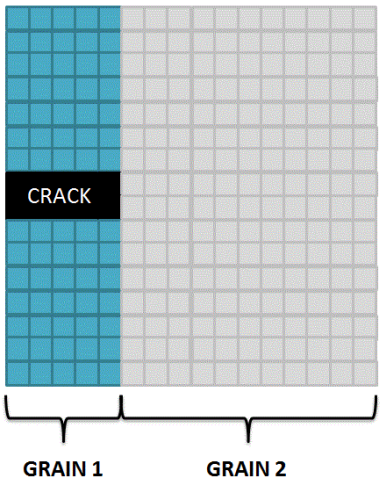

Figure 51. Example crystal showing a cracked grain (blue) adjacent to an uncracked grain (grey).

As in the Stage I algorithm, elements within a grain are assigned to crystallographic bands. This is shown for the proposed scenario in Figure 52. In the Figure and in this example, two sets of planes are considered. The band width for the planes considered is the same between the two sides of the figure and the planes of the bands extend into the paper.

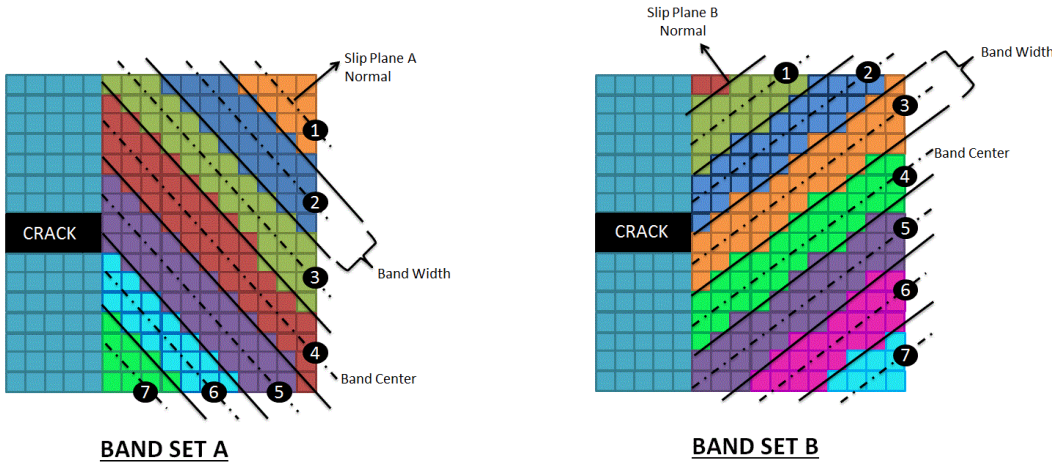

Figure 52. Sets of bands corresponding to two slip planes (referred to as A and B) within Grain 2.

Out of the 14 bands shown, only three are in contact with the crack and thus eligible volumes for crack extension: band 5 from the left set of bands (set A) and bands 2 and 3 from the right set of bands (set B). For the sake of the example we will consider band 3 from the right set and band 5 from the left set as the bands with the maximal FIP values.

In this scenario both band 5A and 3B are considered to have crack driving forces (FIP values) of the same order of magnitude, and a crack propagating through Grain 2 would likely grow in increments along both slip planes, illustrated by the solid black lines in Figure 53. The partitioning of the crack growth between the slip planes is assumed to be proportional to the crack growth rates (da/dN) on the planes, which is also proportional to the FIP values on these planes (assuming the threshold is small compared to the scaled FIP, $A(\beta_i)\,\mathrm{FIP}^{\alpha}$, see Eqn. 37). Therefore, the overall net direction of crack propagation can be captured by an intermediate plane that lies in-between the planes of alternating propagation and is weighted by the relative FIP values of the two parent planes. This approach is somewhat analogous to the ΔCTD description of Stage II cracks of Li [66], except the FIP- ΔCTD relation employed in this work also captures the cyclic crack tip opening displacement (ΔCTOD), assumed by Li to be negligible in comparison to the crack tip sliding displacement (ΔCTSD) for crystallographic cracks. The procedure for determining the intermediate plane is discussed further in the implementation section of this chapter.

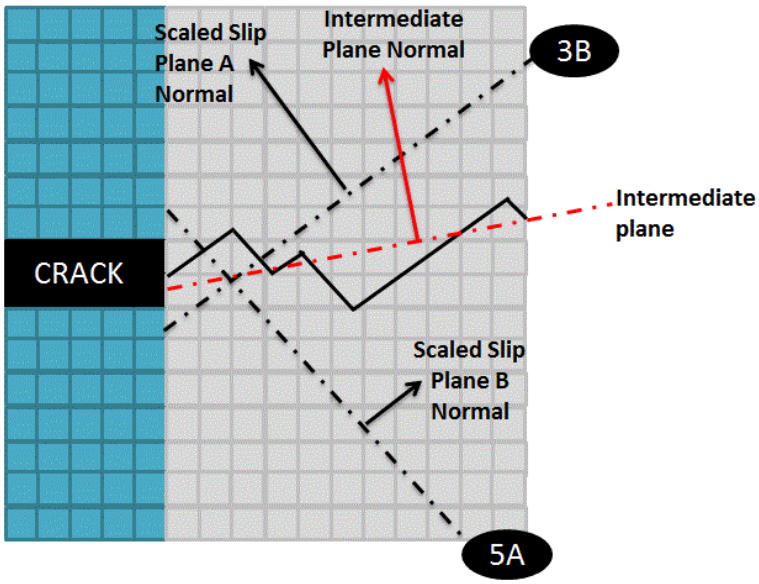

Figure 53. Intermediate plane capturing the net direction of the Stage II crack as it grows on two slip planes.

Once the constants associated with the general form of the plane equation have been determined for the intermediate plane, elements in the grain are assigned to the intermediate band if their centroids lie within half the band width from the plane. This is illustrated for the example bi-crystal by the green voxels in Figure 54. Similar to the Stage I implementation of the code, the intermediate band with the shortest life is selected as the crack propagation volume, and damage is applied to all elements within the band.

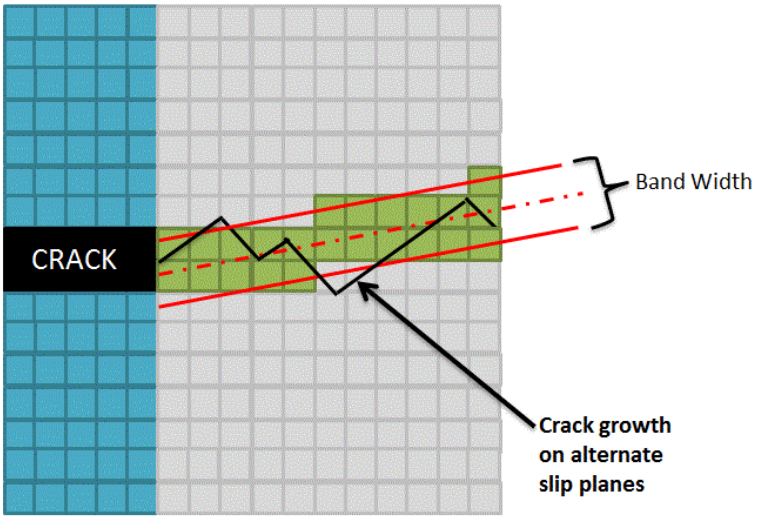

Figure 54. Path of the crack through Grain 2 (green elements) based on the point-to-plane distance between element centers and the intermediate plane.

The implementation of the intermediate band concept requires departing from some of the methodology employed previously. In the Stage I algorithms bands of elements were referenced by the grain, layer, and plane to which they belonged. Additionally, in order to identify which band an element belongs to the orientation of the grain and the location of its centroid must be known. This approach works for bands parallel to slip planes within the grain but is insufficient to describe a randomly oriented plane. A plane of arbitrary orientation in the global Cartesian coordinate system has the general equation

$$ax + by + cz + d = 0 \qquad (44)$$

where a, b, c and d are four constants. The same plane can also be represented in Hessian normal form

$$\bar{n} \cdot x = -p\,. \qquad (45)$$

Here the three components of the unit normal (n_x, n_y, n_z) to the plane are defined as

$$n_x = \frac{a}{\sqrt{a^2 + b^2 + c^2}}$$
$$n_y = \frac{b}{\sqrt{a^2 + b^2 + c^2}} \qquad (46)$$
$$n_y = \frac{c}{\sqrt{a^2 + b^2 + c^2}}$$

and the constant p is given by

$$p = \frac{d}{\sqrt{a^2 + b^2 + c^2}} \cdot \qquad (47)$$

To generate the list of elements within a band given the constants of the general plane equation requires calculating the absolute point-to-plane distance for the centroid of eligible elements and the plane under consideration; if the point-to-plane distance is less than or equal to half of the band width the element is assigned to that band on elements. For the fatigue simulations, bands of elements are generated on a grain by grain basis, so the eligible elements for a given band are limited to those within the grain. Therefore, this methodology allows a unique band of elements to be defined by the grain number and the four constants of a plane.

The Stage II crack growth algorithms employ the same approach used by the Stage I code to calculate the nucleation band and life. Therefore, the cracks nucleate in the same grain and have the same life for both the Stage I and Stage II algorithms. The calculation of the Stage II life begins by generating a list of elements adjacent to the crack. Following the approach of Castelluccio, the criteria for adjacency to the crack is that the element share a face with an element within the crack, as opposed to an edge or vertex (this concept will be explored further in the results section). All grains containing elements adjacent to the crack are eligible to crack during the current life evaluation. The

algorithm loops over the grains adjacent to the crack to find the two crystallographic bands with the highest averaged FIP values.

Once the two bands of highest FIP on separate planes have been located, the next task is to calculate the intermediated plane. Assuming that the rate of propagation on each plane is proportional to the FIP value on that plane, the normal to the intermediate plane can be obtained by the vector sum of the scaled normal of each of the parent planes, i.e.,

$$\begin{aligned} \bar{n}_1^{scaled} &= \left(\left(1+\beta_1\right)\mathrm{FIP}_1\right)\times\bar{n}_1 \\ \bar{n}_2^{scaled} &= \left(\left(1+\beta_2\right)\mathrm{FIP}_2\right)\times\bar{n}_2 \\ \bar{n}_{\mathrm{int}} &= \bar{n}_1^{scaled}+\bar{n}_2^{scaled}\,. \end{aligned} \qquad (48)$$

Here β_1 and β_2 are factors that account for the enhancement effect on plastic strain for bands with neighbors of low misorientation, defined as

$$\beta_{1,2} = \frac{\sum_i^n \omega^i \mathrm{D}_{nd}{}^i}{d_{gr}^{ref}}\,. \qquad (49)$$

Note that β_1 and β_2 are similar to the β_i parameter employed by Castelluccio for Stage I growth, without the influence of the diameter of the current band, which is accounted for later in the MSC life calculation process. With the normal of the intermediate plane defined, 3 out of the 4 constants needed for the general definition of a plane are known. The remaining constant, d, is obtained by enforcing the criteria that the intermediate plane must contain the line of intersection of the two parent planes. Given the Hessian normal forms of the two parent planes, we define

$$m = \begin{bmatrix} \bar{n}_1 & \bar{n}_2 \end{bmatrix}^{\mathrm{T}}$$
$$b = -\begin{bmatrix} p_1 \\ p_2 \end{bmatrix} \qquad (50)$$
$$x = \begin{bmatrix} x_0 \\ y_0 \\ z_0 \end{bmatrix}$$

and use a linear solver to find a particular x such that $mx = b$. The coordinates of a point on the line of intersection are then given by (x_0, y_0, z_0), and the direction vector by the null space of m [106]. Rearranging the general equation for a plane we obtain

$$d = -(ax_0 + by_0 + cz_0). \qquad (51)$$

Now that the 4 constants defining the intermediate plane are known, elements within the grain are assigned to plane if the element centroid (x_e, y_e, z_e) has a point-to-plane distance from the intermediate plane of half the band-width or less. The point-to-plane distance for the element centroid is defined according to

$$D = \frac{|ax_e + by_e + cz_e + d|}{\sqrt{a^2 + b^2 + c^2}} \qquad (52)$$

where a, b, c and d are the four constants of the general plane equation of the intermediate plane.

The crack growth rate on the intermediate plane is modeled by

$$\left.\frac{da}{dN}\right|_{msc}^{\text{int}} = \phi\left\langle A\left(\beta^{\text{int}}\,\text{FIP}^{\text{int}} + \left(\beta_1 \text{FIP}_1 + \beta_2 \text{FIP}_2\right)\right) - \Delta\text{CTD}_{th}\right\rangle. \qquad (53)$$

This equation is similar to the equation for Stage I growth, with the exception of the value of FIP^{int}, which is the sum of the FIP values on the parent planes, i.e.,

$$\mathrm{FIP}^{\mathrm{int}} = \mathrm{FIP}_1 + \mathrm{FIP}_2 \tag{54}$$

and the value of β_{int}, which captures the influence of the diameter of the current band length on the propagation life, i.e.,

$$\beta^{\mathrm{int}} = \frac{\mathrm{D}_{st}}{d_{gr}^{ref}}. \tag{55}$$

Here, D_{st} is the length of the band currently being evaluated and d_{gr}^{ref} is the mean grain diameter of the microstructure used for constitutive model calibration. Assuming the same variance in $\mathrm{FIP}^{\mathrm{int}}$ as FIP_0^{α} during the cracking of the band, the life of the intermediate plane can be determined through analytical integration of the crack growth rate, i.e.,

$$N\big|_{msc}^{\mathrm{int}} = \int_0^1 \frac{da_i}{dN}\bigg|_{msc}^{\mathrm{int}} - N_{history} = \left[\frac{1}{\sqrt{c_1 c_2}} \tanh^{-1}\left(\mathrm{D}_{st}\sqrt{\frac{c_1}{c_2}}\right)\right] - N_{history} \tag{56}$$

where c_1 and c_2 are constants defined according to

$$\begin{aligned} c_1 &= \phi\left(A\left(\beta^{\mathrm{int}}\,\mathrm{FIP}^{\mathrm{int}} + \left(\beta_1\mathrm{FIP}_1 + \beta_2\mathrm{FIP}_2\right)\right) - \Delta\mathrm{CTD}_{th}\right) \\ c_2 &= \frac{\phi 2A\left(\beta^{\mathrm{int}}\,\mathrm{FIP}^{\mathrm{int}} + \left(\beta_1\mathrm{FIP}_1 + \beta_2\mathrm{FIP}_2\right)\right)}{\left(\mathrm{D}_{st}\right)^2} \end{aligned} \tag{57}$$

Once the life of the intermediate plane has been determined, the calculation is repeated for each grain that contains elements in contact with the crack. The band formed by the intermediate plane with the minimum life is then selected as the crack propagation volume. Note that this approach reduces to the same formulation employed in the Stage I algorithm if only one slip system is active in the candidate grain to crack.

4.7: Implementation

The introduction of crack propagation through volumes that were not pre-defined before the start of the simulation adds significant complexities to the implementation of the algorithms developed by Castelluccio [2]. Previously, the code was implemented primarily in the ABAQUS User External Database subroutine (UEXTERNALDB) with minor modifications to the UMAT to allow information to pass between the two subroutines and to handle degradation of the elastic stiffness tensor. Both the UMAT and UEXTERNALDB subroutines are written in the Fortran 95 programming language, which requires that all variables have pre-declared types and that all arrays are dimensioned before use. This feature makes programs written in Fortran computationally efficient, but can be cumbersome when dealing with large numbers of lists with variable quantities of members (bands of elements for instance).

Therefore, the portions of the code handling FIP averaging, life determination and selecting the cracked elements were moved to a separate program written in Python [105]. The features of the python language make it easier to handle arbitrary bands of elements using the list or dictionary data structures. Other advantages of writing this portion of the code in Python are numerous and include increased ease of debugging, increased readability of the code, and a large library of built-in modules that simplify tasks such as logging code execution and file I/O operations. Additionally, the python sub-program allows for the ability to run the fatigue life calculations outside of the ABAQUS environment. This means that once a simulation has been completed, the fatigue algorithms can be re-run using the FIP data generated during cycling (which remains valid as long as the predicted crack path remains the same) in order to rapidly

assess the impact of changes of particular variables or the fatigue algorithms, or debug the code after introducing modifications.

The UEXTERNALDB subroutine retains the task of calculating FIPs and is responsible for calling the Python sub-program. The flow of the UEXTERNALDB is shown in Figure 55. Once the UEXTERNALDB is called by ABAQUS after the completion of a loading increment, its first task is to read the arrays containing the shear strains and normal stresses for each element and slip system, which are stored in the COMMONBLOCK. Using these values, the cyclic plastic strain range over the current cycle is calculated and then used to evaluate the FIP^{α} values for all elements in the mesh.

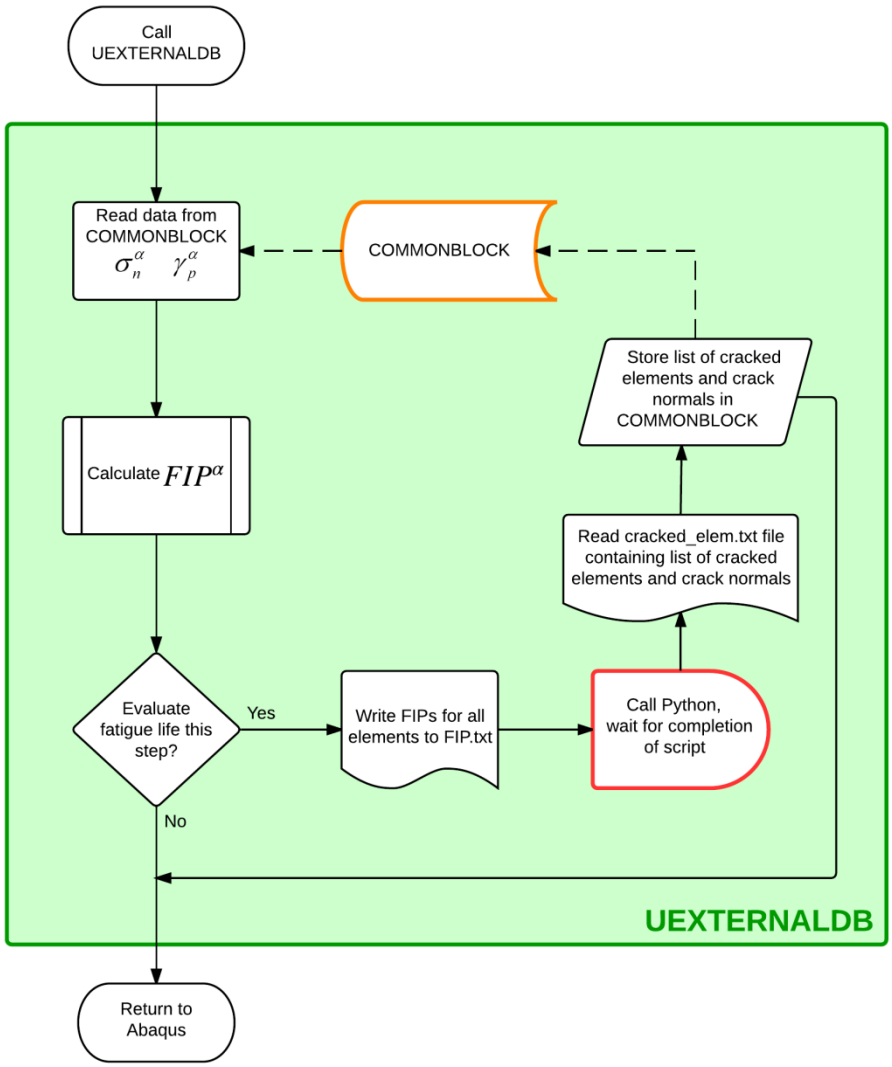

Figure 55. Flow chart illustrating the functionality of the UEXTERNALDB.

When the increment completed prior to the UEXTERNALDB call corresponds to the end of a cycle, the UEXTERNALDB checks if the fatigue life must be calculated on after this particular cycle. If true, the FIP^α values for all elements in the mesh are written to a file and then the UEXTERNALDB calls the sub-program implemented in Python and waits for it to complete the calculation of the fatigue life. One the Python program has finished, the UEXTERNALDB reads in the list of cracked elements and crack plane normal

vectors and stores them in the COMMONBLOCK. When the storage of the variables is complete or if the fatigue life does not have to be evaluated on this call, the UEXTERNALDB returns control to ABAQUS.

The functionality of the Python sub-program called from the UEXTERNALDB is illustrated in Figure 56. First, the program reads the FIP values for each element and slip system that were stored in a text file by the UEXTERNALDB and begins the task of averaging the FIP values by band. Once the band averaged FIPs are obtained, the Python script calculates either the nucleation life in all grains (according to Eqn. 36) or the MSC propagation life (according to Eqn, 56 if the Stage II model is active or Eqn. 43 if the Stage I model is active) of bands adjacent to the crack, depending on how far the simulation has progressed. The band with the minimum life is then set as cracked, and the list of elements within this band and normal vectors of the crack are appended to a text file in the simulation folder. Python then exits and returns control to the UEXTERNALDB, which reads in the list of cracked elements and the crack normal vectors.

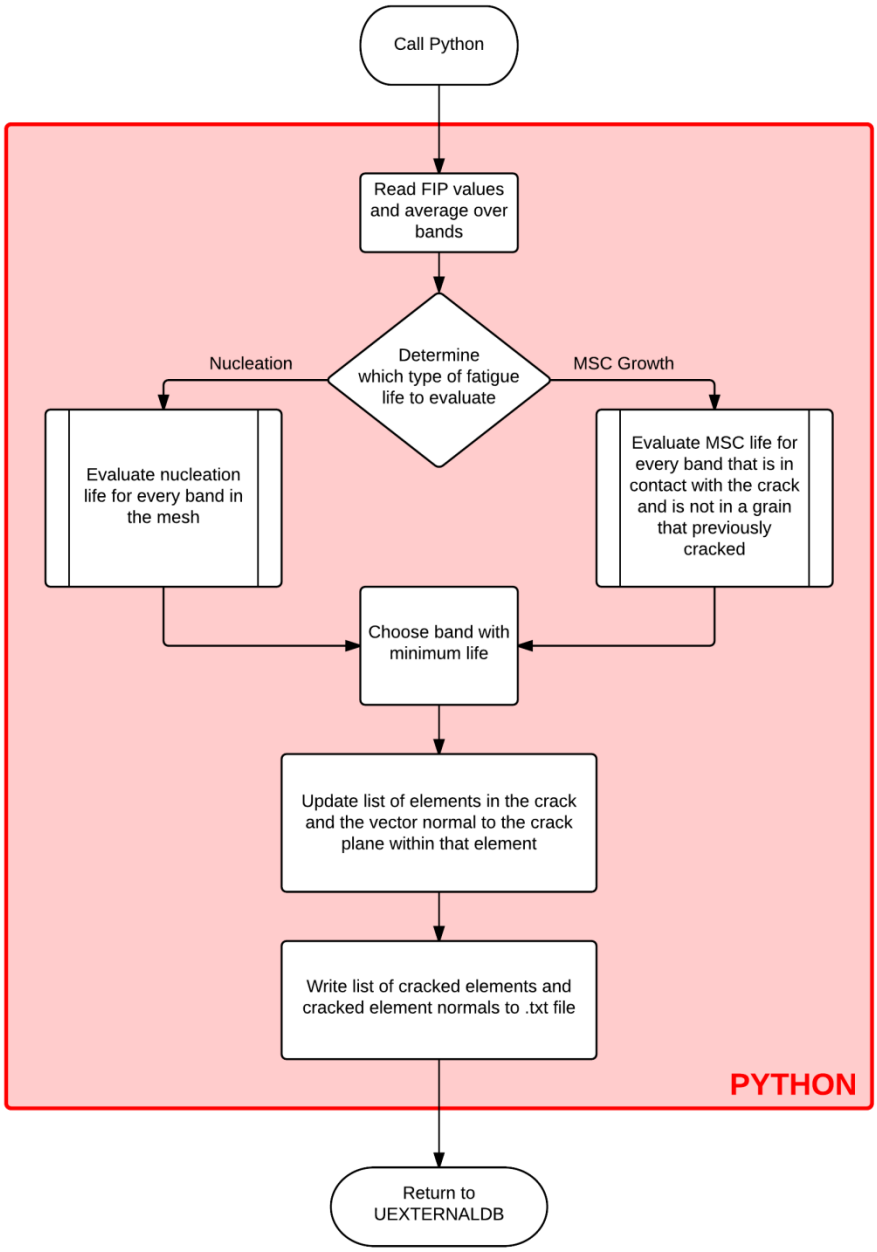

Figure 56. Flow chart illustrating the steps completed by the python sub-program after being called by the UEXTERNALDB.

Additional information regarding the implementation of the fatigue algorithms in the UEXTERNALBD and Python sub-program is available in Appendix A.

In order to illustrate the progression of a typical fatigue simulation, a 2D example is presented in Figure 57. The hypothetical microstructure consists of 8 grains, and 3 grains are cracked over the course of the simulation. A total of 17 loading steps and 8 complete computational cycles are applied, with the nucleation life of the hypothetical microstructure calculated after the 3^{rd} complete cycle and the MSC propagation life of the 2^{nd} and 3^{rd} grain to crack calculated after 5^{th} and 7^{th} computational cycle, respectively. In this example, loading is uniaxial with a 0.4% applied strain amplitude and $R_\varepsilon = -1$.

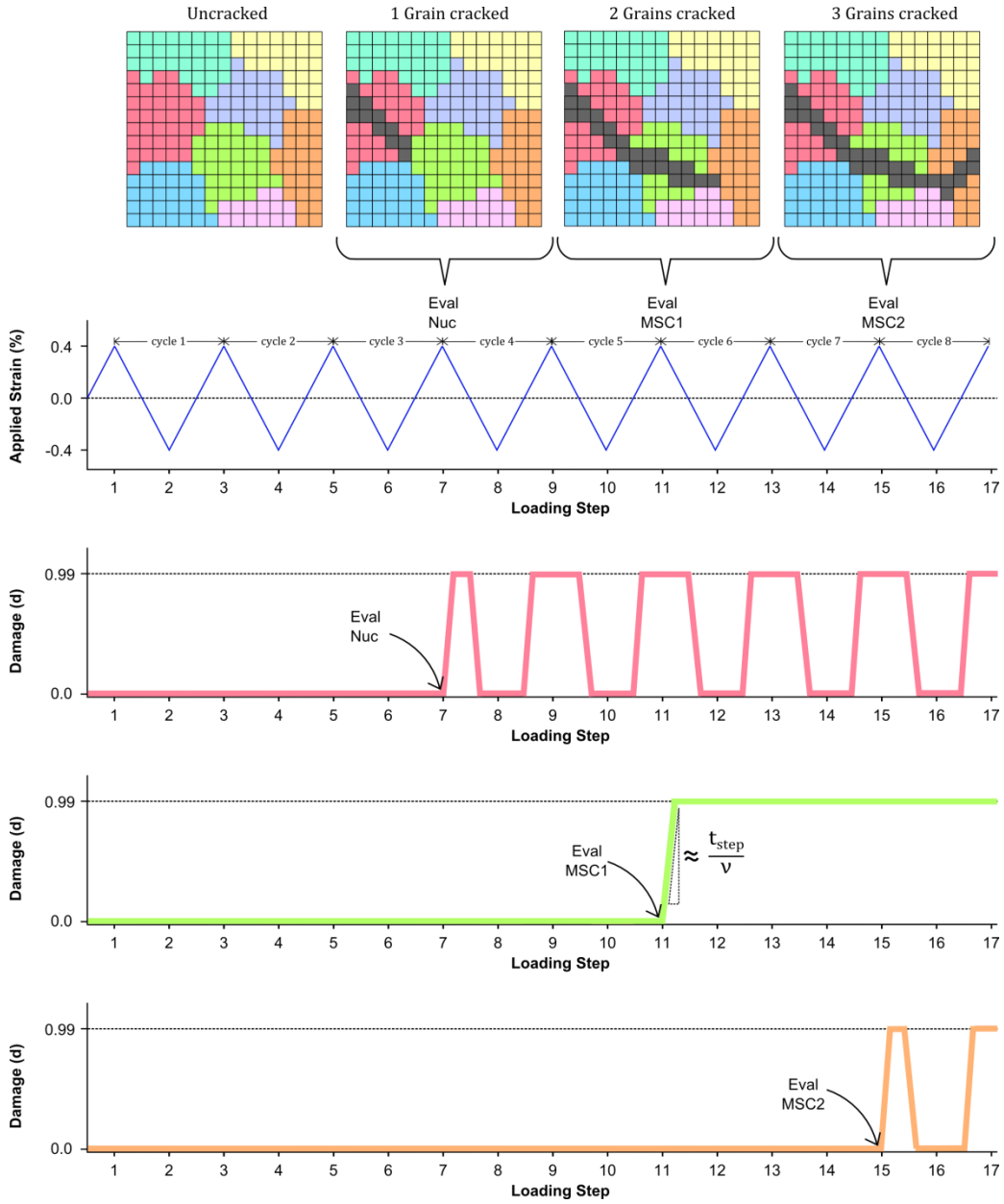

Figure 57. An example of crack propagation in a 2D microstructure, illustrating the crack path, applied loading, and damage.

The damage of each cracked band over the course of the simulation is also shown, with the line color corresponding to the coloration of the parent grain containing the band that cracks. At the beginning of the simulation all bands within the mesh are undamaged. Then, at the end of the 3rd computational cycle (end of 7th loading step), the nucleation

life is evaluated and the band with minimum life (within the light red grain) is cracked. At this point, the crack plane is in tension, so the damage is ramped up to its maximum value of 0.99. As the 8^{th} loading step progress the damage normal to cracked plane in the red grain becomes compressive and the damage is ramped back down to 0 to restore the stiffness of the element. This process repeats until the end of the example. The second grain to crack (light green) has damage applied after the 11^{th} cycle (corresponding to MSC1) and in this example the stress normal to the crack plane remains tensile throughout the loading cycle. Thus, once damage is applied in this band there is no recovery of stiffness. Life of the third grain to crack (orange) is evaluated after cycle 7, and the damage varies from 0 to 0.99 in the same way as the first band to crack as the stress normal to the crack plane varies from compressive to tensile.

4.8: Conclusions

This Chapter addressed the theoretical and computational basis of the algorithms employed in this research to model the nucleation and propagation of microstructurally small fatigue cracks in Stages I and II. The calculation of FIP^{α} was presented, along with the FIP to ΔCTD relation that allows FIP to be employed in the calculation of the MSC growth rate. The mesh generator was also introduced, along with the crystallographically-based averaging bands.

In the Stage I focused implementation of Castelluccio the crystallographically-based bands served as both the FIP averaging and crack propagation volumes. To enable the model to capture Stage II fatigue crack growth, the concept of an intermediate plane of elements was introduced. The driving force on this intermediate plane is a function of the two non-coplanar, crystallographic parent bands with the highest band averaged FIP

values. The intermediate plane contains the line of intersection of the two parent planes, and its orientation depends on the relative magnitudes of the band averaged FIPs on those same planes. This formulation reduces to the Stage I model of Castelluccio if only one slip system is active in the grain being evaluated, and retains the same mesoscale approach where damage is applied to planar bands containing multiple elements rather than on an element-by-element basis. Additionally, the implementation of these algorithms in the ABAQUS UEXTERNALDB and Python sub-program was discussed.

CHAPTER 5: APPLICATION OF THE MESOSCALE MODEL TO AL 7075-T6

5.1: Introduction

This chapter presents the results obtained using the mesoscale fatigue model to evaluate fatigue crack nucleation and microstructurally small fatigue crack growth behavior in Al 7075-T6. The chapter begins by introducing the boundary and loading conditions applied to the meshes. Next, the calibration of the fatigue model constants for Al 7075-T6 is presented. The remainder of the chapter focuses on the results obtained with the fatigue model, including:

- Results under uniaxial loading and shear loading at different applied strain amplitudes and applied strain ratios, which are compared to experimental data.
- Comparison of results obtained using the Stage I and Stage II fatigue algorithms.
- Comparison of fatigue simulation results obtained using the three constitutive model variants introduced in Chapter 3.
- Simulations are conducted to assess the effect of k in the FIP parameter.
- Simulations conducted to evaluate the effects of mesh density, simulation volume, and choice of band width.

The chapter concludes by summarizing the results and describing the key findings of this work.

5.2 Meshes and Boundary Conditions

The majority of the simulations performed in this chapter where conducted using a voxellated polycrystalline mesh with a cubic geometry and 60 μm side lengths. The volume was meshed with 2.5 μm elements, for a total of 13,824 elements. A mean grain size of 14 μm was used, and each of the 10 microstructural instantiations created contained 150 randomly oriented grains. The few modified mesh configurations that were used to investigate the effects of meshing on the fatigue results are described in detail in the section that presents those results.

The boundary conditions employed for uniaxial loading and shear loading are illustrated schematically in Figure 58. Uniaxial loading is modeled by prescribing displacements to all nodes on the top XZ face (Y=60 μm in the Figure 58 example) in the X-direction and holding all nodes on the bottom XZ face (Y=0 μm in the Figure 58 example) fixed in the X-direction. Additionally, in order to prevent rigid body motion the following nodal boundary conditions are enforced:

- The origin at (0, 0, 0) is fixed to have zero displacement in all directions.
- The vertex node at (1, 0, 0) is fixed to have zero displacement in the Z-direction.
- The vertex node at (0, 0, 1) is fixed to have zero displacement in the X-direction.

These conditions prevent rotation or translation of the mesh, but allow for contraction or expansion of the positive YZ face in the X-direction and of the positive XY face in the Z-direction. Hence, the sides are effectively traction-free. Simple shear loading was modeled by applying a relative displacement to the nodes in the XZ-plane faces of the mesh (at Y=0 μm and Y=60 μm for the meshes in Figure 58) in the Y-direction. In this case, periodic boundary conditions were enforced on the YZ faces, requiring that the

difference of displacements for opposing nodes is zero in X, Y, and Z. Additionally, the same nodal boundary conditions used to prevent rigid body motion in the uniaxial simulations were employed for simulations conducted under simple shear.

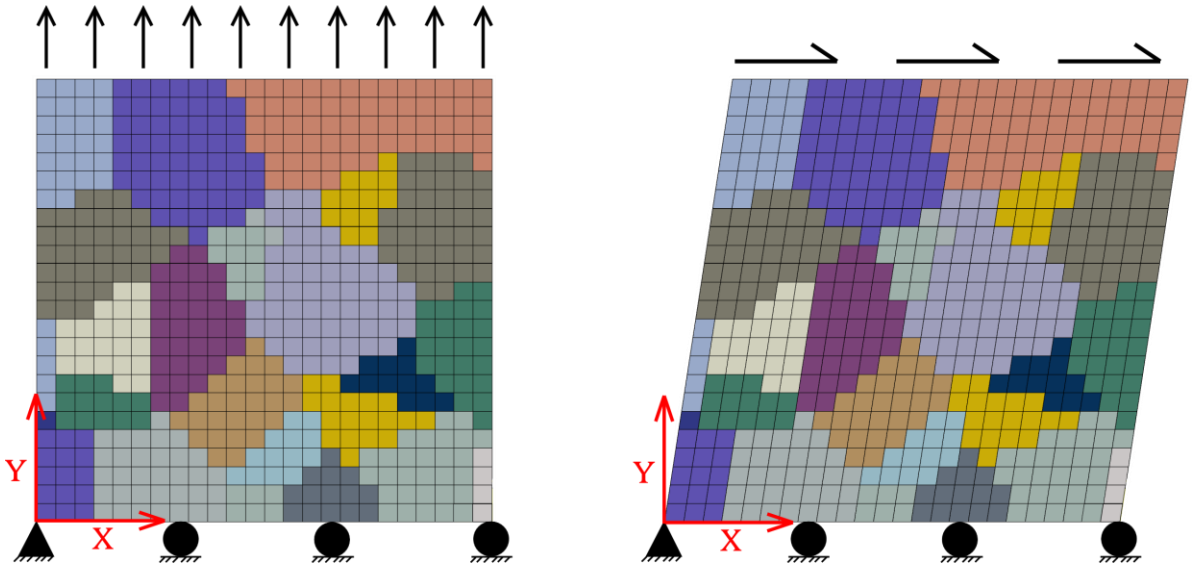

Figure 58. Diagram of uniaxial boundary conditions (left) and shear boundary conditions (right) used in the fatigue simulations.

Note that the boundary conditions of the fatigue simulations differ from those of the simulations used to evaluate the constitutive response of the material, which employed 3D periodic boundary conditions. In contrast, for the loaded uniaxially fatigue simulations there is no enforced periodicity. For all the simulations conducted in this research the loading is applied quasi-statically at a strain rate of approximately $1x10^{-4}$ s^{-1}.

5.2.1: Definition of Equivalent Shear Strain Amplitude

To compare results between simulations conducted under uniaxial tension-compression and shear loading, the equivalent uniaxial, nominal strain amplitude ($\bar{\varepsilon}_a$) was defined for nominally elastic loading conditions as

$$\bar{\varepsilon}_a = \varepsilon_a \tag{58}$$

for uniaxial loading, and as

$$\bar{\varepsilon}_a = \gamma_a / (1+\nu) \tag{59}$$

for shear loading. The value of the elastic Poisson's ratio was taken to be 0.345, commonly reported for aluminum [107]. In the remainder of this chapter, any references to the applied strain amplitude are understood to be in terms of the equivalent uniaxial strain amplitude unless otherwise noted.

5.3: Calibration of the Fatigue Constants

Fatigue crack nucleation and MSC propagation data can be difficult to find in the open literature, particularly under loading conditions of interest. The data that are published in the open literature are typically limited to a small number of cracks due to the time- and labor-intensive nature of collecting such data, and the associated conflicting requirements of resolution and field of view. The experimental data chosen to calibrate the fatigue model were obtained by Tokaji et al. [56], who investigated the effects of applied stress ratio and amplitude on MSC crack growth in Al 7075-T6. The experimental data of interest were collected under R=-1, σ_{max} = 270 MPa, uniaxial stress-controlled cyclic loading, with a stress concentration factor of 1.02 in the shallow notch where cracks were observed to form. The equivalent strain-controlled loading conditions for the simulations was calculated by dividing the product of peak nominal stress with the stress concentration factor (275.4 MPa) by the elastic modulus from simulations used to fit the constitutive model (69 GPa). Simulations were conducted on smooth specimens under fully reversed (R_ε = -1), uniaxial strain-controlled cycling at a strain amplitude of

0.4% to match the experimental conditions used by Tokaji et al. [56]. A total of 10 simulations, each with a different microstructural instantiation (14 μm mean grain size) were conducted, and FIP_0 values for each of the first eight grains to crack are summarized by a box-and-whisker plot in Figure 59.

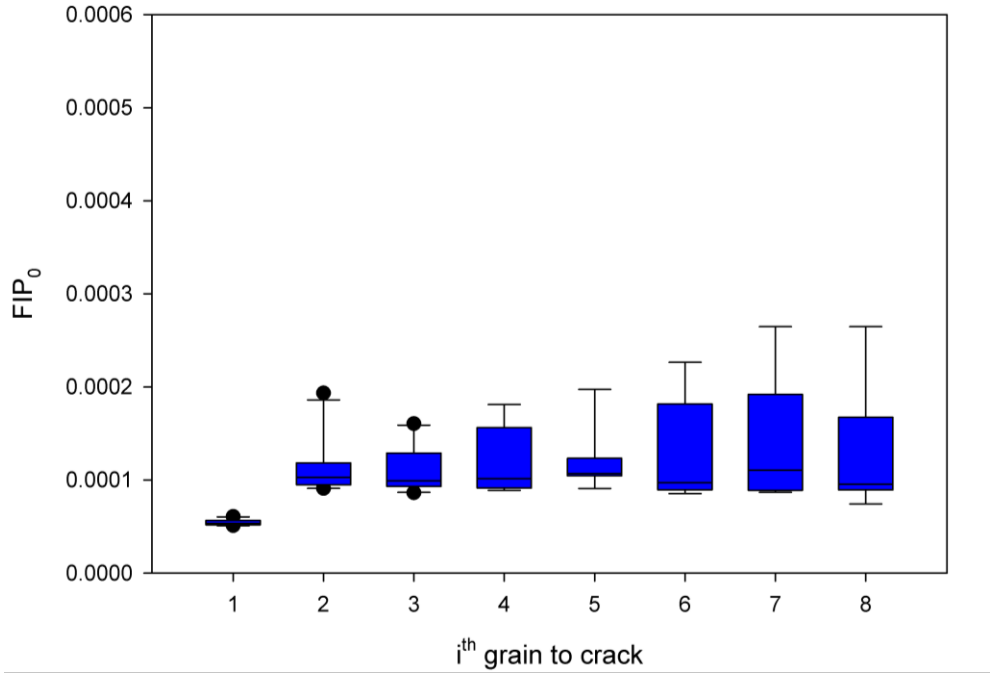

Figure 59. Box-and-whisker plot of the initial FIP value in the first 8 grains to crack across 10 instantiations, under R_ε = -1, ε_a = 0.4% uniaxial strain controlled cycling. Simulations were conducting using material model OW44.

Note that in Figure 59 two different forms of the initial FIP at the onset of crack growth in each grain, FIP_0, are employed: in the first grain to crack FIP_0 is calculated based on a single slip system, FIP^α, whereas in subsequent grains to crack FIP_0 corresponds to the FIP on the intermediate plane, which is a sum of the contributions from the FIP^α values on the parent planes. The number of cycles to nucleate a crack is correlated to experimental data by parameter α_g, which is a measure of mechanical irreversibility during the nucleation process. To estimate α_g, Eqn. 36 can be rearranged into the form

$$\alpha_g = \mathrm{N}_{nuc} \frac{d_{gr}}{\left(\mathrm{FIP}^{\alpha}\right)^{-2}}, \qquad (60)$$

where d_{gr} is the size of the current grain plus a contribution of the neighboring grain that depends on the misorientation between the two grains. Although the nucleation lives of the cracks considered by Tokaji et al. [56] are not explicitly given, it is possible to estimate the cycles required to crack the first grain using data for crack surface length vs. cycle ratio (N/N_f) where the number of cycles to failure (N_f) is known for that loading condition. These data are plotted in Figure 60.

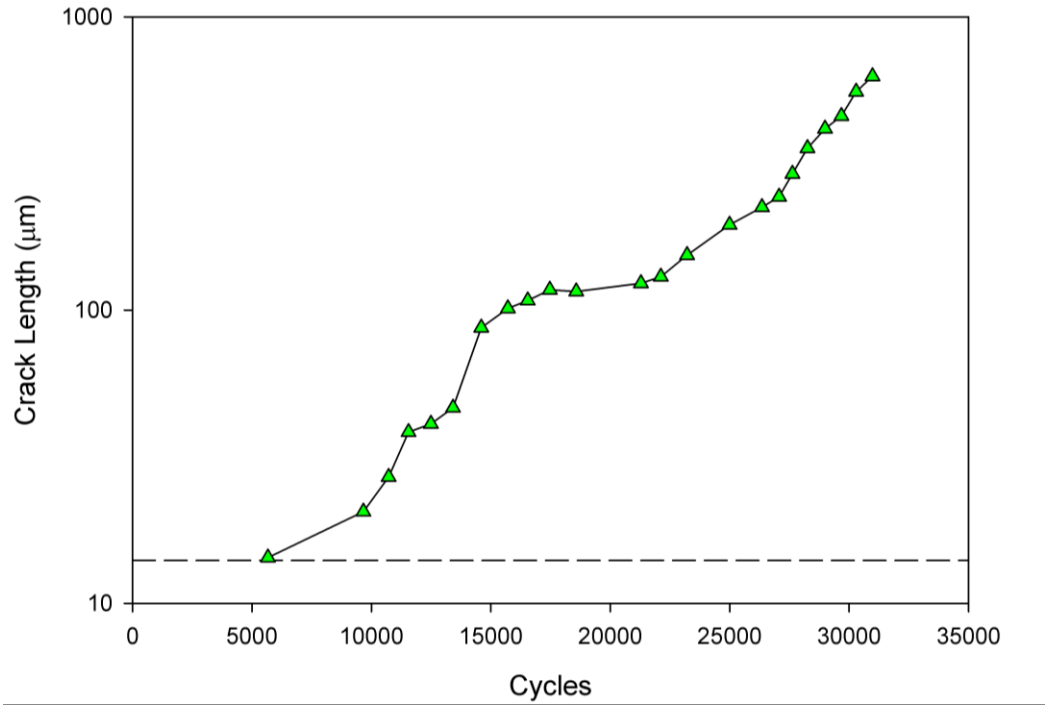

Figure 60. Crack length vs. cycles based on experimental data from [56] at an equivalent strain amplitude of 0.4% and under fully reversed, uniaxial loading conditions.

The dashed line in Figure 60 is drawn at a crack length of 14 µm, corresponding to the mean grain size in both the simulations and the experiments they emulate. From the intersection of this line with the crack growth data in the Figure, the life to grow the crack

to a length of approximately 1 grain size (the nucleation life) is computed to be 5,670 cycles. While this is certainly a rough approximation, in absence of better data it provides an acceptable order of magnitude estimate for the number of cycles required to nucleate a crack under the loading conditions considered. The maximum FIP_0 in the nucleant grain for the simulations considered was 6.072×10^{-5} (corresponding to the 1st grain to crack in Figure 59). Using these values and assuming that the crack nucleates in a grain of mean diameter with no influence from low-misorientation neighbors, Eqn. 60 yields a value for α_g of 2.9×10^{-4} μm-cycles. Overall, the effect of accounting for low-misorientation neighbors is insignificant in comparison to the uncertainty that arises from having only a single data point available with which to estimate a value for α_g, and thus it is a reasonable assumption to neglect the influence of these neighbors. Of course, this estimate can certainly be refined as more highly resolved and detailed data become available regarding nucleation, particularly as related to cracks forming at nonmetallic particles.

A similar approach can be employed to estimate the parameters controlling the rate of crack propagation using the Stage II crack propagation algorithm. The parameter of interest is A, which relates the band averaged FIP value to the ΔCTD through Eqn. 32. The parameter A can be estimated by assuming:

- b = 1, simulations conducted for RR1000 and copper [2] suggest that the FIP scales nearly linearly with ΔCTD, but this must be validated for Al 7075-T6 in future work.
- β = 1, obtained by assuming that d_{gr}^{ref} is equal to the mean value d_{gr} (14 μm) of propagating cracks in the simulations conducted to fit A.
- $\Delta CTD_{th} = 2.86 \times 10^{-4}$ μm, the Burgers vector for pure FCC Al [22].

- $FIP^{\alpha} = 1.93x10^{-4}$, the maximum FIP in the 2nd grain to crack.
- $\phi = 0.35$ following arguments by Xue et al. [22] and McDowell et al. [24].
- $\frac{da}{dN} = 2.14x10^{-3}$ μm/cycle, the crack growth rate reported by Tokaji et al. for the simulated loading conditions for a crack length of approximately 14 μm.

These assumptions result in an estimated value of $A = 33.1$. This methodology for estimating the fatigue parameters differs somewhat from that of Castelluccio [2], who conducted simulations using meshes with an explicit crack in order to obtain the relation between ΔCTD and band-averaged FIP for the RR1000 constitutive model. It should also be noted that this calibration is for the Stage II Fatigue model coupled with the OW44 constitutive model, and will be referred to as Calibration A. Previously, fitting of the fatigue constants was done using the Stage I fatigue model coupled with the G31 constitutive model, referred to as Calibration B. This older calibration employed an α_g value of $6x10^{-3}$ μm-cycles and an A value of 22.4, which were obtained using the same methodology employed to generate Calibration A. In general for the results presented in this chapter, the Stage II simulations employ Calibration A, while the comparative simulations illustrating the differences between the fatigue results obtained using different versions of the constitutive model employ Calibration B, unless otherwise noted. The calibration of the model is validated by comparing simulated crack growth rates to the experimental data of Tokaji et al. [56] and the experimental data of Zhao and Jiang [108], which are presented in within the next section of this chapter in Figure 62 and Figure 65, respectively.

5.4: Stage II Fatigue Algorithm Results

This Section presents results from fatigue simulations conducted using the Stage II algorithm coupled with the OW44 constitutive model version to assess the response to cyclic uniaxial or shear loading. All simulations presented in this section employed a cubic mesh with 60 μm sides, 2.5 μm elements, and 14 μm equiaxed grains with random orientation, which are discussed in detail in Section 5.2.

5.4.1 Cyclic Uniaxial Results

For the set of uniaxial simulations four different applied stain amplitudes were considered: 0.2%, 0.3%, 0.4% and 0.5%. Simulations were conducted at applied strain ratios of -1 and 0.5, and 10 microstructural instantiations were evaluated under each loading, for a total of 60 uniaxial simulations. In each simulation, 20 complete computational loading cycles were applied, and 8 grains were allowed to crack before the simulation was terminated. Figure 61 is a semi-log plot of crack length vs. cycles for uniaxial simulations conducted with fully reversed straining conditions ($R_\varepsilon = -1$).

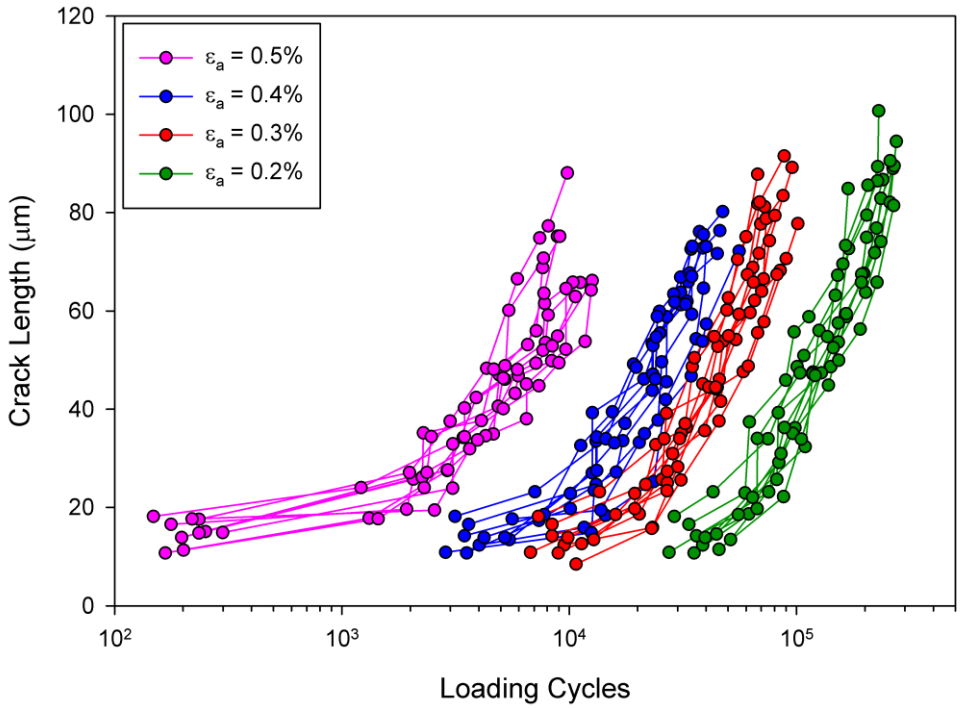

Figure 61. Crack growth under uniaxial, fully reversed loading at various strain amplitudes, ε_a=0.2%, 0.3%, 0.4% and 0.5%.

The results shown in Figure 61 agree with expectations; higher applied strain amplitudes produce shorter fatigue lives. One interesting aspect of Figure 61 is that the cycle increment of propagation over a grain is longer at smaller applied strain amplitudes, i.e., within a given grain, bands containing more elements are cracked preferentially as the applied strain is reduced. This effect is visible in Figure 61 as an increase in crack length after the crack has propagated through 8 grains from the highest to lowest applied strain amplitudes. Examining the data for simulations conducted at 0.5% applied strain (shown in magenta) we calculate that the average crack length has reached approximately 69 μm by the end of the simulation when 8 grains have cracked. In contrast, the average crack length for simulations conducted at a strain amplitude of 0.2% has reached 89 μm by the end of the simulation, despite cracking the same number of grains. The results for the

0.3% and 0.4% strain amplitude cases lie in the middle, with average crack lengths of approximately 74 μm and 72 μm, respectively, after cracking 8 grains.

The crack propagation rate in simulations conducted under fully reversed, uniaxial stain-controlled loading at 0.4% applied strain amplitude can be compared to the crack growth rate data obtained by Tokaji et al. [56] under equivalent stress-controlled cyclic loading. For the simulations, the crack propagation rate is calculated according to the secant method given in ASTM E647 [109] where

$$\frac{da}{dN} = \frac{a_n - a_{n-1}}{N_n - N_{n-1}}. \qquad (61)$$

The secant methodology was used over the more traditionally employed incremental polynomial approach for two reasons. The first is small quantity of d*a*/dN data produced for each crack: if a total of 8 grains cracked during a simulation, only 7 d*a*/dN data points are produced using the secant method. Applying an incremental polynomial would lead to a large reduction in the data available for consideration. Second, in the MSC propagation regime any smoothing introduced by polynomial or averaging based approaches can obscure the variability introduced by the interaction of the crack tip with the microstructure [110, 111], which is the behavior of interest in this research.

The experimentally measured crack growth rate data of Tokaji et al. are plotted on a log-log scale in Figure 62, along with the simulated crack growth rate data calculated by the secant method. The methodology used to determine the experimental values of d*a*/dN was not mentioned in the paper published by Tokaji et al.

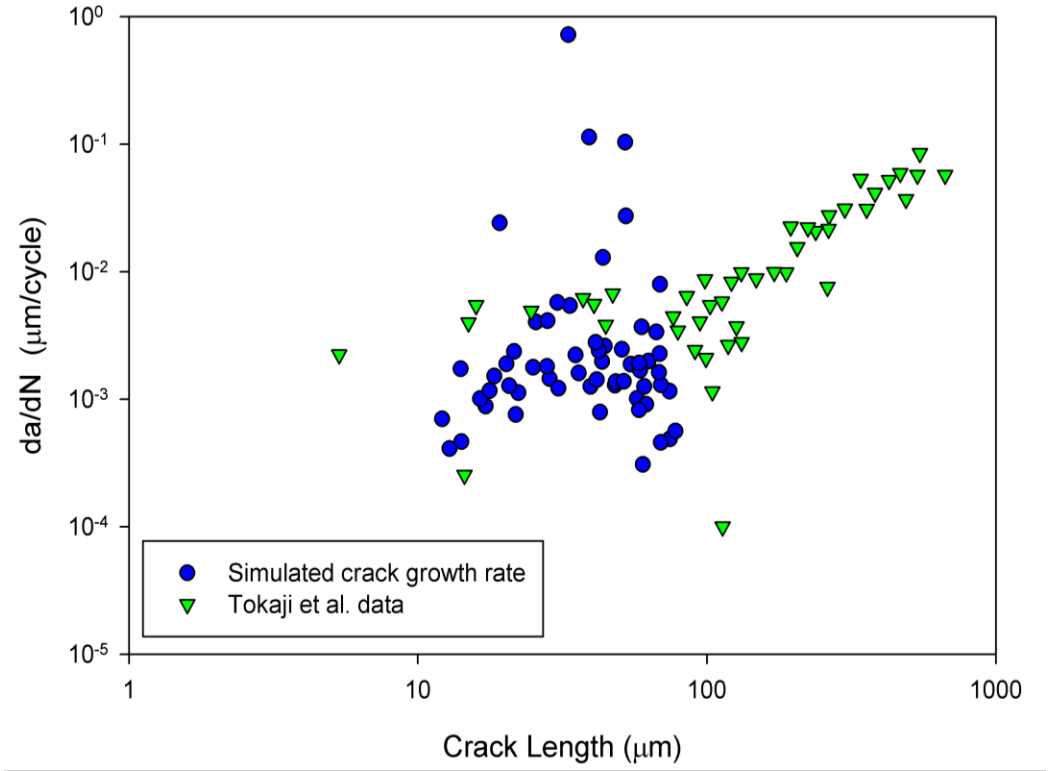

Figure 62. Comparison of crack growth rate data from uniaxial simulations to the experimental data of Tokaji et al. [56] at an applied strain amplitude of 0.4% and fully reversed loading.

There is a large degree of scatter in the simulated crack growth rates in Figure 62, with minimum and maximum rates of crack propagation differing by more than 3 orders of magnitude. Aside from a few outliers, the average rate of crack propagation (shown by dashed line) lies well within the experimental range observed by Tokaji et al.

There are a few differences between the experimental data and simulated data that must be discussed to understand the limitations of the comparison. The most significant is that the experimental data are based on measurements of surface cracks at periodic increments during the cyclic loading, while the simulated crack lengths are calculated as the square root of the area of the crack after each grain fails. This has a few important implications. First, surface cracks may behave somewhat differently than cracks within the interior of a specimen, appearing to arrest or retard on the surface while continuing to

propagate internally. Second, assuming a semi-circular surface crack, a crack length calculation based on the square root of the area would predict a crack length approximately 37% shorter than the actual length of the crack along the surface of the specimen. Experimental observations of crack length are also conducted at set intervals and thus the crack growth rate is an average rate over the period between observations. Therefore, any brief periods of rapid crack growth may be offset by periods of slower growth and not reflected in the collected data. Finally, the data published by Tokaji et al. are limited, considering only the growth rate at two crack tips.

Additional simulations were performed to assess the impact of an imposed mean strain on the uniaxially loaded meshes at applied strain amplitudes of 0.3% and 0.4%. These simulations employed an imposed strain ratio (R_ε) of 0.5, which produced an equivalent stress ratio (R_σ) of approximately 0. The results for the 0.3% and 0.4% applied strain amplitude cases with an imposed mean strain are compared to the results at the same applied strain amplitude but under fully reversed loading in Figure 63 and Figure 64, respectively.

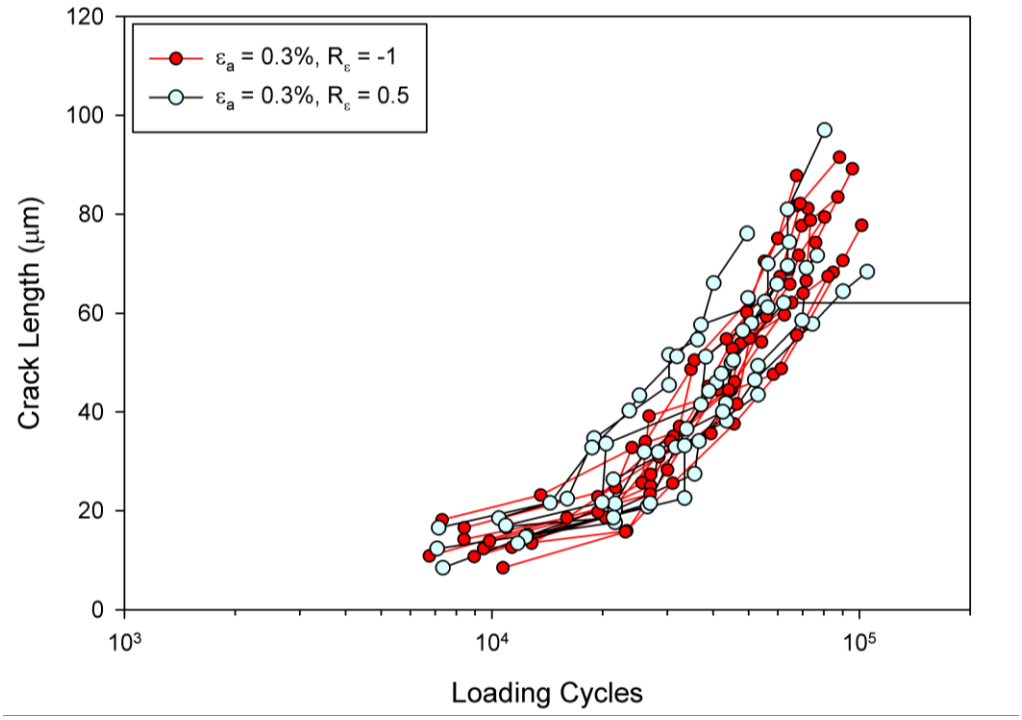

Figure 63. A comparison of crack growth under uniaxial loading at ε_a = 0.3% and applied strain ratios of R_ε = -1 and R_ε = 0.5.

The data for the 0.3% applied strain amplitude cases plotted in Figure 63 show a slight impact of the imposed mean stress/strain. Comparing the shortest lives to reach a crack length of 60 μm for both cases, the imposed mean strain reduces number of cycles by approximately 11%. The reduction in the average life to reach the same crack length is smaller, with the applied mean strain reducing the average number of cycles to a crack length of 60 μm by just 8%.

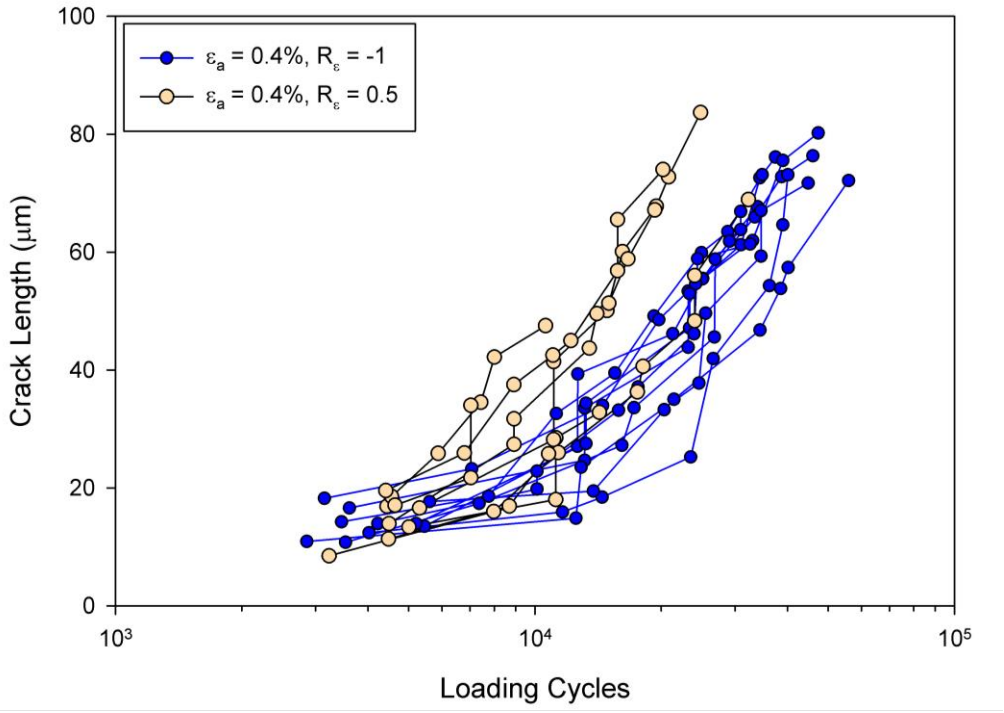

Figure 64. A comparison of crack growth under uniaxial loading at ε_a = 0.4% and applied strain ratios of R_ε = -1 and R_ε = 0.5.

The detrimental effect of the imposed mean stress/strain on the predicted fatigue lives is significantly more pronounced for the 0.4% applied strain amplitude cases, plotted in Figure 64. The shortest life to reach 60 μm in the presence of a mean strain is 42% shorter than the shortest life to reach the same length under uniaxial loading conditions. Similarly, the average number of cycles to reach a length of 60 μm is reduced by 39% by the presence of a mean strain during cycling.

Results from the simulations conducted under uniaxial loading are compared to experimental results obtained by Zhao and Jiang [108], shown in Figure 65.

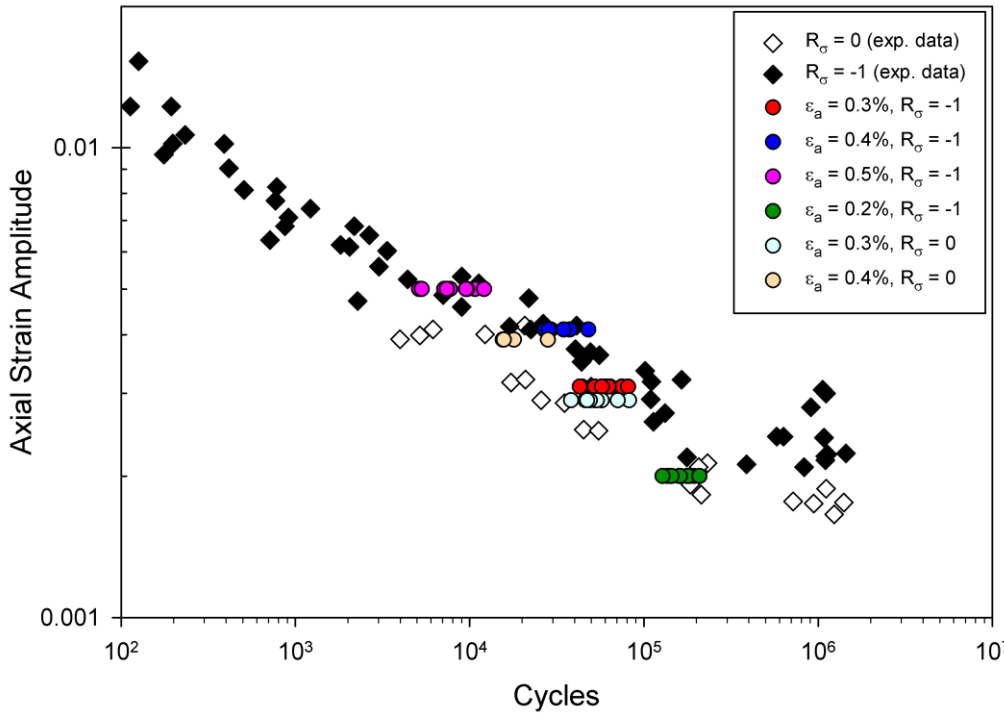

Figure 65. Comparison of data from uniaxial fatigue simulations and uniaxial experimental data from [108]. Results for the 0.3% and 0.4% applied axial strain amplitude cases are shifted by +0.01% strain when R_σ = -1 and by -0.01% strain when R_σ = 0 to increase the clarity of the plot.

It is important to note that for the experimental data (black and white symbols), axial strain amplitude is plotted against cycles to complete specimen failure, while for simulation results (aqua, blue, and red) axial strain amplitude is plotted against cycles to grow the crack to a length of 60 µm. Assuming that the majority of the life is consumed by nucleation and early crack growth in the low strain amplitude HCF regime, we would expect life to grow a crack to 60 µm to be comparable to the total life of the experimental data. In the LCF regime, by contrast, we would expect nucleation lives to be significantly shorter than the total life. Therefore, in the plot it is evident that the simulated fatigue lives are within the correct order of magnitude for both the fully reversed loading cases

(R_σ = -1) and the cases with an imposed mean strain/stress (R_σ = 0). However, the detrimental effect of mean stress is not as pronounced in the simulations as in the experiments, particularly for the 0.3% applied strain amplitude cases. Possible explanations for this trend are presented in Section 5.4.3.

5.4.2 Cyclic Shear Results

Additional fatigue simulations were conducted using the Stage II algorithm coupled with the OW44 constitutive model version to assess the response to cyclic, simple shear loading. Three different applied equivalent stain amplitudes were considered: 0.3%, 0.4% and 0.5%. Simulations were conducted at applied strain ratios of -1 and 10 microstructural instantiations were evaluated under each loading, for a total of 60 shear simulations. In each simulation, 20 complete computational loading cycles were applied, and 8 grains were allowed to crack before the simulation was terminated. The crack growth results for the shear simulations are compared to the results obtained under the equivalent uniaxial loading at applied equivalent strain amplitudes of 0.5%, 0.4% and 0.3% in Figure 66, Figure 67, and Figure 68, respectively.

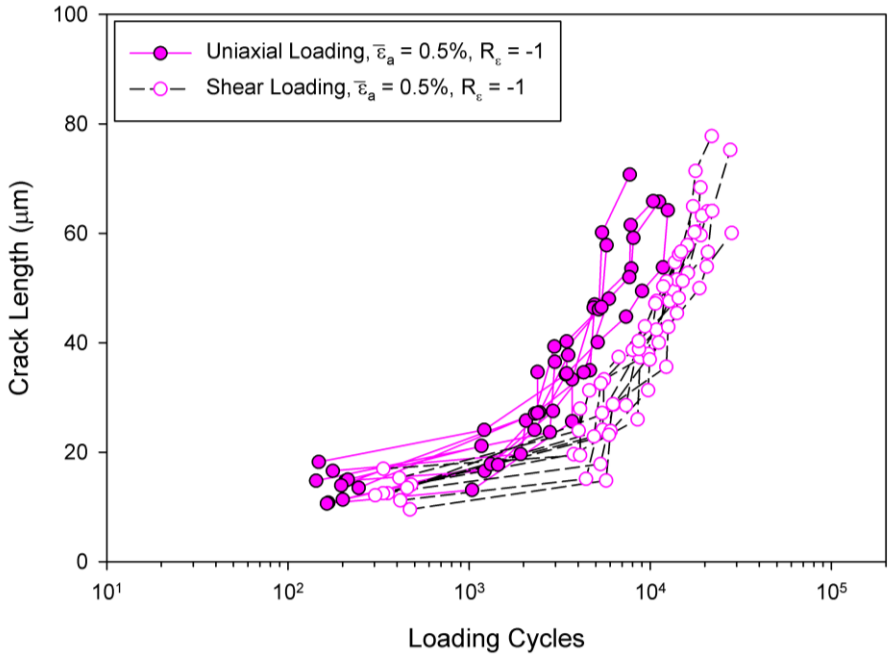

Figure 66. Comparison of crack growth under uniaxial and shear loading. In both cases loading is fully reversed and conducted at an applied equivalent strain amplitude ($\bar{\varepsilon}_a$) of 0.5%.

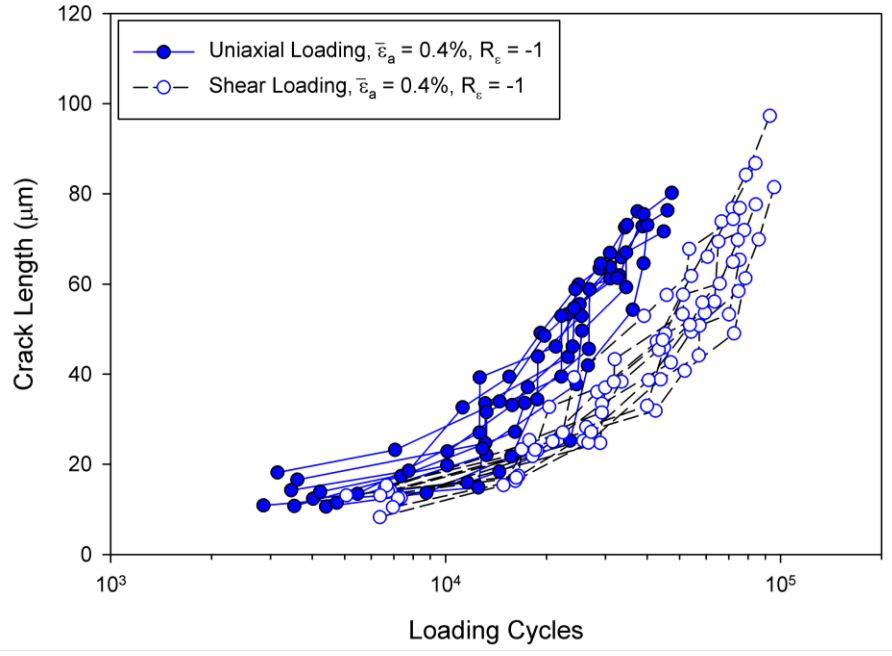

Figure 67. Comparison of crack growth under uniaxial and shear loading. In both cases loading is fully reversed and conducted at an applied equivalent strain amplitude ($\bar{\varepsilon}_a$) of 0.4%.

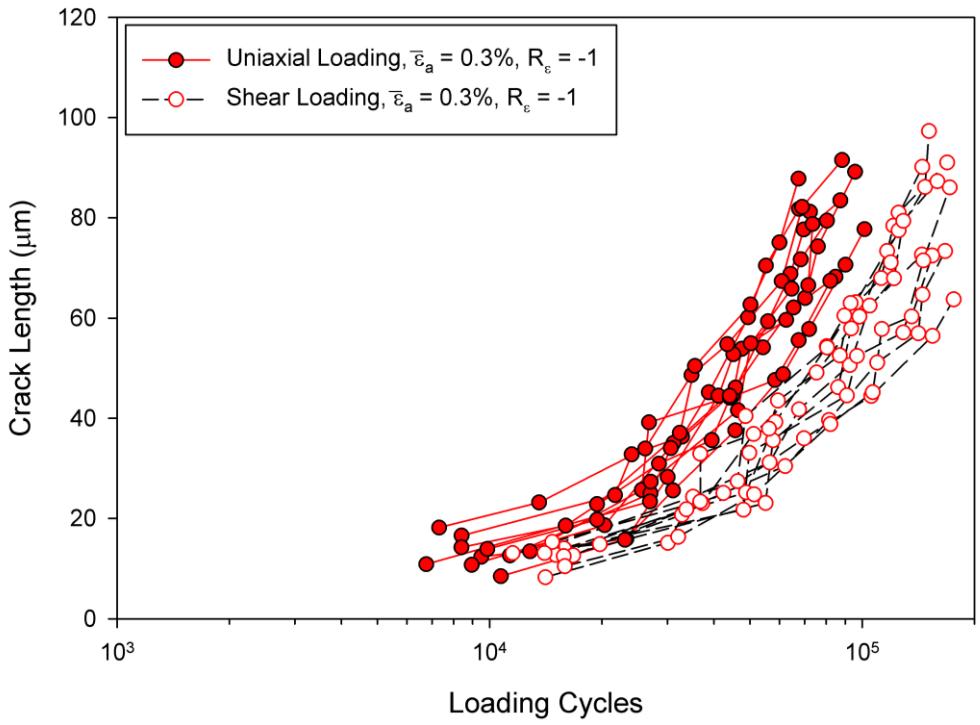

Figure 68. Comparison of crack growth under uniaxial and shear loading. In both cases loading is fully reversed and conducted at an applied equivalent strain amplitude ($\bar{\varepsilon}_a$) of 0.3%.

The results plotted in Figure 66, Figure 67, and Figure 68 all show the same trend, with longer fatigue lives predicted under simple shear loading than for the same equivalent uniaxial strain amplitude.

An additional set of 10 simulations was conducted at equivalent strain amplitude of 0.4% with an imposed mean shear strain of 0.5. The results from this set of simulations are plotted in Figure 69 along with data obtained under simple shear loading at an applied strain amplitude of 0.4% but with no mean strain.

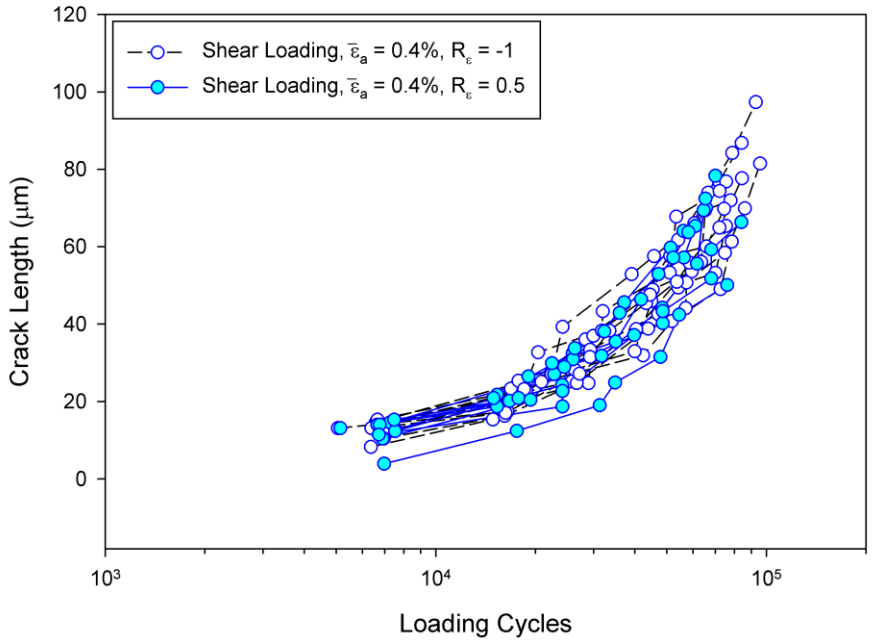

Figure 69. Comparison of crack growth under shear loading with and without imposed mean shear strains (R_ε = 0.5 and R_ε = -1). In both cases loading is conducted at an applied equivalent strain amplitude ($\bar{\varepsilon}_a$) of 0.4%.

It is clear from the overlapping data sets shown in Figure 69 that the model predicts no detrimental effect of imposed mean shear strains. This is in agreement with experimental results, as mean shear stress effects are not typically observed in fatigue, at least for fatigue crack initiation where the crack length is on the order of several hundred microns.

Results from the simulations conducted under simple shear loading are compared to experimental results obtained by Zhao and Jiang [108], shown in Figure 70. Note that for the experimental data of Zhao and Jiang [108], shear strain amplitude is plotted against cycles to failure, which they defined for this case to be either a 10% load drop of the formation of a fatigue crack visible to the naked eye, while for the simulated data shear strain amplitude is plotted against cycles to grow a crack to 60 μm. Additionally, the results obtained at an applied equivalent strain amplitude of 0.4% (corresponding to

$\gamma_a^{eq} = 0.538\%$) are shifted slightly on the shear strain amplitude axis so that both data sets are visible, and the lack of mean shear strain effects are apparent.

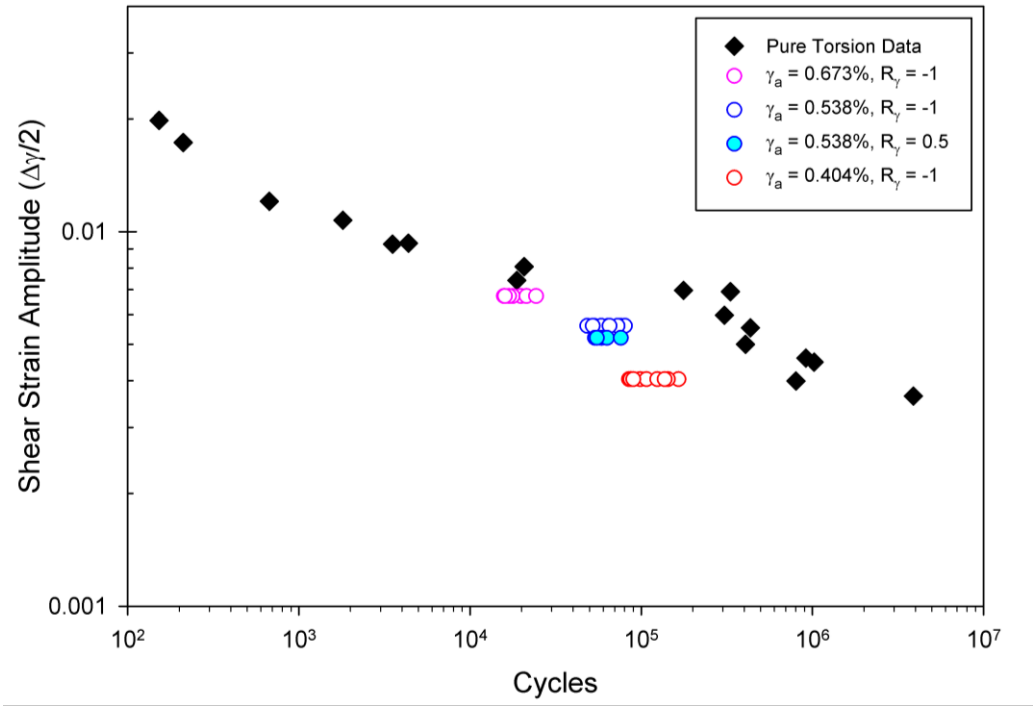

Figure 70. Comparison of data from shear fatigue simulations and shear experimental data from [108].

The data plotted in Figure 70 indicate that the simulations yield results that are conservative by approximately an order of magnitude. This trend is consistent for all applied shear strain amplitudes considered, but it does appear that at applied shear strain amplitudes larger than 0.673%, results from simulations will merge with experimentally observed lives.

5.4.3 Discussion of Shear and Uniaxial Results

The overly conservative lives under shear loading and the smaller-than-experimentally-observed reduction of fatigue lives due to a mean stress/strain require an

explanation. The most likely explanation is that the discrepancy is a result of a failure to fully account for the influence of nucleant particles. In this work, the life to crack the nucleant grain is modeled by Eqn. 36, a power-law formulation where the nucleation life, N_{nuc}, is a function of the grain diameter, band averaged FIP^{α}, and the parameter α_g which captures the degree of irreversibility in the nucleation process and is fit to experimentally observed lives to nucleate a crack. As discussed in Chapter 2, for Al 7075-T6 fatigued in ambient environments cracks tend to form at the interface between fractured constituent particles and the matrix ($N_{inc,part}$ per Eqn. 7) before propagating through the nucleant grain. The current nucleation law lumps the process of incubation at a fractured particle and growth through the nucleant grain into a single equation, incorporating the effect of the constituent particles into the value of α_g. This is partly why the value of α_g used in this work differs significantly from the value found by Castelluccio for RR1000, an alloy in which cracks nucleate in favorable oriented surface grains through the formation of PSBs and intrusions and extrusions on the specimen surface. By homogenizing the effect of cracked inclusions into the α_g parameter, the role that particle geometry, a significant source of variability in the incubation and nucleation process, is lost.

A second possibly is that the discrepancy between simulated and experimental results in shear and uniaxial loading with a mean stress/strain arises as a result of an incorrect value of *k* in the FS FIP. The parameter *k* controls the influence of the normal stress term on the magnitude of the FIP, and in this work *k* was taken to have a value of 0.5 in absence of available data for fitting. Larger values of *k* would increase the difference in FIP^{α} values, and thus fatigue lives, between uniaxial and shear loading and between uniaxial loading with and without a mean stress/strain. Recalibration would be

needed to again match experimentally observed uniaxial lives and crack propagation rates, but calibration of *k* offers a possible pathway to unifying results under multiple loading conditions more closely to what is experimentally observed.

5.4.4 FIP Ratio

The stage II growth model introduced in Chapter 4 employed the concept of an intermediate plane of crack propagation, with its orientation derived from the contributions of the two parent planes, and a driving force that is a summation of the averaged FIP^{α} values on the parent planes, referred to FIP_1 and FIP_2. If the values of FIP_1 and FIP_2 are nearly equal, the crack grows in a stage II manner. However, if one parent plane has a driving force much larger than the other, the growth of the crack will approximate stage I behavior. This can be captured by the ratio of the FIP values on the two parent planes, FIP_2/ FIP_1, where FIP_2 is the smaller of the two values. If the value of this ratio is close to unity, the two parent planes have nearly equal contributions to the growth of the crack, i.e. stage II growth. However, low values of FIP_2/ FIP_1 indicate dominance of a single slip system and near stage I growth.

FIP ratio vs. crack length data for the uniaxial, fully reversed simulations considered in Section 5.4.1 are plotted in Figure 71. The plot also includes horizontal lines that correspond to the average FIP ratio during MSC propagation through 8 grains at a given applied strain amplitude. Note that all cracks are assumed to nucleate and grow through the nucleant grain in stage I, and thus initially have a FIP ratio of zero.

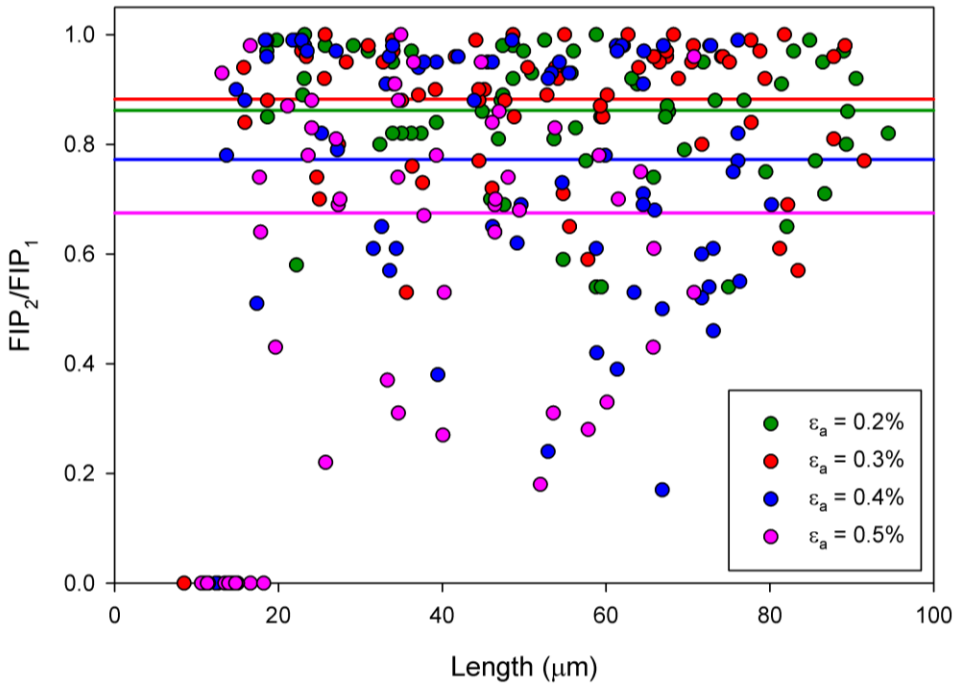

Figure 71. FIP ratio vs. crack length for simulations conducted under uniaxial, fully reversed loading at strain amplitudes of ε_a=0.2%, 0.3%, 0.4% and 0.5%.

The general trend observed in Figure 71 is that increasing applied strain results in increasingly stage I crack propagation character (smaller FIP_2/FIP_1 values), and vice versa. This is illustrated more clearly in Figure 72, which only plots FIP ratio data for the highest and lowest applied strain amplitudes considered during the uniaxial, fully reversed loading simulations.

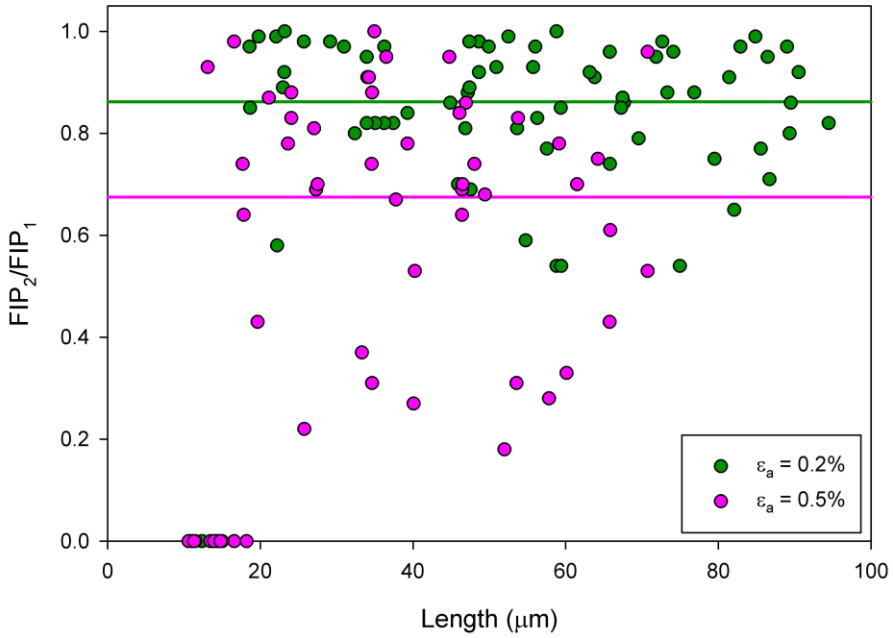

Figure 72. FIP ratio vs. crack length for simulations conducted under uniaxial, fully reversed loading at strain amplitudes of ε_a=0.2% and 0.5%.

Note that even at the highest applied strain amplitude of 0.5%, the average FIP ratio of 0.675 still indicates predominantly stage II growth. The trend of increasing average FIP ratio with decreasing applied strain amplitude roughly mirrors the trend of increasing average crack length with decreasing applied strain amplitude shown in Figure 61. Thus, the discrepancy in final lengths observed in Figure 61 can be attributed to differences in FIP ratio, with a higher stage II growth character favoring longer final crack lengths. A similar difference of final crack lengths is observed in Figure 80, which compares results from the stage I and stage II growth algorithms.

The trend of increasing average FIP ratio with decreasing applied strain amplitude is also seen in the simulations considering shear loading. The FIP ratios for the simulations conducted under fully reversed simple shear loading at equivalent applied strain amplitudes of 0.3%, 0.4% and 0.5% are plotted in Figure 73.

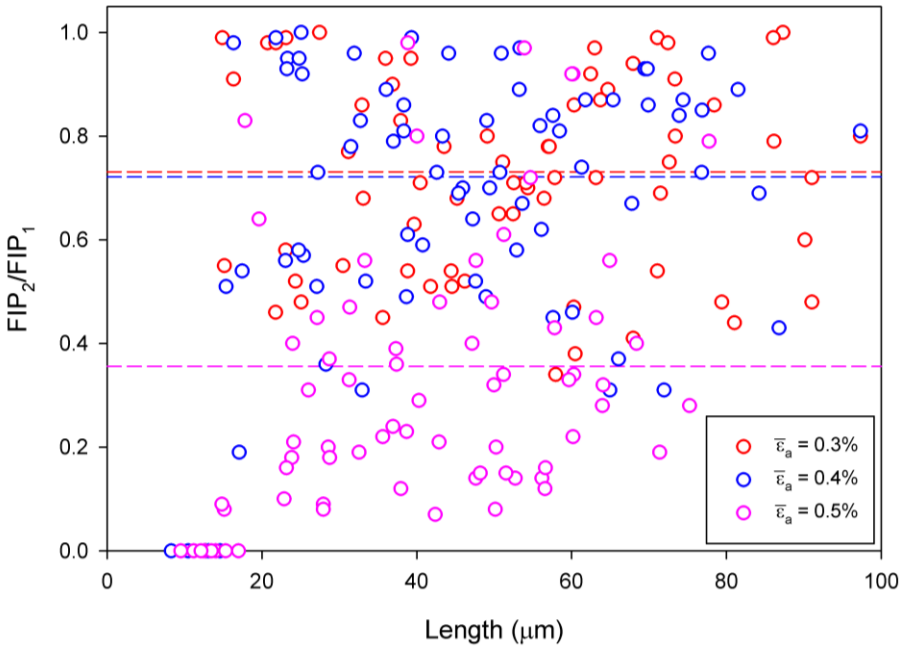

Figure 73. FIP ratio vs. crack length for simulations conducted under fully reversed shear loading at applied equivalent strain amplitudes ($\bar{\varepsilon}_a$) of 0.3%, 0.4%, and 0.5%.

Again, similar to Figure 71, the simulations conducted with the highest applied shear strain have the lowest FIP ratio, indicating tendency towards greater stage I growth character at higher applied strains. The 0.3% and 0.4% applied shear cases have nearly the same FIP ratio, indicating that MSC growth occurs in primarily a stage II fashion in these simulations.

Comparing the FIP ratio between uniaxial and shear simulations conducted at the same applied strain amplitude, we see that the uniaxial loading favors a higher average FIP ratio, and thus stage II growth. This is illustrated in Figure 74, a plot of FIP ratio vs. crack length for both the simulations conducted under uniaxial loading and shear loading at an applied equivalent strain amplitude of 0.5%.

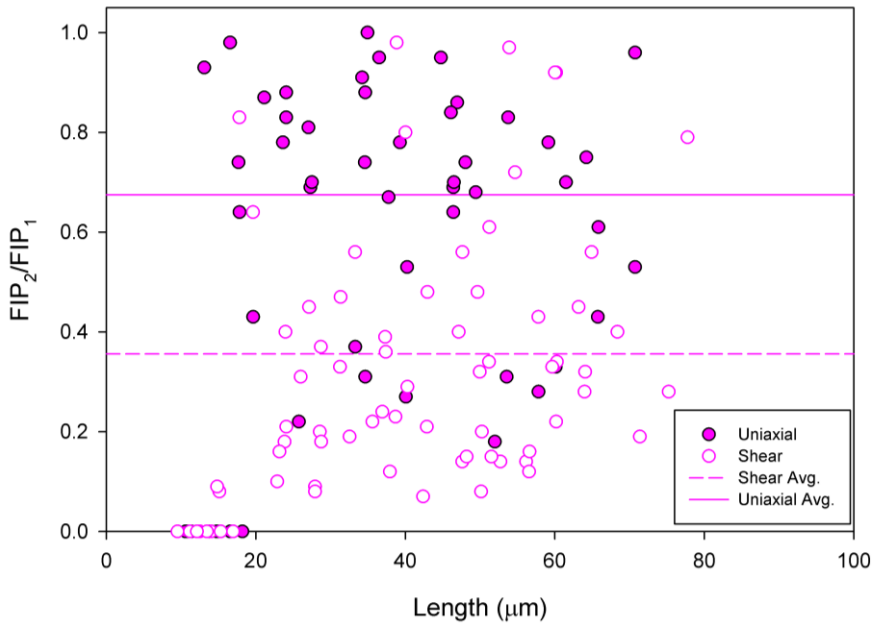

Figure 74. Comparison of FIP ratio vs. crack length for simulations conducted under fully reversed shear and uniaxial loading at an applied equivalent strain amplitude ($\bar{\varepsilon}_a$) of 0.5%.

The average FIP ratios plotted in Figure 74 have a value of 0.68 for the uniaxially loaded cases, and a value of 0.36 for the cases loaded in shear, representing a significant shift towards stage I type growth when loaded in shear. Although the plots are not included for the sake of brevity, the simulations conducted at equivalent applied strain amplitudes of 0.3% and 0.4% undergo a similar reduction in average FIP ratio when loaded in shear. For the 0.3% applied strain cases the average FIP ratio is reduced from 0.88 under uniaxial loading to 0.73 under shear loading, and for the 0.4% applied strain amplitude cases the average FIP ratio is reduced from 0.77 under uniaxial loading to 0.72 under shear loading.

A reduction in the average FIP ratio is also observed in the presence of an applied mean stress/strain. This is shown for the simulations conducted at an applied strain amplitude of 0.4% in Figure 75.

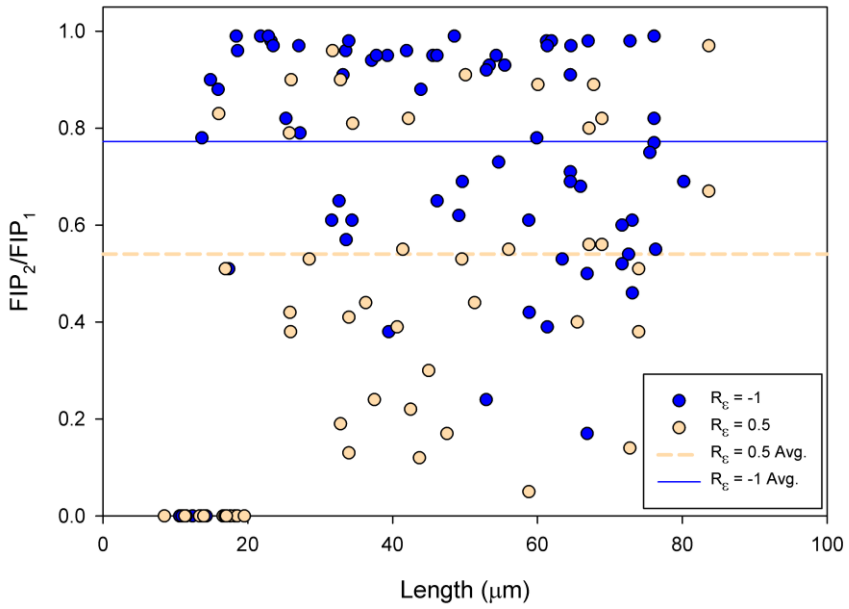

Figure 75. Comparison of FIP ratio vs. crack length for uniaxially loaded simulations conducted at a strain amplitude of 0.4%, with applied strain ratios of R_ε = -1 and R_ε = 0.5.

The reduction in average FIP ratio shown the Figure is fairly significant, from 0.77 in the case of fully reversed loading to 0.54 under the presence of a mean stress/strain. The trend observed in Figure 75 for the 0.4% applied strain amplitude cases is also representative of the results observed at an applied strain amplitude of 0.3%, where the presence of a mean stress due to the imposed strain ratio of R_ε = 0.5 reduces the average FIP ratio from 0.88 under fully reversed loading to 0.67. For all the results presented in this section, no trend in FIP ratio is observed with increasing crack length.

5.4.5 Size of Crack Relative to Computational Volume

In this chapter, the majority of simulations conducted were run until a total of 8 grains had cracked. As shown in Sections 5.4.1 and 5.4.2 considering uniaxial and shear results, the final crack length in these simulations can approach 100 μm. Considering the simulation volume is a polycrystalline cube with 60 μm sides and 14 μm grains, a total crack length of 100 μm seems very significant. However, this total length is obtained

through a summation of the length of each increment of crack growth and is not calculated based on the total projected area of the crack, which is somewhat smaller. To illustrate this, we will present the results from a single simulation in which 8 grains were allowed to crack and the crack grew to a final length of 74.8 µm, but that is generally representative of the progression of a typical simulation. In this simulation, both the element size and band width were 2.5 µm and the loading was uniaxial and fully reversed at 0.4% applied strain amplitude.

The total number of elements within the crack and the percentage of cracked elements out of the total elements in the mesh are plotted against the i^{th} grain to crack in Figure 76.

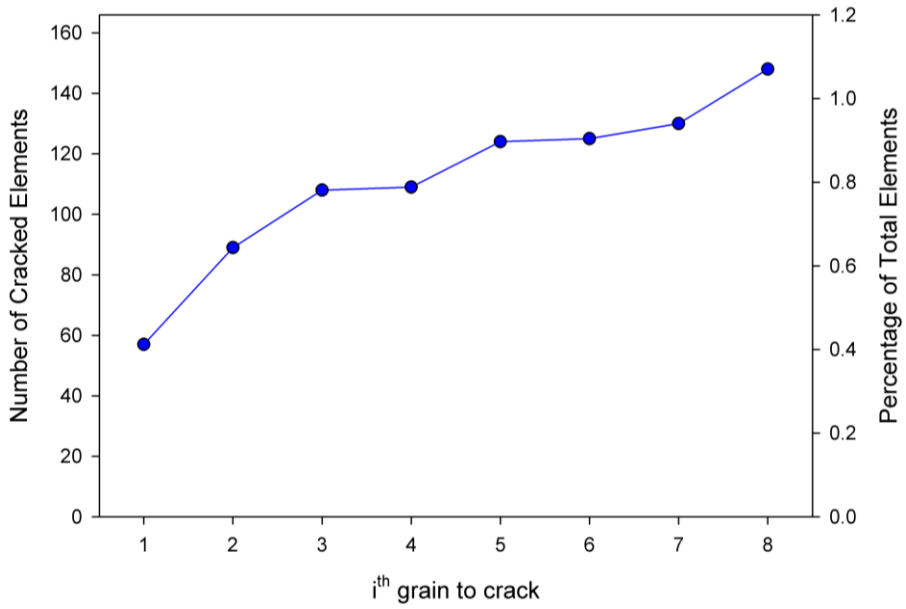

Figure 76. Progression of a typical simulation in terms of the number and percentage of cracked elements.

At the end of the simulation, the crack contains a total of 148 elements, representing less than 1.2% of the 13,824 elements in the mesh. Because the mesh has a cubic geometry with 60 µm sides and 2.5 µm elements, the cross section contains 576 elements. If we

assume that the crack grew entirely on one cross sectional plane, the total area of the crack would be 25.7% of the cross-sectional area of the mesh. In reality, due to the non-planar nature of the crack growth the actual projected area of the crack would be a somewhat smaller percent of the cross sectional area. Thus, overall the presence of the crack has only a small effect on macroscopic stress-strain response of the mesh in response to loading. This is shown in Figure 77 and Figure 78, which compare the stress-elastic strain response on the 1st complete computational loading cycle (when there is no crack present) to the response on the 20th computational cycle when 8 grains have been cracked. A slight decrease in stiffness is visible in the tensile loading portion of Figure 77 on the 20th cycle, which is recovered during the compressive half of the loading cycle as the crack closes.

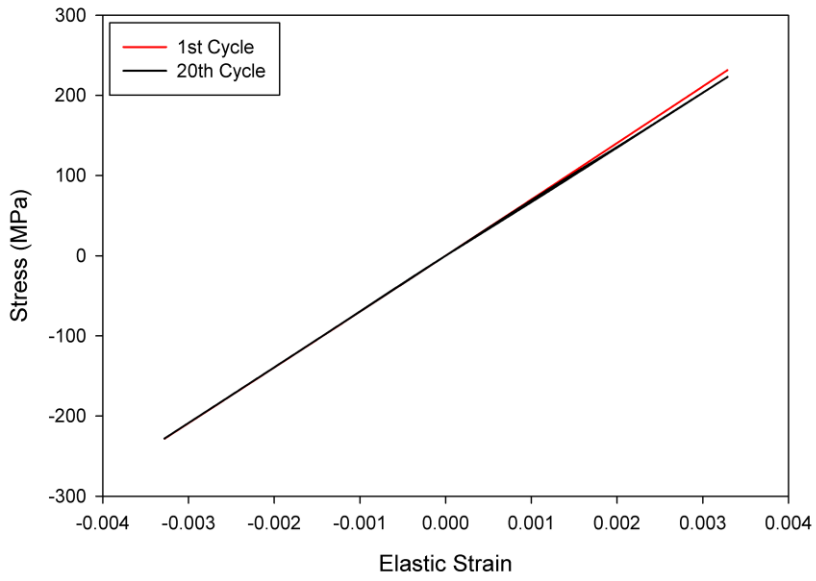

Figure 77. Comparison of the elastic strain response to loading before the addition of a crack (1st cycle) and after cracking 8 grains (20th cycle).

The compressive portions of the loading cycles are omitted in Figure 78 to better illustrate the reduction in stiffness under tensile loading due to the presence of the crack.

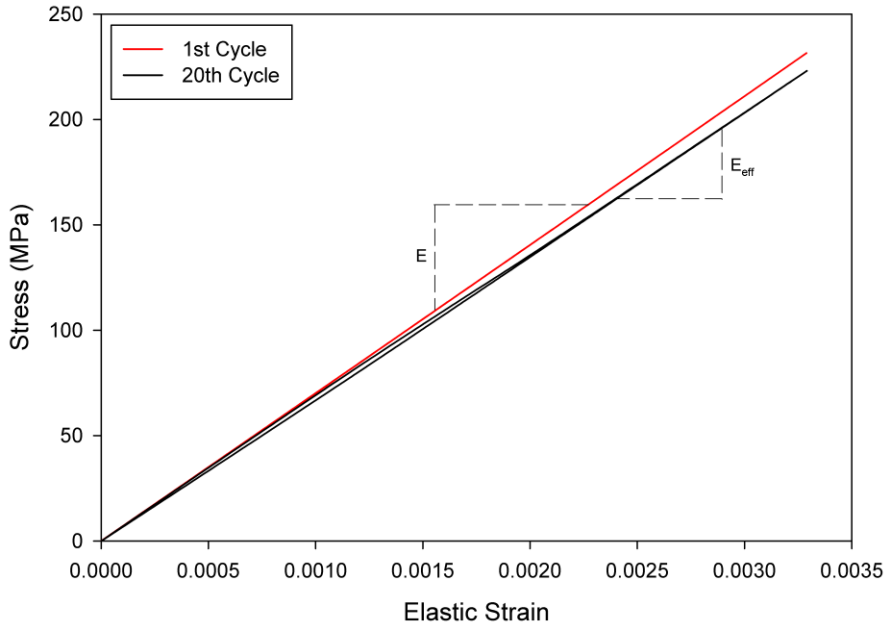

Figure 78. Comparison of the elastic strain response to loading before the addition of a crack (1st cycle) and after cracking 8 grains (20th cycle) for the tensile portions of the loading cycles.

The Young's Modulus (E) was calculated to be 70.4 GPa for the initial loading cycle, and after the 20th loading cycle the effective Young's Modulus due to the damage (E_{eff}) was calculated to be 67.8 GPa. Also visible in Figure 78 is a slight hysteresis in the elastic response during the tensile portion of the 20th cycle due to the application and recovery of damage on individual elements.

5.5 Comparison of Fatigue Algorithms

Figure 79 is a plot of the predicted crack propagation through the same microstructural instance using both the Stage I and Stage II fatigue growth algorithms. The mesh consisted of 150 grains and cracks were allowed to propagate through a total 8 grains before the simulations were terminated. The number of the grain containing the cracked band is included on plot to illustrate the general path of the crack.

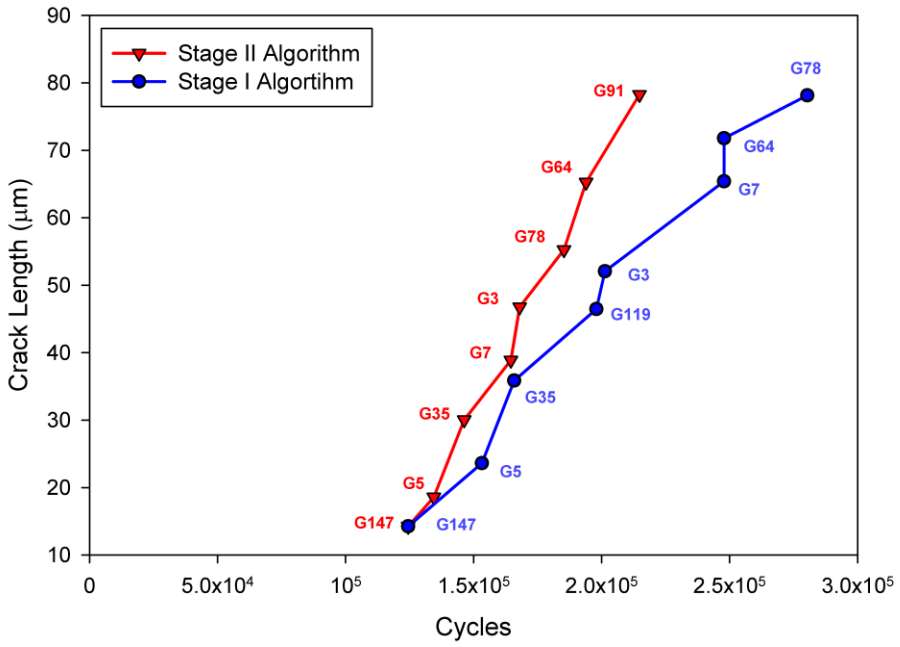

Figure 79. Comparison of predicted crack growth by Stage I and Stage II algorithms for a single microstructural instantiation. Generated using the OW44 Model subjected to R_ε=-1, ε_a = 0.4% uniaxial strain controlled cycling. Scale is linear.

The fatigue constants (corresponding to Calibration B) were taken to be the same in both simulations so that the results obtained using the two algorithms would be directly comparable. Both the Stage I and Stage II algorithms employ the same nucleation law, and thus nucleate in the same grain on the same cycle for a specific microstructure instantiation. Following nucleation, the two cracks propagate through the microstructure

slightly differently, with the SII crack growing faster than the SI crack. Out of the 8 grains allowed to crack, the SI and SII cracks propagated within 7 of the same grains, with a slight variation in the order of cracking after the 3rd cracked grain. Both cracks grow to a very similar length (78.1 µm vs. 78.3 µm) during the course of the simulation.

The crack propagation data for all 10 microstructural instantiations considered are plotted in Figure 80. The overall trends in the Figure match those of the single instantiation, with the exception of the crack length at the end of the simulation. The average crack length after cracking 8 grains predicted by the Stage I algorithm is 66.1 µm, while the Stage II algorithm predicts an average crack length of 77 µm.

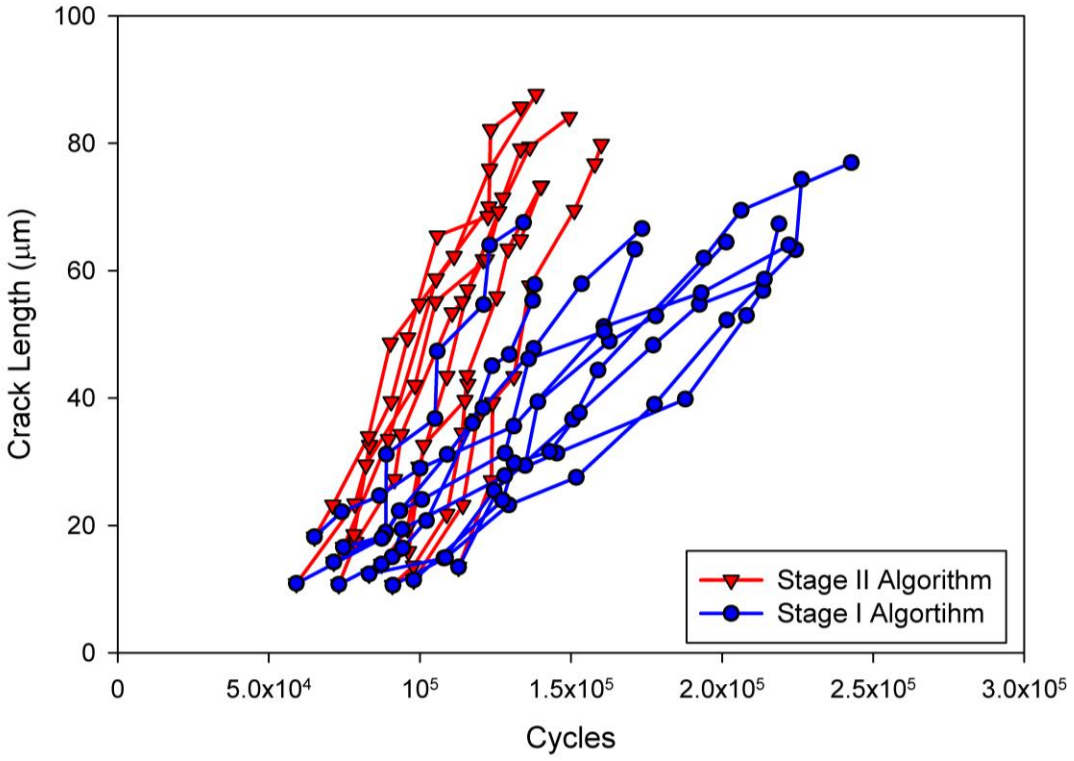

Figure 80. Comparison of predicted crack growth by Stage I and Stage II algorithms for 10 microstructural instantiations. Generated using the OW44 Model subjected to R_ε = -1, ε_a = 0.4%, uniaxial strain controlled cycling. Scale is linear.

The average number of cycles to grow a crack to 60 μm is approximately 120,000 cycles when calculated with the Stage II algorithm and 180,000 cycles using the Stage I algorithm, or about 50% longer. However, the Stage I algorithm predicts a significantly larger scatter in predicted fatigue lives: the standard deviation of the cycles to reach 60 μm for the Stage I algorithm is almost 30,000 cycles, while the Stage II algorithm has a standard deviation of only 12,000 cycles. Similarly, the range of lives predicted by the Stage I algorithm is more than double the range predicted by the Stage II algorithm.

The difference in crack propagation rates between the Stage I and Stage II algorithms is illustrated more clearly Figure 81 which compares the simulated crack propagation rates of each with the experimental data of Tokaji et al. [56].

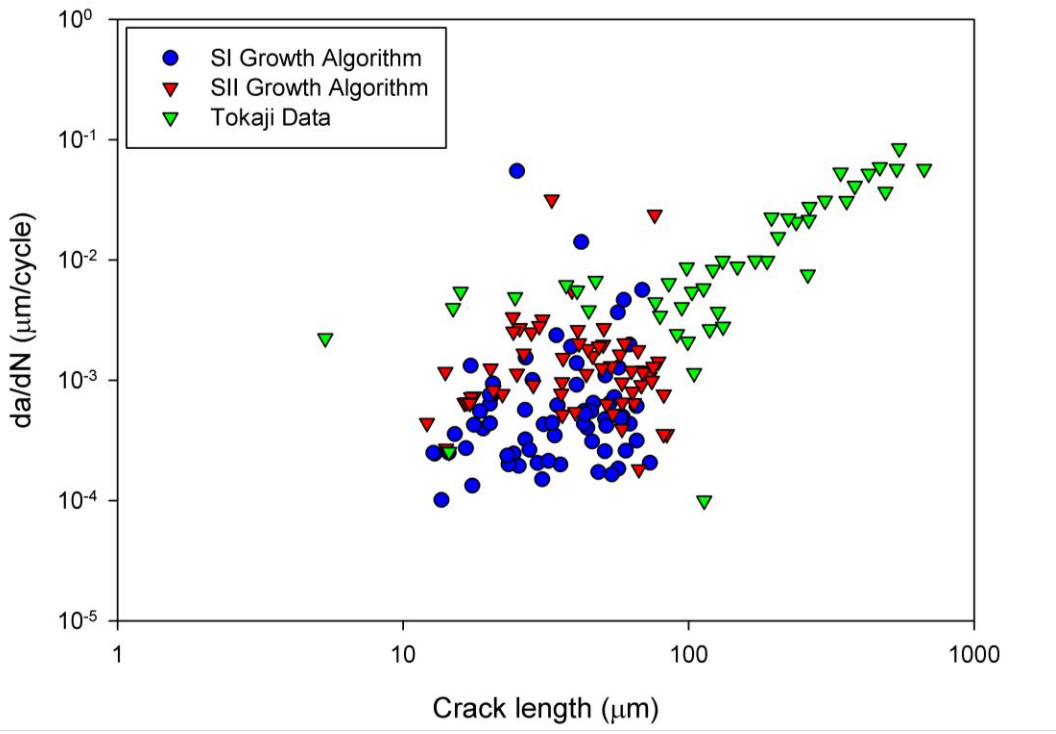

Figure 81. Crack growth rate obtained using the Stage I and Stage II algorithms compared to the experimental data of Tokaji et al. [56] for $R_\varepsilon = -1$, $\varepsilon_a = 0.4\%$, uniaxial strain controlled cycling.

In the Figure, we can see both the higher average growth rates for the Stage II algorithm and the larger degree of variability predicted by the Stage I algorithm. Both the maximum and minimum growth rates in Figure 81 were predicted by the Stage I algorithm. Note that the data plotted in Figure 81 were obtained using fatigue model Calibration B coupled with constitutive model version OW44. Calibration B was derived using the G31 constitutive model version, and because of the significant differences between these two constitutive models (explored further in Section 5.6) the results are not expected to be quantitatively accurate, but the comparison to Tokaji data is included to give the reader a sense of the difference between the Stage I and Stage II growth rates compared to the scatter in experimental data.

Similar trends are observed in Figure 82, a box-and-whisker plot of the FIP value in the band of minimum life for each of the 8 grains to crack in the 10 microstructural instantiations considered. Note that the FIP value plotted for the Stage I results corresponds to FIP_0^{α}, the driving force on a single slip system, while for the Stage II results the driving force on the intermediate plane, FIP^{int}, is plotted after the nucleant grain.

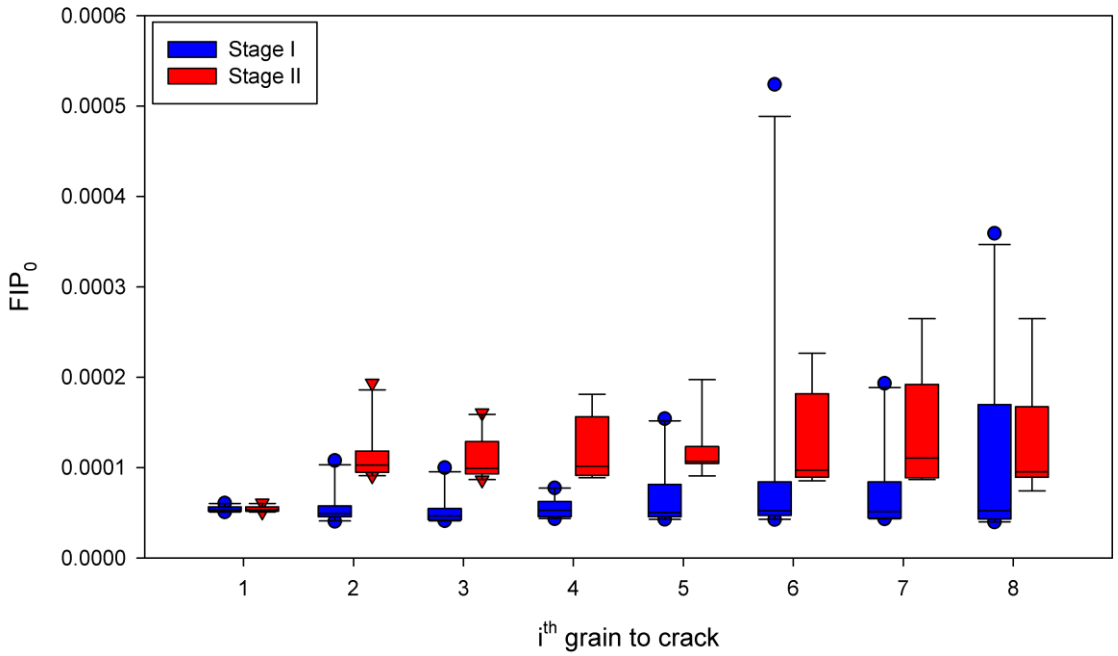

Figure 82. Comparison of FIP values of the i^{th} grain to crack for the Stage I and Stage II algorithms for 10 microstructural instantiations. Generated using the OW44 Model subjected to $R_\varepsilon = -1$, $\varepsilon_a = 0.4\%$, uniaxial strain controlled cycling.

This plot reinforces the trends observed in Figure 80 and Figure 81, with generally higher levels of FIP for the Stage II algorithm, and higher degrees of scatter in the FIP values of the Stage II algorithm. For both fatigue models, the average FIP exhibits little variance as crack grows from the 1^{st} grain to the 8^{th} grain. However, the range in FIP values does increase substantially as the crack propagates, especially from the nucleant grain to the 2^{nd} grain to crack.

The change in FIP from the nucleant grain to the 2^{nd} grain to crack is highlighted in highlighted in Figure 83. Note that in the nucleant grain, the FIPs are the same for both the Stage I and Stage II algorithms, because they employ the same nucleation relation.

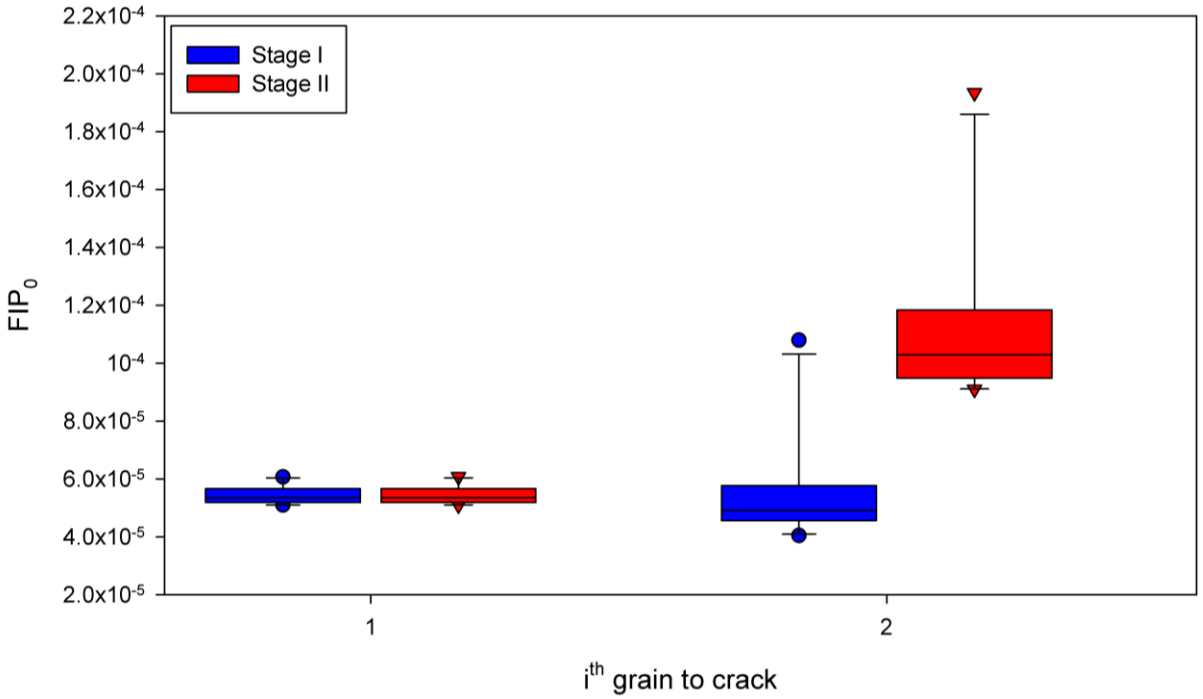

Figure 83. Comparison of FIP values of the 1st and 2nd grains to crack for the Stage I and Stage II algorithms for 10 microstructural instantiations. Generated using the OW44 Model subjected to R_ε = -1, ε_a = 0.4%, uniaxial strain controlled cycling.

Following nucleation, the median FIP in the 2nd grain to crack (calculated by the Stage I algorithm) decreases by approximately 8% from the median FIP in the nucleant grain. This differs from the results of Castelluccio in RR1000, who observed that in that alloy system, the median FIP in the 2nd grain to crack was approximately 40% lower than in the nucleant grain [2]. This is attributed to the notched specimen geometry employed by Castelluccio, which created a local stress concentration in the nucleant grain not present in the smooth mesh geometries used in this work.

The data considered by Castelluccio in RR1000 also display a slight increase in the range of FIP values from the 1st to 2nd grain to crack, but the effect is much more pronounced in the simulations of Al 7075-T6. The increase in the variability of FIP observed in Al 7075-T6 compared to RR1000 is perhaps due to the higher propensity for

multi-slip in the aluminum alloy. If a single slip system is active within a grain, the state of plastic strain can be captured entirely by maximum value of FIP^{α}. However, if there are multiple slip systems active and the total plastic strain is proportioned among them, and the maximum value of FIP^{α} does not uniquely characterize the plastic strain state, and elements or grains with the same effective measures of plastic strain may have significant differences in FIP^{α} depending on how the plastic strain is proportioned between the slip systems. In contrast, a FIP summated over all slip systems would be expected to exhibit a similar degree of variability under both single and multi-slip conditions.

5.6: Fatigue Results From Different Constitutive Model Versions

Uniaxial simulations were conducted on a set of 10 microstructural instantiations using both the G31 and OW44 models to assess how the various forms of constitutive models affect the lives predicted by the fatigue algorithms. The meshes were subjected to 20 cycles loading at an applied strain amplitude (ε_a) of 0.4%. For each instantiation and version of constitutive model, a simulation was conducted under both fully reversed loading ($R_\varepsilon = -1$) and with an imposed mean strain ($R_\varepsilon = 0.5$). Nucleation life was evaluated after the 3rd computational cycle, and MSC growth lives were evaluated every 2 cycles following nucleation (5th cycle, 7th cycle etc.) until a total of 8 grains were cracked. The comparison simulations were conducted using fatigue model calibration B and the Stage I growth algorithm. Results are shown in Figure 84 with data obtained with the G31 version of the constitutive model in blue and data obtained using version OW44

in red. Solid symbols denote fully reversed loading and hollow symbols denote results from loading with a mean strain.

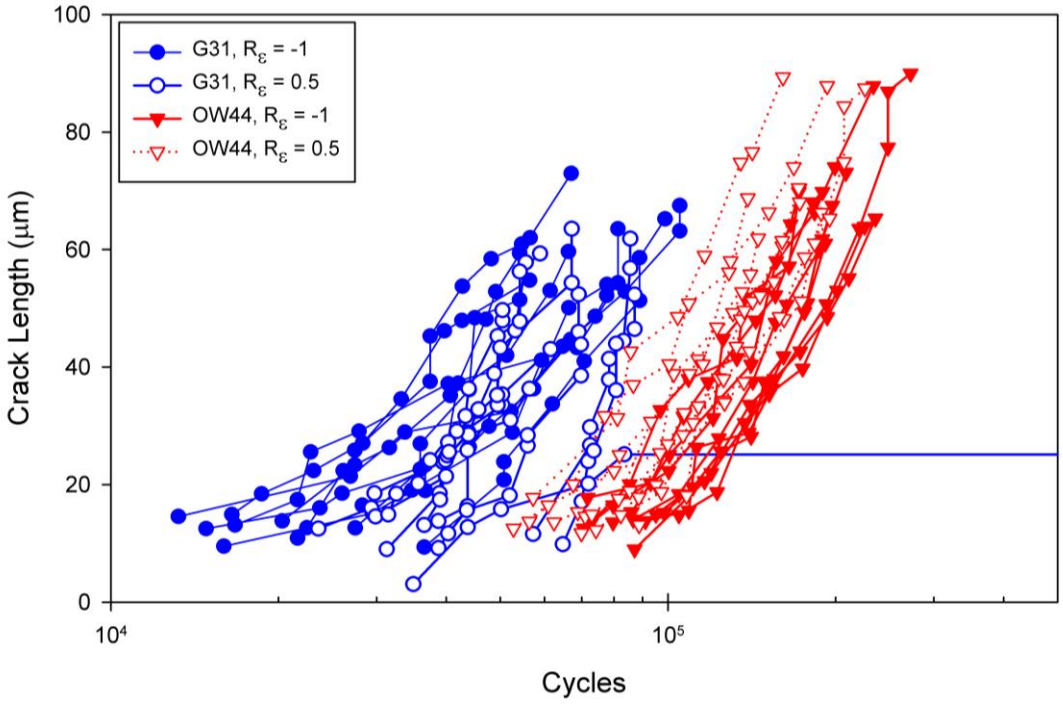

Figure 84. Comparison of fatigue lives between OW44 and G31 constitutive models under uniaxial loading with ε_a = 0.4%, and R_ε = -1 or 0.5.

There are a few key differences between results obtained using the two material models. First, simulations using the OW44 constitutive model correctly capture the slight reduction in fatigue lives caused by the imposed mean strain (and resultant mean stress). This is a significant improvement over the G31 model, which predicts *longer* fatigue lives when cycled with a positive mean strain/stress. This is due to the reduction in cyclic plastic strain range predicted by the G31 model when loaded with a mean stress/strain compared to when the model is loaded under fully reversed conditions, as discussed in Chapter 3. The incorrect trend in fatigue lives predicted by the G31 model was the

impetus behind the development and introduction of the OW44 model, as well as proper description of ratcheting and mean stress relaxation, which are related, of course.

Second, the OW44 model predicts longer fatigue lives than the G31 model despite the OW44 model predicting a larger degree of macroscopic cyclic plasticity under this particular loading condition. Explanation requires comparing the FIP^{α} values for simulations conducted with the same microstructural instantiation and loading but with the different constitutive models. Figure 85 compares all FIP^{α} values (sorted from highest to lowest) within a mesh over the 3rd computational cycle obtained using the G31 and OW44 models. The mesh is comprised of 8,000 elements and with 12 FIP^{α} values for each element there are 96,000 FIPs to compare.

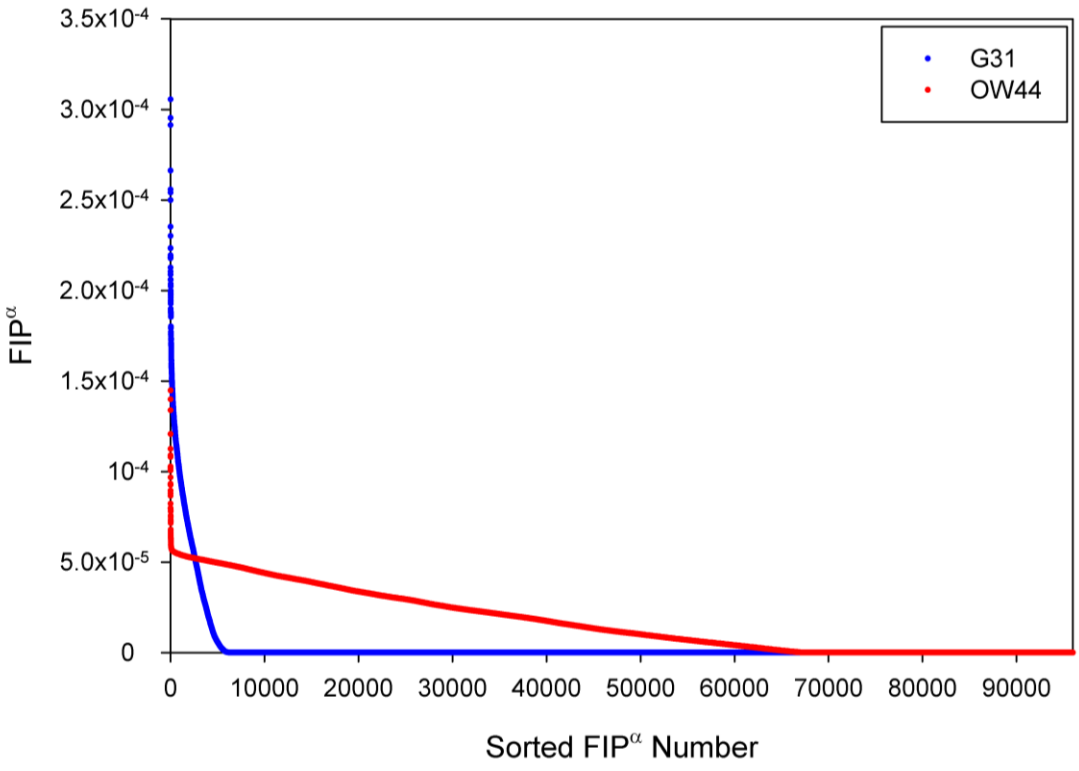

Figure 85. Comparison of FIP values during the 3rd computational cycle obtained using the G31 and the OW44 constitutive models under uniaxial loading with ε_a = 0.4%, and R_ε = -1.

Figure 85 shows that the G31 model predicts maximum FIP^{α} values that are approximately twice as high as those predicted by the OW44 model. Also note the large number of near zero FIP^{α} values predicted by the G31 model and the crossover in sorted FIP^{α} values at approximately 3000 out of 96,000 total FIPs. While the G31 model has a larger number of high FIPs, the OW44 model has a much greater number of moderately high FIP^{α} values. This trend holds within individual elements and grains, with the G31 model predicting plastic strain on a single system and the OW44 model predicting plastic strain on multiple slip systems. The difference in active slip systems is due primarily to the value of drag stress selected for the models. Both models were calibrated using a non-evolving drag stress, but the value is much lower in the OW44 model than in the G31 model (35 MPa vs 130 MPa). Because of this difference, the resolved shear stress on many slip systems is of sufficient magnitude to cause some amount of plastic strain when using the OW44 model, whereas the same resolved shear stress would have been insufficient to induce plastic strain on that particular slip system for the G31 model. The data were re-plotted on a semi-log scale in Figure 86 to more clearly display the high FIP regime.

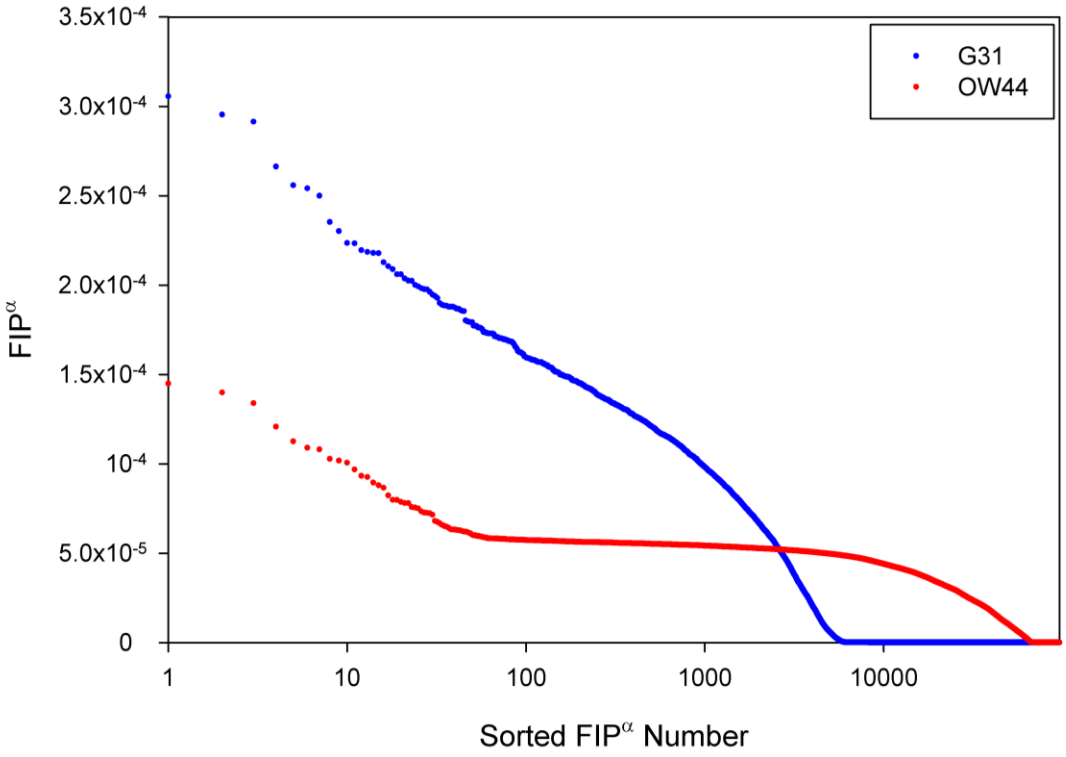

Figure 86. Semi-log plot of FIP values during the 3rd computational cycle obtained using the G31 and the OW44 constitutive models under uniaxial loading with ε_a = 0.4%, and R_ε = -1.

The increased number of active slip systems for OW44 explains why the OW44 model predicts longer lives. For simulations conducted using the G31 constitutive model, most grains have only a single slip system active. In contrast, the plastic strain in the OW44 model is carried among multiple slip systems, and although the average amount of plastic strain is larger, the maximum plastic strain on a single slip system is typically smaller than results from the G31 model. Not only does this emerge from fitting ratcheting and mean stress relaxation, as well as specimen level plasticity, but it is consistent with physical understanding of the multi-slip character of Al alloys, which is physically a product of their high stacking fault energy [31, 33]. The Stage I-focused fatigue algorithm only considers FIP values for a single slip system at a time, and therefore

predicts shorter lives for the G31 model due to higher peak FIP^{α} values. The longer lives predicted for the OW44 model highlight the importance of developing Stage II fatigue algorithms that can account for the influence of cyclic plastic strain on multiple slip systems within a grain.

Additional simulations were conducted to compare the performance of the G31, OW44, and OW57 versions of the constitutive model. These simulations were conducted under both uniaxial and shear loading conditions. The meshes were subjected to strain controlled loading at an equivalent strain amplitude ($\bar{\varepsilon}_a$) of 0.33% for both fully reversed loading ($R_\varepsilon = -1$) and with an imposed mean strain ($R_\varepsilon = 0.5$). Nucleation life was evaluated after the 5^{th} computational cycle, and MSC growth lives were evaluated every 2 cycles following nucleation (7^{th} cycle, 9^{th} cycle, etc.) until a total of 8 grains were cracked. Results are shown in Figure 87. Note that results from the G31 model are omitted due to the absence of cracks within the simulations caused by low levels of plastic strain (model G31 has a large value of drag stress). Data in red corresponds to results from model OW44 while data in green correspond to simulations conducted with model OW57. Solid symbols denote fully reversed loading and hollow symbols denote results from loading with a mean strain, while circular symbols denote uniaxial loading and diamonds represent shear loading cases.

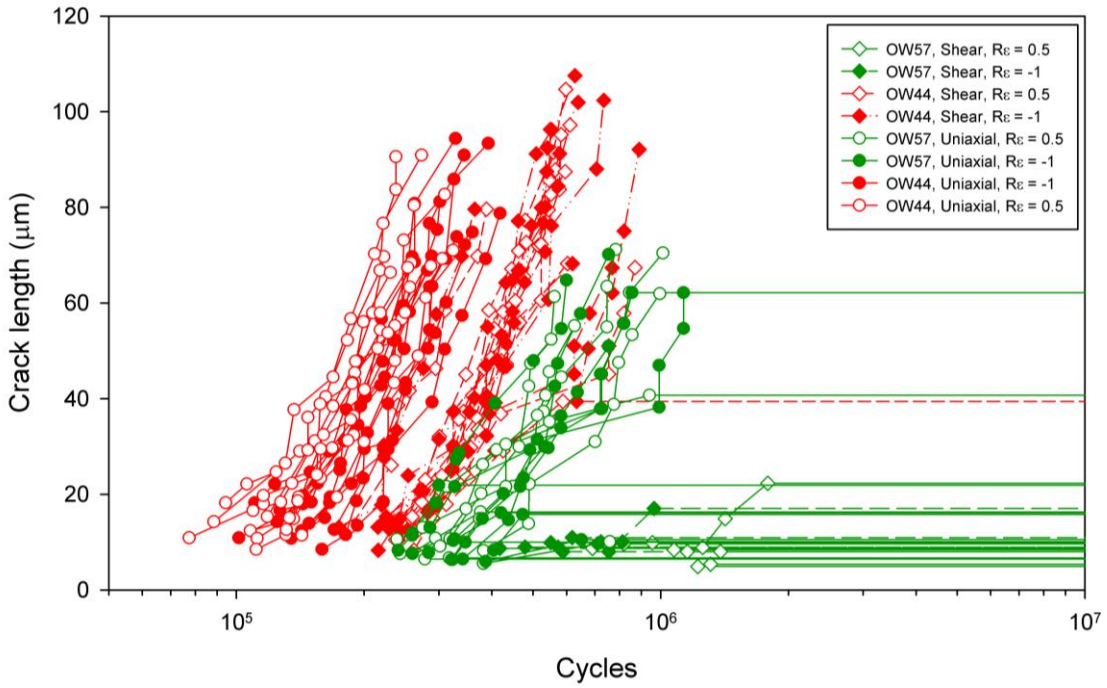

Figure 87. Comparison of fatigue lives between OW44 and OW57 constitutive models. Loading is shear or uniaxial with an applied equivalent strain amplitude ($\bar{\varepsilon}_a$) of 0.33%, and with an applied strain ratio (R_ε) of 0.5 or -1.

The key difference between the OW44 model and the OW57 model is that for almost all cases, the OW44 model predicts shorter fatigue lives and crack propagation over grains in larger cycle increments. This is due largely to the difference in drag stress evolution between the two models; model OW44 has a constant low valued drag stress (35 MPa) and the OW57 model has an evolving drag stress that saturates at a much higher value (100 MPa). Figure 87 illustrates the importance of the constitutive model when conducting fatigue simulations; the differences in results obtained under uniaxial vs. shear loading or at different strain ratios are smaller than the differences that result from using similar constitutive models calibrated to the same experimental data.

Results for the OW44 model are shown in Figure 88 with the shear loading cases further distinguished from uniaxial loading cases by plotting in black hollow (R_ε = 0.5) or

red and black (R_ε = -1) diamonds with dashed connecting lines. There is an observable strain ratio effect for the simulations conducted under uniaxial loading conditions, which is consistent with experimental observations. The simulations conducted with a mean shear strain do not experience a similar detriment in fatigue life, as is expected based on general experimental trends. Another feature of note in in Figure 88 is that shear lives are approximately double those under the equivalent uniaxial strain amplitude. These results are consistent with those presented in Section 5.5 which considered the same microstructural instantiations, material model, and loading conditions, but with the Stage II fatigue model with updated calibration (calibration A).

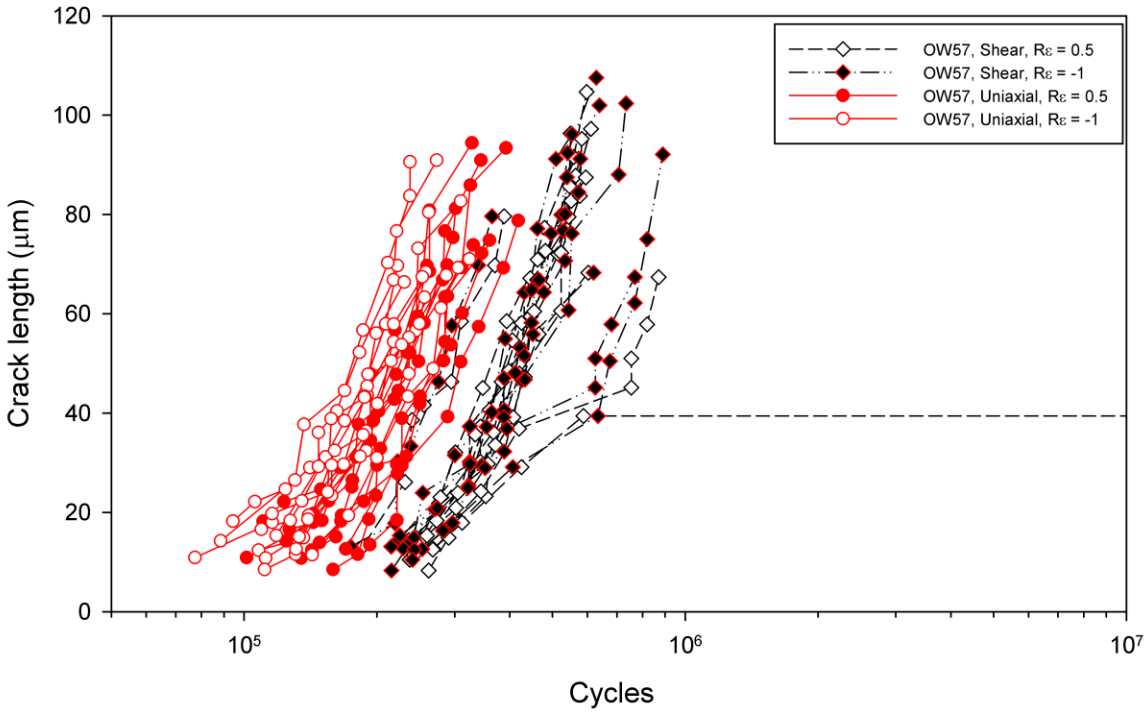

Figure 88. Comparison of shear and uniaxial results from the OW44 constitutive model cycled at an equivalent strain amplitude ($\bar{\varepsilon}_a$) of 0.33%, with either R_ε = 0.5 or R_ε = -1.

Results for the OW57 model are shown in Figure 89 with the shear loading cases further distinguished from uniaxial loading cases by plotting in black hollow (R_ε = 0.5) or green and black (R_ε = -1) diamonds with dashed connecting lines. Unlike the results obtained using model OW44 or the results shown in the previous report using model OW57 cycled at a strain amplitude of 0.4%, there is no discernable effect of mean strain on the predicted fatigue life in Figure 89. In addition, all of the simulations loaded in shear arrested rapidly, with the longest simulation cracking a total of only 3 grains before arresting.

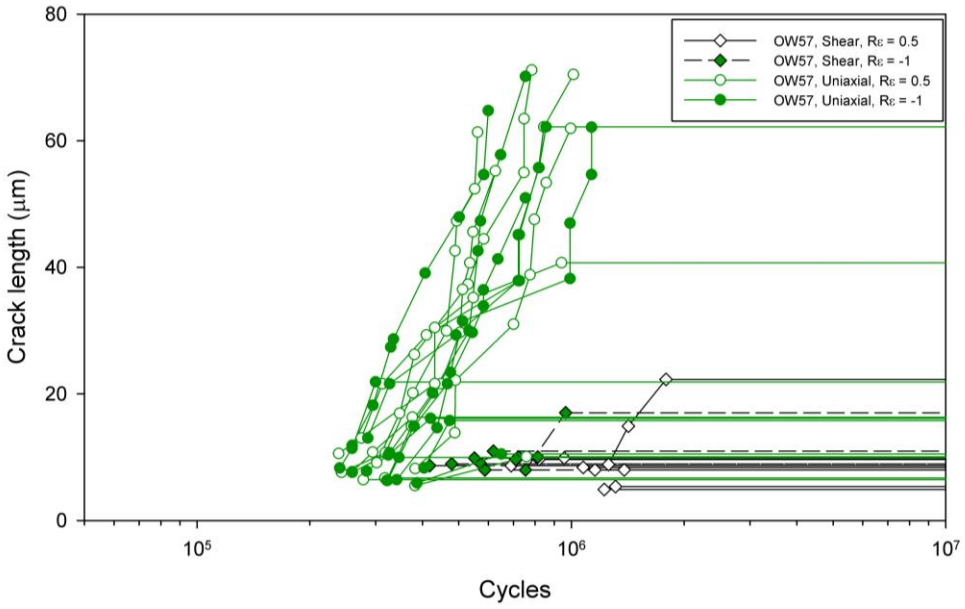

Figure 89. Plot of fatigue crack growth results using the OW57 constitutive model cycled at an equivalent strain amplitude of 0.33%.

The lack of crack growth under shear loading suggests that the saturation value of the drag stress is too high, resulting in levels of plasticity that are insufficient to drive crack growth.

The interplay of the constitutive model explored in this section, including the representation of slip system activity, ratcheting, mean stress relaxation, etc., indicates a

very important aspect of the current MSC modeling framework. Namely, one should apply this framework in conjunction with physically-based and validated crystal plasticity models. This differs conceptually from the notions of fracture mechanics, where only a few crack growth parameters are assumed sufficient to capture differences among materials. In the present framework, the constitutive model reigns supreme as providing driving forces for crack growth, the parameters of which are relatively straightforward to estimate apart from numerous experiments.

5.7: Volume Effects

Two additional mesh configurations were created to study the effect of mesh volume and total number of grains considered on the simulated fatigue behavior. Both mesh configurations used a mean grain size of 14 μm, an element size of 5 μm and a band width of 5 μm. The larger mesh (see Figure 90 left) had a volume of $(100\ \mu m)^3$ and a total of 696 grains, while the smaller mesh (see Figure 90 right) had a volume of $(50\ \mu m)^3$ and a total of 87 grains, $1/8^{th}$ the volume of the larger coarse mesh. A total of 35 microstructural instantiations were created for each mesh configuration. The average number of elements per grain of 11.5 is the same for both configurations.

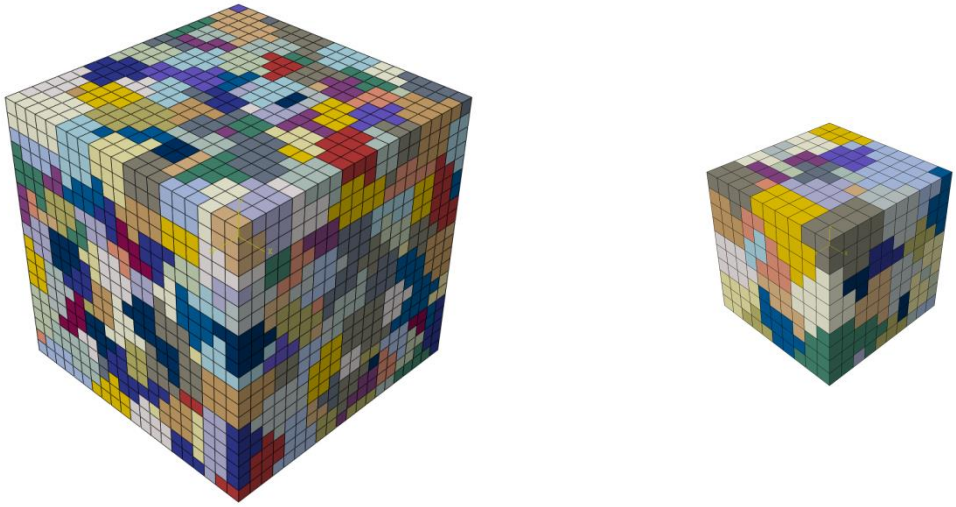

Figure 90. Comparison of the meshes used to evaluate the effects of simulation volume and grains considered on fatigue lives. Relative volumes of the two mesh configurations are shown to scale.

A comparison of the crack growth lives predicted for uniaxial, fully reversed, tension-compression simulations conducted at a strain amplitude of 0.4% is shown in Figure 91. Results from the larger mesh are plotted in red while results from the smaller mesh are plotted in magenta.

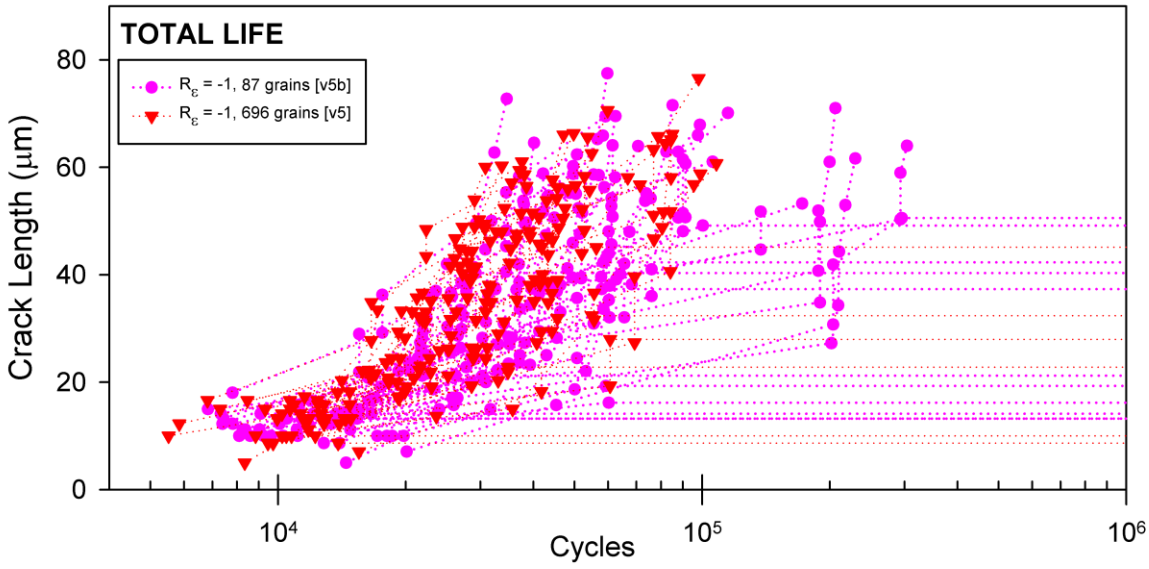

Figure 91. A comparison of crack propagation in meshes with varying volume, ε_a = 0.4%, R_ε = -1.

There are two particularly noteworthy aspects of Figure 91. The first is the outcropping of six cracks with predicted life longer than $1x10^5$ cycles, and the higher rate of arrest (nonpropagating cracks) observed for the mesh with the smaller volume. This effect is likely due to the higher probability of a crack within the smaller volume mesh coming into contact with the surface of the overall volume element. The bands along the surface of the mesh have fewer neighboring bands (due to the non-periodic nature of these simulations) than a band within the center of the mesh; thus the crack has fewer candidate bands to extend along and a lower probability of being in contact with a favorably oriented grain.

The second noteworthy aspect is the difference in nucleation lives between the two coarse meshes. This is seen more clearly in Figure 92, which plots the predicted number of cycles and crack length after nucleating and growing through the first grain for both meshes.

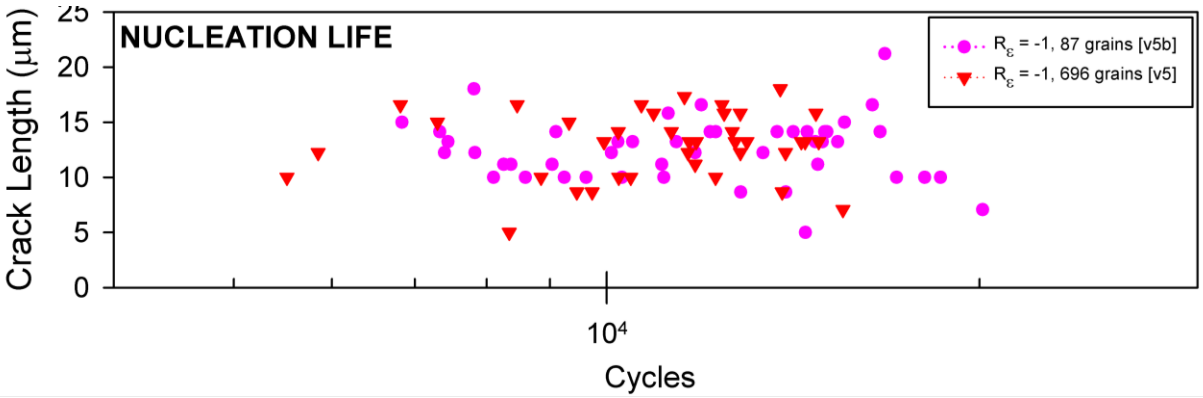

Figure 92. A comparison of crack nucleation in in meshes with varying volume under uniaxial loading, ε_a = 0.4%, R_ε = -1.

In Figure 23, nucleation lives for the mesh containing a larger number of grains are shifted slightly to the left of the nucleation lives of the mesh with a smaller volume. This

effect is caused by the higher probability of finding a favorably oriented grain in which to nucleate a crack in the mesh with the larger number of grains considered.

The magnitude of the effect is slight and suggests that for simulations randomly oriented grains, a computational volume encompassing approximately 100 grains is sufficient to approximate the spread in nucleation lives. Note that a much larger number of grains and microstructural instantiations would be needed to needed to properly evaluate the extreme value statistics associated with nucleation.

Note that these simulations were conducted using the G31 version of constitutive model, fatigue model calibration B, and the Stage I growth algorithm. While the results using these parameters may not match the results obtained using different versions of constitutive model and fatigue model quantitatively, they qualitatively capture the trends that arise due to modifications of the mesh configuration.

5.8: Mesh Refinement Effects

An additional mesh configuration was introduced to explore the effects of mesh refinement on the fatigue algorithms. This mesh configuration had a volume of $(50\ \mu m)^3$ and a total of 87 grains, with an element size of 2.5 μm. Both mesh configurations used a mean grain size of 14 μm and a band width of 5 μm. In this section, the mesh with a volume of $(50\ \mu m)^3$, 87 grains, and 5 μm elements introduced in the previous section is referred to as the coarse mesh, while the additional mesh with the same volume and number of grains, but with a 2.5 μm element size, is referred to as the refined mesh. Example instantiations of both the coarse and refined meshes are shown in Figure 93.

Figure 93. Coarse mesh with 5 μm elements (left) compared to a refined mesh with 2.5 μm elements. Both mesh configurations have the same volume and number of grains.

Figure 94 is a semi-log plot of crack length vs. cycles for uniaxial, fully reversed, tension-compression simulations conducted at a strain amplitude of 0.4% using the coarse and refined meshes. For this set of simulations, 35 instantiations of each mesh were considered and a total of 6 grains were allowed to crack. Results for the coarse mesh are plotted in magenta and results for the refined mesh are plotted in blue.

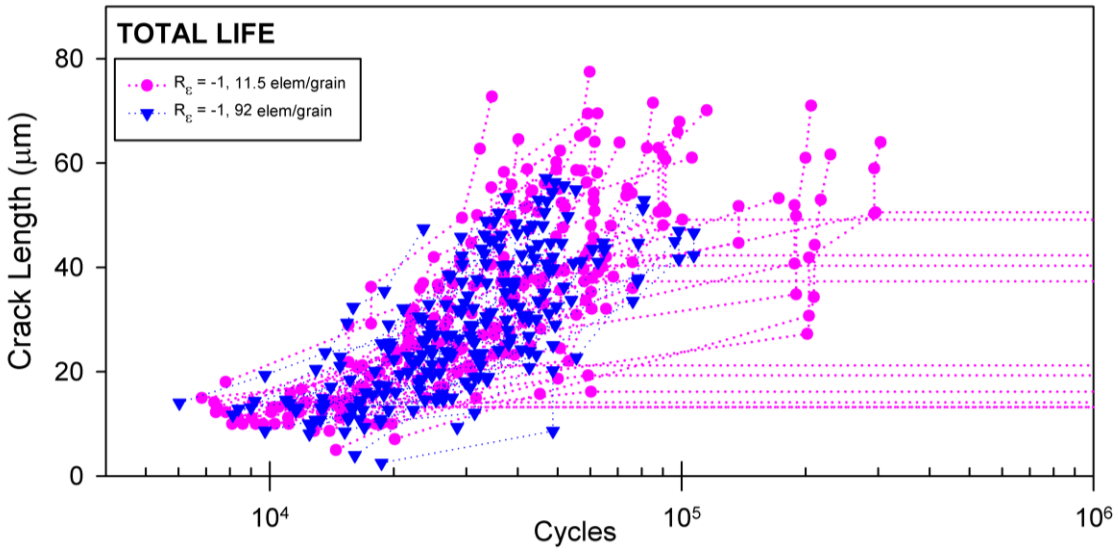

Figure 94. A comparison of crack growth in coarse and refined meshes under uniaxial loading, ε_a = 0.4%, R_ε = -1.

The largest difference in predicted crack growth between the coarse and refined mesh is the final crack length after cracking 6 grains. For the coarse mesh, most cracks have grown to approximately 70 μm in length by the end of the simulation. However, the refined meshes have only grown to a length of approximately 60 μm after cracking the same number of grains. Additionally, there is a sharp reduction in the number of run-outs predicted for the refined mesh, with none of the 35 simulations arresting, compared to 11 for the coarse mesh. The lack of run-outs observed for the refined mesh suggests that the run-outs observed for the coarse mesh simulations are entirely a product of the level of mesh refinement.

The total life comparison considered in Figure 94 can be further separated into the life to nucleate and grow the crack to the size of one grain (referred to as "nucleation life" in the context of the simulations), and subsequent propagation through the microstructure. A comparison of the predicted nucleation life and initial crack size is presented in Figure 95.

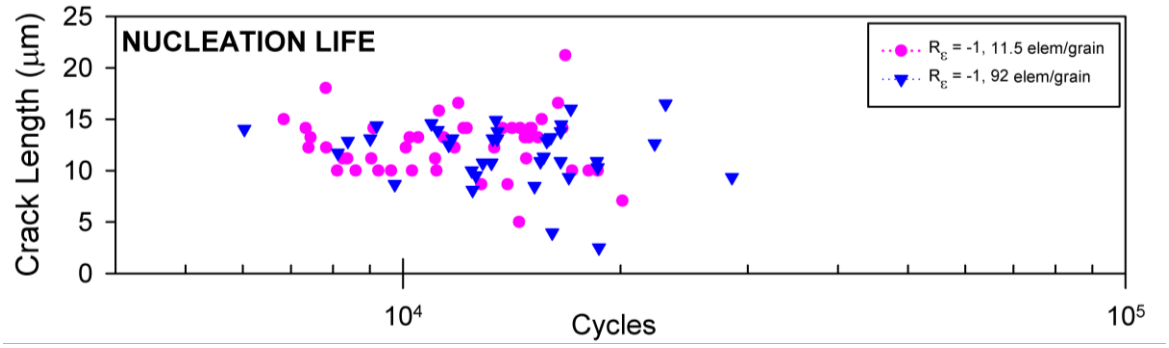

Figure 95. A comparison of predicted number of cycles and crack length after nucleating and growing through the first grain for coarse (magenta circles) and refined (blue triangles) meshes. Loading is uniaixal ε_a = 0.4% and R_ε = -1.

In the Figure we can see that overall the predicted nucleation lives are similar for both meshes. The more refined mesh appears to predict a slightly wider range of nucleation lives, although most of the predicted nucleation life values overlap. The predicted propagation lives for the coarse and refined meshes are plotted in Figure 96. To generate this plot, every crack considered in Figure 94 is assumed to nucleate at 10,000 cycles with a length of 5 µm, and growth through the 5 subsequent grains to crack is plotted.

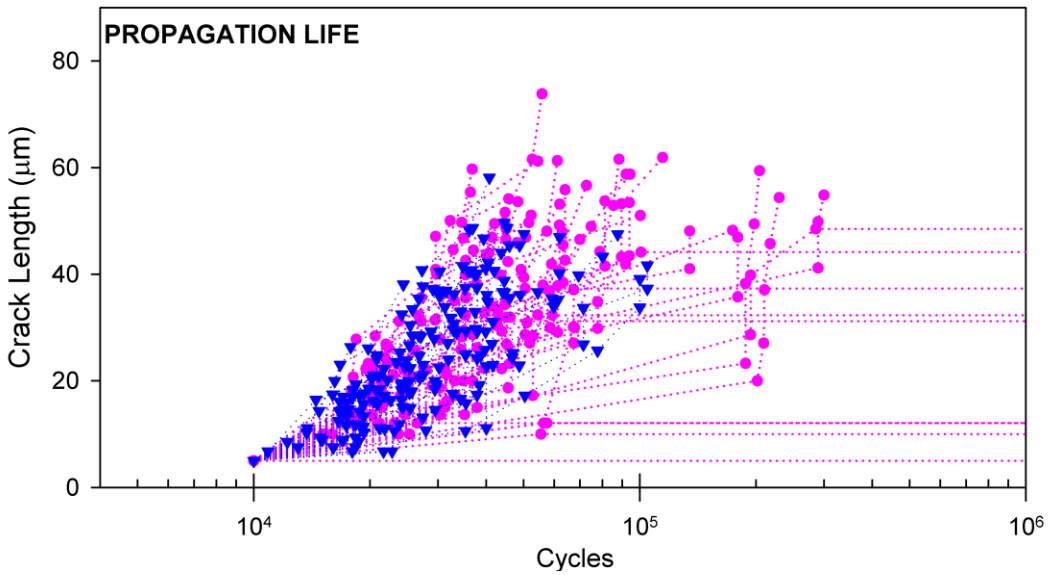

Figure 96. A comparison of crack propagation in uniaxially loaded coarse and refined meshes, ε_a = 0.4%, R_ε = -1.

For both mesh sizes, crack growth rates appear to be similar with much of the crack propagation data overlapping. However, cracks in the more refined mesh tend to propagate in smaller increments, i.e. cracking smaller bands within a grain. This results in a shorter overall crack length after cracking six grains despite the average crack growth rate being slightly higher than that of the coarse mesh.

To explain why cracks propagate in smaller increments in the refined mesh than in the coarse mesh (even though both meshes have the same grain size and nominal band

width) requires examination of the distribution of band lengths within the two respective meshes. The length of each band is calculated according to

$$\text{Band length} = \left(\text{Mesh Size}\right)\sqrt{\frac{\text{Mesh Size}}{\text{Band Width}} \times \#\text{ of Elements in Band}}\,. \qquad (62)$$

Figure 97 is a histogram that compares the length of all bands within 5 coarse meshes and 5 refined meshes. To create the histogram band lengths were binned in 2 μm groups. Due to the discrete nature of the possible band lengths, finer binning produces gaps in the histogram which makes direct comparison between the two meshes more difficult. The 5 refined meshes had a total of 6690 bands and the coarse mesh had a total of 5484 bands, approximately 82% of the quantity of bands in the refined meshes.

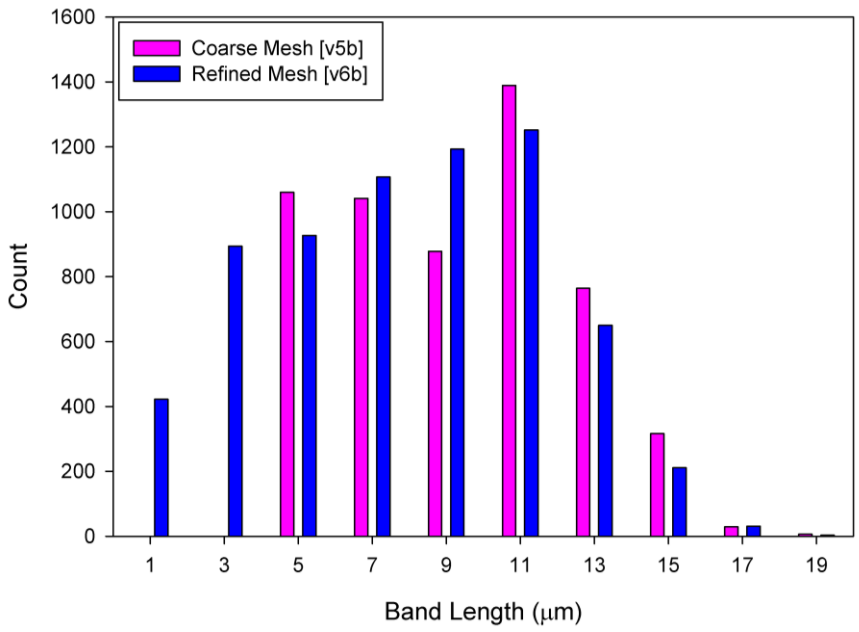

Figure 97. Distribution of band lengths within the coarse mesh and refined mesh. For both meshes the mean grain diameter is 14 μm and the band width is 5 μm. Loading is uniaxial with ε_a = 0.4% and R_ε = -1.

In the Figure we can see that while both meshes have a nominal band width of 5 μm, the refined mesh (with 2.5 μm element size) has a significant number of bands with a length smaller than 5 μm, which is the smallest possible band size in the coarse mesh. The average band length is 9.1 μm in the coarse mesh and 7.9 μm in the refined mesh. It is this difference in average band length that likely accounts for the majority of the difference in total length after cracking 6 grains.

To further investigate mesh refinement effects, the FIP value of the cracked band in the i^{th} grain to crack, for both coarse and refined meshes, is plotted in Figure 98. The FIP values in the plot are the average value obtained across 35 simulations, each considering a distinct microstructural instantiation.

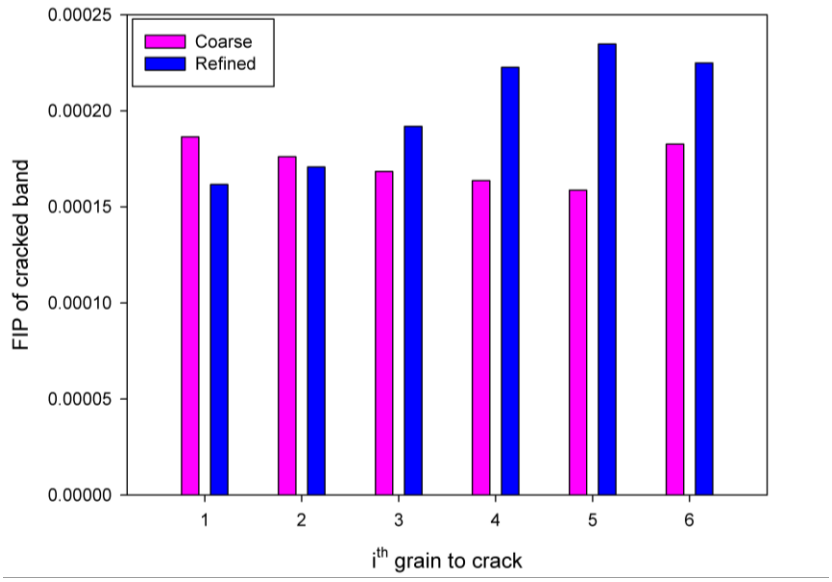

Figure 98. A comparison of the average FIP values of the i^{th} cracked bands in coarse and refined meshes, $\varepsilon_a = 0.4\%$, $R_\varepsilon = -1$.

In the nucleant grain, the average FIP in the cracked band is higher for the coarse mesh, resulting in the shorter nucleation lives observed in Figure 95. In the 3^{rd} to 6^{th} grains to

crack, however, the FIP of the cracked band is higher for the refined mesh. This could possibly be due to the more refined mesh more accurately capturing the stress and strain intensification effects of the crack, and explains the slightly faster rate of crack propagation for the refined mesh observed in Figure 96.

Overall, the difference in predicted fatigue lives between simulations conducted with the coarse and refined meshes is fairly insignificant, aside from the increased rate of run-outs observed in the with the coarser meshes, which suggests that at this loading amplitude any run-outs are a primarily a result of the mesh refinement. This is an important finding, as the coarse meshes have almost an order of magnitude fewer elements per grain than do the refined meshes. Therefore, significant computational savings can be realized by employing a coarser mesh with only small losses in accuracy, but at the cost of increased run-outs. These run-outs are undesirable because they result in early termination of the simulation, consuming computational resources while producing little valuable data. The ideal mesh refinement would be coarse enough significantly reduce the computational cost of each simulation, but refined enough to prevent a large number of run-outs from occurring. More simulations would be needed to assess the optimal level of mesh refinement, but the simulations presented in this section suggest it is bounded between 92 and 11 average elements per grain.

5.9 Band Size Effects

The width of the crystallographic bands used as FIP^{α} averaging volumes and as the crack propagation path in the Stage I algorithm corresponds physically to the width of PSBs observed to form when the material is cyclically loaded. As noted previously, for planar slip materials such as RR1000 these persistent slip bands are well defined, but for Al

7075-T6, which exhibits more homogeneous deformation, the band width parameter has a less direct physical analog. There are however, practical considerations when selecting the width of the bands. For purposes of uniformity in actual thickness between the bands (after elements have been assigned based on the location of their centroids), the band width should be a multiple of the element size rather than an arbitrary length. The band width should also not be smaller than the element size to avoid the formation of bands with disconnected elements. For the microstructure considered in this thesis (with equiaxed 14 μm grains), these band width requirements, coupled with the need to sample a sufficient number of grains while retaining computational feasibility, lead to typical band widths equal to either one or two elements in thickness. For the meshes used to generate the results presented in Sections 5.4 through 5.6 (see Figure 46), this corresponds to a band width of either 2.5 μm or 5.0 μm. A 5.0 μm band width was employed in the simulations presented in Sections 5.4 through 5.6, but the use of a 2.5 μm band width would have been equally valid in terms of physical justification. To investigate the effect of choosing a band width of either one or two elements in thickness on the predicted fatigue lives, two sets of microstructural instantiations were created. The first set of 10 instantiations corresponded exactly to the mesh geometry used to generate the results in Sections 5.4 through 5.6, with 60 μm side lengths, 2.5 μm cubic elements, 14 μm grains, and 5.0 μm band widths. The second set of 10 instantiations differed only in the width of the bands, which was taken to be 2.5 μm. A comparison of the resultant bands in an example grain of approximately the same volume between the two instantiations is shown in Figure 99.

Figure 99. A comparison of a grain with a band width of two elements in thickness (left) compared to a grain of similar size but with a band width equal to a single element in thickness (right). Each band of elements is represented by a separate color.

Fatigue simulations were performed on these two sets of microstructural instantiations with different band widths in order to assess the effect of band width on the resultant fatigue lives. Loading was uniaxial at an applied strain amplitude of 0.4%, and $R_\varepsilon = -1$. Lives were evaluated using the Stage I algorithm, and a total of 8 grains were allowed to crack before the simulation was terminated. The results are shown in Figure 100 on a linear scale to emphasize the similarity between the data sets.

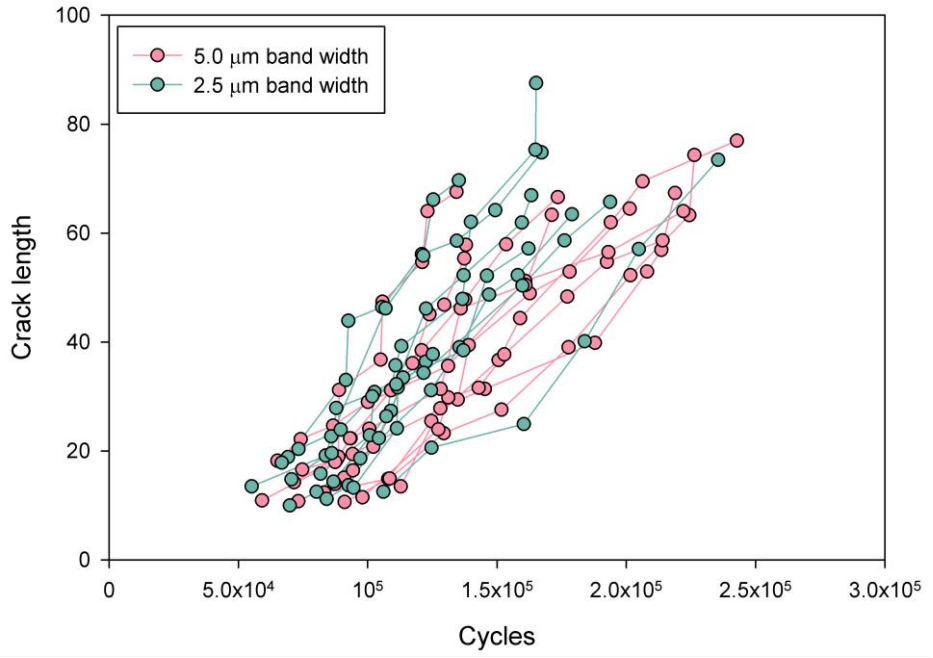

Figure 100. Comparison of results obtained using microstructural instantiations that differ only in the size of the band width. Loading is fully reversed, uniaxial tension-compression conducted at ε_a = 0.4%.

The results in Figure 100 illustrate that the effect of band width on the fatigue lives predicted is fairly small, as no discernable trend is easily visible and most of the data for the two band widths considered are overlapping. Comparing the average number of cycles to grow a crack to 60 μm for the two cases there is a slight increase lives when employing a 5.0 μm band width, with an average life to 60 μm crack length of approximately 182,000 cycles, compared to 161,000 cycles for the 2.5 5.0 μm band width cases. This represents only 13% increase in predicted fatigue lives when employing bands encompassing twice the averaging volume, and illustrates the relative insensitivity of the fatigue algorithms to the choice of band width within the limits outlined in the introduction to this section.

5.10 Application of Stage II Algorithm to Coarse Meshes

The results presented in Sections 5.7 through 5.9 considered the insensitivity of the stage I fatigue algorithm to changes in mesh geometry. The data presented in those Sections lead to the conclusion that the stage I fatigue crack growth algorithm is fairly insensitive to changes in mesh geometry up to the limits discussed in the respective sections. In this Section, data will be presented for simulations conducted with the stage II algorithm, comparing the results obtained for the refined meshes used to generate the bulk of the results presented in this chapter to results obtained using a much smaller, coarser mesh originally developed for debugging purposes.

The refined mesh that was employed to generate the data presented in Sections 5.4 through 5.6 consisted of 150 Grains with a 14 μm average grain size. The refined mesh had 60 μm sides and 2.5 μm elements, for a total of 13,824 elements. Fatigue simulations conducted using this mesh until 8 grains had cracked took in excess of 900 CPU hours to complete. In contrast, the coarse mesh consisted of 30 Grains with a 14 μm average grain size. This coarse mesh had 35 μm sides and 5.0 μm elements, for a total of 343 elements. Fatigue simulations conducted using this mesh until 8 grains had cracked took approximately 2 CPU hours to complete using the coarse mesh, a reduction in computational resources by a factor of 450 compared to the refined mesh. Two example microstructural instantiations, one representing the refined mesh and one representing the coarse mesh are presented in Figure 101.

Figure 101. A comparison of the refined (left) and coarse (right) meshes used to assess the mesh dependence of the Stage II algorithm.

Four loading conditions were considered for the set of comparison simulations, at applied strain amplitudes of 0.3% and 0.4%, with applied strain ratios (R_ε) of -1 and 0.5. Loading was uniaxial in all cases, and simulations were conducted until 8 grains cracked.

The results for the refined mesh loaded with applied strain amplitudes of 0.3% and 0.4% under fully reversed, uniaxial conditions are reproduced from Section 5.4.1 in Figure 102. Ten microstructural instantiations were considered at each loading condition considered in Figure 102.

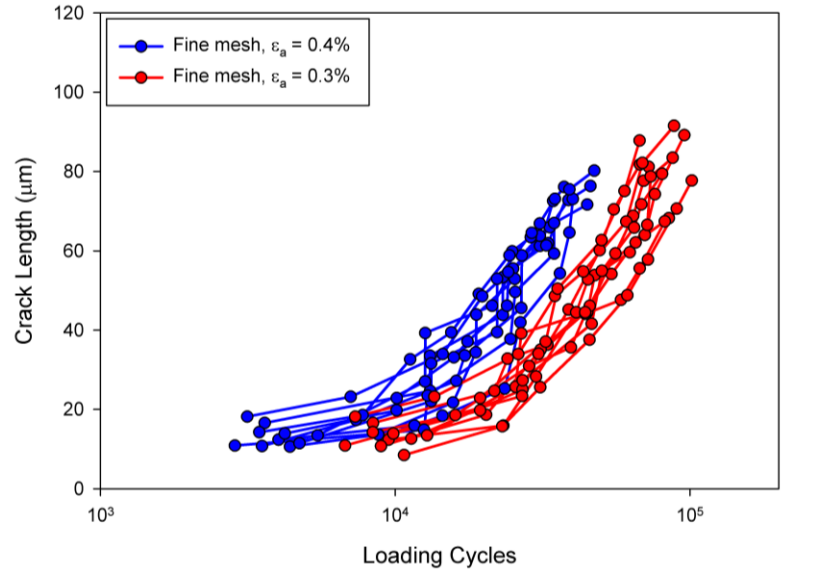

Figure 102. Crack growth in 10 microstructural instantiations of the refined mesh under uniaxial, fully reversed loading at applied strain amplitudes of ε_a= 0.3% and 0.4%.

Results from simulations conducted using the same loading conditions of 0.3% and 0.4% applied strain amplitude with R_ε = -1 on 50 microstructural instantiations of the coarse mesh are shown in Figure 103.

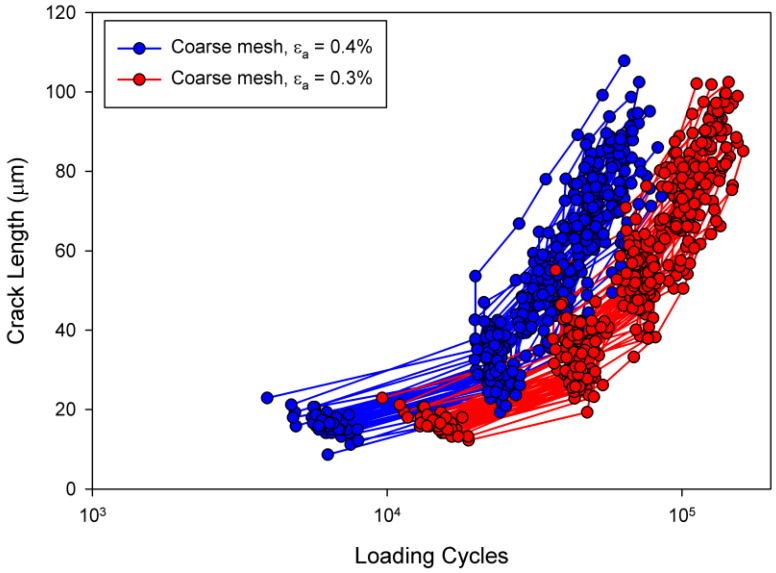

Figure 103. Crack growth in 50 microstructural instantiations of the coarse mesh under uniaxial, fully reversed loading at applied strain amplitudes of ε_a= 0.3% and 0.4%.

Through comparison of Figure 102 and Figure 103, which are plotted using the same scale and axis limits, it is clear that the vastly different mesh geometries predict similar fatigue lives and capture the same trends when subjected to the same loading conditions. Direct comparisons results obtained using the two different mesh geometries under fully reversed, uniaxial loading at strain amplitudes of 0.3% and 0.4% are presented in Figure 105 and Figure 104, respectively, with results from the refined mesh geometry plotted in red or blue, and results from the coarse mesh plotted in black.

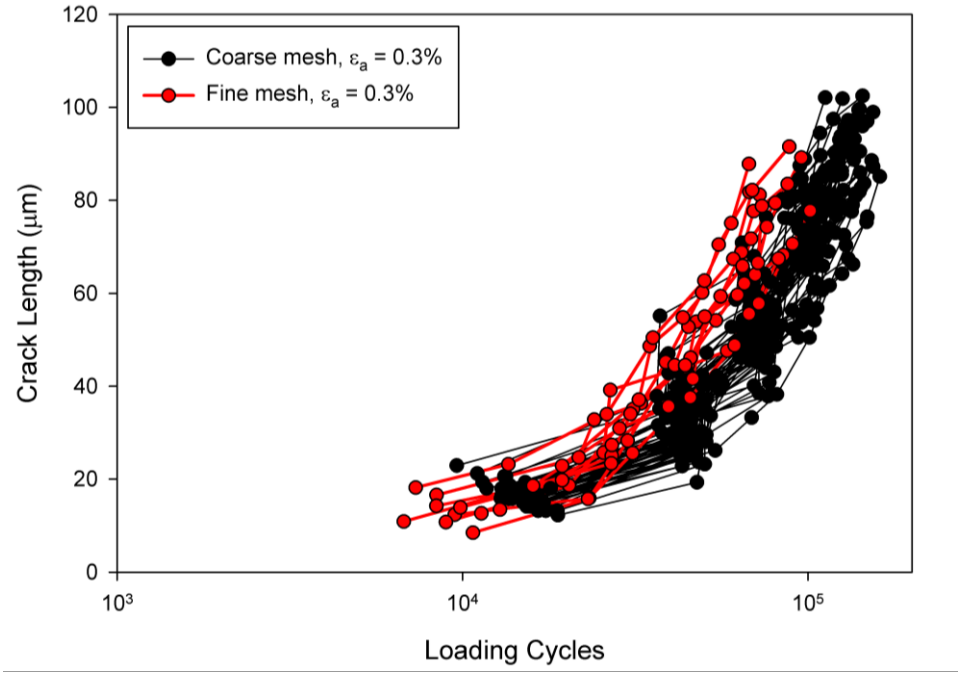

Figure 104. Comparison of crack growth in 50 microstructural instantiations of the coarse mesh (plotted in black) and 10 instantiations of the refined mesh (plotted in red) loaded at ε_a = 0.3% and R_ε = -1.

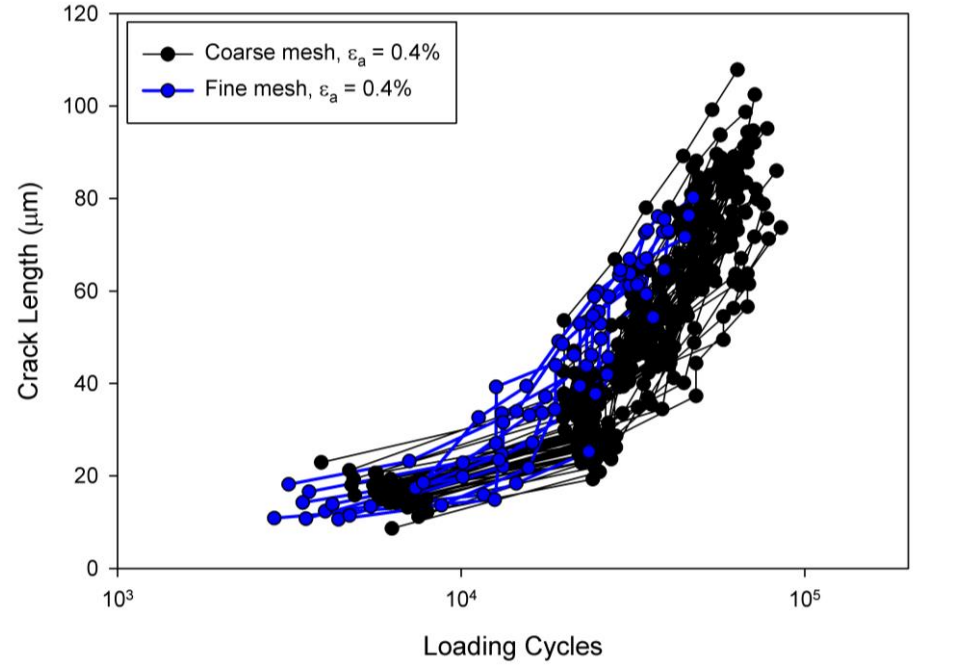

Figure 105. Comparison of crack growth in 50 microstructural instantiations of the coarse mesh (plotted in black) and 10 instantiations of the refined mesh (plotted in blue) loaded at ε_a = 0.4% and R_ε = -1.

The data plotted in Figure 105 and Figure 104 show that on average the coarse mesh geometries predict longer fatigue lives than the more refined meshes under identical loading conditions. Additionally, the coarse mesh geometries predict a longer crack length after cracking 8 grains than in the simulations conducted with the more refined mesh geometry. However, there is a significant overlap between the results predicted using the two mesh geometries.

The results also show clear differences in the nucleation regime, with shorter nucleation lives predicted by the refined mesh geometry. As discussed in Section 5.7, this effect can be partly explained by the higher probability of finding a favorable oriented gain in the more refined mesh geometry which encompasses a larger simulated volume, and thus samples more grains. However, this effect is offset by the increased number of microstructural instantiations considered for the coarse mesh geometry: although each refined mesh instantiation sampled 5 times as many grains as each coarse mesh instantiation (150 vs 30), simulations were conducted on 5 times as many coarse mesh microstructural instantiations as refined mesh instantiations (50 coarse instantiations vs 10 refined instantiations). Thus, the consistent difference in observed nucleation lives between the two mesh geometries is more probably due to the larger effect of the imposed boundary conditions on the smaller mesh.

Additional simulations were performed on the coarse mesh geometry to assess whether this much smaller geometry could capture the observed detriment in fatigue lives when cycled with an imposed mean stress/strain. Again, the applied loading conditions were identical to those presented in Section 5.4.1, with cyclic uniaxial loading at applied strain amplitudes of 0.3% and 0.4% at strain ratio (R_ε) of 0.5 for 20 computational

loading cycles. The results from simulations conduced at a strain amplitude of 0.3% are plotted in Figure 106, with the fully reversed data in red and the cases with an imposed mean strain in white and black.

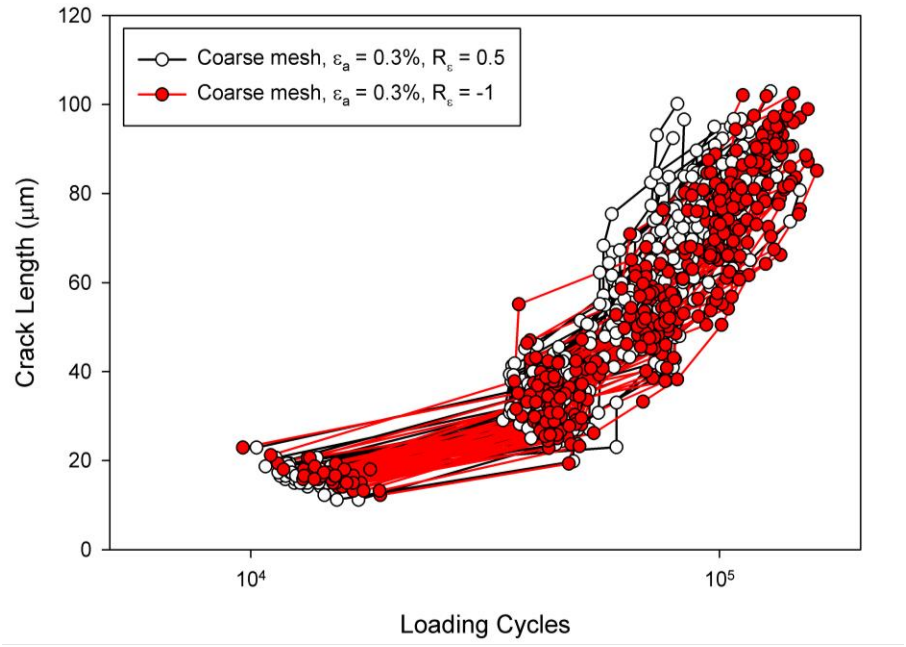

Figure 106. Crack growth in 50 microstructural instantiations of the coarse mesh under uniaxial loading at an applied strain amplitude of ε_a = 0.3% and with R_ε = -1 or 0.5.

A slight detriment to the predicted fatigue lives when loaded with R_ε = 0.5 is observed in both the nucleation and propagation regimes shown in Figure 106, but most of the data overlap between the two cases. To quantitatively assess the impact of the mean stress we can compare the shortest life to reach a length of 90 μm, and the average life to a crack length of 90 μm for both the R_ε = -1 and R_ε = 0.5 cases. The decrease in average life to a 90 μm crack length was 14%, and the decrease in shortest life the same crack length was 15%.

In comparison, Figure 107 is a plot of the 0.4% strain amplitude simulation data, with the fully reversed data in blue and the R_ε = 0.5 data black and white.

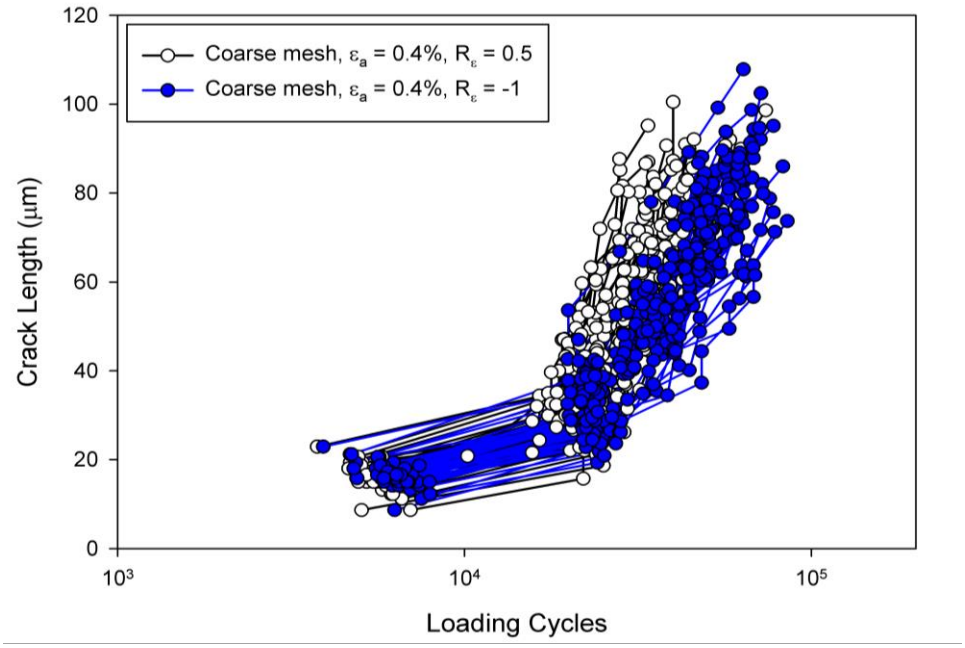

Figure 107. Crack growth in 50 microstructural instantiations of the coarse mesh under uniaxial loading at an applied strain amplitude of ε_a = 0.4% and with R_ε = -1 or 0.5.

The detriment to fatigue lives due to the presence of a mean strain/stress is more pronounced at this strain amplitude, with a decrease in the average life to a 90 μm crack length of 24%, and a decrease in the shortest life to the same length of 34%.

Results from the simulations conducted with the coarse meshes compared to experimental results obtained by Zhao and Jiang [108] in Figure 108. Again, it is important to note that the life data of Zhao and Jaing correspond to macroscopic specimen separation (failure), while the simulated results consider life to grow the crack to a length of 90 μm. Additionally, the coarse meshes predict longer lives than the refined meshes under equivalent loading conditions, and because the parameters were calibrated with a refined mesh, this skews the coarse mesh results to the right (towards longer lives). However, the purpose of Figure 108 is to illustrate the relative difference between the

experimental and simulated decrease in fatigue lives in response to a mean stress/strain, rather than an exact numerical life prediction.

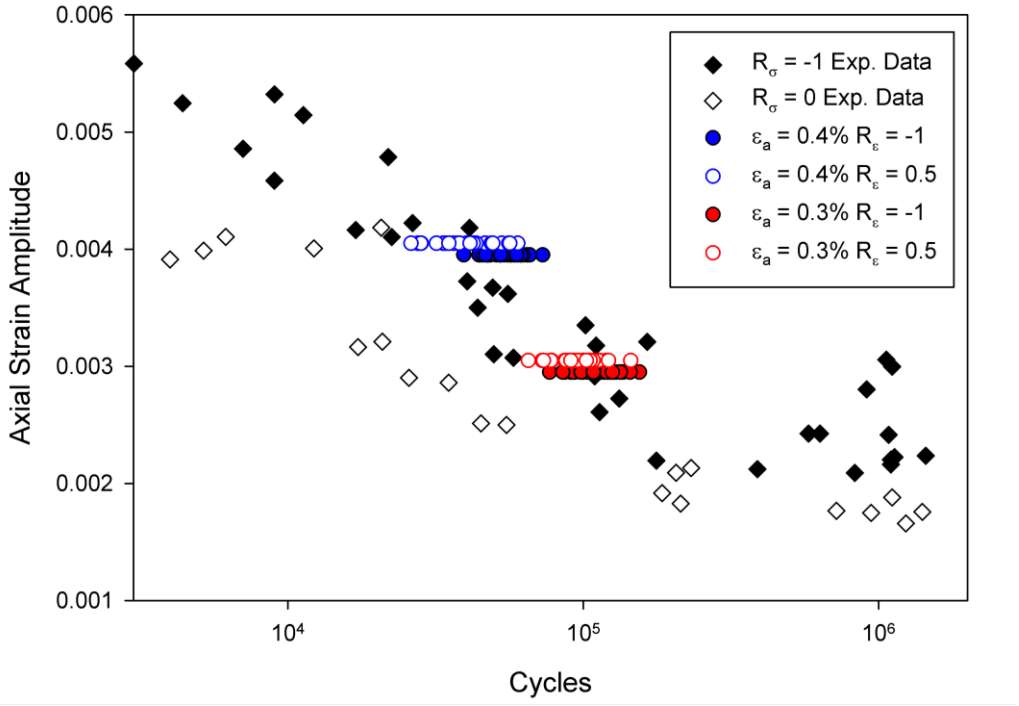

Figure 108. Comparison of results from stage II fatigue simulations conducted using the coarse mesh geometry and uniaxial experimental data from [108].

Note that the trends observed in Figure 108 qualitatively match those seen in Figure 65 for refined meshes subjected to the same loading conditions. For simulations conducted with both levels of mesh refinement there is an observable reduction in the predicted fatigue lives due to the presence of a mean stress during cycling, an effect which is more pronounced for the 0.4% applied strain amplitude cases than for the 0.3% applied amplitude cases. The reductions in average life to reach a prescribed crack length are similar for both the coarse and refined meshes, with the 0.3% applied strain amplitude cases undergoing a reduction of 14% and 8%, respectively, and the .4% applied strain

amplitude cases undergoing a reduction of 24% for the coarse meshes and 39% for the more refined mesh geometries.

The ability of the coarse mesh geometries to predict similar fatigue lives and the same observed trends as simulations conducted with highly refined mesh geometries is particularly encouraging because of the massive reduction in computational cost of the simulations conducted with the smaller, coarser microstructural volumes. However, at this level of mesh coarseness, boundary effects are certainty present because the crack represents a significant fraction of the total mesh volume. For this reason, the level of mesh coarseness studied in this Section (approximately 10 elements per grain) probably represents the lower limit of mesh geometry that will still produce acceptable results.

5.11: Conclusions

This chapter presented results obtained using the mesoscale fatigue algorithm to model nucleation and MSC growth in Al 7075-T6. After discussing calibration of the fatigue constants using experimental data, numerous scenarios were investigated using the model, including the fatigue behavior under uniaxial and shear loading at a range of applied strain amplitudes, the effect of constitutive model on the predicted fatigue lives, and differences between the Stage I and Stage II algorithms. The key findings of this chapter are summarized below.

- The OW44 constitutive model coupled with the Stage II fatigue crack growth algorithm shows good correlation with experimental data and trends under uniaxial and shear loading. The model correctly predicts the detrimental effect of mean stress on the fatigue life.

- The constitutive model has a significant impact the fatigue life predictions and FIP distributions, even for models that were calibrated to the same macroscopic, fully-reversed cyclic loading data and are based on the same flow rule. The effect of the constitutive model on the predicted fatigue lives was found to be larger than the differences between uniaxial and shear loading, or between loading with different R_ε values. Only loading at different applied strain amplitudes was found to have the same degree of impact on the fatigue lives.
- The Stage II algorithm predicts faster growth rates than the Stage I algorithm, but the degree of scatter in predicted fatigue lives is reduced. This is partly attributed to the larger FIP averaging domain of the Stage II model, which considers the driving force in two bands rather than only one for the Stage I model. This effectively doubles the FIP averaging volume, and thus reduces variability accordingly.
- Mesh dependency is significantly reduced by the averaging of FIPs over the band volume. Reducing the element size by a factor of 2 had only a small impact on the predicted fatigue lives, most of which was due to the change in the distribution of band lengths. Similarly, employing a much smaller simulated volume had only a small effect. This is an important result, as computational evaluation of the fatigue algorithms using the smaller volume coarse meshes is significantly faster than evaluation of the more refined mesh of the same volume. Therefore, these coarse meshes can be employed in situations where a large number of simulations are needed for statistical analysis without significant loss of accuracy.

CHAPTER 6: CONCLUSIONS AND DIRECTIONS FOR FUTURE WORK

6.1: Summary

This work modeled the cyclic stress-strain response of polycrystalline Al 7075-T6 using a crystal plasticity based constitutive relation, which was then applied to model the nucleation and early growth of 3D microstructurally small fatigue cracks through several grains. The response of the model under asymmetric cyclic loading was evaluated and it was found that the model predicted an unrealistically high magnitude of plastic ratcheting and associated mean stress relaxation. Such a high degree of ratcheting is not experimentally observed for Al 7075-T6 (when cycled at room temperature at the applied strain ranges considered in this work) and is an artifact of the simple Armstrong-Frederick back stress evolution. The over-prediction of the ratcheting response by Armstrong-Frederick back stress hardening laws has been observed by many researchers in traditional J_2 plasticity, but there is no research of which this author is aware regarding similar findings for the Armstrong-Frederick hardening laws at the slip system level in crystal plasticity. It is often tacitly assumed that the intergranular interactions are somehow responsible for modifying the polycrystalline response to account for proper description of ratchetting, but this does not appear to be the case for Al 7075-T6, characterized by high symmetry fcc structure and ability to cross slip. A modification to the back stress evolution equation was implemented, based on the work of Ohno and Wang [85] and a polycrystal macroscopic model proposed by McDowell [86]. This is the first time such a back stress hardening law has been employed to model the back stress

evolution at the individual slip system level in a crystal plasticity model. An additional model with Ohno-Wang type back stress hardening and an evolving drag stress was also introduced. All versions of the constitutive model shared a common flow rule and differed only in the calibration and form of back stress and drag stress evolution equations. All models were calibrated to the same experimental data, and the cyclic stress-strain curves at 1% and 1.8% strain amplitude were nearly identical. However, significant differences were observed between the models at applied strain amplitudes below the point of macroscopic yielding (<0.6%). Additionally, the models showed very different responses to cyclic loading with an imposed mean stress/strain. Overall, the model employing the Ohno-Wang back stress hardening law and a constant drag stress was best able to fit fully reversed cyclic stress-strain data and match mean stress relaxation data at the applied strain amplitudes of interest. Later in the thesis, it is shown that this model properly captures trends of mean stress dependence in MSC fatigue crack growth.

An enhanced algorithm for modeling MSC crack growth was introduced, based on a format originally developed by Castelluccio [2], and intended originally for planar slip alloys and Stage I crack formation and early growth. The enhanced Stage II fatigue algorithm captures the driving force on multiple slip systems and allows for crack propagation along arbitrary planes that are not defined before the simulations, but are instead determined by the FIP fields within a grain. Such a model is critical for simulating the growth of microstructurally small cracks in alloys with an early transition to Stage II growth, such as Al alloys. The fatigue model was first implemented using the computational framework established by Castelluccio, who developed the algorithms

within the Abaqus UEXTERNALDB [4] subroutine. This framework was simplified significantly by shifting of the implementation of the fatigue algorithms from the UEXTERNALDB into another program written in Python [105].

The fatigue model was then applied to Al 7075-T6 and simulations were conducted under a range of loading conditions. The results of the simulations for polycrystalline microstructure instantiations loaded uniaxially and in shear were in good agreement with experimental results. Additionally, the model correctly captured the detrimental effects of mean stress on the fatigue life.

Results from simulations that employed different versions of the constitutive model were then compared. The difference in predicted fatigue lives between the three versions of the constitutive models was found to be substantial, highlighting the crucial role of appropriate physically-based constitutive laws in these 3D MSC growth algorithms.

Results were obtained using the Stage I and Stage II algorithms to model the same microstructure instantiations and identical loading conditions to compare these algorithms. As expected, the Stage II algorithm was observed to predict higher rates of crack propagation under the same loading, because the model accounts for the diving force on multiple slip systems. The Stage II algorithm also showed a reduced degree of variability from the Stage I algorithm, which is likely a result of considering a FIP averaging domain of roughly twice the volume.

The effects of differences in mesh configuration on the predicted fatigue lives were also examined and it was found that overall the impact of such changes is small. This is encouraging for applications that require a large number of simulations, such as

the evaluation of the extreme value statistics on surrogate driving force measures associated with fatigue, because smaller volumes with coarse meshing have significantly reduced computational requirements.

6.2: Directions for Future Research

With the Stage II fatigue model in place it is now possible to quantitatively study the factors that promote either Stage I or Stage II growth in this alloy. The nature of MSC growth in Al 7075-T6 is a hotly debated issue in the literature, and a model that incorporates the underlying physics of the problem could be instrumental in gaining a deeper understanding of what controls such behavior.

Now that the fatigue model and constitutive model have both been shown to correlate well with experimental data, it is possible to employ the models to explore concepts that would otherwise require prohibitively numerous experiments. Follow-on work is currently underway to explore the gamma plane proposed by Brown and Miller [10] using the models developed in this Thesis to predict the propagation of MSC cracks under a wide range of multiaxial loading conditions.

While developing a 3D MSC growth framework for one specific material has certainly has value, the model is of little use outside of that specific application unless it can be quickly adapted to a new material system and associated constitutive model. Thus, any fatigue model that can be applied to existing constitutive models easily and without major modification to the constitutive model itself will have a greater impact on future research and will be more likely to be employed. With the implementation of the fatigue algorithms within the Python based external program, the fatigue model and constitutive relations can be developed and maintained separately. With some small additions to the

Python code, the necessary modifications to the constitutive model needed for compatibility with the MSC formation and growth framework can be reduced to a bare minimum. This would allow the multistage MSC formation and early growth framework to be quickly adapted to a new constitutive model.

There are a few aspects of the MSC formation and growth framework for which improvement could be made. First is the verification of the modeling assumptions, primarily the fitting of the FIP to ΔCTD relation. This work fit the FIP to match experimental crack growth rate data, while the previous work of Castelluccio [2] employed simulations of single crystals with explicitly modeled cracks in order to estimate the FIP to ΔCTD relation. Now that there is a higher degree of confidence in the constitutive model for Al 7075-T6, the simulations of cracked single crystals should be performed in order to verify the values of the parameters employed in this work and the linear variation of ΔCTD with FIP observed by Castelluccio. Second, a methodology should be developed to evaluate the twist and tilt angles between the crack and candidate bands for propagation (which can both be non-crystallographic during Stage II growth), accounting for the increase in driving force that would be needed to propagate a crack across grain boundaries of high twist/tilt compared to the boundary of between more closely aligned planes. Third, while results under uniaxial loading conditions are in good agreement with available experimental data, the predicted MSC fatigue lives under shear loading are conservative by approximately an order of magnitude. As discussed in Chapter 5, the incorporation of an additional incubation term into the equation governing the life of the nucleant grain offers a promising pathway to address this discrepancy with experimental results.

APPENDIX A

Functionality of the UMAT, UEXTERNALDB, and Python sub-program

The UEXTERNALDB and Python sub-program handle the large majority tasks associated with the fatigue algorithms, but the UMAT does contain critical sections of code that allow the fatigue algorithms to function. This Appendix is focused on explaining the details of operation and interaction of the UMAT, UEXTERNALDB, and Python sub-program in a complete and concise way. Several flowchart-type diagrams have been reproduced from earlier Chapters in enhanced levels of detail to explain the intent behind some aspects of the code.

The implementation of these user subroutines and external programs is illustrated in Figure 109. The first section of user written code accessed by Abaqus at the start of a simulation is the UEXTERNALDB. Abaqus passes in an integer valued variable named "LOP" into the UEXTERNALDB each time it is called to indicate from where in the analysis process the UEXTERNALDB is being called. For example, LOP = 0 corresponds to the very first call of the UEXTERNALDB, before any loading has occurred. This call is only performed once. After this call to the UEXTERNALDB, the application of loading begins in the form of steps. These steps are divided smaller sub-steps called increments. For each loading increment, the UEXTERNALDB is called at least twice: before the increment (LOP = 1) and after the increment has converged (LOP = 2). In between these two calls of the UEXTERNALDB, the UMAT is called to return the stress tensor and Jacobian for each element. During the process of calculating these quantities, the UMAT may request sub-division of the current increment by setting PNEWDT to a value less than 1. In this case, the current increment is abandoned and

restarted. Additionally, if convergence of the global FE equations is not obtained by Abaqus, it may restart the increment as well. In both of these cases, it is critical to note two things:

1) The UMAT will have written data to the COMMONBLOCK for non-converging increments, so this data is probably erroneous.

2) The UEXTERNALDB will be called again for the same increment number with LOP = 1 when the increment is restated.

Therefore it is paramount that the data stored in the COMMONBLOCK is not read until the increment has converged, which corresponds to LOP = 2. After the last converged increment of a step, the Python program is run if either Eval_nuc or Eval_MSC are true. This process repeats until the simulation reaches the end, or the crack arrests and is terminated by the UMAT.

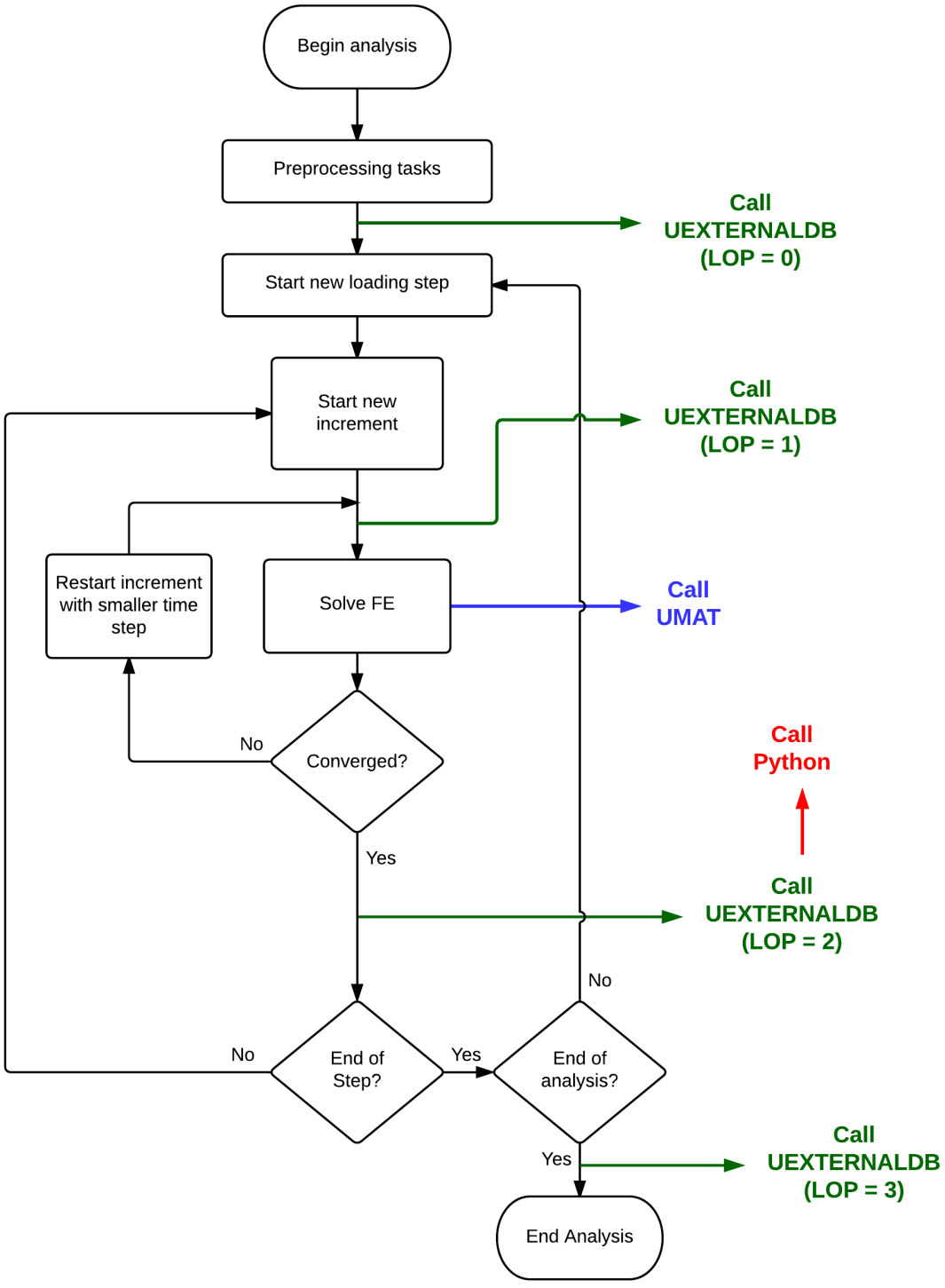

Figure 109. Diagram of the relation between the UMAT, UEXTERNALDB, and Python sub-program within the ABAQUS environment.

UMAT

The tasks relevant to the fatigue calculation executed by the UMAT are:

1) Degradation of the elastic stiffness tensor

1a) Tracking current damage value and increasing/decreasing based on the stress normal to the crack plane

1b) Calculating stress normal to the crack plane

2) Calculation and storage of quantities for FIP calculation

2a) Calculate and store current plastic shear strains for each element and slip system

2b) Calculate and store current normal stresses for each element and slip system

The flow of the UMAT is illustrated in Figure 110, with focus on only the tasks carried out to implement the fatigue algorithms. The first task the UMAT performs (related directly to the fatigue algorithms) is checking for crack arrest, stored as a logical variable named "crack_arrested" in the COMMONBLOCK. If "crack_arrested" is true, the UMAT calls the Abaqus subroutine XIT to terminate the simulation. Note that this task would more logically be performed by the UEXTERNALDB, but Abaqus does not allow XIT to be called from that particular user subroutine. Next, the UMAT calculates the damaged elastic stiffness tensor. If the element is not in the crack and thus undamaged, this calculation yields the standard stiffness tensor. Then, if the element is in the crack (damaged), the value of the damage is increased or decreased depending on if the plane of the crack is in tension or compression, respectively. The UMAT then performs its primary task of calculating the stress tensor and Jacobian for the element. Once this is complete, updated arrays for the fatigue calculations are stored in either the COMMONBLOCK or as SDVs to be read in the next time the UMAT is called for that

particular element. Note that while both the UMAT and UEXTERNALDB are executed in the Fortran 95 environment, they are written in fixed from format and the majority of the syntax corresponds to that of Fortran 77.

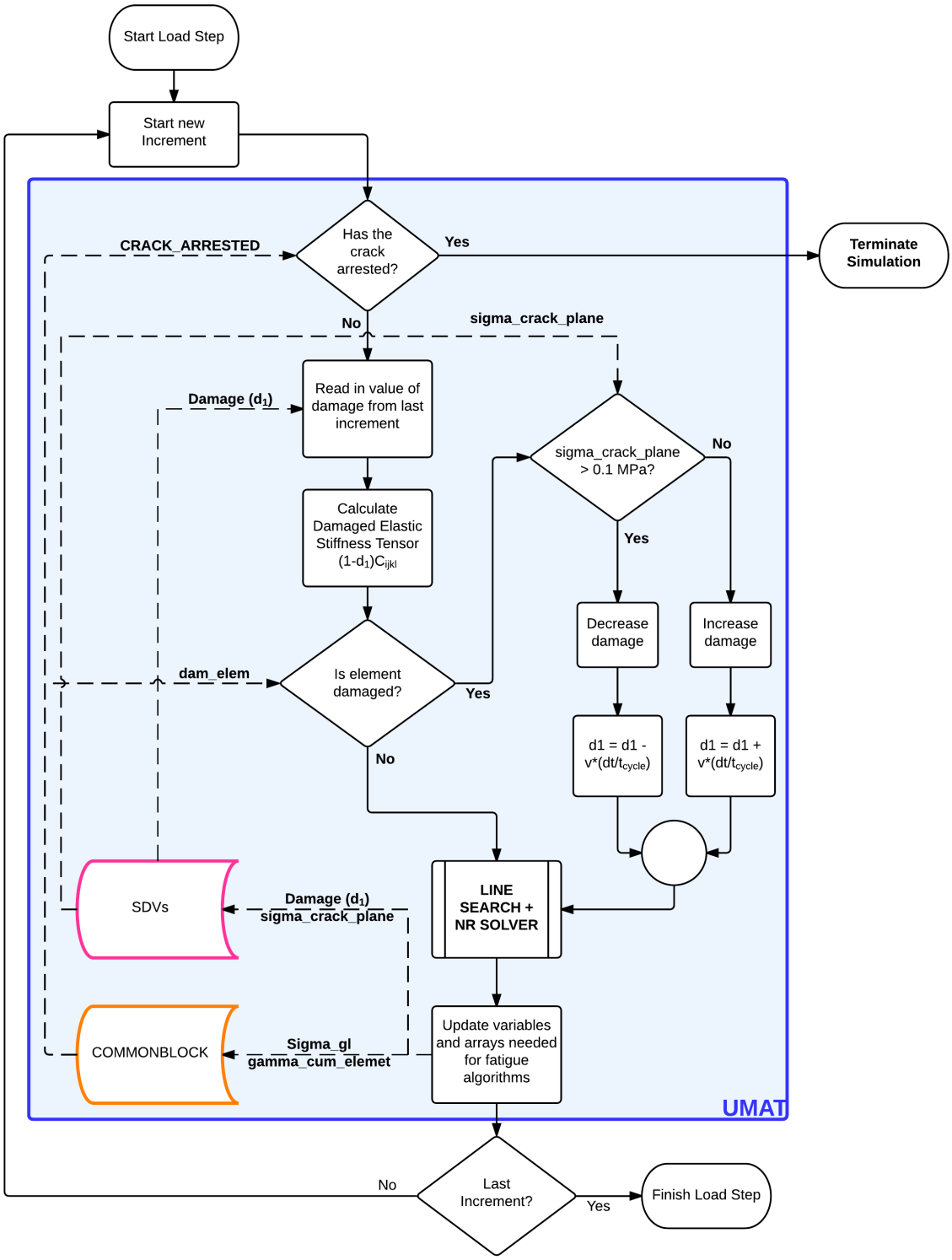

Figure 110. Flow of UMAT containing tasks that are carried out in support of the fatigue algorithms.

UEXTERNALDB

In previous implementations, the UEXTERNALDB performed the majority of the fatigue related calculations. However, the implementation employed in this thesis has shifted away from this and transitioned the fatigue calculations to an external program written in Python. The UEXTENALDB still retains some critical tasks, which can be summarized as:

1) Read plastic shear strains for each element (from gamma_cum_element array) and store the values at the start and end of the cycle, and store the minimum and maximum values over the cycle for each slip system of each element.

2) Calculate cyclic plastic shear strain range and ratcheting strains for each slip system of each element.

3) Calculate FIP^{α} for each slip system of each element and store in text file for python program.

4) Call the python program and wait for it to finish.

5) Read the list of cracked elements written by the python program and check for crack arrest. Store the list of cracked elements in the COMMONBLOCK so that they may be accessed by the UMAT. Store the CRACK_ARRESTED flag in the COMMONBLOCK if it exists so the simulation may be terminated.

The flow of the UEXTERNALDB execution is shown in Figure 111. One important task of the UEXTERNALDB besides the calculation of the variables associated with the fatigue evaluation is determining if the fatigue life (either nucleation or MSC) should be evaluated during this particular call. For this to occur, two conditions must be satisfied:

1) The Eval_Nuc or Eval_MSC flag is true

2) pre_step is true

The fatigue algorithms must be calculated following the completion of a loading cycle, and should logically occur at the end of the second loading step in that cycle. However, the UEXTERNALDB has no way of knowing if it is being called for the last increment of a particular loading step. Therefore, the fatigue life must be evaluated before the start of the next loading step. This is tracked by the logical variable ‘pre_step’ which is set to true if the UEXTERNALDB is being called with LOP = 1 for the first increment of a step. Note that pre_step could theoretically occur multiple times if the first increment of the loading step fails to converge, but because each new step begins with a very small initial increment size such an occurrence is unlikely.

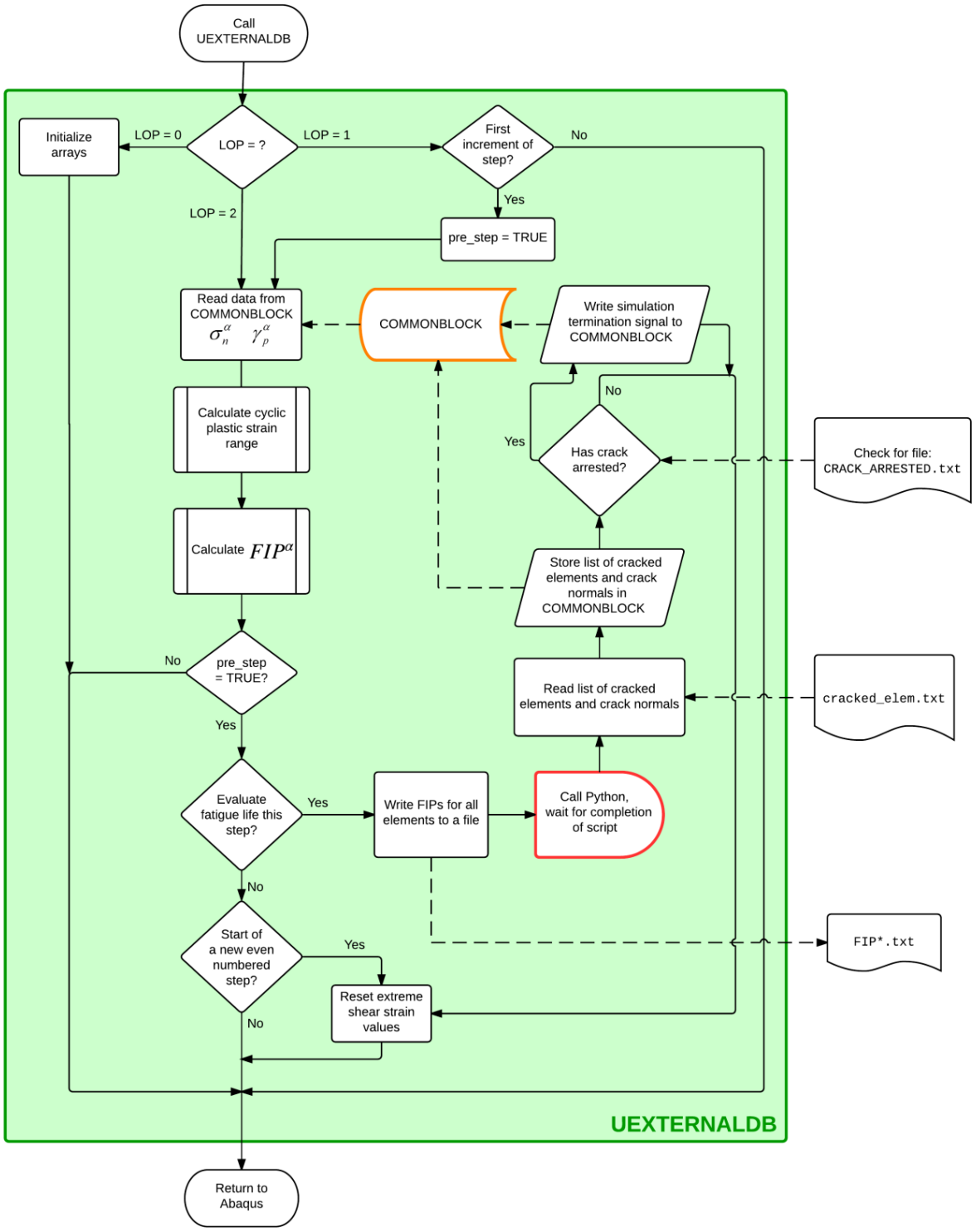

Figure 111. Tasks performed by the UEXTERNALDB.

Python Program

The tasks performed by the Python sub-program are split into multiple functions and modules for clarity, ease of debugging, and future expandability. The sections are:

Main.py – This module controls the execution of the fatigue algorithms and is responsible for calling or including all the additional python modules. The nucleation and MSC fatigue lives for both Stage I and Stage II growth are calculated by this module. The Main.py program accepts a number of options when called:

- *-nABQ*: If this option is included the program sequentially evaluates all the fatigue lives for which FIP data is available. This command is primarily used for post-processing or debugging.
- *-SI*: The program runs assuming a Stage I growth algorithm.
- *-nH*: The Stage I or Stage II algorithms run without history counting (explained in Chapter 4) active.

crack_neighbors.py – This module updates the lists of elements, grains, and bands that are in contact with the crack. The code in this module is directly executed by Main.py before the evaluation of MSC lives.

elem_in_plane.py – this module contains the function elem_in_plane(grain #, a, b, c, d) which determines the elements which comprise an arbitrary plane based on the grain number and the four constants of a plane, using the point-to-plane distance formula. The band width of the plane is read in from the global_vars.py module.

functions.py – as the name might suggest, this module contains a number of important functions:

- list_elem_in_band(grain, layer, plane) – returns a list of elements in a given crystallographic band, determined by reading the input file and scanning for the matching element set.
- list_elem_in_grain(grain) – returns a list of elements in a given grain, determined by reading the input file and scanning for the matching element set.
- FIP_el_update(i^{th} cracked grain) – Updates the FIP arrays based on values after most recent complete cycle. This must be called before fatigue lives are evaluated. Reads the FIP*.txt files and parses them into lists.
- Average_FIP(element list, slip system, list of FIPs) – calculates the volume averaged FIP on a particular slip system for a set of elements.

global_vars.py – This code reads in the constants associated with the mesh geometry (from Geom_def.txt) and the fatigue life calculation (from Definitions.txt). In addition it configures the error, information, and debugging logging (written to PythonLog.txt).

initialize_lists.py – This module is an executable section of code that runs each time Main.py is called. Its task is to initialize the numerous lists of elements and microstructural attributes needed for the evaluation of the fatigue life, and save them as serialized objects for fast future access using the python built-in pickle module. Thus these serialized lists, dictionaries, etc. are referred to collectively as "pickled objects". If the code senses that a given pickled object already exists in the run folder, it skips initialization and simply loads the object into memory for subsequent use by Main.py.

intermediate_plane.py –contains the function int_pln_cnsts(a_1, b_1, c_1, d_1, a_2, b_2, c_2, d_2, FIP_1, FIP_2) which returns the four constants of an intermediate plane defined by the

parent plane 1 and 2 and the two FIP values on these respective planes. The task executed by this function correspond to Eqn. 48, 50, and 51 given in Chapter 4.

Plane_eqn_const.py – this module contains the function Plane_eqn_const(grain, layer, plane) which returns the four constants of a plane in global coordinates of the input crystallographic plane.

Serialized Objects

In addition to the *.py files listed above, the working directory where the fatigue simulation is run will contain numerous pickled objects, which are serialized lists, dictionaries, etc. that serve two purposes. First, they contain information about the mesh which is somewhat time consuming to generate. This way, such information must only be generated during the first call of the program and can just be read into memory during subsequent calls. Second, they serve to pass variables between different sequential calls of the Python program. For instance, they keep track of which grains and elements have cracked as the simulation progresses. Most of these pickled objects are generated during the execution of initialize_lists.py.

- band_d_gr_nd.p – a dictionary object with a key of (G,L,SS) and a value corresponding to the increase in length of the band referenced by the key due to low misorientation neighbors. Generated by reading in d_gr_nd.txt which is written during the 1st call of the UEXTERNALDB.
- band_elem.p - a dictionary object that stores key: (Grain, Layer, Slip System), value: list of elements that band contains.

- band_history.p - a dictionary object that stores key: (Grain, Layer, Slip System), value: history information of the band. The value is only non-zero if the band was in contact with the crack during the last life evaluation.
- band_length.p – a dictionary object that stores key: (Grain, Layer, Slip System), value: length of band.
- crack_cycles.p – list containing the total cycles consumed after the i^{th} grain to crack
- crack_len.p – list containing the crack length after the i^{th} grain to crack
- crack_plane_normal.p – normal vector to the crack plane for each element, value is [0, 0, 0] if the element is not cracked.
- cracked_elem.p – list of elements within the crack.
- cracked_grain.p – list of grains that have been cracked.
- el_cntr.p – list containing the centroid of each element. Accessed by el_cntr[0-2][element # - 1] where indices 0 through 2 correspond to coordinates X through Z. Note that this list is zero indexed so raw element number cannot be used to access.
- elem_in_band.p – a dictionary of elements within a given band accessed by a (G,L,P) triplet.
- elem_in_grain.p – a list containing lists of element within a given grain. Accessed by elem_in_grain[grain #] which returns the list of elements.
- FIP_ratios.p – The ratio of (FIP_2 / FIP_1) calculated during the evaluation of the Stage II MSC life. Values closer to 1 indicate a higher propensity for Stage II growth, while very low values (~0.1) indicate near Stage I growth.

- grain_cntr.p – A list containing 3 lists of the grain centroids, corresponding to the X, Y, Z coordinates. For example, grain_cntr[0][4] accesses the X-coordinate of the centroid of grain 5 (due to 0 indexing of grains).
- grain_of_elem.p – A list containing the grain number to which a given element belongs. Accessed by grain_of_elem[element #]. Note that this list not zero indexed so the raw element number can be used to access the list.
- grain_orient.p – a list object containing the three Euler angles that define the orientation of a given grain, accesses by grain_orient[0-2][grain #] with 0-2 corresponding to the 3 Euler angles.
- min_life_band.p – A list soring the identifier of the band with minimum life determined to crack during each call of Main.py. If the band is a crystallographic band (corresponding to nucleation or MSC evaluation with only the Stage I algorithm active) the band is identified with a (G,L,P) triplet, else for arbitrary bands of elements (Stage II growth), the plane is identified by the grain number and four constants of a plane (G, a, b, c, d).
- min_life_val.p – A list storing the minimum life of the band determined to crack during each call of Main.py. The total fatigue life is obtained by summing all the values in this list.

The execution of the python program after being called by the UEXTERNALDB is illustrated in Figure 112.

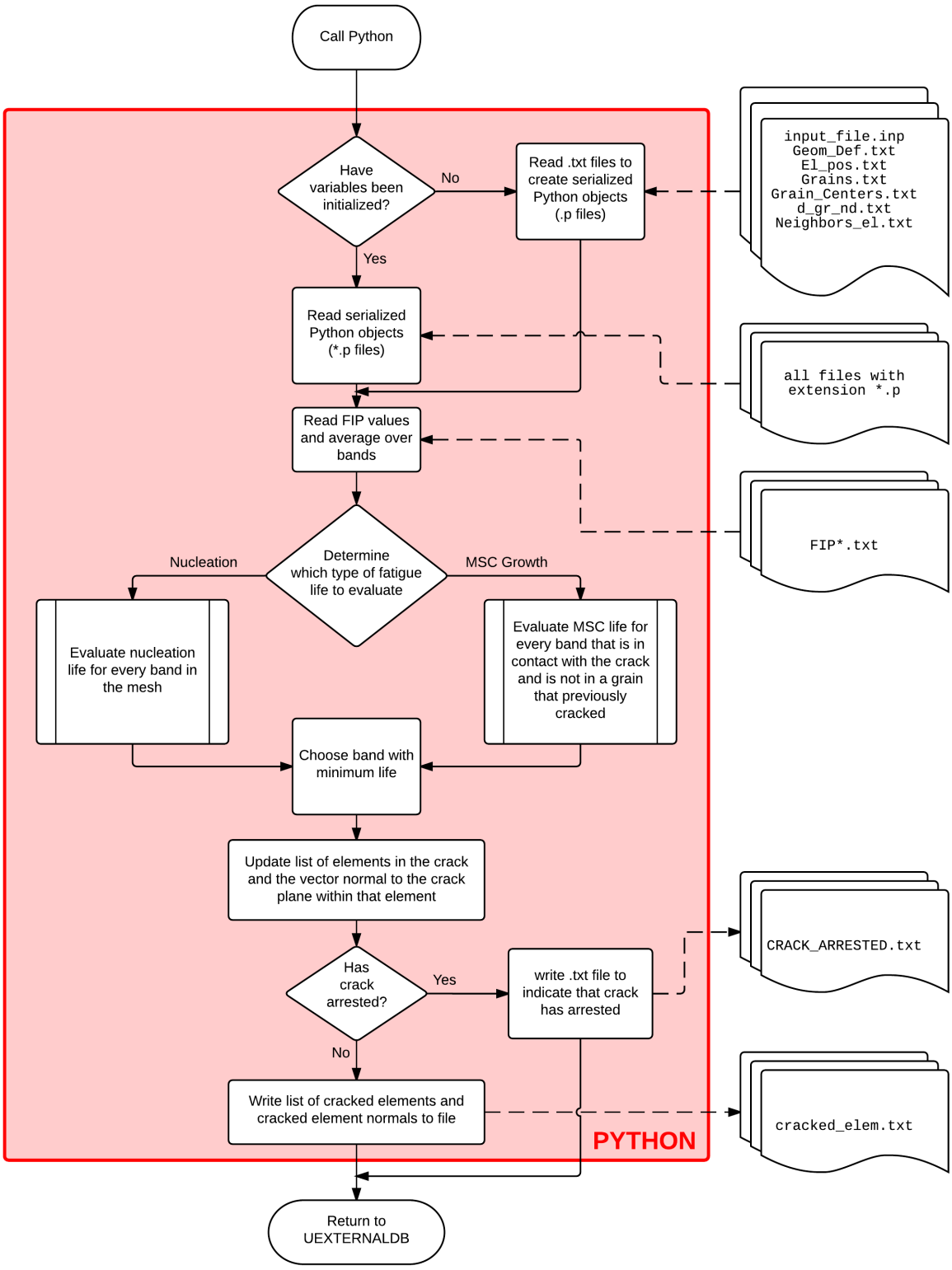

Figure 112. Flow chart of the execution of the Python program after being called by the UEXTERNALDB.

Text Files

Files required to run the fatigue simulation:

- Common_block_Alv02.txt – defines the arrays and variables stored in common memory accessible by both the UMAT and UEXTERNALDB.
- d_gr_nd.txt – file containing the contribution to band length due to low-misorientation neighbors.
- Definitions.txt – list of the fatigue constants
- disAngle.txt – lists the angle of disorientation between neighboring grains
- El_pos.txt - list of the X, Y, Z coordinate of the center of each element
- Geom_Def.txt – file containing constants associated with the mesh geometry, such as the number of elements, the mesh size, etc.
- Grain_Centers.txt – file containing the X, Y, Z coordinate of the centroid of each grain.
- Grains.txt – list of all the grains in the mesh and their crystallographic orientation as defined by the three Euler angles.
- Min_dist.txt – a large file containing information about the connectivity among bands.
- Neighbor_grains.txt – for each grain this contains both the total number of neighboring grains, and the number (as in the reference index) of each of these neighboring grains. For grain n, the number of neighboring grains is found on line (2n-1) and the index number of each of these neighbors is listed on line (2n).
- Neighbors_el.txt – a sequential list of the elements neighboring a given element. The row corresponds to the element number, and columns 1-26 contain the

number of the element occupying that neighbor position. If the number is 0, than the element has no neighbor in that position.

- Num_layer.txt - This file summarizes which grain and layer each element belongs to, as well as its orientation as defined by the three Euler angles.

Files potentially present in the run folder after execution of a simulation:

- CRACK_ARRESTED.txt – empty text file written by the python program if it determines the crack has arrested. The UEXTERNALDB checks for the presence of this file and terminates the simulation if found to avoid wasting computational resources.
- cracked_elem.txt – contains a list of the elements within the crack and the normal vector of the crack plane for each element.
- CrackGrowth_py.txt – file containing the summary of the crack length vs cycles and the FIP value in the cracked band.
- CSSC_Data_11.txt – Cyclic stress strain data in the X direction, averaged over all elements within the mesh.
- FIP_MSC#_el.txt – List of FIP^{α} for each of the 12 slip systems for each element in the mesh. A sequentially numbered file is generated by the UEXTERNALDB for each grain to crack. For instance, if 10 grains are cracked during a simulation, the run folder will contain the files FIP_MSC2_el.txt through FIP_MSC10.txt.
- FIP_Nuc_el.txt - List of FIP^{α} for each of the 12 slip systems for each element in the mesh. Only one of these files is generated by the UEXTERNALDB before the nucleation life is evaluated.

- PythonLog.txt – Contains logging and debugging information written during the call of the python program from the UEXTERNALDB. Options for what is written to this file are configurable in global_vars.py.

COMMONBLOCK

The COMMONBLOCK is a feature of Fortran that allows data to be shared between separate Fortran programs, and is used in this implementation to pass arrays and variables between the UMAT and the UEXTERNALDB subroutines. The COMMONBLOCK allocates a region of computer memory for storage of variables and arrays that is accessible by all programs that share the same COMMONBLOCK declaration. Note that COMMONBLOCK variables are persistent over the execution of the simulation, meaning that they remain unchanged from step to step and increment to increment unless explicitly modified. The storage of variables within the COMMONBLOCK can lead to hard to detect errors if care is not taken during their storage and access. To minimize the risk of this occurrence, each variable passed between the UMAT and UEXTERNALDB is assigned to its own uniquely named COMMONBLOCK. Although it is possible to store multiple variables or arrays within a single named COMMONBLOCK, this is not advised because of the higher propensity for error. Additionally, the COMMONBLOCK is implemented in a text file that is included during the compiling of the UMAT and UEXTERNALDB to insure that the blocks are declared identically in both programs (i.e. all arrays and variables have the same name, size, and type).

REFERENCES

1. Alcoa, *7075 Datasheet.* 2013.
2. Castelluccio, G., *A Study On The Influence Of Microstructure On Small Fatigue Cracks*. Ph.D. Thesis, 2012, Georgia Institute of Technology: Altanta, GA.
3. McGinty, R.D., *Multiscale Repersentation of Polycrystalline Inelasticity*. 2001, Georgia Institute of Technology. p. 407.
4. ABAQUS, *FEM software V6.9, Simulia Corp., Providence, RI, USA*. 2009.
5. Paris, P.C., Gomez, and Anderson, *A rational analytic theory of fatigue.* The Trend in Engineering, 1961. **13**: p. 9-14.
6. Suresh, S., *Fatigue of Materials*. 2nd ed. Vol. 2013. 2001: Cambridge University Press.
7. McClung, R.C., et al. *ANALYSIS OF SMALL CRACK BEHAVIOR FOR AIRFRAME APPLICATIONS*. in *FAA/NASA International Symposium on Advanced Structural Integrity Methods for Airframe Durability and Damage Tolerance*. 1994. Hampton, VA.
8. McDowell, D.L., *Basic issues in the mechanics of high cycle metal fatigue.* International Journal of Fracture, 1996: p. 103-45.
9. Socie, D.F. and G.B. Marquis, *Multiaxial Fatigue.* 2000, Warrendale, Pa: Society of Automotive Engineers, Inc.
10. Brown, M.W. and K.J. Miller, *A Theory for Fatigue Under Multiaxial Stress-Strain Conditions.* Proceedings of the Institute of Mechanical Engineers, 1973. **187**: p. 745-756.
11. Fatemi, A. and D.F. Socie, *A critical plane approach to multiaxial fatigue damage including out-of-phase loading.* Fatigue & Fracture of Engineering Materials & Structures, 1988. **11**(2).
12. Socie, D.F., *Critical plane approaches for multiaxial fatigue damage assessment*, in *Advances in Multiaxial Fatigue*, D.L. McDowell and R. Ellis, Editors. 1993, ASTM: Philidelphia. p. 7-36.
13. McDowell, D.L. and J.Y. Berard, *A Delta-J Based Approach to Biaxial Fatigue.* Fatigue & Fracture of Engineering Materials & Structures, 1992. **Volume 15**(Issue 8).
14. McDowell, D.L., *Multiaxial Fatigue Strength*. ASM Handbook Vol. 19. Vol. 19. 1996: ASM.
15. McDowell, D.L. and F.P.E. Dunne, *Microstructure-sensitive computational modeling of fatigue crack formation.* International Journal of Fatigue, 2010. **32**(9): p. 1521-1542.
16. Shenoy, M., J. Zhang, and D.L. McDowell, *Estimating fatigue sensitivity to polycrystalline Ni-base superalloy microstructures using a computational approach.* Fatigue & Fracture of Engineering Materials and Structures, 2007. **30**(10): p. 889-904.
17. Przybyla, C., et al., *Microstructure-sensitive modeling of high cycle fatigue.* International Journal of Fatigue, 2010. **32**(3): p. 512-525.

18. Bozek, J.E., et al., *A geometric approach to modeling microstructurally small fatigue crack formation: I. Probabilistic simulation of constituent particle cracking in AA 7075-T651*. Modelling and Simulation in Materials Science and Engineering, 2008. **16**(6): p. 065007.
19. Hochhalter, J.D., et al., *A geometric approach to modeling microstructurally small fatigue crack formation: II. Physically based modeling of microstructure-dependent slip localization and actuation of the crack nucleation mechanism in AA 7075-T651*. Modelling and Simulation in Materials Science and Engineering, 2010. **18**(4): p. 045004.
20. Hochhalter, J.D., et al., *A geometric approach to modeling microstructurally small fatigue crack formation: III. Development of a semi-empirical model for nucleation.* Modelling and Simulation in Materials Science and Engineering, 2011. **19**(3): p. 035008.
21. Castelluccio, G.M., W.D. Musinski, and D.L. McDowell, *Recent developments in assessing microstructure-sensitive early stage fatigue of polycrystals.* Current Opinion in Solid State and Materials Science, 2014.
22. Xue, Y., et al., *Microstructure-based multistage fatigue modeling of aluminum alloy 7075-T651*. Engineering Fracture Mechanics, 2007. **74**(17): p. 2810-2823.
23. Xue, Y., et al., *Micromechanisms of multistage fatigue crack growth in a high-strength aluminum alloy.* Acta Materialia, 2007. **55**(6): p. 1975-1984.
24. McDowell, D.L., et al., *Microstructure-based fatigue modeling of cast A356-T6 alloy*. Engineering Fracture Mechanics, 2003. **70**: p. 49-80.
25. Johnston, S.R., et al., *Three-dimensional finite element simulations of microstructurally small fatigue crack growth in 7075 aluminium alloy.* Fatigue & Fracture of Engineering Materials and Structures, 2006. **29**(8): p. 597-605.
26. Lankford, J., D.L. Davidson, and K.S. Chan, *The Influence of Crack Tip Plasticity in growth of small fatigue cracks.* Metallurgical Transactions A, 1984. **15A**(August).
27. Burns, J.T., J.M. Larsen, and R.P. Gangloff, *Effect of initiation feature on microstructure-scale fatigue crack propagation in Al–Zn–Mg–Cu.* International Journal of Fatigue, 2012. **42**: p. 104-121.
28. International, A., *Aluminum and Aluminum Alloys*. ASM Specialty Handbook, ed. J.R. Davis. 1993, Materials Park, OH: ASM International.
29. Nguyen, Thompson, and Bernstein, *Microstructural Effects on Hydrogen Embrittlement in a high purity 7075 aluminum alloy.* Acta Metallurgica, 1987. **35**(10): p. 2417-2425.
30. Li, J.-f., et al., *Mechanical properties, corrosion behaviors and microstructures of 7075 aluminium alloy with various aging treatments.* Transactions of Nonferrous Metals Society of China, 2008. **18**(4): p. 755-762.
31. LaFarie-Frenot, M.C. and C. Gasc, *Influence of age hardening on fatigue crack propagation behavior in 7075 aluminm alloy in vacuum.* Fatigue & Fracture of Engineering Materials & Structures, 1983. **6**(4): p. 329-344.
32. Starke, E.A. and J.C. Williams, *Microstructure and the Fracture Mechanics of Fatigue Crack Propagation*, R.P. Wei and R.P. Gangloff, Editors. 1989, ASTM.
33. Lin, F. and E.A. Starke, *The effect of Copper content and degree of recrystallization on the fatigue resistance of 7XXX-type Aluminum Alloys - II.*

Fatigue Crack Propagation. Materials Science and Engineering, 1980. **43**: p. 65-76.
34. Bucci, R.J., G. Nordmark, and E.A. Starke, *Selecting Aluminum Alloys to Resist Failure by Fracture Mechanisms*. 1996, ASM.
35. Jordon, J.B., et al., *Damage and stress state influence on the Bauschinger effect in aluminum alloys.* Mechanics of Materials, 2007. **39**(10): p. 920-931.
36. Gupta, V.K. and S.R. Agnew, *Fatigue crack surface crystallography near crack initiating particle clusters in precipitation hardened legacy and modern Al-Zn-Mg-Cu alloys.* International Journal of Fatigue, 2011. **33**(9): p. 1159-1174.
37. Harlow, D.G., J. Nardiello, and J. Payne, *The effect of constituent particles in aluminum alloys on fatigue damage evolution: Statistical observations.* International Journal of Fatigue, 2010. **32**(3): p. 505-511.
38. Payne, J., et al., *Observations of fatigue crack initiation in 7075-T651.* International Journal of Fatigue, 2010. **32**(2): p. 247-255.
39. Weiland, H., et al., *Microstructural aspects of crack nucleation during cyclic loading of AA7075-T651.* Engineering Fracture Mechanics, 2009. **76**(5): p. 709-714.
40. Li, P. and N.J. Marchand, *Crack Initiation Mechanisms in Low Cycle Fatigue of Aluminum Alloy 7075-T6.* Materials Science and Engineering, 1989. **A119**: p. 41-50.
41. Lankford, J., *The Growth Of Small Fatigue Cracks In 7075-T6 Aluminum.* Fatigue & Fracture of Engineering Materials & Structures, 1982. **5**(3): p. 233-248.
42. Pearson, *Initiation Of Fatigue Cracks In Commerical Al Alloys and the Subsequent Propagation of Very Short Cracks.* Engineering Fracture Mechanics, 1975.
43. Mayer, H., R. Schuller, and M. Fitzka, *Fatigue of 2024-T351 aluminium alloy at different load ratios up to 10E10 cycles.* International Journal of Fatigue, 2013. **57**: p. 113-119.
44. Halliday, M.D., C. Cooper, and P. Bowen, *On small fatigue crack growth and crack closure under mixed-mode and through zero loading in the aluminium alloys 2024-T351 and 8090-T8771.* International Journal of Fatigue, 2007. **29**(7): p. 1195-1207.
45. Merati, A., *A study of nucleation and fatigue behavior of an aerospace aluminum alloy 2024-T3.* International Journal of Fatigue, 2005. **27**(1): p. 33-44.
46. Marines, I., X. Bin, and C. Bathias, *An understanding of very high cycle fatigue of metals.* International Journal of Fatigue, 2003. **25**(9-11): p. 1101-1107.
47. Laz, P.J. and B.M. Hillberry, *Fatigue life prediction from inclusion initiated cracks.* International Journal of Fatigue, 1997. **20**(4): p. 263-270.
48. Bowles, C.Q. and J. Schijve, *The role of inclusions in fatigue crack initiation in an aluminum alloy.* International Journal of Fracture, 1971. **9**(2).
49. Kung, C.Y. and M.E. Fine, *Fatigue Crack Initiation and Microcrack Growth in 2024-T4 and 2124-T4 Aluminum Alloys.* Metallurgical Transactions A, 1979. **10A**(May).
50. Grosskreutz and Shaw, *Critical mechanisms in the development of fatigue cracks in aluminum 2024.* Procedings of the Second International Conference on Fracture, 1969: p. 620-629.

51. Oswald, L.E., *Effects of microstructure on high-cycle fatigue of an Al-Zn-Mg-Cu alloy (Al-7055)*, in *Materials Science and Engineering*. 2003, University of Pittsburgh.
52. Ritchie, R.O. and S. Suresh, *The fracture mechanics similitude concept: questions concerning its application to the behavior of short fatigue cracks.* Materials Science and Engineering, 1983. **57**(2): p. L27-L30.
53. Zurek, A.K., M.R. James, and W.L. Morris, *The Effect of Grain Size on Fatigue Growth of Short Cracks.* Metallurgical Transactions A, 1982. **14A**(August).
54. Tanaka, K., S. Matsuoka, and M. Kimura, *Fatigue Strength of 7075-T6 Aluminium Under Axial And Torsion Loading.* Fatigue & Fracture of Engineering Materials & Structures, 1984. **7**(3): p. 195-211.
55. Bu, R. and R.I. Stephens, *Comparison of short and long fatigue crack growth in 7075-T6 aluminum.* Fatigue & Fracture of Engineering Materials & Structures, 1986. **9**: p. 35-48.
56. Tokaji, K., T. Ogawa, and Y. Kameyama, *The effects of stress ratio on the growth behavior of small fatigue cracks in aluminum alloy 7075-T6 (with special interest in stage I crack growth).* Fatigue & Fracture of Engineering Materials & Structures, 1990. **13**(4): p. 411-421.
57. Petit, J. and K. Kosche, *Stage I and Stage II propagation of short and long cracks in Al-Zn-Mg Alloys.* 1992.
58. Kaynak and Ankara, *Short fatigue crack growth in Al 2024 and 7075.* Engineering Fracture Mechanics, 1992. **43**(5): p. 769-778.
59. Akiniwa, Y., K. Tanaka, and E. Matsui, *Statistical Characteristics of Propagation of Small Fatigue Cracks in Smooth Specimins of Aluminum Alloy 2024-T3.* Materials Science and Engineering, 1988. **A104**: p. 105-115.
60. Lankford, J. and D.L. Davidson, *Fatigue Crack Micromechanisms In Ingot 7075.* Acta Metallurgica, 1983. **31**(8): p. 1273-1284.
61. Chan, K.S., J. Lankford, and D.L. Davidson, *A Comparison of Crack-Tip Field Parameters for Large and Small Fatigue Cracks* ASME Journal of Engineering Materials and Technology, 1986. **108**: p. 206-213.
62. White, P., S. Barter, and L. Molent, *Observations of crack path changes caused by periodic underloads in AA7050-T7451.* International Journal of Fatigue, 2008. **30**: p. 1267-1278.
63. Suresh, S., A.K. Vasudevan, and P.E. Bretz, *Mechanicsms of Slow Fatigue Crack Growth in High Strength Aluminum Alloys: Role of Microstructure and Enviroment.* Metallurgical Transactions A, 1984. **15A**: p. 10.
64. Lankford, J., *The Effect Of Environment On The Growth Of Small Fatigue Cracks.* Fatigue & Fracture of Engineering Materials & Structures, 1983. **6**(1): p. 15-31.
65. Forsyth, P.J.E., *Fatigue Damage and Crack Growth in Aluminum alloys.* Acta Metallurgica, 1963. **11**(July).
66. LI, C., *Vector ctd analysis for crystallographic crack growth.* 1990.
67. Neumann, P., *Coarse Slip Model of Fatigue.* Acta Metallurgica, 1969. **17**(September): p. 1219-1225.
68. Neumann, P., *New experiments concerning the slip processes at propagating fatigue cracks- I.* Acta Metallurgica, 1974. **22**(September): p. 1155-1165.

69. Gupta, V.K., R.P. Gangloff, and S.R. Agnew, *Diffraction characterization of microstructure scale fatigue crack growth in a modern Al–Zn–Mg–Cu alloy.* International Journal of Fatigue, 2012. **42**: p. 131-146.
70. Ro, Y., S.R. Agnew, and R.P. Gangloff, *Environmental Fatigue-Crack Surface Crystallography for Al-Zn-Cu-Mg-Mn/Zr.* Metallurgical and Materials Transactions A, 2008. **39**(6): p. 1449-1465.
71. Hochhalter, J.D., *Finite Element Simulations Of Fatigue Crack Stages In AA 7075-T651 Microstructure*. Ph.D. Thesis, 2010, Cornell University: Ithaca, NY.
72. Gates, N. and A. Fatemi, *Notched fatigue behavior and stress analysis under multiaxial states of stress.* International Journal of Fatigue, 2014.
73. Misak, H.E., et al., *Crack growth behavior of 7075-T6 under biaxial tension–tension fatigue.* International Journal of Fatigue, 2013. **55**: p. 158-165.
74. Vasudevan, A.K. and S. Suresh, *Influence of Corrosion Deposits on Near-Threshold Fatigue Crack Growth Behavior in 2XXX and 7XXX Series Aluminum Alloys.* Metallurgical Transactions A, 1982. **13A**(December).
75. Wei, R.P., et al., *Fracture Mechanics and Surface Studies of Fatigue Crack Growth in an Aluminum Alloy.* Metallurgical Transactions A, 1980. **January**: p. 151-158.
76. Sun, Y., Q. Peng, and G. Lu, *Quantum mechanical modeling of hydrogen assisted cracking in aluminum.* Physical Review B, 2013. **88**(10).
77. Bucci, R.J., et al., *Ranking 7XXX Aluminum Alloy FCG resistance under constant amplitude and spectrum loading*, in *Effect of Load Spectrum Variables on Fatigue Crack Initiation and Propagation*, D.F. Bryan and J.M. Potter, Editors. 1980.
78. Darvish and Johansson, *FCG studies under combination of single overload and cylic condesnsation enviroment.* Engineering Fracture Mechanics, 1995.
79. Zhao, T., J. Zhang, and Y. Jiang, *A study of fatigue crack growth of 7075-T651 aluminum alloy.* International Journal of Fatigue, 2008. **30**(7): p. 1169-1180.
80. Suresh, S., *Micromechanisms of fatigue crack growth retardation following overloads.* Engineering Fracture Mechanics, 1983. **18**(3): p. 577-593.
81. Bilby, B.A., L.R.T. Gardner, and A.N. Stroh. *Continuous distributions of dislocations and the theory of plasticity*. in *Extrait des Actes du IXe Congre`s International de MeÅLcanique AppliqueÅLe*. 1957. Bruxelles.
82. Lee, E.H., *Elastic-Plastic Deformation at Finite Strains.* Journal of Applied Mechanics, 1969. **36**: p. 1-6.
83. Asaro, R.J., *Micromechanics of crystals and polycrystals*. Technical report (Brown University. Division of Engineering), MRL E-139. 1982, Providence, R.I.: Division of Engineering, Brown University. 144.
84. Frederick, C.O. and P.J. Armstrong, *A mathematical representation of the multiaxial Bauschinger effect*. 1966: G.E.G.B. Report RD/B/N 731.
85. Ohno, N. and J.D. Wang, *Kinematic hardening rules with critical state of dynamic recovery, Part I: Formulation and basic features for ratchetting behavior.* International Journal of Plasticity, 1993. **9**: p. 375-390.
86. McDowell, D.L., *Stress state dependence of cyclic ratchetting behavior of two rail steels.* International Journal of Plasticity, 1995. **11**(4): p. 397-421.
87. Kocks, U.F., *The Relation Between Polycrystal Deformation and Single-Crystal Deformation* Metallurgical Transactions, 1970. **1**(May): p. 1121-1143.

88. Yan, J., et al., *Latent Hardening in Aluminium Single Crystals under Cyclic Loading.* physica status solidi (a), 1990. **122**: p. 195-205.
89. Laird, C., *The General Cyclic Stress-Strain Response of Aluminum Alloys*, in *Cyclic Stress Strain and Plastic Deformation Aspects of Fatigue Crack Growth*. 1976, ASTM.
90. Colin, J., *Deformation History and Load Sequence Effects on Cumulative Fatigue Damage*. Ph.D. Thesis, 2009, University of Toledo: Toledo, OH. p. 264.
91. Arcari, A., *Enhanced strain-based fatigue methodology for high strength aluminum alloys*, in *Engineering Mechanics*. Ph.D. Thesis, 2010, Virginia Polytechnic Institute and State University. p. 245.
92. Renard, A., et al., *The Cyclic Stress-Strain Response of a Polycrystalline Al-Zn-Mg Alloy and Commercial Alloys Based on this System.* Materials Science and Engineering, 1983. **60**: p. 113-120.
93. Chaboche, *On some modifications of kinematic hardening to improve the description of ratchetting effects.* International Journal of Plasticity, 1991. **7**: p. 661-678.
94. Chaboche, J.L. and D. Nouailhas, *Constitutive Modeling of Ratchetting Effects—Part I: Experimental Facts and Properties of the Classical Models.* Journal of Engineering Materials and Technology, 1989. **111**: p. 384-392.
95. Chaboche, J.L. and D. Nouailhas, *Constitutive Modeling of Ratchetting Effects—Part II: Possibilities of Some Additional Kinematic Rules.* Journal of Engineering Materials and Technology, 1989. **111**: p. 409-416.
96. Bower, A.F., *Cyclic Hardening Properties Of Hard-Drawn Copper And Rail Steel.* Journal of the Mechanics and Physics of Solids, 1989. **37**(4): p. 455-470.
97. Arcari, A., R. De Vita, and N.E. Dowling, *Mean stress relaxation during cyclic straining of high strength aluminum alloys.* International Journal of Fatigue, 2009. **31**(11-12): p. 1742-1750.
98. Arcari, A. and N.E. Dowling, *Modeling mean stress relaxation in variable amplitude loading for 7075-T6511 and 7249-T76511 high strength aluminum alloys.* International Journal of Fatigue, 2012. **42**: p. 238-247.
99. McDowell, D.L., *Simulation-based strategies for microstructure-sensitive fatigue modeling.* Materials Science and Engineering: A, 2007. **468-470**: p. 4-14.
100. Musinski, W., *Novel methods for microstructure-sensitive probabilistic fatigue notch factor*. Masters Thesis, 2010, Georgia Institute of Technology: Atlanta, GA.
101. Turkmen, H.S., et al., *On the mechanical behaviour of AA 7075-T6 during cyclic loading.* International Journal of Fatigue, 2003. **25**(4): p. 267-281.
102. Groeber, M.A. and M.A. Jackson, *DREAM.3D: A Digital Representation Environment for the Analysis of Microstructure in 3D.* Integrating Materials and Manufacturing Innovation, 2014. **3**(5).
103. Tanaka, K. and T. Mura, *A dislocation model for fatigue crack initiation.* Journal of Applied Mechanics, 1981. **48**(1): p. 97-103.
104. Chan, K.S., *A Microstructure-Based Fatigue-Crack-Initiation Model.* Metallurgical and Materials Transactions A, 2003. **43A**: p. 43-58.
105. *Python Software Foundation. Python Language Reference, version 2.7*. Available at http://www.python.org].

106. Weisstein, E.W. *Plane-Plane Intersection*. MathWorld--A Wolfram Web Resource. http://mathworld.wolfram.com/Plane-PlaneIntersection.html [cited 2015 3/23/2015].
107. Dowling, N.E., *Mechanical Behavior of Materials*. 2nd ed. 1998, Upper Saddle River, NJ: Prentice Hall.
108. Zhao, T. and Y. Jiang, *Fatigue of 7075-T651 aluminum alloy.* International Journal of Fatigue, 2008. **30**(5): p. 834-849.
109. Materials, A.S.f.T.a., *E 647-95a*, in *Standard test method for measurement of fatigue crack growth rates*. 1999: Philadelphia, PA. p. 577–613.
110. Donnelly, E. and D. Nelson, *A study of small crack growth in 7075-T6.* International Journal of Fatigue, 2002. **24**(11): p. 1175-1189.
111. Kendall, J.M. and J.E. King, *Short fatigue crack growth behaviour: data analysis effects.* International Journal of Fatigue, 1988. **10**(3): p. 163-170.